Spatiotemporal dynamics of continuum neural fields

2012 J. Phys. A: Math. Theor. 45 033001

(http://iopscience.iop.org/1751-8121/45/3/033001)

IOP PUBLISHING JOURNAL OF PHYSICS A: MATHEMATICAL AND THEORETICAL

J. Phys. A: Math. Theor. **45** (2012) 033001 (109pp) doi:10.1088/1751-8113/45/3/033001

TOPICAL REVIEW

Spatiotemporal dynamics of continuum neural fields

Paul C Bressloff

Department of Mathematics, University of Utah, 155 South 1400 East, Salt Lake City, UT 84112, USA

E-mail: bressloff@math.utah.edu

Received 21 July 2011, in final form 11 November 2011
Published 14 December 2011
Online at stacks.iop.org/JPhysA/45/033001

Abstract

We survey recent analytical approaches to studying the spatiotemporal dynamics of continuum neural fields. Neural fields model the large-scale dynamics of spatially structured biological neural networks in terms of nonlinear integrodifferential equations whose associated integral kernels represent the spatial distribution of neuronal synaptic connections. They provide an important example of spatially extended excitable systems with nonlocal interactions and exhibit a wide range of spatially coherent dynamics including traveling waves oscillations and Turing-like patterns.

PACS numbers: 87.19.L−, 87.19.lj, 87.19.lp, 87.19.lq, 87.10.Ed, 05.40.−a

(Some figures may appear in colour only in the online journal)

Contents

1. Introduction 2
2. From neural networks to neural fields 3
   2.1. Conductance-based model of a neuron 3
   2.2. Synaptic processing 6
   2.3. Dendritic filtering of synaptic inputs 8
   2.4. Rate-based neural network models 9
   2.5. Spatially structured networks and neural fields 13
3. Traveling waves 17
   3.1. Traveling fronts in a scalar neural field 18
   3.2. Wave stability and Evans functions 20
   3.3. Traveling pulses in adaptive neural fields 23
   3.4. Adaptive neural field model of wave propagation during perceptual switching 29
   3.5. Wave propagation failure in inhomogeneous neural fields 32
   3.6. Spatially structured oscillations and spiral waves 37

4. Persistent spatially localized activity states (bumps) 40
4.1. Exact bump solutions in a 1D neural field with lateral inhibition 40
4.2. Exact bump solutions in a 2D neural field with lateral inhibition 45
4.3. Stimulus-driven bumps 50
5. Neural pattern formation 56
5.1. Turing mechanism for cortical pattern formation 56
5.2. Neural field model of primary visual cortex (V1) 60
5.3. Pattern formation in the ring model of a single hypercolumn 66
5.4. Pattern formation in a coupled hypercolumn model 69
5.5. Geometric visual hallucinations 79
6. Stochastic neural field theory 81
6.1. Population density method and mean field theory 82
6.2. Stochastic rate-based models 88
6.3. Patterns and waves in stochastic neural fields 90
6.4. Path integral representation of stochastic neural fields 95
7. Discussion 100
Acknowledgments 101
References 102

1. Introduction

Analysis of the dynamical mechanisms underlying spatially structured activity states in neural tissue is crucially important for understanding a wide range of neurobiological phenomena, both naturally occurring and pathological. For example, neurological disorders such as epilepsy are characterized by spatially localized oscillations and waves propagating across the surface of the brain [1], whilst traveling waves can be induced *in vitro* by electrically stimulating disinhibited cortical slices [2–5]. Spatially coherent activity states are also prevalent during the normal functioning of the brain, encoding local properties of visual stimuli [6], representing head direction [7], and maintaining persistent activity states in short-term working memory [8, 9]. One of the major challenges in neurobiology is understanding the relationship between spatially structured activity states and the underlying neural circuitry that supports them. This has led to considerable recent interest in studying reduced continuum neural field models in which the large-scale dynamics of spatially structured networks of neurons is described in terms of nonlinear integrodifferential equations, whose associated integral kernels represent the spatial distribution of neuronal synaptic connections. Such models, which build upon the original work of Wilson, Cowan and Amari [10–12], provide an important example of spatially extended excitable systems with nonlocal interactions. As in the case of nonlinear partial differential equation (PDE) models of diffusively coupled excitable systems [13, 14], neural field models can exhibit a rich repertoire of spatiotemporal dynamics, including solitary traveling fronts and pulses, stationary pulses and spatially localized oscillations (breathers), spiral waves, and Turing-like patterns [15, 16]. In recent years, neural fields have been used to model a wide range of neurobiological phenomena, including wave propagation in cortical slices [4, 17] and *in vivo* [18], geometric visual hallucinations [19, 20], EEG rhythms [21–24], orientation tuning in primary visual cortex (V1) [25, 26], short term working memory [27, 28], control of head direction [29], and motion perception [30].

In this review we present a detailed survey of the nonlinear dynamics of continuum neural fields. In particular, we give a pedagogical account of analytical methods for solving these integrodifferential equations, which are adapted from previous studies of nonlinear PDEs. These include regular and singular perturbation methods, weakly nonlinear analysis and pattern

formation, symmetric bifurcation theory, Evans functions and wave stability, homogenization theory and averaging, and stochastic processes. We also consider exact methods of solution based on the use of Heaviside nonlinearities. Although we mainly focus on dynamical aspects of neural fields, we also highlight various neurobiological applications. The structure of the review is as follows. We begin by describing the sequence of simplifying approximations that can be used to derive continuum neural field equations starting from a conductance-based model of a network of synaptically coupled spiking neurons (section 2). This provides the necessary background for understanding the biological basis of neural field equations and how they relate to discrete neural network models. We then systematically cover three distinct forms of spatiotemporal dynamics, traveling waves (section 3), spatially localized persistent activity states (section 4), and neural pattern formation (section 5). In the last case, we focus on neural field models of primary visual cortex (V1), which is the first region of the cerebral cortex to process visual information from the eyes. We end the review by discussing some recent work on extending neural field equations to take into account the effects of noise (section 6).

2. From neural networks to neural fields

We begin by describing the basic biological components of synaptically coupled networks of spiking neurons. We consider conductance-based models of action potential generation (section 2.1), synaptic processing (section 2.2), and dendritic processing (section 2.3). We then highlight a sequence of approximations that can be made to reduce a network of spiking neurons to an effective rate-based model, distinguishing between voltage-based and activity-based versions along the lines of Ermentrout [15, 31]. This provides a biological perspective on well-known neural network models such as Hopfield networks [32]. Finally, we consider spatially structured neural networks, which are needed in order to represent the spatial organization of cerebral cortex, and show how to derive from these various forms of neural field equations in the continuum limit (section 2.5). The advantage of a continuum rather than a discrete representation of spatially structured networks is that various techniques from the analysis of PDEs can be adapted to study the nonlinear dynamics of cortical patterns, oscillations and waves, which will be explored in the remainder of the review.

2.1. Conductance-based model of a neuron

Cortical neurons typically consist of a cell body (or soma) where the nucleus containing DNA is located, a branching output structure known as the axon and a branching input structure known as the dendritic tree, see figure 1. Neurons mainly communicate with each other by sending electrical impulses or spikes (action potentials) along their axons. (Some neurons are also coupled diffusively via gap junctions [33].) These axons make contacts on the dendrites of other neurons via microscopic junctions known as synapses. The arrival of an electrical spike at a synaptic junction leads to the flow of electrical current along the dendritic tree of the stimulated neuron. If the total synaptic current from all of the activated synapses forces the electrical potential within the cell body to cross some threshold, then the neuron fires a spike. The standard biophysical model for describing the dynamics of a single neuron with somatic membrane potential V is based upon conservation of electric charge:

$$C\frac{\mathrm{d}V}{\mathrm{d}t} = -I_{\mathrm{con}} + I_{\mathrm{syn}} + I_{\mathrm{ext}}, \tag{2.1}$$

where C is the cell capacitance, I_{con} is the membrane current, I_{syn} denotes the sum of synaptic currents entering the cell and I_{ext} describes any externally injected currents. Ions can diffuse in and out of the cell through ion specific channels embedded in the cell membrane. Ion

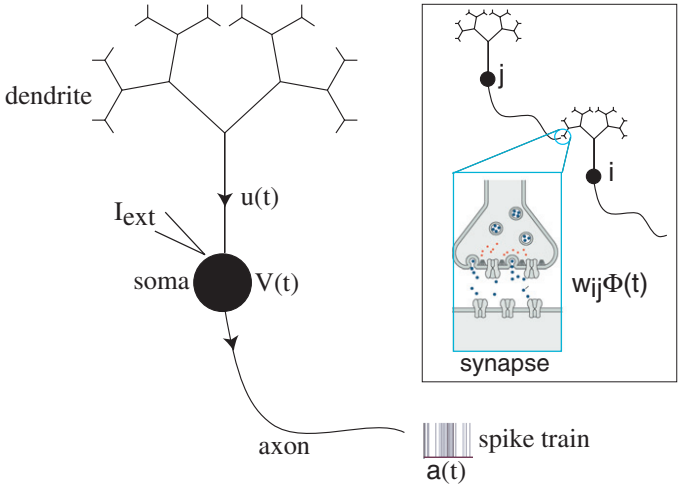

Figure 1. Basic structure of a neuron. Inset shows a synaptic connection from an upstream or presynaptic neuron labeled j and a downstream or postsynaptic neuron labeled i. w_{ij} denotes the weight or strength of the synapse and $\Phi(t)$ is the time course of synaptic processing. See text for details.

pumps within the cell membrane maintain concentration gradients, such that there is a higher concentration of Na^+ and Ca^{2+} outside the cell and a higher concentration of K^+ inside the cell. The membrane current through a specific channel varies approximately linearly with changes in the potential V relative to some equilibrium or reversal potential, which is the potential at which there is a balance between the opposing effects of diffusion and electrical forces. Summing over all channel types, the total membrane current (flow of positive ions) leaving the cell through the cell membrane is

$$I_{\text{con}} = \sum_s g_s(V - V_s), \tag{2.2}$$

where g_s is the conductance due to channels of type s and V_s is the corresponding reversal potential.

The generation and propagation of an action potential arises from nonlinearities associated with active membrane conductances. Recordings of the current flowing through single channels indicate that channels fluctuate rapidly between open and closed states in a stochastic fashion. Nevertheless, most models of a neuron use deterministic descriptions of conductance changes, under the assumption that there are a large number of approximately independent channels of each type. It then follows from the law of large numbers that the fraction of channels open at any given time is approximately equal to the probability that any one channel is in an open state. The conductance g_s for ion channels of type s is thus taken to be the product $g_s = \bar{g}_s P_s$ where $\bar{g}_s$ is equal to the density of channels in the membrane multiplied by the conductance of a single channel and P_s is the fraction of open channels. The voltage-dependence of the probabilities P_s in the case of a delayed-rectifier K^+ current and a fast Na^+ current were originally obtained by Hodgkin and Huxley [34] as part of their Nobel prize winning work on the generation of action potentials in the squid giant axon. The delayed-rectifier K^+ current is responsible for repolarizing a neuron after an action potential. One finds that opening of the K^+ channel requires structural changes in 4 identical and independent subunits so that $P_K = n^4$ where n is the probability that any one gate subunit has opened. In the case of the

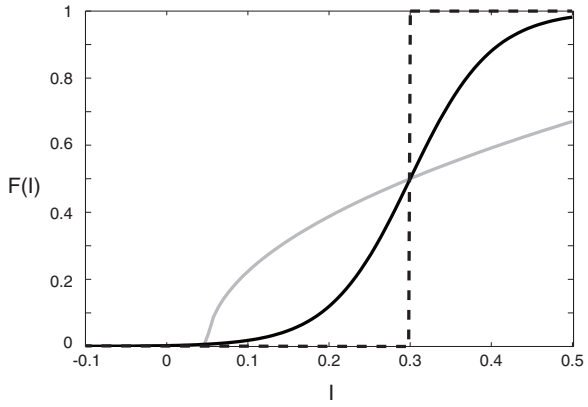

Figure 2. Various forms of the nonlinear firing-rate function $F(I)$. Sigmoid function (black curve) and Heaviside function (dashed curve) have a threshold $\kappa = 0.3$, whereas the square root function (gray curve) has a critical current $I_c = 0.05$.

fast Na^+ current, which is responsible for the rapid depolarization of a cell leading to action potential generation, the probability of an open channel takes the form $P_{Na} = m^3 h$ where m^3 is the probability that an activating gate is open and h is the probability that an inactivating gate is open. Depolarization causes m to increase and h to decrease, whereas hyperpolarization has the opposite effect. The dynamics of the gating variables m, n, h are usually formulated in terms of a simple kinetic scheme that describes voltage-dependent transitions of each gating subunit between open and closed states. More specifically, for each $X \in \{m, n, h\}$

$$\frac{dX}{dt} = \alpha_X(V)(1 - X) - \beta_X(V)X, \tag{2.3}$$

where $\alpha_X(V)$ is the rate of the transition *closed* $\rightarrow$ *open* and $\beta_X(V)$ is the rate of the reverse transition *open* $\rightarrow$ *closed*. The transition rates are typically bounded, monotonic functions of the voltage V.

For the moment, let us ignore synaptic currents and consider what happens as the external input I_{ext} is increased. Experimentally it is found that most cortical neurons switch from a resting state characterized by a low rate of (noise-driven) spontaneous firing to an active state characterized by either tonic (regular, repetitive) firing or bursting [35]. There has been considerable theoretical work on the transitions from resting to active states in conductance-based models based on bifurcation theory, see [31, 36] for excellent recent reviews. We will focus on tonic firing neurons, since these comprise the majority of cells in cortical networks. In the case of constant input $I_{\text{ext}} = I$, the firing rate a (number of spikes per second) of the neuron is a nonlinear function of the input:

$$a = F(I) \tag{2.4}$$

with the form of F depending on the nature of the bifurcation to repetitive firing. A common bifurcation scenario in conductance-based models of cortical neurons is a saddle node on an invariant circle [31, 36], so that close to the bifurcation point, see figure 2, we have

$$F(I) = F_0\sqrt{I - I_c}, \tag{2.5}$$

where I_c is the critical current for onset of regular spiking. If one includes stochastic effects arising from synaptic and membrane noise, for example, then the effective mean firing rate becomes a smooth sigmoid-like function of injected current, which is often modeled as

$$F(I) = \frac{F_0}{1 + \mathrm{e}^{-\eta(I-\kappa)}}, \tag{2.6}$$

where η is the gain and κ is the firing threshold. In the high-gain limit $\eta \to \infty$, this reduces to a Heaviside firing rate function

$$F(I) = F_0 H(I - \kappa) = \begin{cases} F_0 & \text{if} \quad I > \kappa \\ 0 & \text{if} \quad I < \kappa \end{cases}. \tag{2.7}$$

Yet another commonly used firing rate function is the piecewise linear function

$$F(I) = \begin{cases} 0, & I < \kappa, \\ \eta(u - \kappa), & \kappa < I < \kappa + \eta^{-1}, \\ 1, & I > \kappa + \eta^{-1}. \end{cases} \tag{2.8}$$

This preserves the hard threshold of the saddle-node on a limit cycle bifurcation but ensures that the firing rate saturates at high input currents.

2.2. Synaptic processing

The basic stages of synaptic processing induced by the arrival of an action potential at an axon terminal is as follows. (See [37] for a more detailed description.) An action potential arriving at the terminal of a presynaptic axon causes voltage-gated Ca^{2+} channels within an active zone to open. The influx of Ca^{2+} produces a high concentration of Ca^{2+} near the active zone [38, 39], which in turn causes vesicles containing neurotransmitter to fuse with the presynaptic cell membrane and release their contents into the synaptic cleft (a process known as exocytosis). The released neurotransmitter molecules then diffuse across the synaptic cleft and bind to specific receptors on the post-synaptic membrane. These receptors cause ion channels to open, thereby changing the membrane conductance and membrane potential of the postsynaptic cell. A single synaptic event due to the arrival of an action potential at time T induces a synaptic current of the form

$$I_{\mathrm{syn}}(t) = g_{\mathrm{syn}}(t - T)(V_{\mathrm{syn}} - V(t)), \tag{2.9}$$

where V is the voltage of the postsynaptic neuron, V_{syn} is the synaptic reversal potential and $g_{\mathrm{syn}}(t)$ is the change in synaptic conductance with $g_{\mathrm{syn}}(t) = 0$ for $t < 0$. A typical form for $g_{\mathrm{syn}}(t)$ is the difference of exponentials

$$g_{\mathrm{syn}}(t) = \bar{g}\left(\frac{1}{\tau_d} - \frac{1}{\tau_r}\right)^{-1} (\mathrm{e}^{-t/\tau_d} - \mathrm{e}^{-t/\tau_r})H(t), \tag{2.10}$$

where $H(t)$ is the Heaviside function, $\bar{g}$ is a constant conductance and $\tau_{r,d}$ are time constants determining the rise and fall of the synaptic response respectively. In the limit $\tau_d \to \tau_r = \alpha^{-1}$, equation (2.10) reduces to the so-called α function

$$g_{\mathrm{syn}}(t) = \bar{g}\alpha(t), \qquad \alpha(t) = \alpha^2 t\, \mathrm{e}^{-\alpha t} H(t). \tag{2.11}$$

In many cases, the rise time is much shorter than the fall time ($\tau_r \ll \tau_d$) so that we have an exponential synapse with $g_{\mathrm{syn}}(t) = \bar{g}\,\mathrm{e}^{-t/\tau_d}$. The sign of V_{syn} relative to the resting potential V_{rest} (typically $V_{\mathrm{rest}} \approx -65$ mV) determines whether the synapse is excitatory ($V_{\mathrm{syn}} > V_{\mathrm{rest}}$) or inhibitory ($V_{\mathrm{syn}} < V_{\mathrm{rest}}$). For simplicity, it is often assumed that a neuron spends most of its time close to rest such that $V_{\mathrm{syn}} - V \approx V_{\mathrm{syn}} - V_{\mathrm{rest}}$, with the factor $V_{\mathrm{syn}} - V_{\mathrm{rest}}$ absorbed into g_{syn}. One is then effectively taking the arrival of a spike as generating a synaptic current rather than a change in conductance.

A single synaptic event due to the arrival of an action potential at time T induces a synaptic current of the form (2.9). As a crude approximation we might try summing individual responses to model the synaptic current arising from a train of action potentials arriving at times T^m, integer m:

$$I_{\rm syn}(t) = \sum_m g_{\rm syn}(t - T^m)(V_{\rm syn} - V(t)). \tag{2.12}$$

Note that this sum only includes spikes for which $T^m < t$ since $g_{\rm syn}(t) = 0$ for $t < 0$ (causality condition). For many synapses such a simple ansatz does not hold, since some form of short-term synaptic depression causes the amplitude of the response to depend on the previous history of presynaptic firing [40, 41]. One way to incorporate this history-dependent effect is to take [42]

$$I_{\rm syn}(t) = \left[\sum_m q(T^m) g_{\rm syn}(t - T^m)\right](V_{\rm syn} - V(t)), \tag{2.13}$$

where the factor $q(T^m)$ reduces the response evoked by an action potential by an amount that depends upon the details of the previous spike train data. One interpretation of the factor q is that it represents a short-term (reversible) reduction in the release probability for synaptic transmission due to a depletion in the number of vesicles that can readily fuse with the cell membrane [43]. In certain cases, it is also possible for a synapse to undergo a temporary facilitation in response to activation, which may be due to the presence of residual calcium in the axonal terminal [43].

A common phenomenological model of synaptic depression is to assume that between spikes $q(t)$ relaxes at a rate τ_q to its steady state value of 1, but that directly after the arrival of a spike it changes discontinuously, that is, $q \to \gamma q$ with $\gamma < 1$. The depression time constant τ_q can vary between around 100 ms and a few seconds [41]. The model for synaptic depression may be written succinctly as

$$\frac{{\rm d}q}{{\rm d}t} = \frac{(1-q)}{\tau_q} - (1-\gamma)\sum_n q(T^n)\delta(t - T^n), \qquad q(0) = 1 \tag{2.14}$$

which has the solution of the form

$$q(T^m) = 1 - (1-\gamma)\sum_{n<m} \gamma^{[m-n-1]\beta}\, {\rm e}^{-(T^m - T^n)/\tau_q}. \tag{2.15}$$

Assuming a regular sequence of incoming spikes $T^n - T^{n-1} = \Delta$ for all n we find that the asymptotic amplitude $q_\infty(\Delta) \equiv \lim_{m\to\infty} q(T^m)$ is given by

$$q_\infty(\Delta) = \frac{1 - {\rm e}^{-\Delta/\tau_q}}{1 - \gamma\, {\rm e}^{-\Delta/\tau_q}}. \tag{2.16}$$

One possible computational role for synaptic depression is as a mechanism for cortical gain control [41]. The basic idea can be understood from the dependence of the asymptotic amplitude $q_\infty(\Delta)$ on the stimulus frequency $f = \Delta^{-1}$. Assuming that $\tau_q \gg \Delta$, we can Taylor expand q_∞ in equation (2.16) to find that $q_\infty(f) \approx \Gamma/f$, where $\Gamma = \tau_q/(1-\gamma)$. The main point to note is that the postsynaptic response per unit time is approximately independent of f (assuming that each spike elicits the same response in the steady-state). This means that the synapse is very sensitive to changes in the stimulus frequency. The instantaneous response to a rapid increase Δf in the stimulus rate is given by $\Gamma \Delta f/f$. In other words, the synapse responds to relative rather than absolute changes in the rate of input stimulation.

Figure 3. Schematic diagram of a neuron consisting of a soma resistively coupled to one end of a dendritic cable. A synaptic conductance change $\Delta g(x,t)$ at position x on the cable induces a synaptic current into the soma at $x = 0$.

2.3. Dendritic filtering of synaptic inputs

So far we have neglected the fact that the synapses of a neuron are spatially distributed across the neuron's dendritic tree. At the simplest level, the dendritic tree can be treated as a passive electrical medium that filters incoming synaptic stimuli in a diffusive manner. The current flow and potential changes along a branch of the tree may be described with a second-order, linear PDE commonly known as the *cable equation* [44, 45]. The cable equation is based on a number of approximations: (i) magnetic fields due to the movement of electric charge can be neglected, (ii) changes in ionic concentrations are sufficiently small so that Ohm's law holds, (iii) radial and angular components of voltage can be ignored so that the cable can be treated as one-dimensional medium, and (iv) dendritic membrane properties are voltage-independent, that is, there are no active elements. Given a distribution of synaptic inputs innervating the dendritic tree, what is the net synaptic current $I_{\rm syn}$ entering the soma or cell body of a neuron? In order to address this problem we consider, for simplicity, a semi-infinite uniform dendritic cable, $0 \leqslant x < \infty$, with the soma located at the end $x = 0$, see figure 3. We assume that the soma is passively coupled to the dendritic cable via a resistor with conductance σ, so that the net synaptic input flowing into the soma is

$$I_{\rm syn} = \sigma\,(v(0,t) - V(t)), \tag{2.17}$$

where $v(x,t)$ is the membrane potential of the cable at position x. The dendritic potential $v(x,t)$ evolves according to the cable equation

$$\tau_m \frac{\partial v(x,t)}{\partial t} = -v(x,t) + \lambda^2 \frac{\partial^2 v(x,t)}{\partial x^2} + r_m I(x,t), \tag{2.18}$$

where τ_m is the membrane time constant, r_m is the membrane resistance, and λ is the corresponding space constant, both of which are determined by the passive electrical properties of the cable. Here $I(x,t)$ is the synaptic current density at location x at time t:

$$I(x,t) = \rho(x) \sum_m g_{\rm syn}(t - T^m(x))[V_{\rm syn} - v(x,t)], \tag{2.19}$$

where $\rho(x)$ is the density of synapses (assuming that they have identical properties) and $\{T^m(x)\}$ is the sequence of spikes arriving into the synapses located at x. In the case of a discrete set of identical synapses at dendritic locations $\{x_m, m = 1, \ldots, M\}$, we have $\rho(x) = \sum_m \delta(x - x_m)$. It follows from current conservation that there is also the boundary condition

$$-\frac{1}{r}\frac{\partial v}{\partial x}(0,t) = \sigma[v(0,t) - V(t)], \tag{2.20}$$

where r is the intracellular resistance per unit length of cable.

We can formally solve the inhomogeneous boundary value problem for $v(0,t)$ using the Green's function G for the semi-infinite cable with a closed boundary [46]:

$$v(0,t) = r_m \int_{-\infty}^{t} \int_{0}^{\infty} G(0,x',t-t')I(x',t')\,\mathrm{d}x'\,\mathrm{d}t' - \sigma r \int_{-\infty}^{t} G(0,0,t-t')[v(0,t') - u(t')]\,\mathrm{d}t', \tag{2.21}$$

with

$$G(x,y,t) = G_0(x-y,t) + G_0(x+y,t), \tag{2.22}$$

and

$$G_0(x,t) = \frac{1}{2\lambda\sqrt{\pi t \tau_m}}\,\mathrm{e}^{-t/\tau_m}\,\mathrm{e}^{-\tau_m x^2/4\lambda^2 t} H(t) \tag{2.23}$$

is the Green's function of the cable equation on an infinite domain. We see that the effective synaptic current I_{syn} flowing into the soma will itself be affected by the cell firing an action potential, due to the dependence of $v(0,t)$ on $V(t)$. However, if the second term on the rhs of equation (2.21) is small compared to the first term arising from synaptic inputs, then the total synaptic input into the soma reduces to

$$I_{\mathrm{syn}}(t) = \sigma r_m \int_{-\infty}^{t} \int_{0}^{\infty} G(0,x',t-t')I(x',t')\,\mathrm{d}x'\,\mathrm{d}t' - \sigma V(t). \tag{2.24}$$

Note that the term $\sigma V(t)$ can be absorbed into the ionic current I_{con}. A similar analysis can also be carried out for more general dendritic topologies with the soma coupled to one of the terminals of the tree. We conclude that under the given approximations, the passive dendritic tree acts like a spatio-temporal linear filter on incoming spike trains, whose properties are determined by the underlying Green's function on the tree. The effects of the dendritic filtering of synaptic inputs on network dynamics is reviewed in some detail by Bressloff and Coombes [47].

2.4. Rate-based neural network models

Let us now consider a network of synaptically coupled cortical neurons labeled $i = 1,\ldots,N$. Denote the sequence of firing times of the jth neuron by $\{T_j^m,\ m \in \mathbf{Z}\}$. The net synaptic current into postsynaptic neuron i due to innervation by the spike train from presynaptic neuron j (see inset of figure 1) is taken to have the general form $\sum_m \Phi_{ij}(t - T_j^m)$, where $\Phi_{ij}(t)$ represents the temporal filtering effects of synaptic and dendritic processing. (For the moment we ignore short-term synaptic depression.) Assuming that all synaptic inputs sum linearly, we find that the total synaptic input to the soma of the ith neuron, which we denote by $u_i(t)$, is

$$u_i(t) = \sum_{j=1}^{N} \sum_{m} \Phi_{ij}\big(t - T_j^m\big) = \sum_{j=1}^{N} \int_{-\infty}^{t} \Phi_{ij}(t-t')a_j(t')\,\mathrm{d}t', \tag{2.25}$$

where we have set

$$a_j(t) = \sum_{m\in\mathbf{Z}} \delta\big(t - T_j^m\big). \tag{2.26}$$

That is, $a_j(t)$ represents the output spike train of the jth neuron in terms of a sum of Dirac delta functions. In order to obtain a closed set of equations, we have to determine the firing times T_i^m. This takes the form of a threshold condition

$$T_i^m = \inf\big\{t, t > T_i^{m-1} | V_i(t) = \kappa, \dot{V}_i(t) > 0\big\}, \tag{2.27}$$

where κ is the firing threshold and the somatic membrane potential $V_i(t)$ evolves according to the conductance-based model

$$C\frac{dV_i}{dt} = -I_{\text{con,i}}(V_i, \ldots) + u_i, \tag{2.28}$$

supplemented by additional equations for the ionic gating variables. (For the moment we are ignoring any external currents.) In general, equations (2.25), (2.27) and (2.28) are difficult to analyze, particularly when N is large. However, considerable simplification can be obtained if the total synaptic current $u_i(t)$ is slowly varying compared to the membrane potential dynamics given by equation (2.28). This would occur, for example, if the network could be partitioned into multiple homogeneous subnetworks each of which consisted of identical neurons firing asynchronously [48]. One is then essentially reinterpreting the activity variables $a_i(t)$ and $u_i(t)$ as mean fields of local populations. The issue of asynchronous states and mean field theory will be considered further in section 6.1. Alternatively, a slowly varying synaptic current would occur if the synapses are themselves sufficiently slow [49, 50]. Under these simplifying assumptions, we can carry out a short-term temporal averaging of equation (2.25) in which we approximate the output spike train $a_j(t)$ by the instantaneous firing rate $a_j(t) = F_j(u_j(t))$ with F_j the corresponding rate function. Equation (2.25) then forms the closed system of integral equations

$$u_i(t) = \int_{-\infty}^{t} \sum_{j=1}^{N} \Phi_{ij}(t - t')F_j(u_j(t'))\, dt'. \tag{2.29}$$

Note that within the mean-field framework F_i would represent the population-averaged rate function of a local homogeneous population of cells rather than a single neuron response function. (In the case of a fully-connected or sparsely connected integrate-and-fire network, which is introduced in section 6.1, it is possible to calculate F_i explicitly [51, 52].) In neural network models, F_i is usually approximated by the sigmoid function (2.6).

As highlighted elsewhere [15, 31], equation (2.29) can be reduced to a system of ordinary differential equations provided that we place rather mild restrictions on the time dependence of $\Phi_{ij}(t)$. First, suppose that $\Phi_{ij}(t) = w_{ij}\Phi_i(t)$ where w_{ij} denotes the synaptic strength of the connection from neuron j to neuron i and $\Phi_i(t)$ determines the time course of the input, which is assumed to depend only on properties of the postsynaptic cell i. Furthermore, suppose that there exists a differential operator $\widehat{L}_i$ such that

$$\widehat{L}_i\Phi_i(t) = \delta(t). \tag{2.30}$$

Applying the operator $\widehat{L}_i$ to both sides of equation (2.29) then leads to a system of differential equations for the currents $u_i(t)$:

$$\widehat{L}_i u_i(t) = \sum_{j=1}^{N} w_{ij}F_j(u_j(t)). \tag{2.31}$$

Note that we could easily convert the total synaptic current $u_i(t)$ into an input voltage $v_i(t) = u_i(t)/\sigma$ using the input conductance σ of figure 3, for example. Thus equation (2.31) is often referred to as a voltage equation and forms the basis of most classical neural networks such as the Hopfield model [32]. On the other hand, if the time course of the inputs depends only on presynaptic parameters, $\Phi_{ij}(t) = w_{ij}\Phi_j(t)$, with Φ_j having inverse differential operator $\widehat{L}_j$, then we obtain a system of differential equations for the so-called synaptic drives

$$v_i(t) = \int_{-\infty}^{t} \Phi_i(t - t')F_i(u_i(t'))\, dt'. \tag{2.32}$$

That is, applying the differential operator $\widehat{L}_i$ to equation (2.32) and using $u_i(t) = \sum_{j=1}^N w_{ij} v_j(t)$ leads to the activity-based model

$$\widehat{L}_i v_i(t) = F_i \left(\sum_{j=1}^N w_{ij} v_j(t) \right). \tag{2.33}$$

The differential operator $\widehat{L}_i$ appearing in equations (2.31) and (2.33) is usually taken to be first order in time:

$$\widehat{L}_i = \frac{\partial}{\partial t} + \frac{1}{\tau_i}, \tag{2.34}$$

with inverse kernel $\Phi_i(t) = H(t)\, \mathrm{e}^{-t/\tau_i}$. In order to relate the effective time constant τ_i to membrane and synaptic time constants, let us assume for simplicity that all synapses are sufficiently close to the soma so that the dendrite simply acts as a first order low pass filter and set (with $V_{\rm rest} = 0$)

$$\Phi_{ij}(t) = \sigma_i r_{m,i} V_{\rm syn,j} \bar{g}_{ij} H(t) \int_0^t \mathrm{e}^{-(t-s)/\tau_{m,i}} h_j(s)\, \mathrm{d}s, \tag{2.35}$$

with

$$h_j(s) = \frac{\tau_{d,j}}{\tau_{d,j} - \tau_{r,j}} (\mathrm{e}^{-s/\tau_{d,j}} - \mathrm{e}^{-s/\tau_{r,j}}). \tag{2.36}$$

We have made explicit that the reversal potential $V_{\rm syn}$ and synaptic rise/fall times $\tau_{r,d}$ only depend on the particular class of synapses innervated by the presynaptic neuron j, whereas the membrane time constant τ_m, resistance r_m and conductance σ are solely properties of the postsynaptic neuron i. Only the maximum conductance $\bar{g}$ is specific to the particular synapse $j \to i$. The various constant factors can be combined to define the synaptic weight w_{ij}. In particular, $w_{ij} \sim V_{\rm syn,j}$ so that the sign of $V_{\rm syn,j}$ (relative to the resting potential) determines whether the synapse is excitatory or inhibitory. If $\tau_m \gg \tau_r, \tau_d$ then the time course is effectively independent of the presynaptic label j and we have the voltage-based model (2.31) with first-order operator $\widehat{L}_i$ and $\tau_i = \tau_m$. On the other hand, if $\tau_d \gg \tau_m, \tau_r$ then we obtain the activity-based model with $\tau_i = \tau_d$.

Synaptic depression. It is relatively straightforward to incorporate synaptic depression into the rate-based network models. Let $q_{ij}(t)$ denote the depression variable associated with synapse $j \to i$. It is assumed to evolve according to an equation of the form (2.14), which we write as

$$\frac{\mathrm{d}q_{ij}}{\mathrm{d}t} = \frac{1 - q_{ij}}{\tau_q} - (1 - \gamma) q_{ij}(t) a_j(t), \tag{2.37}$$

where $a_j(t)$ denotes the output of neuron j. Within the rate-based framework, we take $a_j = F_j(u_j)$ with u_j satisfying the modified integral equation (cf equation (2.25))

$$u_i(t) = \sum_{j=1}^N \int_{-\infty}^t \Phi_{ij}(t - t') q_{ij}(t') a_j(t')\, \mathrm{d}t'.$$

Since all depression variables $\{q_{ij}, i = 1, \ldots, N\}$ for fixed j have a common input drive $a_j(t)$, it follows that

$$\tau_q \frac{\mathrm{d}(q_{ij} - q_{i'j})}{\mathrm{d}t} = -[q_{ij} - q_{i'j}],$$

and thus $q_{ij}(t) \to q_{i'j}(t) = q_j(t)$ for all $i, i' = 1, \ldots, N$. In other words, after an initial transient of duration τ_q, we can identify all depression variables associated with a given

presynaptic neuron j. If we now assume that $\Phi_{ij}(t) = w_{ij}\Phi_j(t)$, we can introduce the synaptic drives (2.32) and derive the modified activity-based model [53–56]

$$\widehat{L}_i v_i(t) = F_i\left(\sum_{j=1}^{N} w_{ij}q_j(t)v_j(t)\right), \tag{2.38}$$

with

$$\frac{\mathrm{d}q_i}{\mathrm{d}t} = \frac{1-q_i(t)}{\tau_q} - (1-\gamma)q_i(t)F_i\left(\sum_{j=1}^{N} w_{ij}q_j(t)v_j(t)\right). \tag{2.39}$$

Similarly, we can derive a corresponding voltage-based model when $\Phi_{ij}(t) = w_{ij}\Phi_i(t)$:

$$\widehat{L}_i u_i(t) = \sum_{j=1}^{N} w_{ij}q_j(t)F_j(u_j(t)). \tag{2.40}$$

with

$$\frac{\mathrm{d}q_i}{\mathrm{d}t} = \frac{1-q_i(t)}{\tau_q} - (1-\gamma)q_i(t)F_i\left(u_i(t)\right). \tag{2.41}$$

Axonal propagation delays. In the above derivation of rate-based models, we have assumed that the spiking of a presynaptic neuron has an instantaneous effect on downstream postsynaptic neurons. This neglects the fact that action potentials take time to propagate along an axon to innervate a synaptic terminal. Let us denote the corresponding axonal delay of synapse $j \to i$ by τ_{ij}. The integral equation (2.25) is then modified according to

$$u_i(t) = \sum_{j=1}^{N}\int_{-\infty}^{t} \Phi_{ij}(t-t')a_j(t'-\tau_{ij})\mathrm{d}t'. \tag{2.42}$$

The corresponding voltage-based model then takes the form of a system of delay-differential equations,

$$\widehat{L}_i u_i(t) = \sum_{j=1}^{N} w_{ij}F_j(u_j(t-\tau_{ij})), \tag{2.43}$$

and similarly for the activity-based model.

Adaptive threshold dynamics. Another biophysical process that can be incorporated into rate-based models is spike frequency adaptation. Spike frequency adaptation causes a neuron's firing rate to decay to a submaximal level and occurs when a potassium current, presumably activated by elevated intracellular calcium, hyperpolarizes the membrane voltage [57–59]. This so-called after hyperpolarization current has a time constant of around 40–120 ms. Spike frequency adaptation can be introduced as a negative current $-c_i$ on the right-hand side of the conductance-based model equation (2.28). Assuming that $c_i(t)$ varies slowly relative to the voltage $V_i(t)$, it can be shown that c_i effectively acts as an adaptive threshold that varies linearly with the firing rate [57]. Thus, the voltage-based model becomes

$$\widehat{L}_i u_i(t) = \sum_{j=1}^{N} w_{ij}F_j(u_j(t) - c_j(t)). \tag{2.44}$$

with

$$\frac{\mathrm{d}c_i}{\mathrm{d}t} = -\frac{c_i(t)}{\tau_c} + \gamma_c F_i(u_i(t) - c_i(t)). \tag{2.45}$$

2.5. Spatially structured networks and neural fields

So far we have not made any assumptions about the topology of the underlying neural network, that is, the structure of the weight matrix **W** with components w_{ij}. If one looks at a region of cortex such as primary visual cortex (V1), one finds that it has a characteristic spatial structure, in which a high density of neurons (10^5 mm^{-3} in primates) are distributed according to an approximately two-dimensional (2D) architecture. That is, the physical location of a vertical column of neurons within the two-dimensional cortical sheet often reflects the specific information processing role of that population of neurons. For example, in V1 there is an orderly retinotopic mapping of the visual field onto the cortical surface, with left and right halves of the visual field mapped onto right and left visual cortices respectively. Superimposed upon this are additional two-dimensional maps reflecting the fact that neurons respond preferentially to stimuli with particular features such as local orientation [60]. (A more detailed description of the functional architecture of V1 is given in section 5.2.) This suggests labeling neurons according to their spatial location in cortex. We now give a heuristic argument for how such labeling leads to a continuum neural field model of cortex, following along similar lines to Gerstner and Kistler [48].

For simplicity, consider a population of neurons distributed along a one-dimensional axis. (Extensions to higher dimensions proceed in a similar fashion.) Suppose that we partition space into segments of length d such that the number of neurons in segment $[nd,\ (n+1)d]$ is $N = \rho d$ where ρ is the cell density. We treat neurons in that interval as a homogeneous population of cells (cortical column) labeled by the integer n, and assume that synaptic interactions between the nth and mth populations only depend on the discrete locations of the populations on the line. Writing $\Phi_{nm}(t) = \rho d\Phi(nd, md, t)$ and $u_n(t) = u(nd, t)$, equation (2.29) becomes

$$u(nd,t) = \rho d \sum_m \int_{-\infty}^t \Phi(nd, md, t-t')F(u(md,t'))\,\mathrm{d}t'.$$

Taking the limit $d \to 0$, the summation on the right-hand side can be replaced by an integral to give

$$u(x,t) = \int_{-\infty}^{\infty}\int_{-\infty}^t \Phi(x,y,t-t')F(u(y,t'))\,\mathrm{d}t'\,\mathrm{d}y, \tag{2.46}$$

where we have absorbed the factor ρ into Φ. Following our derivation of the discrete voltage-based model (2.31), suppose that we can decompose the integral kernel as

$$\Phi(x,y,t) = w(x,y)\Phi(t), \qquad \Phi(t) = \mathrm{e}^{-t/\tau}H(t).$$

That is, we assume that there is only one type of neuron so that the temporal kernel $\Phi(t)$ is independent of the presynaptic label y and the postsynaptic label x. Applying the differential operator $\hat{L}_t = \partial_t + \tau^{-1}$ to the integral equation for u then leads to the scalar neural field equation

$$\frac{\partial}{\partial t}u(x,t) = -\frac{u(x,t)}{\tau} + \int_{-\infty}^{\infty} w(x,y)F(u(y,t))\,\mathrm{d}y. \tag{2.47}$$

Alternatively, we could have applied the differential operator $\widehat{L}_t$ to the corresponding synaptic drive $v(x,t) = \int_{-\infty}^t \Phi(t-t')F(u(x,t'))\,\mathrm{d}t'$ to obtain the activity-based neural field model

$$\frac{\partial}{\partial t}v(x,t) = -\frac{v(x,t)}{\tau} + F\left(\int_{-\infty}^{\infty} w(x,y)v(y,t)\,\mathrm{d}y\right). \tag{2.48}$$

Following the same basic procedure, it is straightforward to incorporate into the neural field equation (2.47) or (2.48) additional features such as synaptic depression [61–63], adaptive

thresholds [61, 64] and axonal propagation delays [22–24, 65–68]. For example, a voltage-based neural field equation with synaptic depression takes the form

$$\frac{\partial}{\partial t}u(x,t) = -\frac{u(x,t)}{\tau} + \int_{-\infty}^{\infty} w(x,y)q(y,t)F(u(y,t))\,\mathrm{d}y,$$
$$\frac{\partial}{\mathrm{d}t}q(x,t) = \frac{1-q(x,t)}{\tau_q} - \beta q(x,t)F\left(u(x,t)\right), \tag{2.49}$$

with $\beta = 1-\gamma$. In the case of axonal delays, $\tau_{ij} \to \tau(x,y)$ in the continuum limit. Assuming that an action potential propagates with constant speed v along the axon, then $\tau(x,y) = |x-y|/v$ so that the voltage-based equation (2.47) becomes

$$\frac{\partial}{\partial t}u(x,t) = -\frac{u(x,t)}{\tau} + \int_{-\infty}^{\infty} w(x,y)F(u(y,t-|x-y|/v))\,\mathrm{d}y. \tag{2.50}$$

Two-dimensional versions of these various models are obtained by taking $x \to \mathbf{x} = (x_1, x_2)$ and $y \to \mathbf{y} = (y_1, y_2)$ with $\mathrm{d}\mathbf{y} = \mathrm{d}y_1\,\mathrm{d}y_2$.

Now suppose that there are M classes of neuron distributed along the line labeled by the population index $a = 1, \ldots M$. Equation (2.46) then generalizes to the multi-population integral equation

$$u_a(x,t) = \int_{-\infty}^{\infty}\int_{-\infty}^{t}\sum_{b=1}^{M}\Phi_{ab}(x,y,t-t')F_b(u_b(y,t'-|x-y|/v_{ab}))\,\mathrm{d}t'\,\mathrm{d}y. \tag{2.51}$$

We have included axonal delays with v_{ab} the conduction velocity along axonal projections from neurons of type b to neurons of type a. Assuming that $\Phi_{ab}(x,y,t) = w_{ab}(x,y)\Phi(t)$ with $\Phi(t) = \mathrm{e}^{-t/\tau}H(t)$, we obtain multi-population neural field equations

$$\frac{\partial u_a}{\partial t} = -\frac{u_a(x,t)}{\tau} + \sum_{b=1}^{M}\int_{-\infty}^{\infty} w_{ab}(x,y)F_b(u_b(y,t-|x-y|/v_{ab}))\,\mathrm{d}y \tag{2.52}$$

and

$$\frac{\partial v_a}{\partial t} = -\frac{v_a(x,t)}{\tau} + F_b\left(\sum_{b=1}^{M}\int_{-\infty}^{\infty} w_{ab}(x,y)v_b(y,t-|x-y|/v_{ab})\,\mathrm{d}y\right). \tag{2.53}$$

The latter is a version of the Wilson–Cowan equations for cortical dynamics [10, 11]. Note that all synapses innervated by a particular type of neuron have the same sign. That is, if type b neurons are excitatory (inhibitory) then $w_{ab}(x,y) \geqslant 0$ ($w_{ab}(x,y) \leqslant 0$) for all $a = 1, \ldots, M$ and (x,y). Thus, one of the major reasons for considering more than one class of neuron is to incorporate both excitatory and inhibitory synapses. It can be argued that since excitatory and inhibitory synapses tend to have different time courses in response to action potentials, one should take $\Phi_{ab}(x,y,t) = w_{ab}(x,y)\Phi_b(t)$, suggesting that the activity-based model (2.53) with $\tau \to \tau_a$ is more biologically realistic than the voltage-based model, at least in the case of excitatory-inhibitory networks [31]. However, in practice, both versions of the neural field equations are used to model cortical dynamics. Since both versions exhibit very similar types of solution. and since most analytical results have been obtained for voltage-based neural fields, we will mainly focus our review on the latter.

Under certain additional simplifying assumptions, it is possible to incorporate inhibition into the scalar neural field equations (2.47) or (2.48) [69]. For example, consider a two-population model ($M = 2$) of excitatory ($a = E$) and inhibitory ($a = I$) neurons evolving according to the pair of equations

$$\frac{\partial u_E}{\partial t} = -\frac{u_E(x,t)}{\tau_E} + \int_{-\infty}^{\infty} w_{EE}(x,y)F_E(u_E(y,t))\,\mathrm{d}y + \int_{-\infty}^{\infty} w_{EI}(x,y)F_I(u_I(y,t))\,\mathrm{d}y \tag{2.54}$$

and

$$\frac{\partial u_I}{\partial t} = -\frac{u_I(x,t)}{\tau_I} + \int_{-\infty}^{\infty} w_{IE}(x,y) F_E(u_E(y,t))\,\mathrm{d}y + \int_{-\infty}^{\infty} w_{II}(x,y) F_I(u_I(y,t))\,\mathrm{d}y, \tag{2.55}$$

with $w_{EE}, w_{IE} \geqslant 0$ and $w_{EI}, w_{II} \leqslant 0$. Now suppose that $w_{II} \equiv 0$, $F_I(u_I) = u_I/\tau_I$ and $\tau_I \ll \tau_E$. It follows that we can eliminate u_I by setting $u_I(x) \sim \tau_I \int_{-\infty}^{\infty} w_{IE}(x,y) F_E(u_E(y,t))\,\mathrm{d}y$, which leads to a scalar equation for u_E of the form (2.47) with effective weight distribution

$$w(x,y) = w_{EE}(x,y) + \int_{-\infty}^{\infty} w_{EI}(x,y') w_{IE}(y',y)\,\mathrm{d}y'. \tag{2.56}$$

It is then possible for $w(x,y)$ to change sign as a function of x, y. (Often w is modeled as a difference of Gaussians or exponentials—the so-called Mexican hat weight distribution.) The reduced model can be used to investigate the effects of inhibition on stationary solutions of neural field equations, see sections 4 and 5. However, in contrast to the full two-population model, it does not support oscillatory solutions (in the absence of axonal delays, higher order synapses or some form of adaptation such as synaptic depression).

Some remarks.

(i) There does not currently exist a multi-scale analysis of conductance-based neural networks that provides a rigorous derivation of neural field equations, although some progress has been made in this direction [65, 70–72]. One crucial step in the derivation of neural field equations presented here was the assumption of slowly varying synaptic currents, which is related to the assumption that there is not significant coherent activity at the level of individual spikes. This allowed us to treat the output of a neuron (or population of neurons) as an instantaneous firing rate. A more rigorous derivation would need to incorporate the mean field analysis of local populations of stochastic spiking neurons into a larger scale cortical model, and to carry out a systematic form of coarse graining or homogenization in order to generate a continuum neural field model. Some of these issues will be discussed in section 6.

(ii) Nevertheless, the heuristic approach does provide a framework for relating parameters of neural field equations to biophysical parameters such as membrane/synaptic time constants and axonal delays, and also prescribes how to incorporate additional physiological processes such as synaptic depression and spike frequency adaptation. Moreover, neural field models make it possible to explore the dependence of cortical dynamics on the detailed anatomy of local and long range synaptic connections, as highlighted in section 5.2.

(iii) Neural field equations support various forms of spatially coherent population activity [15, 64], including traveling waves (section 3), spatially localized persistent activity states or bumps (section 4), and spatially periodic patterns (section 5). As highlighted in the introduction, neural fields have been used to model a wide range of neurobiological phenomena. One of the major modeling issues is determining how such phenomena depend on the synaptic weight distribution w, which represents the underlying large-scale anatomy of cortex. It is usually assumed that w depends on the Euclidean distance between interacting cells within the 2D cortical sheet so that $w(\mathbf{x},\mathbf{y}) = w(|\mathbf{x}-\mathbf{y}|)$. However, this is an oversimplification of the detailed architecture of cortex [73–77], as we discuss in section 5.2. A related simplification is to take axonal delays to depend on Euclidean distance according to $|\mathbf{x}-\mathbf{y}|/v$, where v is the speed of propagation.

(iv) There are two main approaches to analyzing the spatiotemporal dynamics of neural field equations. The first method is based on the original work of Amari [12], in which one

establishes the existence of nonlinear traveling wave and stationary bump solutions by explicit construction, see sections 3 and 4 and the review [16]. This is possible if one takes the firing rate function F in voltage-based models to be the Heaviside (2.7). It is also possible to study the linear stability of such solutions by constructing an associated Evans function, whose zeros determine the spectrum of the resulting linear operator [78–80]. The constructive approach of Amari [12] has been particularly useful in providing explicit insights into how spatiotemporal network dynamics depends on the structure of the synaptic weight kernel as well as various physiological parameters. Moreover, in certain cases it is possible to use singular perturbation methods [17, 69] or fixed point theorems [81, 82] to extend results for neural fields with Heaviside nonlinearities to those with more realistic sigmoidal nonlinearities, see also [83].

(v) The second method is based on bifurcation theory, following the original work of Ermentrout and Cowan [19], in which one investigates the emergence of spatially periodic stationary and oscillatory patterns through a combination of linear stability analysis, weakly nonlinear analysis, symmetric bifurcation theory, and numerical simulations, see section 5 and the review [84]. Rigorous functional analytical techniques combined with numerical bifurcation schemes have also been used to study the existence and (absolute) stability of stationary bump solutions for a general class of neural field models with smooth firing rate functions [85, 86].

(vi) In this review we will focus on analytical methods that are applied directly to the integro-differential equations of neural field theory. We note, however, that several groups have constructed equivalent PDE models for neural fields with axonal propagation delays, which take the form of damped inhomogeneous wave equations [21–24, 65]. The basic idea is to assume a particular form for the synaptic weight distribution and to use Fourier transforms. Consider, for example, a 2D version of the multi-population integral equation (2.51). Suppose that $\Phi_{ab}(\mathbf{x},\mathbf{y},t)=w_{ab}(|\mathbf{x}-\mathbf{y}|)\Phi(t)$ and introduce the auxiliary field

$$\Psi_{ab}(\mathbf{x},t)=\int_{\mathbb{R}^2} w_{ab}(|\mathbf{x}-\mathbf{y}|)F_b(\mathbf{y},t-|\mathbf{x}-\mathbf{y}|/v_{ab})\,\mathrm{d}\mathbf{y}, \tag{2.57}$$

where we have set $F_b(\mathbf{y},t)=F_b(u_b(\mathbf{y},t))$. Fourier transforming this equation with

$$\widehat{\Psi}_{ab}(k,\omega)=\int_{\mathbb{R}^2}\int_{-\infty}^{\infty} \mathrm{e}^{-\mathrm{i}(\mathbf{k}\cdot\mathbf{r}+\omega t)}\Psi_{ab}(\mathbf{x},t)\mathrm{d}t\,\mathrm{d}\mathbf{x} \tag{2.58}$$

and

$$w_{ab}(r)=\frac{w_{ab}^0}{2\pi}\,\mathrm{e}^{-r/\sigma_{ab}}, \tag{2.59}$$

we find that

$$\widehat{\Psi}_{ab}(k,\omega)=w_{ab}^0\frac{\mathcal{A}_{ab}(\omega)}{(\mathcal{A}_{ab}(\omega)^2+k^2)^{3/2}}\widehat{F}_b(k,\omega) \tag{2.60}$$

with $\mathcal{A}_{ab}(\omega)=1/\sigma_{ab}+\mathrm{i}\omega/v_{ab}$. If one now makes a long-wavelength approximation by Taylor expanding the denominator of the above equation about $k=0$ and rearranging to give $(\mathcal{A}_{ab}(\omega)^2+3k^2/2)\widehat{\Psi}_{ab}(k,\omega)=\widehat{F}_b(k,\omega)$, one can then apply the inverse Fourier transform to derive the damped wave equation

$$\left[\left(\frac{1}{\sigma_{ab}}+\frac{1}{v_{ab}}\partial_t\right)^2-\frac{3}{2}\nabla^2\right]\Psi_{ab}(\mathbf{x},t)=w_{ab}^0F_b(u_b(\mathbf{x},t)). \tag{2.61}$$

The current $u_a(\mathbf{x},t)$ is then related to the field $\Psi_{ab}(\mathbf{x},t)$ according to

$$u_a(\mathbf{x},t)=\int_{-\infty}^{t}\Phi(t-t')\sum_b\Psi_{ab}(\mathbf{x},t')\,\mathrm{d}t', \tag{2.62}$$

which can itself be converted to a PDE by applying the inverse operator $\widehat{L}_t$. There have also been various extensions of the PDE theory including improvements upon the long-wavelength approximation [87] and incorporation of network inhomogeneities [77]. The damped wave equation (2.61) and its generalizations have been used extensively to study EEG rhythms [21–24]. (PDE models have also been used to study single and multi-bump stationary solutions of scalar neural field equations, in which the time-independent equations reduce to fourth-order differential equations with a Hamiltonian structure [28, 88].)

(vii) In this review we focus on applications of non-local neural field equations to dynamical phenomena that occur on spatial scales that do not extend beyond a few centimeters, which holds for cortical slices and individual cortical areas such as primary visual cortex. In such cases axonal propagation delays tend to be relatively small and can be neglected. On the other hand, models of larger-scale phenomena such as the EEG require the incorporation of propagation delays. In this case, approximating the non-local neural field equation by a corresponding brain-wave equation allows the development of efficient numerical schemes for simulating large-scale cortical activity.

3. Traveling waves

A common *in vitro* method for studying the propagation of electrical activity in networks of neurons is to remove a slice of brain tissue and bathe it in a pharmacological medium that blocks the effects of inhibition. Synchronized discharges can be evoked by a weak electrical stimulus to a local site on the slice and each discharge propagates away from the stimulus at a characteristic speed of about 60–90 mm s^{-1} [2–4, 89]. This is illustrated in figure 4. The underlying mechanism for the propagation of such waves appears to be synaptic in origin rather than diffusive, in contrast to the much faster propagation of action potentials along the axons of individual neurons. In certain cases, local stimulation of a disinhibited slice can induce spatially localized oscillations in population activity at a frequency 1–10 Hz, such that during each oscillation cycle the population emits elevated activity that propagates as a traveling pulse [5, 90] or even a spiral wave (in the case of tangential cortical slices) [18]. A variety of sensory stimuli have been linked to propagating waves *in vivo*. For example, a number of studies of vertebrate and invertebrate olfactory bulbs have shown odor stimuli can elicit oscillations and propagating waves [91, 92]. Similarly, a small visual stimulus can evoke a propagating wave in visual cortex [93–96], and stimulating a single whisker can trigger a wave in rat barrel cortex [97]. Evoked waves are not only a neural correlate of sensory stimuli, but can occur during movement preparation and execution [98]. Finally, spatially localized oscillations and traveling waves can also be the signature of certain neurological diseases including epilepsy [1, 99].

Neural field models have played an important role in developing our understanding of network-based mechanisms underlying propagating activity in normal and pathological brain states. As in studies of reaction-diffusion systems, it is important to distinguish between wave propagation in bistable, excitable, and oscillatory neural media. In the first case, there exist two stable stationary homogeneous states and the neural medium supports the propagation of traveling fronts. On the other hand, an excitable neural medium has a single stable homogeneous state and supports the propagation of traveling pulses. Finally, an oscillatory neural medium is one in which the background state of all neurons is oscillatory—wave propagation is then characterized by a spatially uniform gradient in the phase of the oscillations [100]. (An excitable medium can also act like an oscillatory medium if there exists a spatially

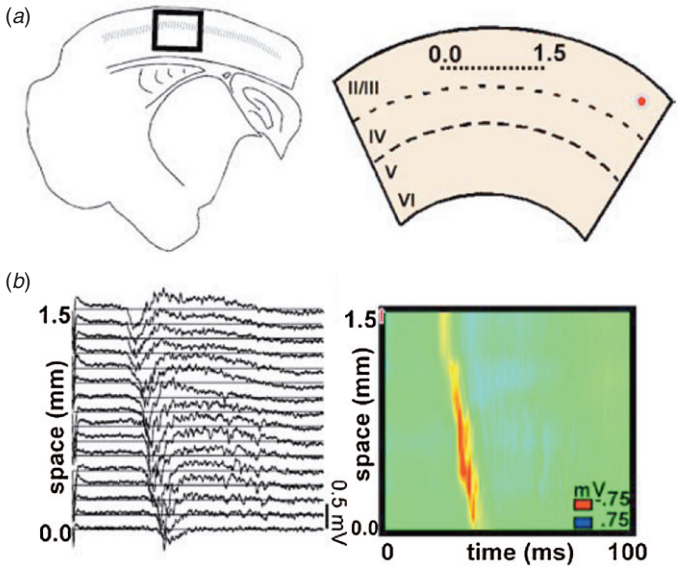

Figure 4. Propagating wave of activity in a brain slice preparation in which inhibition has been blocked (reprinted with permission from [3]). (*a*) Schematic of a slice removed from the somatosensory cortex of the rat. The cortex is a thin (sub-millimeter) layered sheet of neurons, see section 5.2. A slice approximately 500 μm thickness is obtained by cutting vertically through the cortical layers. (*b*) A multi-electrode array placed into layers II/III of the slice records extracellularly the propagation of a wave. (*c*) Pseudocolor plot of propagating activity.

localized population of pacemaker cells.) We will mainly focus on waves in non-oscillatory neural media. We begin by showing how Amari's constructive method can be used to analyze the existence (section 3.1) and stability (section 3.2) of solitary traveling fronts in a 1D scalar neural field. (Since there is strong vertical coupling between layers of a cortical column, it is possible to treat a thin vertical cortical slice as an effective 1D medium.) In order to relate the models to experiments on disinhibited cortical slices, we assume that the weight distribution is purely excitatory. This is also motivated by the observation that epileptic seizures are often associated with greatly enhanced levels of recurrent excitation [1]. In section 3.3 we extend the analysis to the case of traveling pulses, which requires the inclusion of some form of local negative feedback mechanism such as synaptic depression or spike frequency adaptation. We also show how singular perturbation methods can be used to analyze the existence of pulses for smooth firing rate functions [17]. We then consider an application of adaptive neural fields to modeling the propagation of visual perception waves (section 3.4). In section 3.5 we review two approaches to analyzing wave propagation failure in inhomogeneous neural media, one based on homogenization theory [20, 101] and the other on interfacial dynamics [102]. Finally, in section 3.6 we briefly describe a possible mechanism for generating spiral waves in oscillatory neural media [62, 103, 104].

3.1. Traveling fronts in a scalar neural field

We begin by using Amari's constructive method [12] to analyze the existence of traveling front solutions of the scalar neural field equation (2.47). Similar analyses are found in [17, 79, 105]. We assume a Heaviside rate function (2.7) and an excitatory weight distribution

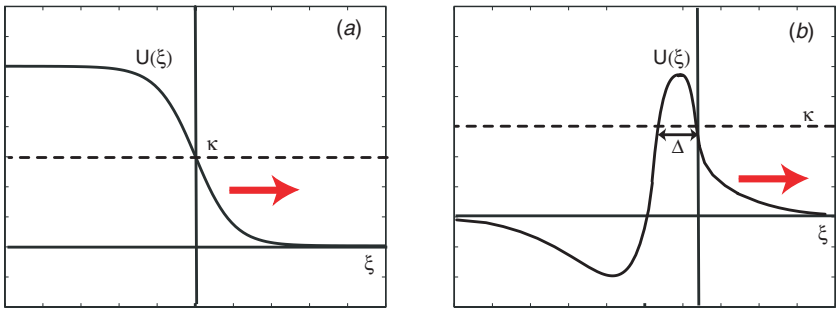

Figure 5. Schematic illustration of 1D traveling wave solutions $U(\xi)$, $\xi = x - ct$ with wavespeed c. (*a*) Traveling wavefront. (*b*) Traveling pulse of width Δ. Dashed horizontal line indicates the threshold value κ.

of the form $w(x, y) = w(x-y)$ with $w(x) \geqslant 0$ and $w(-x) = w(x)$. We also assume that $w(x)$ is a monotonically decreasing function of x for $x \geqslant 0$. A common choice is the exponential weight distribution

$$w(x) = \frac{1}{2\sigma} \mathrm{e}^{-|x|/\sigma}, \tag{3.1}$$

where σ determines the range of synaptic connections. The latter tends to range from 100 μm to 1 mm. The resulting neural field equation is

$$\frac{\partial u(x,t)}{\partial t} = -u(x,t) + \int_{-\infty}^{\infty} w(x-x')F(u(x',t))\,\mathrm{d}x', \tag{3.2}$$

with $F(u) = H(u-\kappa)$. We have fixed the units of time by setting $\tau = 1$. If τ is interpreted as a membrane time constant then $\tau \sim 10$ ms. In order to construct a traveling front solution of (3.2), we introduce the traveling wave coordinate $\xi = x - ct$, where c denotes the wavespeed, and set $u(x,t) = U(\xi)$ with $\lim_{\xi\to-\infty} U(\xi) = U_+ > 0$ and $\lim_{\xi\to\infty} U(\xi) = 0$ such that $U(\xi)$ only crosses the threshold κ once, see figure 5. Here $U_+ = \int_{-\infty}^{\infty} w(y)\mathrm{d}y$ is a spatially uniform fixed point solution of (3.2). Since equation (3.2) is equivariant with respect to uniform translations, we are free to take the threshold crossing point to be at the origin, $U(0) = \kappa$, so that $U(\xi) < \kappa$ for $\xi > 0$ and $U(\xi) > \kappa$ for $\xi < 0$. Substituting this traveling front solution into equation (3.2) then gives

$$-cU'(\xi) + U(\xi) = \int_{-\infty}^{0} w(\xi - \xi')\,\mathrm{d}\xi' = \int_{\xi}^{\infty} w(x)\,\mathrm{d}x \equiv W(\xi), \tag{3.3}$$

where $U'(\xi) = \mathrm{d}U/\mathrm{d}\xi$. Multiplying both sides of the above equation by $\mathrm{e}^{-\xi/c}$ and integrating with respect to ξ leads to the solution

$$U(\xi) = \mathrm{e}^{\xi/c}\left[\kappa - \frac{1}{c}\int_0^{\xi} \mathrm{e}^{-y/c} W(y)\,\mathrm{d}y\right]. \tag{3.4}$$

Finally, requiring the solution to remain bounded as $\xi \to \infty$ ($\xi \to -\infty$) for $c > 0$ (for $c < 0$) implies that κ must satisfy the condition

$$\kappa = \frac{1}{|c|}\int_0^{\infty} \mathrm{e}^{-y/|c|} W(\mathrm{sign}(c)y)\,\mathrm{d}y. \tag{3.5}$$

Thus, one of the useful aspects of the constructive method is that it allows us to derive an explicit expression for the wavespeed as a function of physiological parameters such as firing

threshold and range of synaptic connections. In the case of the exponential weight distribution (3.1), the relationship between wavespeed c and threshold κ is

$$c = \frac{\sigma}{2\kappa}[1-2\kappa] \text{ (for } \kappa < 0.5), \qquad c = \frac{\sigma}{2}\frac{1-2\kappa}{1-\kappa} \text{ (for } 0.5 < \kappa < 1). \tag{3.6}$$

This establishes the existence of a unique front solution for fixed κ, which travels to the right ($c > 0$) when $\kappa < 0.5$ and travels to the left ($c < 0$) when $\kappa > 0.5$. As we will show in section 3.2, the traveling front is stable.

Given the existence of a traveling front solution for a Heaviside rate function, it is possible to extend the analysis to a smooth sigmoid nonlinearity using a continuation method [82]. We briefly summarize the main result. Consider the scalar neural field equation (3.2) with F given by the sigmoid function (2.6), and $W(x)$ non-negative and symmetric with normalization $\int_{-\infty}^{\infty} W(x)\mathrm{d}x = 1$. Suppose that the function $\widetilde{F}(u) = -u + F(u)$ has precisely three zeros at $u = U_\pm, U_0$ with $U_- < U_0 < U_+$ and $\widetilde{F}'(U_\pm) < 0$. It can then be shown that (modulo uniform translations) there exists a unique traveling front solution $u(x,t) = U(\xi)$, $\xi = x - ct$, with

$$-cU'(\xi) + U(\xi) = \int_{-\infty}^{\infty} w(\xi - \xi')F(U(\xi'))\,\mathrm{d}\xi', \tag{3.7}$$

and $U(\xi) \to U_\pm$ as $\xi \to \mp\infty$ [82]. Moreover, the speed of the wave satisfies

$$c = \frac{\Gamma}{\int_{-\infty}^{\infty} U'(\xi)^2 F'(U(\xi))\,\mathrm{d}\xi}, \tag{3.8}$$

where $F'(U) = \mathrm{d}F/\mathrm{d}U$ and

$$\Gamma = \int_{U_-}^{U_+} \widetilde{F}(U)\,\mathrm{d}U. \tag{3.9}$$

Since the denominator of equation (3.8) is positive definite, the sign of c is determined by the sign of the coefficient Γ. In particular, if the threshold $\kappa = 0.5$ and the gain of the sigmoid $\eta > 4$, see equation (2.6), then there exists a pair of stable homogeneous fixed points with $U_- = -U_+$, which in turn implies that $\Gamma = 0$ and the front solution is stationary. Note that this analysis has been extended to a more general form of nonlocal equations by Chen [106]

3.2. Wave stability and Evans functions

Suppose that the scalar neural field equation (3.2) has a traveling wave solution $u(x,t) = U(\xi)$, $\xi = x - ct$ with $c > 0$. Following Coombes and Owen [79], it is convenient to rewrite the neural field equation in the integral form

$$u(x,t) = \int_{-\infty}^{\infty}\int_{0}^{\infty} w(y)\Phi(s)F(u(x-y,t-s))\,\mathrm{d}s\,\mathrm{d}y, \tag{3.10}$$

with $\Phi(t) = \mathrm{e}^{-t}H(t)$. For this representation, the front solution satisfies

$$U(\xi) = \int_{-\infty}^{\infty}\int_{0}^{\infty} w(y)\Phi(s)F(U(\xi - y + cs)\,\mathrm{d}s\,\mathrm{d}y. \tag{3.11}$$

In order to determine the stability of the front solutions, we transform to traveling wave coordinates by setting $u(x,t) = U(\xi,t) = U(\xi) + \varphi(\xi,t)$, and Taylor expand to first order in φ. This leads to the linear integral equation

$$\varphi(\xi,t) = \int_{-\infty}^{\infty}\int_{0}^{\infty} w(y)\Phi(s)F'(U(\xi - y + cs))\varphi(\xi - y + cs, t-s)\,\mathrm{d}s\,\mathrm{d}y. \tag{3.12}$$

We now seek solutions of equation (3.12) of the form $\varphi(\xi,t) = \varphi(\xi)\mathrm{e}^{\lambda t}$, $\lambda \in \mathbf{C}$, which leads to the eigenvalue equation $\varphi = \mathcal{L}(\lambda)\varphi$. That is,

$$\varphi(\xi) = \int_{-\infty}^{\infty}\int_{\xi-y}^{\infty} w(y)\Phi((s+y-\xi)/c)\,\mathrm{e}^{-\lambda(s+y-\xi)/c}F'(U(s))\varphi(s)\frac{\mathrm{d}s}{c}\,\mathrm{d}y, \tag{3.13}$$

where we have performed the change of variables $cs + \xi - y \to s$. The linear stability of the traveling front can then be determined in terms of the spectrum $\sigma(\mathcal{L})$ of $\mathcal{L}$.

It is first useful to recall some basic definitions regarding the spectrum of a linear operator [107]. Suppose that the eigenfunctions $\varphi(\xi)$ belong to a Banach space $\mathcal{B}$ (complete, normed vector space). In practice, we will simply require that $\varphi(\xi)$ is a bounded smooth function on $\mathbb{R}$ that decays exponentially at $\xi \to \pm\infty$. Introduce the so-called inverse or resolvent operator $\mathcal{R}(\lambda) = [\mathcal{L}(\lambda) - I]^{-1}$, where I denotes the identity operator. We can then decompose the spectrum $\sigma(\mathcal{L})$ into the following disjoint sets. λ is an element of the point or discrete spectrum if $\mathcal{R}(\lambda)$ does not exist; λ is an element of the continuous spectrum if $\mathcal{R}(\lambda)$ exists, is defined on a dense subset of $\mathcal{B}$, but is not bounded; λ is an element of the residual spectrum if $\mathcal{R}(\lambda)$ exists but its domain is not dense in $\mathcal{B}$. We refer to elements of the discrete spectrum as eigenvalues and the union of the continuous and residual spectra as the essential spectrum. Given the spectrum of the linear operator defined by equation (3.13), the traveling wave is said to be linearly stable if [108]

$$\max\{\mathrm{Re}(\lambda) \,:\, \lambda \in \sigma(\mathcal{L}),\ \lambda \neq 0\} \leqslant -K \tag{3.14}$$

for some $K > 0$, and $\lambda = 0$ is a simple eigenvalue of λ. The existence of at least one zero eigenvalue is a consequence of translation invariance. Indeed, differentiating equation (3.11) with respect to ξ shows that $\varphi(\xi) = U'(\xi)$ is an eigenfunction solution of equation (3.13) with $\lambda = 0$. In the case of PDEs, it is known that the discrete spectrum of the operator obtained by linearizing about a traveling wave solution may be associated with the zeros of a complex analytic function known as the Evans function. Evans [109] originally developed the formalism within the context of the stability of solitary pulses in diffusive Hodgkin–Huxley type equations describing action potential propagation in nerve axons. Since then the Evans function construction has been extended to a wide range of PDEs, see the review [108]. It has also recently been applied to neural field equations [78–80, 110–112] and more general nonlocal problems [113]. Moreover, for neural fields with Heaviside firing rate functions, the Evans function can be calculated explicitly. This was first carried out by Zhang [78] who applied the method of variation of parameters to the linearized version of the integro-differential equation (3.2). Here we will follow closely the more direct integral formulation of Coombes and Owen [79].

Setting $F(U) = H(U - \kappa)$ in equation (3.12) and using the identity

$$H'(U(\xi) - \kappa) = \delta(U(\xi) - \kappa) = \frac{\delta(\xi)}{|U'(0)|}, \tag{3.15}$$

gives

$$\varphi(\xi) = \frac{\varphi(0)}{c|U'(0)|} \int_{-\infty}^{\infty} w(y)\Phi((y-\xi)/c)\, \mathrm{e}^{-\lambda(y-\xi)/c}\, \mathrm{d}y. \tag{3.16}$$

In order to obtain a self-consistent solution at $\xi = 0$, we require that

$$\varphi(0) = \frac{\varphi(0)}{c|U'(0)|} \int_{0}^{\infty} w(y)\Phi(y/c)\, \mathrm{e}^{-\lambda y/c}\, \mathrm{d}y, \tag{3.17}$$

We have used the fact that $\Phi(y) = 0$ for $y < 0$, which is a consequence of causality. Hence, a nontrivial solution exists provided that $\mathcal{E}(\lambda) = 0$, where

$$\mathcal{E}(\lambda) = 1 - \frac{1}{c|U'(0)|} \int_{0}^{\infty} w(y)\Phi(y/c)\, \mathrm{e}^{-\lambda y/c}\, \mathrm{d}y. \tag{3.18}$$

Equation (3.18) can be identified with the Evans function for the traveling front solution of the scalar neural field equation (3.10). It is real-valued if λ is real. Furthermore, (i) the complex number λ is an eigenvalue of the operator $\mathcal{L}$ if and only if $\mathcal{E}(\lambda) = 0$, and (ii) the algebraic

multiplicity of an eigenvalue is equal to the order of the zero of Evan's function [78–80]. We briefly indicate the proof of (i) for $\Phi(t) = \mathrm{e}^{-t}H(t)$. Equation (3.16) becomes

$$\begin{aligned}\varphi(\xi) &= \frac{\varphi(0)}{c|U'(0)|}\,\mathrm{e}^{(\lambda+1)\xi/c}\int_{\xi}^{\infty} w(y)\,\mathrm{e}^{-(\lambda+1)y/c}\,\mathrm{d}y,\\ &= \varphi(0)\left[1-\frac{1}{c|U'(0)|}\int_{0}^{\xi} w(y)\,\mathrm{e}^{-(\lambda+1)y/c}\,\mathrm{d}y\right]\mathrm{e}^{(\lambda+1)\xi/c}\end{aligned}$$

which in the limit $\xi\to\infty$ gives

$$\lim_{\xi\to\infty}\varphi(\xi) = \varphi(0)\mathcal{E}(\lambda)\lim_{\xi\to\infty}\mathrm{e}^{(\lambda+1)\xi/c}. \tag{3.19}$$

Assuming that $\mathrm{Re}\lambda > -1$ (which turns out to be to the right of the essential spectrum), then $\varphi(\xi)$ will be unbounded as $\xi\to\infty$ unless $\mathcal{E}(\lambda) = 0$. That is, if $\mathcal{E}(\lambda) = 0$ then $\varphi(\xi)$ is normalizable, the resolvent operator is not invertible and λ is an eigenvalue.

It is also straightforward to show that $\mathcal{E}(0) = 0$, which we expect from translation invariance. First, setting $F(U) = H(U-\kappa)$ in equation (3.11) and differentiating with respect to ξ shows that

$$U'(\xi) = -\frac{1}{c}\int_{-\infty}^{\infty} w(y)\Phi((y-\xi)/c)\,\mathrm{d}y. \tag{3.20}$$

Thus, defining

$$\mathcal{H}(\lambda) = \int_{0}^{\infty} w(y)\Phi(y/c)\mathrm{e}^{-\lambda y/c}\,\mathrm{d}y \tag{3.21}$$

we see that $c|U'(0)| = \mathcal{H}(0)$ and, hence,

$$\mathcal{E}(\lambda) = 1-\frac{\mathcal{H}(\lambda)}{\mathcal{H}(0)}. \tag{3.22}$$

It immediately follows that $\mathcal{E}(0) = 0$.

In order to determine the essential spectrum, consider the inhomogeneous equation

$$\varphi(\xi) - \frac{\varphi(0)}{c|U'(0)|}\int_{-\infty}^{\infty} w(y)\Phi((y-\xi)/c)\,\mathrm{e}^{-\lambda(y-\xi)/c}\,\mathrm{d}y = h(\xi) \tag{3.23}$$

for some normalizable smooth function h on $\mathbb{R}$. Assuming that λ does not belong to the discrete spectrum, $\mathcal{E}(\lambda)\neq 0$, we can expresses the constant $\varphi(0)$ in terms of $h(0)$ by setting $\xi = 0$ in equation (3.23): $\varphi(0) = h(0)/\mathcal{E}(\lambda)$. Thus,

$$\varphi(\xi) = h(\xi) + \frac{1}{\mathcal{E}(\lambda)}\frac{h(0)}{c|U'(0)|}\int_{-\infty}^{\infty} w(y)\Phi((y-\xi)/c)\,\mathrm{e}^{-\lambda(y-\xi)/c}\,\mathrm{d}y. \tag{3.24}$$

Fourier transforming this equation using the convolution theorem gives

$$\widehat{\varphi}(k) = \widehat{h}(k) + \frac{1}{\mathcal{E}(\lambda)}\frac{h(0)}{c|U'(0)|}\widehat{\omega}(k)\widehat{\Phi}(kc+i\lambda) \tag{3.25}$$

where

$$\widehat{\varphi}(k) = \int_{-\infty}^{\infty}\varphi(y)\,\mathrm{e}^{\mathrm{i}ky}\,\mathrm{d}y \tag{3.26}$$

etc. Now suppose that for a given value of k there exists $\lambda = \lambda(k)$ for which $[\widehat{\Phi}(kc+i\lambda(k))]^{-1} = 0$. It follows that the right-hand side of equation (3.25) blows up if $\lambda = \lambda(k)$, that is, the dispersion curve belongs to the essential spectrum.

For the sake of illustration, let us calculate the zeros of the Evans function in the case of the exponential weight function (3.1). Substituting $\Phi(t) = \mathrm{e}^{-t}$ and $w(y) = \mathrm{e}^{-|y|/\sigma}/2\sigma$ in equation (3.21) gives

$$\mathcal{H}(\lambda) = \frac{1}{2\sigma}\frac{1}{\sigma^{-1}+\lambda/c+1/c} \tag{3.27}$$

so that [79]

$$\mathcal{E}(\lambda) = \frac{\lambda}{c/\sigma + 1 + \lambda}. \tag{3.28}$$

It follows that $\lambda = 0$ is the only zero of the Evans function and it is a simple root (since $\mathcal{E}'(0) > 0$). Furthermore, in the particular case $\Phi(t) = \mathrm{e}^{-t}$, we have $[\widetilde{\Phi}(kc + \mathrm{i}\lambda)]^{-1} = 1 - \mathrm{i}kc + \lambda$ so that the essential spectrum is $\lambda(k) = -1 + \mathrm{i}kc$, that is, a vertical line in the complex plane at $\mathrm{Re}\lambda = -1$. It follows that the corresponding traveling front (it it exists) is stable.

The above example illustrates one of the powerful features of the constructive method based on Heavisides. Not only is it possible to construct exact traveling wave solutions and derive formulas for the speed of the wave, but one can also explicitly construct the Evans function that determines wave stability. The method extends to multi-population neural field models, neural fields with axonal propagation delays, and adaptive neural fields [79]. (Although taking the high-gain limit of a smooth firing rate function is not very realistic from a biological perspective, one finds that many of the basic features of traveling waves persist for finite gain.) In the particular case of axonal delays, it can be shown that delays reduce the speed of a wave but do not affect its stability properties. For example, given a right moving traveling front solution of the scalar neural field equation (2.50) with $\tau = 1$ and exponential weights, one finds that the speed of the wave is [66, 79]

$$c = \sigma \frac{1 - 2\kappa}{2\kappa + \sigma(1 - 2\kappa)/v}, \tag{3.29}$$

where v is the propagation speed along an axon, and the Evans function is

$$\mathcal{E}(\lambda) = \frac{\lambda}{c/\sigma + (1 - c/v) + \lambda}. \tag{3.30}$$

3.3. Traveling pulses in adaptive neural fields

Traveling fronts are not particularly realistic, since populations of cells do not stay in the excited state forever. Hence, rather than a traveling front, propagating activity in cortex is usually better described as a traveling pulse. (One example where fronts rather than pulses occur is wave propagation during binocular rivalry [114–117], see section 3.3.3.) One way to generate a traveling pulse is to include some form of synaptic inhibition, provided that it is not too strong [12]. However, even in the absence of synaptic inhibition, most neurons possess intrinsic negative feedback mechanisms that slowly bring the cell back to resting voltages after periods of high activity. Possible nonlinear mechanisms include synaptic depression or spike frequency adaptation as discussed in section 2. However, most analytical studies of traveling pulses in neural field models have been based on a simpler linear form of adaptation introduced by Pinto and Ermentrout [17]. (For an analysis of waves in neural fields with nonlinear adaptation, see for example [61, 64].) The linear adaptation model is given by

$$\begin{aligned} \frac{\partial u(x,t)}{\partial t} &= -u(x,t) + \int_{-\infty}^{\infty} w(x - x') F(u(x',t))\, \mathrm{d}x' - \beta q(x,t) \\ \frac{1}{\epsilon}\frac{\partial q(x,t)}{\partial t} &= -q(x,t) + u(x,t), \end{aligned} \tag{3.31}$$

where ϵ and β determine the rate and amplitude of linear adaptation. We first show how to construct a traveling pulse solution of equation (3.31) in the case of a Heaviside rate function $F(u) = H(u - \kappa)$, following the particular formulation of [78, 112]. We then indicate how singular perturbation methods can be used to construct a traveling pulse for smooth F, as carried out by Pinto and Ermentrout [17]. The introduction of adaptation means that the neural

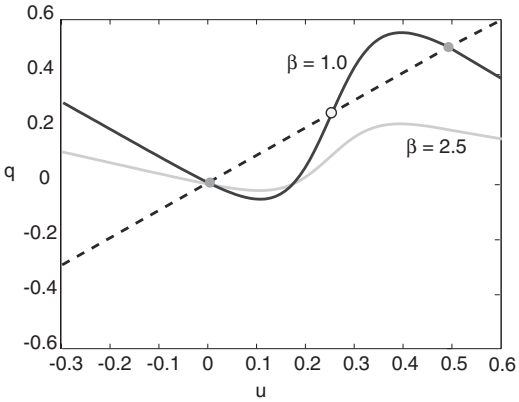

Figure 6. Plot of nullclines for space-clamped planar system $\dot{u} = -u + F(u) - \beta u, \epsilon^{-1}\dot{q} = -q + u$ with $F(u) = 1/(1 + \mathrm{e}^{-\eta(u-\kappa)})$. Nullcline $q = -u + F(u)]/\beta$ for $\beta = 1.0$ ($\beta = 2.5$) intercepts straight nullcline $q = u$ at three fixed points (one fixed point) and the corresponding spatially extended network acts as a bistable (excitable) medium. Other parameters are $\eta = 20, \kappa = 0.25$.

field can act either as an excitable medium or as a bistable medium, see figure 6, depending on parameter values. In the former case, the neural field supports traveling pulses and in the latter case traveling fronts. We will focus on the former here. Note, however, that linear (or nonlinear) adaptation can have a nontrivial effect on the propagation of traveling fronts [105, 118]. This is due to the occurrence of a symmetry breaking front bifurcation analogous to that found in reaction diffusion systems [119–122]. That is, a stationary front can undergo a supercritical pitchfork bifurcation at a critical rate of adaptation, leading to bidirectional front propagation. As in the case of reaction diffusion systems, the front bifurcation acts as an organizing center for a variety of nontrivial dynamics including the formation of oscillatory fronts or breathers. The latter can occur, for example, through a Hopf bifurcation from a stationary front in the presence of a weak stationary input inhomogeneity [105].

3.3.1. Exact traveling pulse solution. Without loss of generality, let us consider a right-moving traveling pulse solution of the form $(u(x,t), q(x,t)) = (U(x-ct), Q(x-ct))$ with $U(\pm\infty), Q(\pm\infty) = 0$ and $U(-\Delta) = U(0) = \kappa$, see figure 5(*b*). Here c, Δ denote the speed and width of the wave, respectively. We also assume that $U(\xi) > \kappa$ for $\xi \in (-\Delta, 0)$ and $U(\xi) < \kappa$ for $\xi < -\Delta$ and $\xi > 0$. Substituting this solution into equation (3.31) with $\xi = x - ct$ then gives

$$\begin{aligned} -cU'(\xi) + U(\xi) + \beta Q(\xi) &= \int_{-\Delta}^{0} w(\xi - \xi')\,\mathrm{d}\xi' \\ -cQ'(\xi) + \epsilon[Q(\xi) - U(\xi)] &= 0. \end{aligned} \tag{3.32}$$

It is useful to rewrite equation (3.32) in the matrix form

$$\begin{pmatrix} 1 & \beta \\ -\epsilon & \epsilon \end{pmatrix} \begin{pmatrix} U \\ Q \end{pmatrix} - c\partial_\xi \begin{pmatrix} U \\ Q \end{pmatrix} = [W(\xi) - W(\xi + \Delta)] \begin{pmatrix} 1 \\ 0 \end{pmatrix}. \tag{3.33}$$

with $W(\xi) = \int_\xi^\infty w(x)\,\mathrm{d}x$. We proceed by diagonalizing the left-hand side of equation (3.33) using the right eigenvectors $\mathbf{v}$ of the matrix

$$\mathbf{M} = \begin{pmatrix} 1 & \beta \\ -\epsilon & \epsilon \end{pmatrix}. \tag{3.34}$$

These are given by $\mathbf{v}_\pm = (\epsilon - \lambda_\pm, \epsilon)^T$ with corresponding eigenvalues

$$\lambda_\pm = \tfrac{1}{2}[1 + \epsilon \pm \sqrt{(1+\epsilon)^2 - 4\epsilon(1+\beta)}]. \tag{3.35}$$

We will assume that ϵ is sufficiently small so that $\beta < (1-\epsilon)^2/4\epsilon$ and consequently $\lambda_\pm$ are real. (For a discussion of the effects of complex eigenvalues $\lambda_\pm$ see [104].) Note that $\mathbf{v}_\pm \mathrm{e}^{\lambda_\pm \xi/c}$ are the corresponding null vectors of the linear operator on the left-hand side of equation (3.33). Performing the transformation

$$\begin{pmatrix} \widetilde{U} \\ \widetilde{Q} \end{pmatrix} = \mathbf{T}^{-1} \begin{pmatrix} U \\ Q \end{pmatrix}, \quad \mathbf{T} = (\mathbf{v}_+ \quad \mathbf{v}_-), \tag{3.36}$$

then gives the pair of equations

$$\begin{aligned} -c\partial_\xi \widetilde{U} + \lambda_+ \widetilde{U} &= \eta_+[W(\xi) - W(\xi+\Delta)] \\ -c\partial_\xi \widetilde{Q} + \lambda_- \widetilde{Q} &= \eta_-[W(\xi) - W(\xi+\Delta)] \end{aligned} \tag{3.37}$$

with $\eta_\pm = \mp 1/(\lambda_+ - \lambda_-)$. Integrating the equation for $\widetilde{U}$ from $-\Delta$ to ∞, we have

$$\widetilde{U}(\xi) = \mathrm{e}^{\lambda_+\xi/c}\left[\widetilde{U}(-\Delta)\mathrm{e}^{\Delta\lambda_+/c} - \frac{\eta_+}{c}\int_{-\Delta}^{\xi} \mathrm{e}^{-\lambda_+\xi'/c}[W(\xi') - W(\xi'+\Delta)]\,\mathrm{d}\xi'\right]. \tag{3.38}$$

Finiteness of $\widetilde{U}$ in the limit $\xi \to \infty$ requires the term in square brackets to cancel. Hence, we can eliminate $\widetilde{U}(-\Delta)$ to obtain the result

$$\widetilde{U}(\xi) = \frac{\eta_+}{c}\int_0^\infty \mathrm{e}^{-\lambda_+\xi'/c}[W(\xi'+\xi) - W(\xi'+\xi+\Delta)]\,\mathrm{d}\xi'. \tag{3.39}$$

Similarly,

$$\widetilde{Q}(\xi) = \frac{\eta_-}{c}\int_0^\infty \mathrm{e}^{-\lambda_-\xi'/c}[W(\xi'+\xi) - W(\xi'+\xi+\Delta)]\,\mathrm{d}\xi'. \tag{3.40}$$

Performing the inverse transformation $U = (\epsilon - \lambda_+)\widetilde{U} + (\epsilon - \lambda_-)\widetilde{Q}$ we have

$$U(\xi) = \frac{1}{c}\int_0^\infty \left[\chi_+ \mathrm{e}^{-\lambda_+\xi'/c} + \chi_- \mathrm{e}^{-\lambda_-\xi'/c}\right][W(\xi'+\xi) - W(\xi'+\xi+\Delta)]\,\mathrm{d}\xi', \tag{3.41}$$

with $\chi_\pm = (\epsilon - \lambda_\pm)\eta_\pm$. The threshold conditions $U(-\Delta) = \kappa$ and $U(0) = \kappa$ then yield a pair of equations whose solutions determine existence curves relating the speed c and width Δ of a pulse to the threshold κ [17, 79, 112].

For the sake of illustration, let w be given by the exponential function (3.1). In the domain $\xi > 0$, there is a common factor of $\mathrm{e}^{-\xi/\sigma}$ in the integrand of equation (3.41) so that $U(\xi) = \kappa \mathrm{e}^{-\xi/\sigma}$ for $\xi > 0$ provided that

$$\kappa = \frac{1}{2}\frac{\sigma(c+\epsilon\sigma)(1-\mathrm{e}^{-\Delta/\sigma})}{c^2 + c\sigma(1+\epsilon) + \sigma^2\epsilon(1+\beta)}. \tag{3.42}$$

(Note that for zero negative feedback ($\beta = 0$), equation (3.42) reduces to the formula for wavespeed of a front in the limit $\Delta \to \infty$.) On the other hand, when $\xi < 0$ one has to partition the integral of equation (3.41) into the separate domains $\xi' > |\xi|$, $|\xi| - \Delta < \xi' < |\xi|$ and $\xi' < |\xi| - \Delta$. This then determines the second threshold condition as well as the asymptotic behavior of $U(\xi)$ in the limit $\xi \to -\infty$:

$$U(\xi) = A_+ \mathrm{e}^{\lambda_+\xi/c} + A_- \mathrm{e}^{\lambda_-\xi/c} + A_0 \mathrm{e}^{\sigma\xi}. \tag{3.43}$$

where the amplitudes $A_\pm$ and A_0 can be determined from matching conditions at the threshold crossing points [17, 112]. Note that the leading edge of the pulse is positive, whereas the trailing edge is negative due to the effects of adaptation. One finds that for sufficiently slow negative feedback (small ϵ) and large β there exist two pulse solutions, one narrow and slow and the other wide and fast. This is illustrated in figure 7. Note that a numerical value of

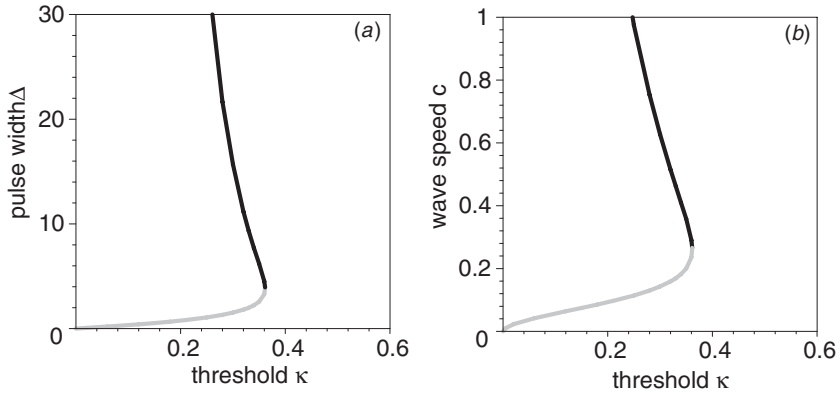

Figure 7. Existence of right-moving traveling pulses in the case of the excitatory network (3.31) with linear adaptation for an exponential weight distribution (3.1). Here $\sigma = 1, \epsilon = 0.01$ and $\beta = 2.5$. (*a*) Plot of pulse width Δ against threshold κ. (*b*) Plot of wave speed c against threshold κ. Stable (unstable) branches indicated by black (gray) curves.

$c \sim 1$ in dimensionless units ($\sigma = \tau = 1$) translates into a physical speed of 60–90 mm s^{-1} if the membrane time constant $\tau = 10$ ms and the range of synaptic connections is $\sigma =$ 600–900 μm.

Numerically, the fast solution is found to be stable [17], and this can be confirmed analytically using an Evans function construction [3, 79, 112]. First, write the neural field equation (3.31) in the integral form

$$u(x,t) = \int_{-\infty}^{\infty}\int_{0}^{\infty} w(y)\Phi(s)F(u(x-y,t-s))\,\mathrm{d}s\mathrm{d}y - \beta\int_{0}^{\infty}\Psi(s)u(x,t-s)\,\mathrm{d}s, \tag{3.44}$$

with $\Phi(t) = \mathrm{e}^{-t}H(t)$ and $\Psi(t) = \int_0^t \Phi(s)\mathrm{e}^{-\epsilon(t-s)}\,\mathrm{d}s$. Linearizing about the pulse solution by setting $u(x,t) = U(\xi) + \varphi(\xi)\mathrm{e}^{\lambda t}$ gives

$$\varphi(\xi) = \int_{-\infty}^{\infty}\int_{\xi-y}^{\infty} w(y)\Phi((s+y-\xi)/c)\,\mathrm{e}^{-\lambda(s+y-\xi)/c}F'(U(s))\varphi(s)\frac{\mathrm{d}s}{c}\,\mathrm{d}y$$
$$-\beta\int_{\xi}^{\infty}\Psi((s-\xi)/c)\,\mathrm{e}^{-\lambda(s-\xi)/c}\varphi(s)\frac{\mathrm{d}s}{c}. \tag{3.45}$$

Proceeding along similar lines to the analysis of front stability in section 3.2, we set $F(U) = H(U-\kappa)$ and use the identity

$$H'(U(\xi)-\kappa) = \delta(U(\xi)-\kappa) = \frac{\delta(\xi)}{|U'(0)|} + \frac{\delta(\xi+\Delta)}{|U'(-\Delta)|}. \tag{3.46}$$

This gives

$$\varphi(\xi) + \beta\int_{\xi}^{\infty}\Psi((s-\xi)/c)\,\mathrm{e}^{-\lambda(s-\xi)/c}\varphi(s)\frac{\mathrm{d}s}{c}$$
$$= \frac{\varphi(0)}{c|U'(0)|}\mathcal{H}(\lambda,\xi) + \frac{\varphi(-\Delta)}{c|U'(-\Delta)|}\mathcal{H}(\lambda,\xi+\Delta), \tag{3.47}$$

where

$$\mathcal{H}(\lambda,\xi) = \int_{\xi}^{\infty} w(y)\Phi((y-\xi)/c)\,\mathrm{e}^{-\lambda(y-\xi)/c}\,\mathrm{d}y. \tag{3.48}$$

Let $\widehat{\mathcal{H}}(\lambda, k)$ denote the Fourier transform of $\mathcal{H}(\lambda, \xi)$ and $\widehat{\mathcal{G}}(\lambda, k)$ denote the Fourier transform of $\Psi(\xi/c)\,\mathrm{e}^{-\xi/c}$. Using Fourier transforms and the convolution theorem, equation (3.47) can then be rewritten as

$$\varphi(\xi) = \frac{\varphi(0)}{c|U'(0)|}\mathcal{B}(\lambda, \xi) + \frac{\varphi(-\Delta)}{c|U'(-\Delta)|}\mathcal{B}(\lambda, \xi + \Delta), \tag{3.49}$$

with $\mathcal{B}(\lambda, \xi)$ the inverse transform of

$$\widehat{\mathcal{B}}(\lambda, k) = \frac{\widehat{\mathcal{H}}(\lambda, k)}{[1 + \beta\widehat{\mathcal{G}}(\lambda, -k)/c]}. \tag{3.50}$$

Finally, the eigenvalues λ are determined by setting $\xi = 0, -\Delta$ and solving the resulting matrix equation $\mathbf{f} = \mathcal{M}(\lambda)\mathbf{f}$ with $\mathbf{f} = (\varphi(0), \varphi(-\Delta))$ and

$$\mathcal{M}(\lambda) = \frac{1}{c}\begin{pmatrix} \dfrac{\mathcal{B}(\lambda, 0)}{|U'(\xi_1)|} & \dfrac{\mathcal{B}(\lambda, \Delta)}{|U'(-\Delta)|} \\ \dfrac{\mathcal{B}(\lambda, -\Delta)}{|U'(0)|} & \dfrac{\mathcal{B}(\lambda, 0)}{|U'(-\Delta)|} \end{pmatrix}. \tag{3.51}$$

It follows that the eigenvalues λ are zeros of the Evans function

$$\mathcal{E}(\lambda) = \mathrm{Det}[\mathbf{1} - \mathcal{M}(\lambda)], \tag{3.52}$$

where $\mathbf{1}$ denotes the identity matrix.

3.3.2. Singularly perturbed pulse solution. In the case of slow adaptation ($\epsilon \ll 1$), Pinto and Ermentrout [17] showed how to construct a traveling pulse solution of equation (3.31) for a smooth firing rate function F by exploiting the existence of traveling front solutions of the corresponding scalar equation (3.2). The method is analogous to the construction of traveling pulses in reaction-diffusion systems [13]. The basic idea is to analyze separately the fast and slow time behavior of solutions to equation (3.31) expressed in traveling wave coordinates:

$$-c\frac{\mathrm{d}U(\xi)}{\mathrm{d}\xi} = -U(\xi) - \beta Q(\xi) + \int_{-\infty}^{\infty} w(\xi - \xi')F(U(\xi'))\,\mathrm{d}\xi', \tag{3.53}$$

$$-c\frac{\mathrm{d}Q(\xi)}{\mathrm{d}\xi} = \epsilon[-Q(\xi) + U(\xi)]. \tag{3.54}$$

We will assume the normalization $\int_{-\infty}^{\infty} w(y)\,\mathrm{d}y = 1$. In the case of fast time, the slow adaptation is taken to be constant by setting $\epsilon = 0$ so that we have the inner layer equations

$$-c\frac{\mathrm{d}U(\xi)}{\mathrm{d}\xi} = -U - \beta Q_0 + \int_{-\infty}^{\infty} w(\xi - \xi')F(U(\xi'))\,\mathrm{d}\xi', \tag{3.55}$$

$$-c\frac{\mathrm{d}Q(\xi)}{\mathrm{d}\xi} = 0. \tag{3.56}$$

Since $Q(\xi) = Q_0$ is a constant, the term βQ_0 can be absorbed into the threshold of the firing rate function F by making the shift $U(\xi) \to U(\xi) + \beta Q_0$. Hence equation (3.55) is equivalent to the scalar equation (3.7), which supports the propagation of traveling fronts. In the case of slow time, we introduce the compressed variable $\zeta = \epsilon\xi$ so that

$$-c\epsilon\frac{\mathrm{d}U(\zeta)}{\mathrm{d}\zeta} = -U(\zeta) - \beta Q(\zeta) + \frac{1}{\epsilon}\int_{-\infty}^{\infty} w([\zeta - \zeta']/\epsilon)F(U(\zeta'))\,\mathrm{d}\zeta', \tag{3.57}$$

$$-c\frac{\mathrm{d}Q(\zeta)}{\mathrm{d}\zeta} = -Q(\zeta) + U(\zeta). \tag{3.58}$$

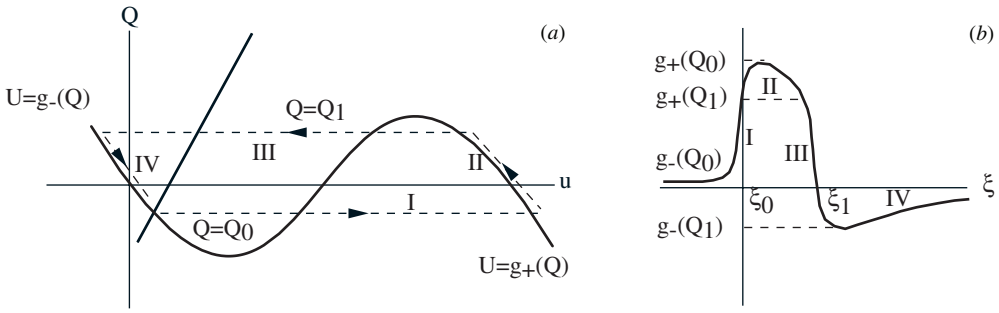

Figure 8. Singular perturbation construction of a traveling pulse in (*a*) the phase-plane and (*b*) traveling wave coordinates. See text for details.

In the limit $\epsilon \to 0$, we have

$$\frac{1}{\epsilon} w([\zeta - \zeta']/\epsilon) \to \delta(\zeta - \zeta') \tag{3.59}$$

so that first equation becomes

$$\beta Q(\zeta) = -U(\zeta) + F(U(\zeta)). \tag{3.60}$$

Inverting this equation yields two branches $U = g_{\pm}(Q)$. Hence we obtain a slow time or outer layer equation on each branch, see figure 8:

$$\frac{\mathrm{d}Q}{\mathrm{d}\zeta} = \frac{1}{c}[Q - g_{\pm}(Q)]. \tag{3.61}$$

The construction of the traveling pulse now proceeds by matching inner and outer solutions [17]. This can be visualized by considering the nullclines of the space-clamped version of equation (3.31), see figure 8. We assume that the gain of F and the strength β of adaptation are such that there is only a single fixed point of the space-clamped system.

(I) Starting at the unique fixed point, use the fast inner equations and the existence results of [82] to construct a leading front solution at $Q = Q_0$ with speed c_0 and matching conditions $\lim_{\xi \pm \infty} U(\xi) = g_{\pm}(Q_0)$.

(II) Use the slow outer equations to determine dynamics of Q along upper branch $U = g_+(Q)$.

(III) The solution leaves upper branch at some point Q_1. Once again use the fast inner equations and [82] to construct a trailing front solution with speed c_1 and matching conditions

$$\lim_{\xi \pm \infty} U(\xi) = g_{\mp}(Q_1).$$

(IV) Finally, use the slow outer equations to determine the return to the fixed point along the lower branch.

In order to establish the existence of a traveling pulse solution, it remains to find a value Q_1 for which $c_1 = -c_0$ so that the leading and trailing edges of the pulse move at the same speed and thus the pulse maintains its shape as it propagates. (Since Q_0 is known so is c_0.) Adapting the formula for the wave speed obtained in [82], we have

$$c_1 = -\frac{\Gamma}{\int_{-\infty}^{\infty} U'^2(\xi) F'(U(\xi))\,\mathrm{d}\xi}, \qquad \Gamma = \int_{g_-(Q_1)}^{g_+(Q_1)} [-U - Q_1 + F(U)]\,\mathrm{d}U. \tag{3.62}$$

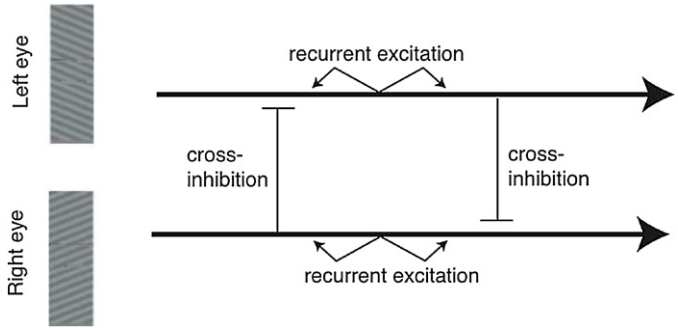

Figure 9. Schematic diagram of a neural field model of perceptual switching. Each 1D neural field corresponds to a different visual percept, which could represent distinct oriented stimuli presented to the two eyes during binocular rivalry.

Unfortunately, it is not possible to derive a closed form expression for the wave speed. However, the existence of a matching speed can be established provided that certain additional assumptions are made regarding the shape of the firing rate function, see [17] for more details.

3.4. Adaptive neural field model of wave propagation during perceptual switching

A number of phenomena in visual perception involve the propagation of a traveling front, in which a suppressed visual percept replaces a dominant percept within the visual field of an observer. A classical example is the wave-like propagation of perceptual dominance during binocular rivalry [114–116]. Binocular rivalry is the phenomenon whereby perception switches back and forth between different images presented to the two eyes. The resulting fluctuations in perceptual dominance and suppression provide a basis for non-invasive studies of the human visual system and the identification of possible neural mechanisms underlying conscious visual awareness [123, 124].

A simple neural field model for wave propagation during perceptual switching is shown in figure 9, see [117]. It is assumed that the two competing visual percepts are represented by the activity in two 1D neural fields. In the case of binocular rivalry, these could represent networks stimulated by left and right eye inputs, respectively. Recurrent connections within each 1D network are assumed to be excitatory, whereas connections between the two networks are inhibitory (cross-inhibition). Slow adaptation is incorporated into the model by taking the network connections to exhibit synaptic depression. The combination of cross-inhibition paired with a slow adaptive process forms the basis of most competitive network models of binocular rivalry [114, 125–129]. However, these studies neglect spatial effects or treat them computationally. The advantage of a continuum neural field model is that it provides an analytical framework for studying perceptual wave propagation [117]. Let $u(x,t)$ and $v(x,t)$ denote the activity of the two networks. The associated neural field equations are a generalization of (2.49):

$$\begin{aligned}\frac{\partial u(x,t)}{\partial t} &= -u(x,t) + \int_{-\infty}^{\infty} w_e(x-x')q_u(x',t)F(u(x',t)))\,\mathrm{d}x' \\ &\quad - \int_{-\infty}^{\infty} w_i(x-x')q_v(x',t)f(v(x',t)))\,\mathrm{d}x' + I_u(x,t) \\ \tau_q\frac{\partial q_u(x,t)}{\partial t} &= 1 - q_u(x,t) - \beta q_u(x,t)F(u(x,t)),\end{aligned} \tag{3.63}$$

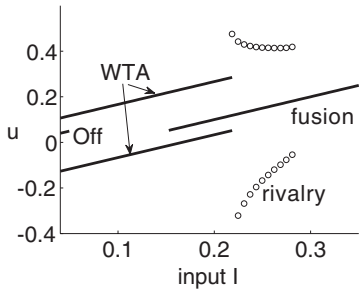

Figure 10. Bifurcation diagram showing homogeneous solutions for the neural field u as a function of the input amplitude I. Solid lines represent stable states, whereas circles represent the maximum and minimum of perceptual switching oscillations. It can be seen that there are regions of off/WTA bistability, WTA/fusion bistability, and fusion/rivalry bistability. Parameters are $\tau_q = 500$, $\kappa = 0.05$, $\beta = 5$, $a_e = 0.4$ and $a_i = -1$.

and

$$\frac{\partial v(x,t)}{\partial t} = -v(x,t) + \int_{-\infty}^{\infty} w_e(x-x')q_v(x',t)F(v(x',t)))\,\mathrm{d}x' - \int_{-\infty}^{\infty} w_i(x-x')q_u(x',t)F(u(x',t)))\,\mathrm{d}x' + I_v(x,t),$$

$$\tau_q \frac{\partial q_v(x,t)}{\partial t} = 1 - q_v(x,t) - \beta q_v(x,t) f(v(x,t)). \tag{3.64}$$

The distribution w_e of recurrent excitatory connections and the distribution of cross-inhibitory connections are both taken to be Gaussians:

$$w_e(r) = \frac{a_e}{\sqrt{2\pi\sigma_e^2}}\,\mathrm{e}^{-\frac{r^2}{2\sigma_e^2}}, \qquad w_i(r) = \frac{a_i}{\sqrt{2\pi\sigma_i^2}}\mathrm{e}^{-\frac{r^2}{2\sigma_i^2}}. \tag{3.65}$$

Depressing synapses are incorporated into the model in the form of the presynaptic scaling factors q_u, q_v. Finally, I_u, I_v represent the effective strength of the stimuli representing the two percepts. We will assume that the unperturbed network has $I_u = I_v = I$ with I a constant input.

In order to construct exact traveling front solutions, let $F(u) = H(u - \kappa)$. It is then straightforward to show that there exist four homogeneous fixed points (U^*, V^*, Q_u^*, Q_v^*) corresponding to an off-state $(U^* < \kappa, V^* < \kappa)$, a fusion state $(U^* > \kappa, V^* > \kappa)$, and two winner-take-all (WTA) states (either $U^* = U_+ > \kappa, V^* = V_- < \kappa$ or $U^* = U_- < \kappa, V^* = V_+ > \kappa$), and all are stable. It can also be shown that equations (3.63) and (3.64) support homogeneous limit cycle oscillations in which there is periodic switching between perceptual dominance consistent with binocular rivalry, for example [128]. Since all the fixed points are stable, it follows that such oscillations cannot arise via a standard Hopf bifurcation. Indeed, there exist bistable regimes where a rivalry state coexists with a fusion state as illustrated in figure 10. (Such behavior persists in the case of smooth sigmoid firing rate functions, at least for sufficiently high gain [128].) Suppose that the full system given by equations (3.63) and (3.64) is initially in a stable WTA state with the v–network dominant, and is then perturbed away from this state by introducing a propagating front that generates a perceptual dominance switch. (Such a switch can be induced experimentally by temporarily introducing a spatially localized increase in the input to one of the networks [114, 116].) Furthermore, suppose that over a finite spatial domain of interest the time taken for the wave front to propagate is much smaller than the relaxation time τ_q of synaptic depression. To a first approximation we can

then ignore the dynamics of the depression variables and assume that they are constant, that is, $(q_u(x,t), q_v(x,t)) = (Q_u, Q_v)$ with $Q_u = 1$ and $Q_v = (1+\beta)^{-1}$. A similar adiabatic approximation can also be made if the network is in an oscillatory state, provided that (a) the duration of wave propagation is short compared to the natural switching period and (b) the induction of the wave does not occur close to the point at which spontaneous switching occurs. In this case Q_u and Q_v will not be given by the WTA fixed point solution, but $Q_u \neq Q_v$.

Consider a traveling front solution of the form $u(x,t) = U(x-ct), \quad v(x,t) = V(x-ct)$, where c is the wave speed and $\xi = x - ct$ is a traveling wave coordinate. Furthermore, $(U(\xi), V(\xi)) \to \mathbf{X}_L$ as $\xi \to -\infty$ and $(U(\xi), V(\xi)) \to \mathbf{X}_R$, as $\xi \to \infty$, where $\mathbf{X}_L = (Q_u a_e + I, I - Q_v a_i)$, $\mathbf{X}_R = (I - Q_u a_i, Q_v a_e + I)$, and $U(\xi)$ $(V(\xi))$ is a monotonically decreasing (increasing) function of ξ. It follows that if $c > 0$ then the wavefront represents a solution in which activity invades the supressed u-network and retreats from the dominant v-network. Given the asymptotic behavior of the solution and the requirements of monotonicity, it follows that $U(\xi)$ and $V(\xi)$ each cross threshold at a single location, which may be different for the two eyes. Exploiting translation invariance we take $U(0) = \kappa$ and $V(\xi_0) = \kappa$. Substituting the traveling front solution into equations (3.63) and (3.64) gives (after integration)

$$U(\xi) = \int_0^\infty \mathrm{e}^{-s} \left[Q_u \int_{\xi+cs}^\infty w_e(y)\,\mathrm{d}y - Q_v \int_{-\infty}^{\xi-\xi_0+cs} w_i(y)\,\mathrm{d}y \right] \mathrm{d}s + I \tag{3.66}$$

$$V(\xi) = \int_0^\infty \mathrm{e}^{-s} \left[Q_v \int_{-\infty}^{\xi-\xi_0+cs} w_e(y)\,\mathrm{d}y - Q_u \int_{\xi+cs}^\infty w_i(y)\,\mathrm{d}y \right] \mathrm{d}s + I. \tag{3.67}$$

Finally, imposing the threshold crossing conditions gives the pair of equations

$$\kappa = \int_0^\infty \mathrm{e}^{-s} \Psi_{\xi_0}(cs)\,\mathrm{d}s + I, \qquad \kappa = \int_0^\infty \mathrm{e}^{-s} \Phi_{\xi_0}(-cs)\,\mathrm{d}s + I, \tag{3.68}$$

with Ψ and Φ defined by

$$\Psi_{\xi_0}(z) = Q_u \int_z^\infty w_e(y)\,\mathrm{d}y - Q_v \int_{-\infty}^{z-\xi_0} w_i(y)\,\mathrm{d}y. \tag{3.69}$$

$$\Phi_{\xi_0}(z) = Q_v \int_z^\infty w_e(y)\,\mathrm{d}y - Q_u \int_{-\infty}^{z-\xi_0} w_i(y)\,\mathrm{d}y. \tag{3.70}$$

In order to establish the existence of a wave speed c and a threshold crossing point ξ_0, define the functions

$$\mathcal{F}_1(c,\xi_0) = \int_0^\infty \mathrm{e}^{-s} \Psi_{\xi_0}(cs)\,\mathrm{d}s, \qquad \mathcal{F}_2(c,\xi_0) = \int_0^\infty \mathrm{e}^{-s} \Phi_{\xi_0}(-cs)\,\mathrm{d}s. \tag{3.71}$$

Taking the difference of the two threshold conditions (3.68) yields the implicit equation

$$\mathcal{F}(c,\xi_0) \equiv \mathcal{F}_1(c,\xi_0) - \mathcal{F}_2(c,\xi_0) = 0. \tag{3.72}$$

It is straightforward to show that for fixed ξ_0,

$$\lim_{c\to\infty} \mathcal{F}(c,\xi_0) > 0, \qquad \lim_{c\to-\infty} \mathcal{F}(c,\xi_0) < 0.$$

Hence, the intermediate value theorem guarantees at least one solution $c = c(\xi_0)$, which is differentiable by the implicit function theorem. If $Q_u = Q_v$, then $\mathcal{F}_1(0,\xi_0) = \mathcal{F}_2(0,\xi_0)$ and the only point where $\mathcal{F}$ vanishes is at $c = 0$. On the other hand, if $Q_v \neq Q_u$ then $\mathcal{F}(0,\xi_0) \neq 0$ for all finite ξ_0 so that $c(\xi_0) \neq 0$. Given a solution $c = c(\xi_0)$ of equation (3.72), the existence of a traveling wavefront solution reduces to the single threshold condition

$$\kappa = \mathcal{F}_1(c(\xi_0),\xi_0) + I. \tag{3.73}$$

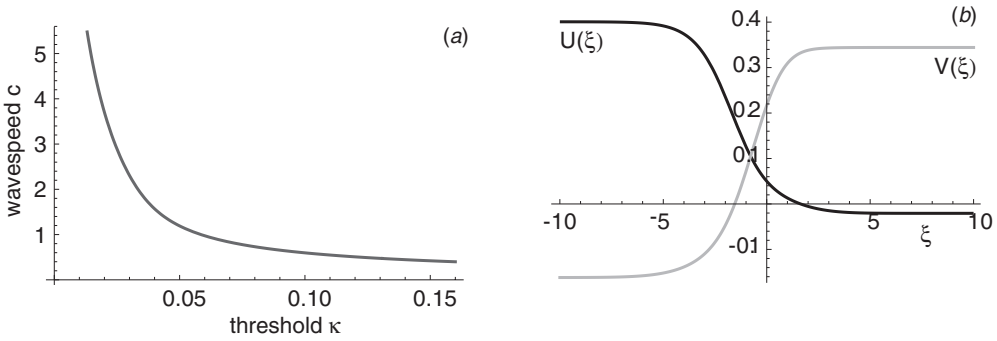

Figure 11. (*a*) Plot of wave speed c as a function of the threshold κ. (*b*) Plot of right-moving traveling front solution in which a high activity state invades the suppressed u-network whilst retreating from the dominant v-network. The default parameters are taken to be $a_i = 1, a_e = 0.4, \sigma_i = 1, \sigma_e = 2, \beta = 5, \kappa = 0.05, I = 0.24, Q_u = 0.42, Q_v = 0.25$ and the corresponding wave speed is $c = 1.2$.

Numerically solving this equations shows that there exists a unique traveling front solution for a range of values of the threshold κ and input I, see figure 11. The model wave speed is of the order $c = 1$ in dimensionless units, that is, $c = \sigma_e/2\tau$ where σ_e is the range of excitation and τ is the membrane time constant. Taking σ_e to be of the order 200 μm and τ to be of the order 10 ms gives a wavespeed of 10 mm s^{-1}, which is consistent with psychophysical experiments on binocular rivalry waves [114, 116].

The above model suggests that slow adaptation plays a crucial role in the generation of perceptual waves. In the absence of any adaptation ($q_u = q_v \equiv 1$), a traveling front solution does not exist, which is consistent with the observation that if there is no cross-inhibition ($w_i \equiv 0$) then the system reduces to two independent 1D neural fields with excitatory connections. In order to construct a front solution that simultaneously invades one network whilst retreating from the other, a ID excitatory neural field without adaptation would have to support a pair of counter-propagating front solutions with speeds $\pm c$, which is not possible (see section 3.1 and [12]). Therefore, some mechanism must be introduced that breaks the exchange symmetry of the two 1D networks. The above analysis shows that this can be achieved by including some form of slow adaptation such as synaptic depression.

3.5. Wave propagation failure in inhomogeneous neural fields

Most studies of neural field theory assume that the synaptic weight distribution only depends upon the distance between interacting populations, that is, $w(x, y) = w(|x - y|)$. This implies translation symmetry of the underlying integrodifferential equations (in an unbounded or periodic domain). As we have reviewed in previous sections, excitatory networks then support the propagation of solitary traveling waves. However, if one looks more closely at the anatomy of cortex, it is clear that its detailed microstructure is far from homogeneous. For example, to a first approximation, primary visual cortex (V1) has a periodic-like microstructure on the millimeter length-scale, reflecting the existence of various stimulus feature maps, see section 5.2. This has motivated a number of studies concerned with the effects of a periodically modulated weight distribution on wave propagation in neural fields [74, 101, 102].

Consider for simplicity the 1D scalar neural field equation (2.47) with periodically modulated weight distribution

$$w(x,y) = w(x-y)[1+\rho K(y/\varepsilon)], \tag{3.74}$$

where ρ is the amplitude of the periodic modulation and ε is the period with $K(x) = K(x+1)$ for all x. (Note that in section 3.3 we used ϵ (rather than ε) to denote the slow rate of adaptation in the adaptive neural field model (3.31).) It will also be assumed that if $\rho = 0$ (no periodic modulation), then the resulting homogeneous network supports a traveling front solution of speed c_0 as analyzed in section 3.1. We will review two alternative methods for analyzing the effects of periodic wave modulation, one based on homogenization theory for small ε [20], and the other based on analyzing interfacial dynamics [102]. Both approaches make use of the observation that for sufficiently small ρ, numerical simulations of the inhomogeneous network show a front-like wave separating high and low activity states. However, the wave does not propagate with constant speed, but oscillates periodically in an appropriately chosen moving frame. This pulsating front solution satisfies the periodicity condition $u(x,t) = u(x+\varepsilon, t+T)$ so that we can define the mean speed of the wave to be $c = \varepsilon/T$.

3.5.1. Homogenization theory. Suppose that the period ε of weight modulations is much smaller than the range of synaptic interactions $\varepsilon \ll \sigma$. (We fix the length scales by setting $\sigma = 1$.) Substituting equation (3.74) into (2.47) and integrating by parts gives

$$\begin{aligned}\frac{\partial u(x,t)}{\partial t} = & -u(x,t) + \int_{-\infty}^{\infty} w(x-x')F(u(x',t))\,\mathrm{d}x' \\ & + \varepsilon \int_{-\infty}^{\infty} A(x'/\varepsilon)\left[w'(x-x')F(u(x',t)) - w(x-x')\frac{\partial F(u(x',t))}{\partial x'}\right]\mathrm{d}x'.\end{aligned} \tag{3.75}$$

Here $A'(x) = \rho K(x)$ with A only having to be defined up to an arbitrary constant. Motivated by the existence of pulsating front solutions, we perform the change of variables $\xi = x - \phi(t)$ and $\tau = t$. Equation (3.75) becomes

$$\begin{aligned}\frac{\partial u}{\partial \tau} = & -u(\xi,\tau) + \int_{-\infty}^{\infty} w(\xi-\xi')F(u(\xi',\tau))\,\mathrm{d}\xi' + \phi'\frac{\partial u(\xi,\tau)}{\partial \xi} \\ & + \varepsilon \int_{-\infty}^{\infty} A\left(\frac{\xi'+\phi}{\varepsilon}\right)\left[w'(\xi-\xi')F(u(\xi',\tau)) - w(\xi-\xi')\frac{\partial F(u(\xi',\tau))}{\partial \xi'}\right]\mathrm{d}\xi'.\end{aligned} \tag{3.76}$$

Next perform the perturbation expansions

$$u(\xi,\tau) = U(\xi) + \varepsilon u_1(\xi,\tau) + \varepsilon^2 u_2(\xi,\tau) + \ldots, \tag{3.77}$$

$$\phi'(\tau) = c_0 + \varepsilon\phi_1'(\tau), \tag{3.78}$$

where $U(\xi)$ is the unique traveling wave solution of the corresponding homogeneous equation (3.7) with unperturbed wavespeed $c = c_0$. The first-order term u_1 satisfies the inhomogeneous linear equation

$$-\frac{\partial u_1(\xi,\tau)}{\partial \tau} + \mathcal{L}u_1(\xi,\tau) = -\phi_1'(\tau)U'(\xi) + h_1(\xi,\phi/\varepsilon), \tag{3.79}$$

where

$$\mathcal{L}u(\xi) = c_0\frac{\mathrm{d}u(\xi)}{\mathrm{d}\xi} - u(\xi) + \int_{-\infty}^{\infty} w(\xi-\xi')F'(U(\xi'))u(\xi')\,\mathrm{d}\xi' \tag{3.80}$$

and

$$h_1 = \int_{-\infty}^{\infty} A\left(\frac{\xi'+\phi}{\varepsilon}\right)\left[-w'(\xi-\xi')F(U(\xi')) + w(\xi-\xi')\frac{\mathrm{d}F(U(\xi'))}{\mathrm{d}\xi'}\right]\mathrm{d}\xi'. \tag{3.81}$$

The linear operator $\mathcal{L}$ has a one-dimensional null-space spanned by U'. The existence of U' as a null-vector follows immediately from differentiating both sides of equation (3.7) with respect to ξ, whereas its uniqueness can be shown using properties of positive linear operators [82]. Therefore, a bounded solution of equation (3.79) with respect to ξ and τ will only exist if the right-hand side of equation (3.79) is orthogonal to all elements of the null-space of the adjoint operator $\mathcal{L}^*$. The latter is defined with respect to the inner product

$$\int_{-\infty}^{\infty} u(\xi)\mathcal{L}v(\xi)\,\mathrm{d}\xi = \int_{-\infty}^{\infty} [\mathcal{L}^* u(\xi)]v(\xi)\,\mathrm{d}\xi, \tag{3.82}$$

where $u(\xi)$ and $v(\xi)$ are arbitrary integrable functions. Hence,

$$\mathcal{L}^* u(\xi) = -c\frac{\mathrm{d}u(\xi)}{\mathrm{d}\xi} - u(\xi) + F'(U(\xi))\int_{-\infty}^{\infty} w(\xi-\xi')u(\xi')\,\mathrm{d}\xi'. \tag{3.83}$$

It can be proven that $\mathcal{L}^*$ also has a one-dimensional null-space [82], that is, it is spanned by some function $V(\xi)$. Equation (3.79) thus has a bounded solution if and only if

$$B_0\phi_1'(\tau) = \int_{-\infty}^{\infty} V(\xi)h_1(\xi,\phi/\varepsilon)\,\mathrm{d}\xi, \tag{3.84}$$

where

$$B_0 = \int_{-\infty}^{\infty} V(\xi)U'(\xi)\,\mathrm{d}\xi. \tag{3.85}$$

Note that B_0 is strictly positive since V and U' can be chosen to have the same sign [82]. Substituting for h_1 using equations (3.81) and (3.78) and performing an integration by parts leads to a differential equation for the phase ϕ:

$$\frac{\mathrm{d}\phi}{\mathrm{d}\tau} = c + \varepsilon\Phi_1\left(\frac{\phi}{\varepsilon}\right), \tag{3.86}$$

where

$$\Phi_1\left(\frac{\phi}{\varepsilon}\right) = \frac{1}{B_0}\int_{-\infty}^{\infty}\int_{-\infty}^{\infty} w(\xi-\xi')A\left(\frac{\xi'+\phi}{\varepsilon}\right) \times\left[V'(\xi)F(U(\xi')) + V(\xi)\frac{\mathrm{d}F(U(\xi'))}{\mathrm{d}\xi'}\right]\mathrm{d}\xi'\,\mathrm{d}\xi. \tag{3.87}$$

The phase equation (3.86) is analogous to the one derived by Keener for a reaction-diffusion model of calcium waves [130]. It implies that there are two distinct types of behavior. If the right-hand side of equation (3.86) is strictly positive then there exists a pulsating front of the approximate form $U(x-\phi(t))$ and the average speed of propagation is $c = \varepsilon/T$ with

$$T = \int_0^{\varepsilon} \frac{\mathrm{d}\phi}{c + \varepsilon\Phi_1\left(\frac{\phi}{\varepsilon}\right)}. \tag{3.88}$$

On the other hand, if the right-hand side of equation (3.86) vanishes for some ϕ then there is wave propagation failure.

In the case of a Heaviside firing rate function $F(u) = H(u-\kappa)$, it is possible to derive an explicit expression for the wavespeed c [74]. The solution for the unperturbed wavefront $U(\xi)$ was derived in section 3.1, so it is only necessary to determine the solution $V(\xi)$ of the adjoint equation (3.83), which becomes

$$cV'(\xi) + V(\xi) = -\frac{\delta(\xi)}{U'(0)}\int_{-\infty}^{\infty} w(\xi')V(\xi')\,\mathrm{d}\xi'. \tag{3.89}$$

This can be integrated to give

$$V(\xi) = -\Theta(\xi)\,\mathrm{e}^{-\xi/c}. \tag{3.90}$$

Given the solutions for $U(\xi)$ and $V(\xi)$, it can then be shown that (3.87) reduces to the form

$$B_0\Phi_1\left(\frac{\phi}{\varepsilon}\right) = W(0)A\left(\frac{\phi}{\varepsilon}\right) + \int_0^\infty A\left(\frac{\phi-\xi}{\varepsilon}\right)\left[\frac{W(\xi)}{c} - w(\xi)\right]\mathrm{d}\xi, \tag{3.91}$$

where

$$W(\xi) = \int_0^\infty \mathrm{e}^{-y/c_0} w(y+\xi)\,\mathrm{d}y \equiv -cU'(\xi), \tag{3.92}$$

and

$$B_0 = \frac{1}{c_0}\int_0^\infty \mathrm{e}^{-\xi/c_0} W(\xi)\,\mathrm{d}\xi. \tag{3.93}$$

Keeping only the lowest order contribution to Φ_1, equation (3.88) reduces to

$$T = \int_0^\varepsilon \frac{\mathrm{d}\phi}{c_0 + \varepsilon\Gamma(c_0)A\left(\frac{\phi}{\varepsilon}\right)} \tag{3.94}$$

with $\Gamma(c_0) = W(0)/B_0$. For the sake of illustration, suppose that the periodic modulation functions K and A are pure sinusoids. Setting $A(x) = \rho\sin(2\pi x)/(2\pi)$ in equation (3.94), we find that

$$T = \frac{\varepsilon}{\sqrt{c_0^2 - \varepsilon^2\rho^2\Gamma(c_0)^2}} \tag{3.95}$$

and, hence,

$$c = \sqrt{c_0^2 - \varepsilon^2\rho^2\Gamma(c_0)^2/(2\pi)^2}. \tag{3.96}$$

This establishes that a sinusoidally varying heterogeneous neural medium only supports a propagating wave if the velocity c_0 of the (unique) solution of the corresponding homogeneous medium satisfies the inequality

$$c_0 \geqslant \varepsilon\rho\Gamma(c_0). \tag{3.97}$$

For the particular example of an exponential distribution (3.1) with $\sigma = 1$, we have $c_0 = (1-2\kappa)/(2\kappa)$ and $\Gamma(c_0) = 1 + c_0$ so that

$$c = c_0\sqrt{1-\gamma_0\rho^2\varepsilon^2}, \qquad \gamma_0 = \frac{1}{2\pi(2\kappa-1)}. \tag{3.98}$$

3.5.2. Interfacial dynamics. The homogenization method provides a reasonable estimate for the mean wavespeed and the critical amplitude ρ for wave propagation failure, provided that the spatial period $\varepsilon \ll 1$. As shown by Coombes and Laing [102] in the case of a Heaviside firing rate function, a more accurate estimate for the wavespeed for larger values of ε can be obtained by analyzing the dynamics of the interface between high and low activity states, provided that the amplitude of periodic modulations is not too large [102]. The basic idea is to change to a co-moving frame of the unperturbed system, $u = u(\xi, t)$ with $\xi = x - c_0 t$ such that equation (2.47) becomes

$$-c_0 u_\xi + u_t = -u + \int_{-\infty}^\infty w(\xi + c_0 t, y)F(u(y - c_0 t, t)\,\mathrm{d}y, \tag{3.99}$$

with w given by equation (3.74) and $F(u) = H(u-\kappa)$. The moving interface (level set) is then defined according to the threshold condition

$$u(\xi_0(t), t) = \kappa. \tag{3.100}$$

Differentiating with respect to t then determines the velocity of the interface in the co-moving frame according to

$$\frac{d\xi_0}{dt} = -\frac{u_t(\xi_0(t),t)}{u_\xi(\xi_0(t),t)}. \tag{3.101}$$

As in the previous homogenization method, suppose that for $\rho = 0$ there exists a traveling front solution $U(\xi)$ of the homogeneous equation (3.7) with speed c_0. Now make the approximation $u_\xi(\xi_0(t),t) = U'(0)$, which is based on the assumption that for small amplitudes ρ, the slope of the traveling front varies sufficiently slowly. Setting $\xi = \xi_0(t)$ in equation (3.99) and using equation (3.3), it is then straightforward to show that [102]

$$\frac{d\xi_0}{dt} = \rho c_0 \frac{\int_0^\infty w(y)K(\xi_0 + c_0 t - y)}{\kappa - \int_0^\infty w(y)\,dy}. \tag{3.102}$$

In order to match up with the previous method, let $K(x) = \sin(2\pi x/\varepsilon)$ and $w(x) = e^{-|x|}/2$. Then $c_0 = (1-2\kappa)/(2\kappa)$ and [102]

$$\frac{d\xi_0}{dt} = c_0\rho\gamma(\varepsilon)\sin\left[\frac{2\pi}{\varepsilon}(\xi_0(t) + c_0 t) + \phi_0(\varepsilon)\right], \tag{3.103}$$

with

$$\gamma(\varepsilon) = \frac{1}{2\kappa - 1}\frac{1}{\sqrt{1+(2\pi/\varepsilon)^2}}, \qquad \tan\phi_0(\varepsilon) = \frac{2\pi}{\varepsilon}. \tag{3.104}$$

The final step is to look for a T-periodic solution of equation (3.103) such that $\xi_0(t) = \xi_0(t+T)$. Setting $x_0 = \xi_0 + c_0 t$ with $x_0 \in [0, \varepsilon]$ and integrating gives

$$\int_0^{x_0} \frac{dx}{1 + \rho\gamma\sin(2\pi x/\sigma + \phi)} = c_0 t. \tag{3.105}$$

This may be evaluated using a half angle substitution

$$c_0 t = \frac{\varepsilon}{\pi}\frac{1}{\sqrt{1-\rho^2\gamma^2}}\tan^{-1}\frac{z}{\sqrt{1-\rho^2\gamma^2}}\Bigg|_{z_0(0)+\rho\gamma}^{z_0(t)+\rho\gamma}, \tag{3.106}$$

where $z_0(t) = \tan[(2\pi x_0(t)/\varepsilon + \phi)/2]$ and $x_0(0) = 0$. A self-consistent pulsating front solution is then obtained by imposing the condition $\varepsilon = x_0(T)$, which then determines the effective speed $c = \varepsilon/T$ to be

$$c = c_0\sqrt{1-\rho^2\gamma(\varepsilon)^2}. \tag{3.107}$$

Note that on Taylor expanding $\gamma(\varepsilon)$ to first order in ε, equation (3.107) recovers the corresponding result (3.98) obtained using homogenization theory. However, the expression derived using interfacial dynamics is more accurate when the period ε increases, provided that the amplitude ρ does not become too large.

Both of the above methods can be extended to the case of periodically modulated traveling pulses (pulsating pulses), see [101] for the homogenization case, in which there are two threshold crossing points. However, one simplifying assumption of both approaches is that in the presence of periodically modulated weights additional threshold crossing points do not occur. Numerical solutions of a neural field equation with linear adaptation have shown that in the case of large amplitude modulations, a pulsating pulse can develop multiple threshold crossing points [101]. That is, the traveling wave represents the envelope of a multibump solution, in which individual bumps are nonpropagating and transient, see figure 12. The appearance (disappearance) of bumps at the leading (trailing) edge of the pulse generates the coherent propagation of the pulse. Wave propagation failure occurs when activity is insufficient to maintain bumps at the leading edge. It would be interesting to extend the homogenization and interfacial methods to account for multiple threshold crossings, as well as other types of inhomogeneities at various spatial scales, some of which could be in the form of quenched disorder [131].

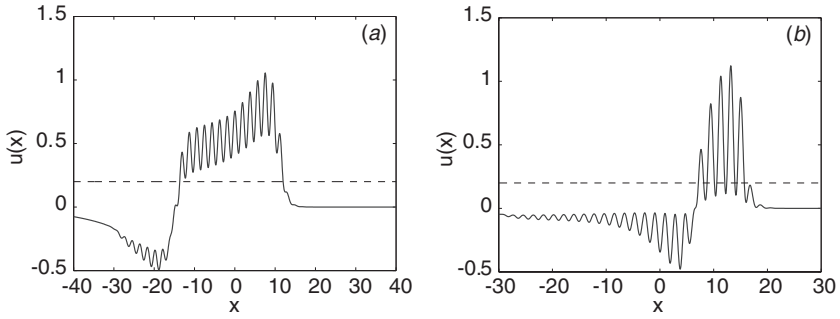

Figure 12. Pulsating pulse solutions in a 1D excitatory neural field with linear adaptation and Heaviside firing rate function, see equation (3.31). The threshold $\kappa = 0.2$, strength of adaptation $\beta = 2.0$, and adaptation rate constant is $\epsilon = 0.04$. The weight distribution is given by $w(x, y) = \rho w(x - y)\sin(2\pi x/\varepsilon)$ with $2\pi\varepsilon = 0.3$ and $w(x)$ an exponential weight function. (*a*) Single bump solution for $\rho = 0.3$. The interior of the pulse consists of non-propagating, transient ripples. (*b*) Multi-bump solution for $\rho = 0.8$. The solitary pulse corresponds to the envelope of a multiple bump solution, in which individual bumps are non-propagating and transient. The disappearance of bumps at one end and the emergence of new bumps at the other end generates the propagation of activity [101].

3.6. Spatially structured oscillations and spiral waves

Spatially localized neural population oscillations arise both *in vivo* and *in vitro* and may be observed experimentally using multi-electrode arrays or voltage-sensitive dye imaging [5]. For example, when neocortical or hippocampal *in vitro* slices are treated with an inhibitory neurotransmitter antagonist such as bicuculline, effectively eliminating inhibition, a localized current stimulus evokes population activity. Such activity may take the form of a spatially localized group of neurons whose population activity oscillates around 1–10 Hz [1, 90, 104]; during each oscillation cycle the population may emit elevated activity that propagates as a traveling pulse [5, 90] or a spiral wave [18, 132]. Spiral waves provide a mechanism for spatially organizing extensive episodes of periodic activity, effectively reducing the dimensionality of the dynamics [132]. A number of organizing mechanisms for such spatiotemporal activity have been suggested [5, 100]. First, a spatially localized pacemaker oscillator could excite successive neighbors in an excitable network. (One possible network mechanism for generating a pacemaker oscillator in an excitable neural medium would be via an instability of a spatially localized breather in the presence of input inhomogeneities [112, 133], see section 4.3.3.) Alternatively, gradual phase delays could propagate in space across an oscillatory neural medium, see below. It follows that activity that propagates away from a focused region of high frequency oscillations may either travel faster than the characteristic time-scale set by the oscillating region, according to dynamics of an excitable medium, or at a speed set by the period of the oscillating core if the rest of the medium is oscillatory as well. Conceivably, this may establish a dynamical systems explanation for the wide range in speed at which seizures spread across the cortex, which can be anywhere from 0.05 mm s^{-1} to 10 cm s^{-1} [1].

Here we briefly highlight a network mechanism for generating spiral waves in an oscillatory neural medium. Troy and Shusterman [103, 104] have shown how a neural field model with strong linear adaptation, see equation (3.31), can act as an oscillatory network that supports target patterns and spiral waves consistent with experimental studies of tangential cortical slices [18]. (For the analysis of spiral waves in the corresponding excitable regime, see [134].) However, since the linear form of adaptation used in these studies is not directly related to physiological models of adaptation, it is difficult to ascertain whether or not the

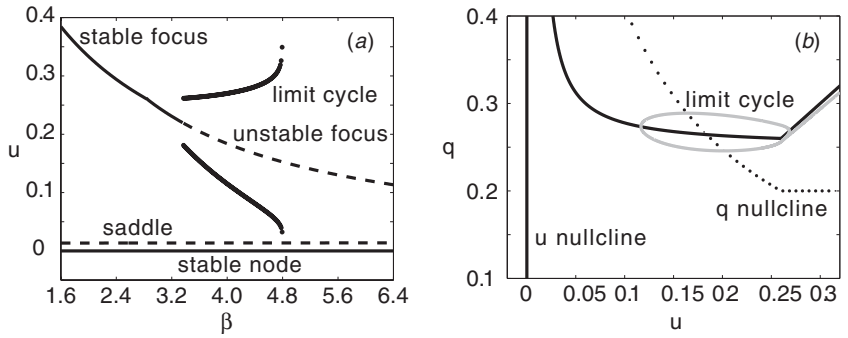

Figure 13. Limit cycle oscillations in the space-clamped system (3.109) for a piecewise linear firing rate function (2.8) with threshold $\kappa = 0.01$, and gain $\gamma = 4$. (*a*) Bifurcation diagram showing fixed points u of the system as a function of β for $\tau_q = 80$. (*b*) Corresponding phase-plane plot of q versus u (gray curve) for $\beta = 4$, showing that the system supports a stable limit cycle [61].

strength of adaptation required is biologically reasonable. This motivated a more recent study of spiral waves in a 2D neural medium involving a nonlinear, physiologically based form of adaptation, namely, synaptic depression [62]. The latter model takes the form

$$\frac{\partial u(\mathbf{r},t)}{\partial t} = -u(\mathbf{r},t) + \int w(|\mathbf{r}-\mathbf{r}'|)q(\mathbf{r}',t)F(u(\mathbf{r}',t))\,\mathrm{d}\mathbf{r}'$$
$$\frac{\partial q(\mathbf{r},t)}{\partial t} = \frac{1-q(\mathbf{r},t)}{\tau_q} - \beta q(\mathbf{r},t)F(u(\mathbf{r},t)). \tag{3.108}$$

It can be shown that the space-clamped model

$$\dot{u}(t) = -u(t) + q(t)F(u(t)), \qquad \dot{q}(t) = \frac{1-q(t)}{\tau_q} - \beta q(t)F(u(t)), \tag{3.109}$$

supports limit cycle oscillations provided that the firing rate function has finite gain. For example, in the case of the piecewise linear firing rate function (2.8), oscillations arise via a subcritical Hopf bifurcation of a high activity fixed point, see figure 13. One then finds that the full network model (3.108) supports a spatially localized oscillating core that periodically emits traveling pulses [62]. Such dynamics can be induced by taking an initial condition of the form

$$(u(\mathbf{r},0), q(\mathbf{r},0)) = (\chi \mathrm{e}^{-(x^2+y^2)/\zeta^2}, 1), \tag{3.110}$$

where χ and ζ parameterize the amplitude and spatial constant of the initial state. An example of a pulse-emitting core is shown in figure 14, which oscillates at a frequency of roughly 3 Hz. Pulses are emitted each cycle, and travel at a speed of roughly 30 cm s^{-1}, which is determined by the period of the oscillations; the latter is set by the time constant of synaptic depression. The initial emission of spreading activity appears as a traveling front which propagates from the region activated by the input current into the surrounding region of zero activity; it travels at the same speed as the subsequent target waves. The front converts each region of the network into an oscillatory state that is phase-shifted relative to the core, resulting in the appearance of a radially symmetric target pattern. Spiral waves can also be induced by breaking the rotational symmetry of pulse emitter solutions [62]. More specifically, if the target pattern produced by the emitter has the top and bottom halves of its domain phase shifted, then the dynamics evolves into two counter-rotating spirals on the left and right halves of the domain. Closer inspection of one of these spirals reveals that it has a fixed center about which activity rotates indefinitely as shown in figure 15.

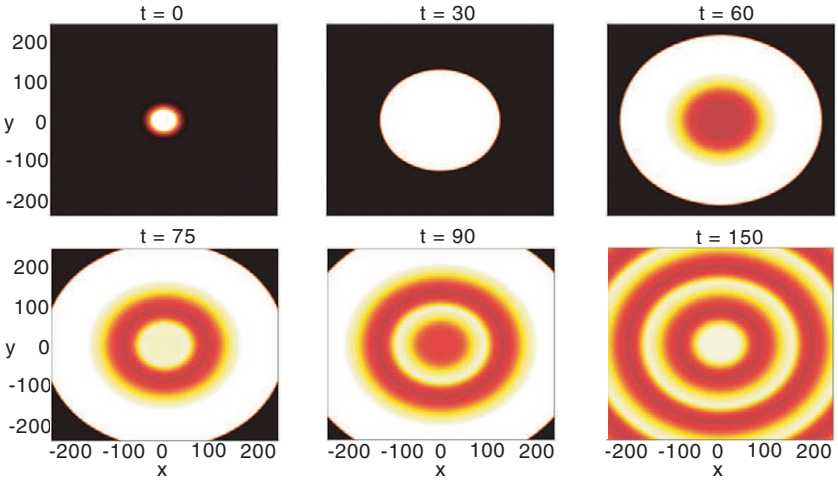

Figure 14. Target patterns in a 2D neural field with synaptic depression induced by an initial condition stimulus specified by equation (3.110) at $t = 0$, where $\chi = 1$ and $\zeta = 25$. Initially, an activated state spreads radially outward, across the entire medium as a traveling front. Then, the localized oscillating core of activity emits a target wave with each oscillation cycle. Eventually, these target waves fill the domain. Each target wave can be considered as a phase shift in space of the oscillation throughout the medium; they travel with the same speed as the initial front. Parameters are $\tau_q = 80$, $\beta = 4$, $\sigma = 4$ and $\kappa = 0.01$ [62].

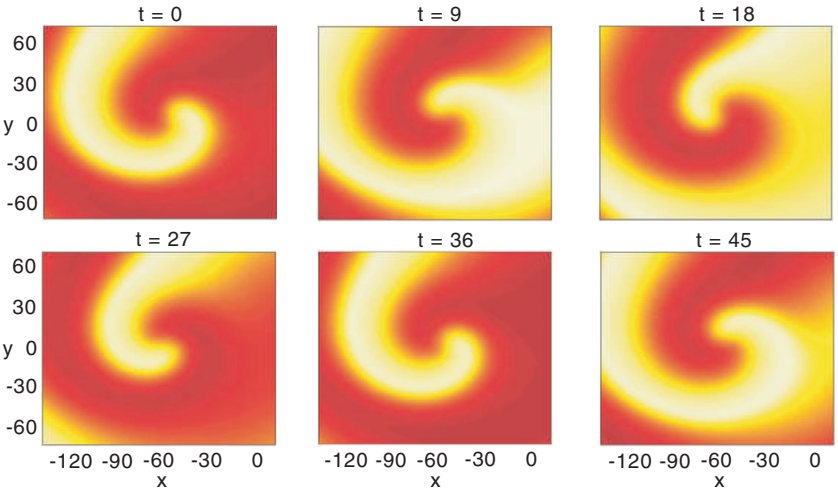

Figure 15. Spiral wave generated by shifting the phase of the top and bottom halves of the target pattern shown in figure 14. The period of the spiral wave oscillation is roughly the same as the period of the oscillation in the space-clamped system. All patches of neurons are oscillating at the same frequency, but phase-shifted as coordinates are rotated about the central phase singularity [62].

4. Persistent spatially localized activity states (bumps)

In section 3 we considered traveling wave solutions of excitatory neural field equations. This was partly motivated by experimental studies of traveling waves in disinhibited cortical slices, as well as the fact that epileptic seizures are often associated with greatly enhanced levels of recurrent excitation. Under normal operating conditions, cortical circuits have significant levels of synaptic inhibition, which tends to preclude the propagation of excitable traveling waves. (Oscillatory phase waves can still occur, however [100].) One new class of solution that emerges in the presence of nonlocal synaptic inhibition (lateral inhibition) is a stationary pulse solution, also known as an activity bump. Such bumps are typically coexistent with a stable low activity state (bistability) so that an initial stimulus is needed in order to transition from the low activity state to the bump. However, the bump persists after removal of the stimulus, so that the bump represents a persistent spatially localized activity state [88].

One of the reasons why persistent activity bumps are of interest is that they are thought to arise in cortical circuits performing certain spatial working memory tasks. Working memory involves cortical 'memory neurons' that establish a representation of a stimulus that persists after the stimulus is removed. A typical experiment is a delayed response task, in which a primate is required to retain information regarding the location of a sensory cue across a delay period between the stimulus and behavioral response. Physiological recordings in prefrontal cortex have shown that spatially localized groups of neurons fire during the recall task and then stop firing once the task has finished [8]. The stimulus response of a cell is characterized by a smooth tuning curve that is peaked at a preferred spatial cue and varies from cell to cell. At the network level the memory of cue location is stored as an activity bump. Persistent activity bumps occur in a number of other systems that encode directional or spatial information, including head direction cells in thalamus and basal ganglia [7] and place cells in the hippocampus [135].

In the following we review some of the analytical methods that have been used to study persistent localized activity states in neural fields. (A very different mechanism for generating a spatially localized persistent state is via a Turing instability on a compact domain, which will be discussed in section 5.) We begin in section 4.1 by describing Amari's original construction of exact bump solution for a 1D scalar neural field equation with Heaviside firing rate function [12]. We show how stable bumps can occur in the case of a so-called Mexican hat weight function representing short-range excitation and long-range lateral inhibition. The stability of the bump depends on whether or not perturbations of the bump boundary (threshold crossing points) grow or decay. In section 4.2, we extend the analysis to the case of radially symmetric 2D bumps. Stability is now determined by the effects of perturbations on the circular bump boundary, which can be analyzed using Fourier methods and properties of Bessel functions [133, 136]. We also briefly describe some of the more complex spatiotemporal dynamics that can arise via instabilities of 2D bumps, including multibump solutions, rotating waves and breathing pulses. In section 4.3 we discuss various studies concerned with how the location of an activity bump is affected by external stimuli, which is important because bump location is thought to encode information about the stimulus.

4.1. Exact bump solutions in a 1D neural field with lateral inhibition

Existence of a 1D bump. Let us return to the scalar neural field equation (3.31) with Heaviside rate function $F(u) = H(u - \kappa)$. This equation was first analyzed in detail by Amari [12], who showed that the network can support a stable stationary bump solution when the weight distribution $w(x)$ is given by a so-called Mexican hat function with the following properties:

(i) $w(x) > 0$ for $x \in [0, x_0)$ with $w(x_0) = 0$
(ii) $w(x) < 0$ for $x \in (x_0, \infty)$
(iii) $w(x)$ is decreasing on $[0, x_0]$
(iv) $w(x)$ has a unique minimum on $\mathbb{R}^+$ at $x = x_1$ with $x_1 > x_0$ and $w(x)$ strictly increasing on (x_1, ∞).

A typical choice of function that satisfies these properties is the so-called Mexican hat function, which is given by a difference-of-Gaussians or a difference of exponentials. The latter takes the form

$$w(|x - x'|) = \mathrm{e}^{-|x-x'|} - A\,\mathrm{e}^{-|x-x'|/\sigma}. \tag{4.1}$$

The Mexican weight function is based on the assumption that there is short-range excitation and longer-range inhibition. Whether or not a Mexican hat function is realistic from the biological perspective depends on which classes of neurons are being taken into account by the neural field model. For example, in visual cortex it is known that excitatory pyramidal cells make both local synaptic contacts as well as longer-range horizontal connections, see section 5.2. However, the latter innervate both excitatory and local inhibitory neurons so they could have a net inhibitory effect, thus providing a possible source of long-range inhibition; whether long-range connections generate net excitation or net inhibition also depends on stimulus conditions [137].

Consider an equilibrium solution $u(x, t) = U(x)$ satisfying

$$U(x) = \int_{-\infty}^{\infty} w(x - x')H[U(x') - \kappa]\,\mathrm{d}x'. \tag{4.2}$$

Let $R[U] = \{x|U(x) > \kappa\}$ be the region over which the field is excited (superthreshold). Equation (4.2) can then be rewritten as

$$U(x) = \int_{R[U]} w(x - x')\,\mathrm{d}x'. \tag{4.3}$$

Exploiting the fact that any solution can be arbitrarily translated so that it is centered at the origin, we define a stationary pulse solution of width Δ to be one that is excited over the interval $(-\Delta, \Delta)$. Let

$$W(x) = \int_0^x w(y)\,\mathrm{d}y, \qquad W_m = \max_{x>0} W(x), \qquad W_\infty = \lim_{x\to\infty} W(x) \tag{4.4}$$

such that $W(0) = 0$ and $W(-x) = -W(x)$. For a bump of width Δ, equation (4.3) reduces to the form

$$U(x) = W(x + \Delta) - W(x - \Delta). \tag{4.5}$$

Since $U(\Delta) = \kappa$, we obtain the following necessary condition for the existence of a bump:

$$W(2\Delta) = \kappa. \tag{4.6}$$

(In order to complete the proof of existence, it is necessary to check that there are no other threshold crossing points. This can be achieved in the case of a Mexican hat weight distribution [12], and is straightforward to verify numerically.) It can also be shown that a bump is stable provided the condition $W'(2\Delta) < 0$ is satisfied, see below. The existence and stability of activity bumps for a given κ can thus be determined graphically as illustrated in figure 16(*b*). For a certain range of values of $\kappa > 0$ one finds bistability between a stable bump and a rest state for which $R[U] = \emptyset$.

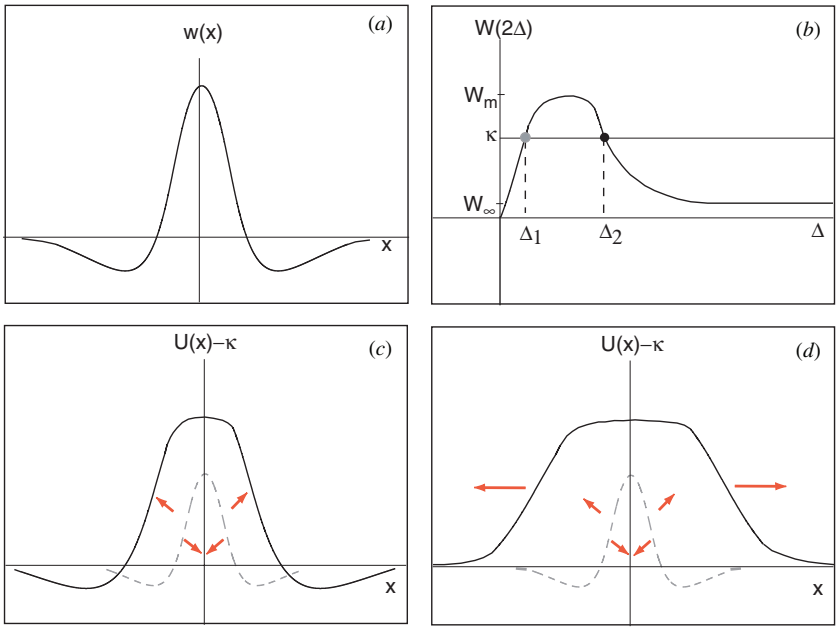

Figure 16. Construction of a solitary pulse in the Amari model. (*a*) The Mexican hat weight distribution w. (*b*) Integral $W(x)$ of $w(x)$. Horizontal line shows the threshold value κ whose intersections with $W(2\Delta)$ determine the allowed stationary pulse solutions. (*c*) Unstable pulse (dashed grey curve) acts as a separatrix between the stable pulse and the rest state. (*d*) Unstable pulse acts as a separatrix between a wavefront and the rest state.

Stability of a 1D bump. The linear stability of a bump can be determined by setting $u(x,t) = U(x) + p(x)\,\mathrm{e}^{\lambda t}$ and expanding to first order in p [69, 79, 133, 138]. This leads to the eigenvalue equation

$$(\lambda + 1)p(x) = \int_{-\infty}^{\infty} w(x - x')\delta(U(x') - \kappa)p(x')\,\mathrm{d}x'. \tag{4.7}$$

Using the identity

$$\delta(U(x) - \kappa) = \left(\frac{\delta(x - \Delta)}{|U'(\Delta)|} + \frac{\delta(x + \Delta)}{|U'(-\Delta)|}\right), \tag{4.8}$$

and setting

$$|U'(\Delta)| = |U'(-\Delta)| \equiv \gamma^{-1} = w(0) - w(2\Delta), \tag{4.9}$$

we have the eigenvalue equation

$$(\lambda + 1)p(x) = \mathcal{L}p(x) \equiv \gamma\,(w(x - \Delta)p(\Delta) + w(x + \Delta)p(-\Delta))\,. \tag{4.10}$$

Following Guo and Chow [138], we now restrict x to the interval $x \in [-\Delta, \Delta]$, so that $\mathcal{L}$ becomes a compact linear operator acting on the space $\mathcal{C}[-\Delta, \Delta]$ of continuous, integrable functions over $[-\Delta, \Delta]$ (with an appropriately defined norm). The linear problem thus reduces to finding the spectrum of $\mathcal{L}$. Since $\mathcal{L}$ is compact, it can be proven that the eigenvalues of $\mathcal{L}$ only have zero as an accumulation point [107], implying that $\lambda = -1$ constitutes the essential spectrum. The discrete spectrum is obtained by setting $x = \pm\Delta$ in the eigenvalue equation (4.10) to give the pair of equations

$$(\lambda + 1)p_+ = \gamma(w(0)p_+ + w(2\Delta)p_-) \tag{4.11}$$

$$(\lambda+1)p_- = \gamma(w(-2\Delta)p_+ + w(0)p_-), \tag{4.12}$$

where $p_\pm = p(\pm\Delta)$. This has the solutions $p_- = \pm p_+$ with corresponding eigenvalues

$$\lambda_\pm = -1 + \gamma(w(0) \pm w(2\Delta)). \tag{4.13}$$

Finally, using the fact that $\gamma^{-1} = w(0) - w(2\Delta)$ we deduce that $\lambda_- = 0$ (reflecting the translation invariance of the system) and $\lambda_+ = \gamma w(2\Delta)$. Thus the bump is stable if $w(2\Delta) = W'(2\Delta) < 0$.

Note that the discrete spectrum is determined completely in terms of the perturbations $p_\pm = p(\pm\Delta)$. This explains why it is also possible to analyze the stability of the bumps by restricting attention to the effects of perturbations at the boundaries of the activity bump as originally formulated by Amari [12]. In particular, if $u(x,t) = U(x) + \varepsilon p(x,t) = 0$ at $x = x \pm \Delta + \varepsilon a_\pm(t)$ with $\varepsilon \ll 1$, then

$$\begin{aligned} 0 &= U(\pm\Delta + \varepsilon a_\pm(t)) + \varepsilon p(\pm\Delta + \varepsilon a_\pm(t), t) \\ &= U(\pm\Delta) + \varepsilon U'(\pm\Delta)a_\pm(t) + \varepsilon p(\pm\Delta, t) + \mathcal{O}(\varepsilon^2), \end{aligned}$$

that is,

$$a_\pm(t) = \pm\gamma p(\pm\Delta, t)$$

since $U(\pm\Delta) = 0$ and $U'(\pm\Delta) = \mp\gamma^{-1}$. It follows that $p_- = p_+$ generates a uniform expansion of the bump ($a_- = -a_+$) and $p_- = -p_+$ generates a shift in the center of the bump ($a_- = a_+$).

There have been various extensions of Amari's original analysis of 1D bumps. Kishimoto and Amari [81] proved the existence of a solitary pulse for a smooth sigmoidal nonlinearity F rather than a Heaviside using a fixed point theorem. Pinto and Ermentrout used singular perturbation theory (see section 3.3.2) to construct a pulse solution for smooth F and slow linear adaptation [69]. More recently, Faugeras *et al* [85, 86] have used a combination of local bifurcation theory, degree theory and multiparameter continuation schemes to study the local and global structure of stationary solutions to neural field equations with smooth F. Other extensions include weight distributions that are not of the lateral inhibition type (for which multiple bump states can arise) [28, 88], spiking rather than rate-based models [139, 140], weakly interacting bumps [105], and bumps in adaptive neural fields [61, 64, 141]. In the latter case, adaptation can induce a bump instability leading to the formation of a traveling pulse.

Bumps in piecewise smooth neural fields. Considerable care must be taken when analyzing the stability of bumps in Heaviside neural fields with a nonlinear form of adaptation such as synaptic depression or spike frequency adaptation [63]. For example, suppose that we set $F(u) = H(u-\kappa)$ in equation (2.49). This results in a piecewise-smooth neural field equation due to the fact that there is an exposed Heaviside function in the dynamics of the depression variable. A stationary bump solution $(U(x), Q(x))$ with associated excited region $R[U] = (-\Delta, \Delta)$ satisfies the pair of equations

$$\begin{aligned} U(x) &= \int_{-\Delta}^{\Delta} Q(x')w(x-x')\,\mathrm{d}x', \\ Q(x) &= 1 - \frac{\tau_q\beta}{1+\tau_q\beta}H(U(x)-\kappa). \end{aligned}$$

Clearly the local stability of such a solution cannot be determined by linearizing the Heaviside version of equation (2.49) due to the discontinuity in $Q(x)$, see figure 17(*a*). Formally speaking, one could take $F(u)$ to be a smooth sigmoid, carry out the linearization about

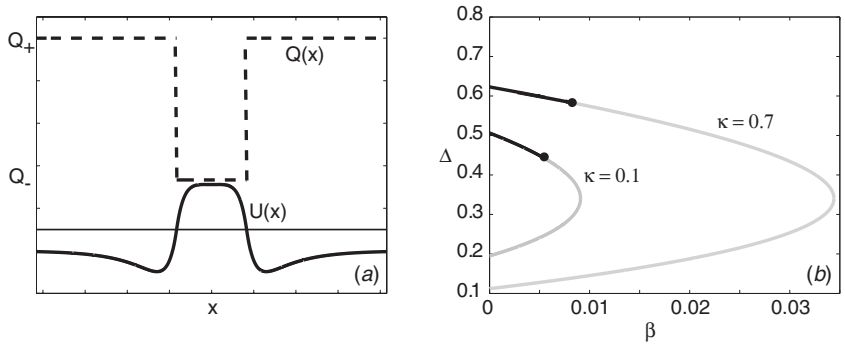

Figure 17. 1D bump in a Heaviside neural field with synaptic depression and Mexican hat weight function (4.1). (*a*) Example of a bump profile showing discontinuity in depression variable with $Q_+ = 1$ and $Q_- = (1 + \tau_q\beta)^{-1}$. (*b*) Existence curves relating bump width Δ to amplitude of synaptic depression β for different values of κ. Black (gray) portions of curves indicate bumps that are numerically stable (unstable). Other parameter values are $A = 0.6$, $\sigma = 4$, $\tau_q = 20$ (*b*).

the bump solution and construct an associated Evans function. The Evans function could then be evaluated analytically by taking the high-gain limit of the sigmoid. However, such a limit is singular and incorrectly predicts that the whole upper branch of each existence curve shown in figure 17 is stable. The breakdown in linear stability analysis can also be seen by considering an arbitrarily small perturbation of the bump that shifts the location of the bump boundary. That is, suppose $u(x,t) = U(x) + \varepsilon\psi(x,t)$ and $q(x,t) = Q(x) + \epsilon\varphi(x,t)$ such that $u(\Delta + \varepsilon a_+(t), t) = \kappa = u(-\Delta + \varepsilon a_-(t), t)$ with $a_\pm \approx \pm\psi(\pm\Delta, t)/|U'(\Delta)|$. A small shift in the location of the bump boundary means that in an infinitesimal neighborhood of the bump boundary the synaptic depression variable will start to switch its steady-state value from $Q_+ = 1$ to $Q_- = (1 + \alpha\beta)^{-1}$ or vice versa according to equation (2.49). That is, $\varphi(x,t)$ will undergo $\mathcal{O}(1/\varepsilon)$ changes over a time-scale determined by τ_q. However, this doesn't necessarily imply that the bump solution is unstable, since the region over which $\varphi(x,t) = \mathcal{O}(1/\epsilon)$ may shrink to zero.

The above observation motivates the introduction of the nonlocal auxiliary field $\Phi(x,t)$ [63],

$$\Phi(x,t) = \int_{-\Delta+\varepsilon a_-(t)}^{\Delta+\varepsilon a_+(t)} w(x-x')\varphi(x',t)\,\mathrm{d}x', \tag{4.14}$$

which will remain $\mathcal{O}(1)$ provided that $\varphi(x,t)$ is $\mathcal{O}(1/\varepsilon)$ over an an interval of $\mathcal{O}(\varepsilon)$. Suppose that we now restrict the class of perturbations $\psi(x,t)$ such that $\psi(\pm\Delta, t)$ do not change sign for any t. We can then derive a system of linear equations for the fields $\psi(x,t)$ and $\Phi(x,t)$ by substituting the solutions $u(x,t) = U(x) + \varepsilon\psi(x,t)$ and $q(x,t) = Q(x) + \epsilon\varphi(x,t)$ into equation (2.49) and expanding to first order in ε. Setting $\psi(x,t) = \psi(x)\,\mathrm{e}^{\lambda t}$ and $\Phi(x,t) = \Phi(x)\,\mathrm{e}^{\lambda t}$ with λ real (so that $\psi(\pm\Delta, t)$ do not change sign) and solving for $\Phi(x)$ then leads to the eigenvalue equation [63]

$$\begin{aligned}(\lambda+1)\psi(x) = {}& \gamma w(x+\Delta)\psi(-\Delta)G(\psi(-\Delta))\left(1 - \frac{\beta H(\psi(-\Delta))}{\lambda + \tau_q^{-1} + \beta}\right) \\ & + \gamma w(x-\Delta)\psi(\Delta)G(\psi(\Delta))\left(1 - \frac{\beta H(\psi(\Delta))}{\lambda + \tau_q^{-1} + \beta}\right)\end{aligned} \tag{4.15}$$

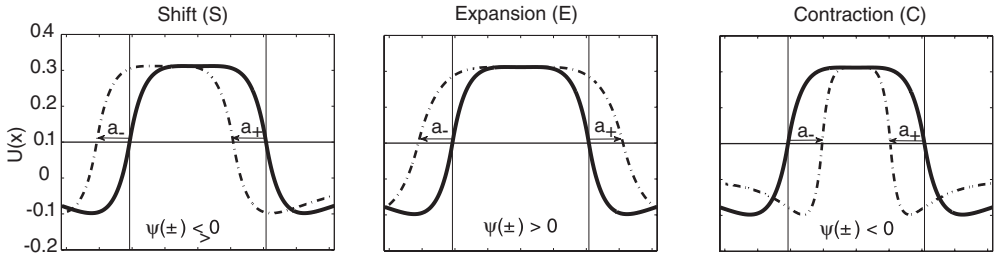

Figure 18. Illustration of shift, expansion and contraction perturbations.

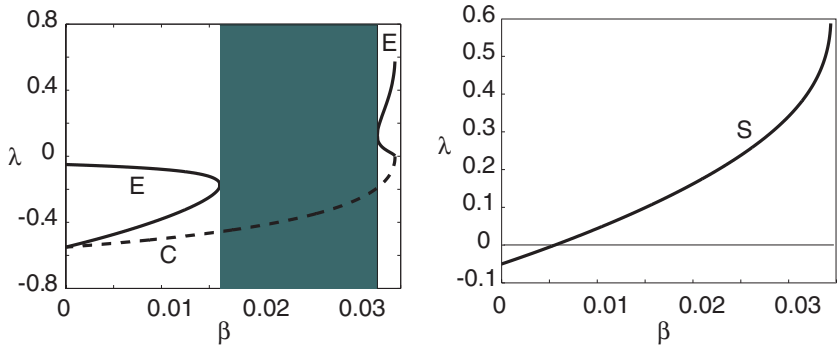

Figure 19. (*a*) Eigenvalues of the expansion (E, solid curves) and contraction (C, dashed curve) perturbations as a function of β for $\kappa = 0.07$, $A = 0.6$, $\sigma = 4$, and $\alpha = 20$. In the gray region, the roots of equation (4.15) are complex thus violating the ansatz that λ is real. (*b*) Corresponding nonzero eigenvalue for shift (S) perturbations.

with

$$G(\psi) = \begin{cases} 1 & \text{if} \quad \psi > 0 \\ (1+\tau_q\beta)^{-1} & \text{if} \quad \psi < 0, \end{cases} \qquad \gamma^{-1} = |U'(\pm\Delta)|. \tag{4.16}$$

We can now determine the (real) discrete spectrum by setting $x = \pm\Delta$ and specifying the signs of $\psi(\pm\Delta)$. We thus have three distinct cases as illustrated in figure 18: (i) $\psi(\pm\Delta) > 0$ (expansions), (ii) $\psi(\pm\Delta) < 0$ (contractions) and (iii) $\psi(\pm\Delta)$ having opposite signs (shifts). The corresponding eigenvalue solutions as a function of the strength of synaptic depression β are shown in figure 19. For a wide range of parameter values, the nonzero eigenvalue branch associated with shift perturbations crosses zero first, and thus induces a bump instability. (There is also a zero eigenvalue due to translation symmetry.) This can be confirmed numerically, whereby increasing β destabilizes the bump leading to a traveling wave solution [63]. Note that since our analysis is restricted to real eigenvalues, we can only derive sufficient conditions for instability (rather than stability) of the bump. However, complex eigenvalues do not appear to contribute to instabilities, at least for the given neural field model with synaptic depression.

4.2. Exact bump solutions in a 2D neural field with lateral inhibition

There have been relatively few studies regarding the existence and stability of bumps in 2D neural fields. Laing and Troy [88] introduced PDE methods to study symmetry-breaking of rotationally symmetric bumps and the formation of multiple bump solutions. However, such

PDE methods can only be applied to specific forms of weight distribution. In particular, they break down if w has compact support. In terms of the original integrodifferential equations, Taylor [142] and Werner and Richter [143] classified some of the disk and annulus shaped solutions for Heaviside rate functions, and analyzed their stability with respect to radial perturbations. However, as shown by Folias and Bressloff [133, 136] and Owen *et al* [144], in order to determine correctly the linear stability of radially symmetric solutions, it is necessary to take into account all possible perturbations of the circular boundary. The resulting spectral problem can be solved using Fourier methods. (An analysis of 2D bumps also appears in a book by Amari, but unfortunately the book has never been translated from the Japanese [247].)

Existence of a 2D bump. The starting point of the analysis of 2D bumps is the scalar neural field

$$\frac{\partial u(\mathbf{r},t)}{\partial t} = -u(\mathbf{r},t) + \int_{\mathbb{R}^2} w(|\mathbf{r}-\mathbf{r}'|)H(u(\mathbf{r}',t)-\kappa)\,\mathrm{d}\mathbf{r}'. \tag{4.17}$$

Consider a circularly symmetric bump solution of radius Δ such that $u(\mathbf{r},t) = U(r)$ with $U(\Delta) = \kappa$, $U(r) \gtrless \kappa$ for $r \lessgtr \Delta$ and $U(r) \to 0$ as $r \to \infty$. Imposing such constraints on a stationary solution of equation (4.17) gives

$$U(r) = \int_0^{2\pi}\int_0^{\Delta} w(|\mathbf{r}-\mathbf{r}'|)r'\,\mathrm{d}r'\,\mathrm{d}\phi'. \tag{4.18}$$

The double integral in (4.18) can be calculated using the Fourier transforms and Bessel function identities [133]. First, express $w(r)$ as a 2D Fourier transform using polar coordinates

$$w(r) = \frac{1}{2\pi}\int_{\mathbb{R}^2} \mathrm{e}^{\mathrm{i}(\mathbf{r}\cdot\mathbf{k})}\widehat{w}(\mathbf{k})\,\mathrm{d}\mathbf{k} = \frac{1}{2\pi}\int_0^{\infty}\left(\int_0^{2\pi}\mathrm{e}^{\mathrm{i}r\rho\cos(\theta-\phi)}\widehat{w}(\rho)\,\mathrm{d}\theta\right)\rho\,\mathrm{d}\rho,$$

where $\widehat{w}$ denotes the Fourier transform of w and $\mathbf{k} = (\rho,\theta)$. Using the integral representation

$$\frac{1}{2\pi}\int_0^{2\pi}\mathrm{e}^{\mathrm{i}r\rho\cos(\theta-\phi)}\,\mathrm{d}\theta = J_0(\rho r),$$

where J_0 is the Bessel function of the first kind, we express w in terms of its Hankel transform of order zero,

$$w(r) = \int_0^{\infty}\widehat{w}(\rho)J_0(\rho r)\rho\,\mathrm{d}\rho, \tag{4.19}$$

which, when substituted into equation (4.18), gives

$$U(r) = \int_0^{2\pi}\int_0^{\Delta}\left(\int_0^{\infty}\widehat{w}(\rho)J_0(\rho|\mathbf{r}-\mathbf{r}'|)\rho\,\mathrm{d}\rho\right)r'\,\mathrm{d}r'\,\mathrm{d}\phi'.$$

Reversing the order of integration and using the addition theorem

$$J_0(\rho\sqrt{r^2+r'^2-2rr'\cos\phi'}) = \sum_{m=0}^{\infty}\epsilon_m J_m(\rho r)J_m(\rho r')\cos m\phi', \tag{4.20}$$

where $\epsilon_0 = 1$ and $\epsilon_n = 2$ for $n \geqslant 1$, we thus have

$$U(r) = 2\pi\Delta\int_0^{\infty}\widehat{w}(\rho)J_0(\rho r)J_1(\rho\Delta)\,\mathrm{d}\rho. \tag{4.21}$$

We have used the identity $J_1(\rho\Delta)\Delta = \rho\int_0^{\Delta}J_0(\rho r')r'\,\mathrm{d}r'$.

For the sake of illustration consider a Mexican hat weight distribution given by a combination of modified Bessel functions of the second kind

$$w(r) = \frac{2}{3\pi}(K_0(r) - K_0(2r) - A(K_0(r/\sigma) - K_0(2r/\sigma))). \tag{4.22}$$

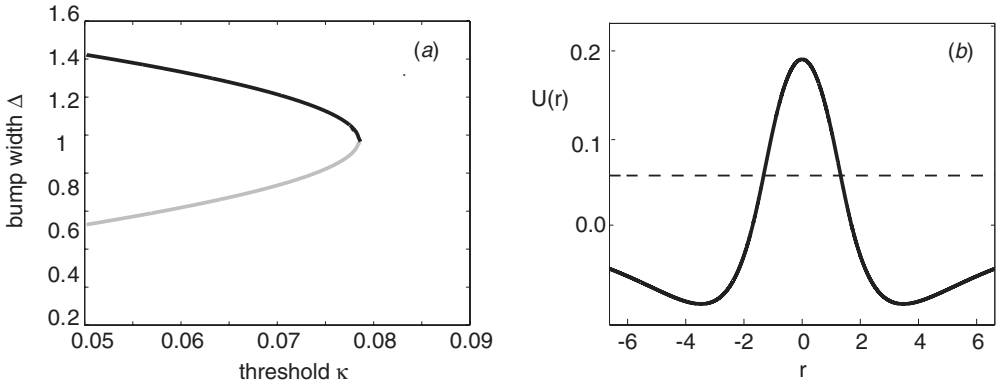

Figure 20. Two-dimensional bumps. (*a*) Plots relating bump radius Δ to threshold κ for Mexican hat function (4.22). Black (gray) curves indicate stable (unstable) branches. Weight parameters are $A = 0.3$, $\sigma = 4$. (*b*) Bump profile when $\kappa = 0.06$ (indicated by dashed horizontal line).

Such a weight function is qualitatively similar to a difference of exponential weight functions $w(r) = (2\pi)^{-1}(\mathrm{e}^{-r} - A\,\mathrm{e}^{-r/\sigma})$. Moreover, following previous studies of two-dimensional neural field models, equation (4.17) can be transformed into a fourth order PDE, which is computationally less expensive to solve numerically [62, 88, 133, 134, 144]. Using the fact that the corresponding Hankel transform of $K_0(sr)$ is $\mathcal{H}(\rho, s) = (\rho^2 + s^2)^{-1}$, we have

$$\widehat{w}(\rho) = \frac{2}{3\pi}(\mathcal{H}(\rho, 1) - \mathcal{H}(\rho, 2) - A(\mathcal{H}(\rho, 1/\sigma) - \mathcal{H}(\rho, 2/\sigma))). \tag{4.23}$$

Thus, the integral (4.21) can be evaluated explicitly by substituting (4.23) into (4.21), and using the identity

$$\int_0^\infty \frac{1}{\rho^2 + s^2} J_0(\rho r) J_1(\rho\Delta)\mathrm{d}\rho \equiv \mathcal{I}(\Delta, r, s) = \begin{cases} \dfrac{1}{s} I_1(s\Delta)K_0(sr), & r > \Delta, \\ \dfrac{1}{s^2\Delta} - \dfrac{1}{s} I_0(sr)K_1(s\Delta), & r < \Delta, \end{cases}$$

where I_ν is the modified Bessel function of the first kind of order ν. Thus, the stationary bump $U(r)$ has the form

$$U(r) = \frac{4\Delta}{3}\left(\mathcal{I}(\Delta, r, 1) - \mathcal{I}(\Delta, r, 2) - A(\mathcal{I}(\Delta, r, 1/\sigma) - \mathcal{I}(\Delta, r, 2/\sigma))\right). \tag{4.24}$$

The bump radius may then be computed by finding the roots Δ of the equation $\kappa = U(\Delta)$ with

$$U(\Delta) = \frac{4\Delta}{3}\Bigg(I_1(\Delta)K_0(\Delta) - \frac{1}{2}I_1(2\Delta)K_0(2\Delta) - A\left(\sigma I_1(\Delta/\sigma)K_0(\Delta/\sigma) - \frac{\sigma}{2}I_1(2\Delta/\sigma)K_0(2\Delta/\sigma)\right)\Bigg). \tag{4.25}$$

(Note that the threshold condition is a necessary but not sufficient condition for proving existence of a 2D bump. One also has to check that there are no other threshold crossing points; this can be established for a purely excitatory neural field with monotonically decreasing weight function [133].) In the case of a Mexican hat weight distribution, there is typically a maximum of two bump solutions as illustrated in figure 20 for w given by equation (4.22). The narrower bump is always unstable as found in 1D. However, the stable upper branch can develop instabilities as the threshold is decreased leading to the formation of multiple bump solutions that break the rotational symmetry [88, 144], see below.

Stability of a 2D bump. In order to determine linear stability of a bump solution $U(r)$, substitute $u(\mathbf{r},t) = U(r) + p(\mathbf{r})\,\mathrm{e}^{\lambda t}$ into equation (4.17) and expand to first order in p using equation (4.18). This gives the eigenvalue equation

$$\begin{aligned}(\lambda+1)p(\mathbf{r}) &= \int w(|\mathbf{r}-\mathbf{r}'|)\delta(U(r')-\kappa))p(\mathbf{r}')\,\mathrm{d}\mathbf{r}' \\ &= \frac{1}{|U'(\Delta)|}\int_0^\infty\int_0^{2\pi} w(|\mathbf{r}-\mathbf{r}'|)\delta(r'-a)p(\mathbf{r}')\,\mathrm{d}\theta' r'\,\mathrm{d}r' \\ &= \frac{\Delta}{|U'(\Delta)|}\int_0^{2\pi} w(|\mathbf{r}-\mathbf{a}'|)p(a,\phi')\,\mathrm{d}\phi', \end{aligned} \tag{4.26}$$

where $\mathbf{a}' = (a,\phi')$. We can now proceed along similar lines to the 1D case by reformulating the problem in terms of finding the spectrum of a compact linear operator acting on continuous, bounded functions $\psi(r,\phi)$ defined on the disk of radius $r \leqslant \Delta$. One class of solution to equation (4.27) consists of functions $p(\mathbf{r})$ that vanish on the boundary, $\psi(a,\phi) = 0$ for all ϕ, such that $\lambda = -1$. This belongs to the essential spectrum, which does not contribute to any instabilities. The discrete spectrum is determined by setting $\mathbf{r} = \mathbf{a} \equiv (\Delta,\phi)$ in equation (4.26):

$$(\lambda+1)p(\Delta,\phi) = \frac{\Delta}{|U'(\Delta)|}\int_0^{2\pi} w\left(2\Delta\sin\left(\frac{\phi-\phi'}{2}\right)\right)p(\Delta,\phi')\,\mathrm{d}\phi', \tag{4.27}$$

where we have simplified the argument of $w(r)$ using

$$|\mathbf{a}-\mathbf{a}'| = \sqrt{2\Delta^2 - 2\Delta^2\cos(\phi-\phi')} = 2\Delta\sin\left(\frac{\phi-\phi'}{2}\right).$$

Equation (4.27) can be solved in terms of Fourier eigenmodes, that is, $p(\Delta,\phi) = P_n(\phi) = c_n\mathrm{e}^{\mathrm{i}n\phi} + \bar{c}_n\mathrm{e}^{-\mathrm{i}n\phi}$ with corresponding eigenvalue λ_n satisfying

$$\lambda_n = -1 + \frac{\Delta}{|U'(\Delta)|}\int_0^{2\pi} w(2\Delta\sin(\phi/2))\,\mathrm{e}^{-\mathrm{i}n\phi}\,\mathrm{d}\phi. \tag{4.28}$$

Note that λ_n is real since (after rescaling ϕ)

$$\mathrm{Im}\{\lambda_n\} = -\frac{2\Delta}{|U'(\Delta)|}\int_0^{\pi} w(2\Delta\sin(\phi))\sin(2n\phi)\,\mathrm{d}\phi = 0,$$

i.e. the integrand is odd-symmetric about $\pi/2$. Hence,

$$\lambda_n = \mathrm{Re}\{\lambda_n\} = -1 + \frac{\Delta}{|U'(\Delta)|}\int_0^{2\pi} w(2\Delta\sin(\phi/2))\cos(n\phi)\,\mathrm{d}\phi, \tag{4.29}$$

with the integrand even-symmetric about $\pi/2$. The Fourier eigenmodes $P_n(\phi)$ can be related to perturbations of the bump boundary. That is, if $u(\mathbf{r},t) = U(r) + \varepsilon p(\mathbf{r},t) = 0$ at $\mathbf{r} \equiv (r,\phi) = (\Delta + \varepsilon a(\phi,t),\phi)$, where $\varepsilon a(\phi,t)$ with $\varepsilon \ll 1$ denotes a small perturbation of the circular bump boundary at polar coordinate (Δ,ϕ) at time t, then

$$\begin{aligned}\kappa &= u(\Delta+\varepsilon a(\phi,t),\phi,t) = U(\Delta+\varepsilon a(\phi,t)) + \varepsilon p(\Delta+\varepsilon a(\phi,t),\phi,t), \\ &\approx U(\Delta) + \varepsilon U'(\Delta)a(\phi,t) + \varepsilon p(\Delta,\phi,t).\end{aligned}$$

Since $U(\Delta) = \kappa$, it follows that

$$a(\phi,t) \approx \frac{p(\Delta,\phi,t)}{|U'(\Delta)|}.$$

Thus, one can decompose time-dependent perturbations of the circular boundary in terms of the Fourier modes $[c_n\,\mathrm{e}^{\mathrm{i}n\phi} + c_n\,\mathrm{e}^{-\mathrm{i}n\phi}]\,\mathrm{e}^{\lambda t}$. Some examples of low-order perturbations of the bump boundary shown in figure 21. It can be seen that the nth order boundary perturbation has D_n symmetry, meaning the resulting solution has the n reflectional and rotational symmetries

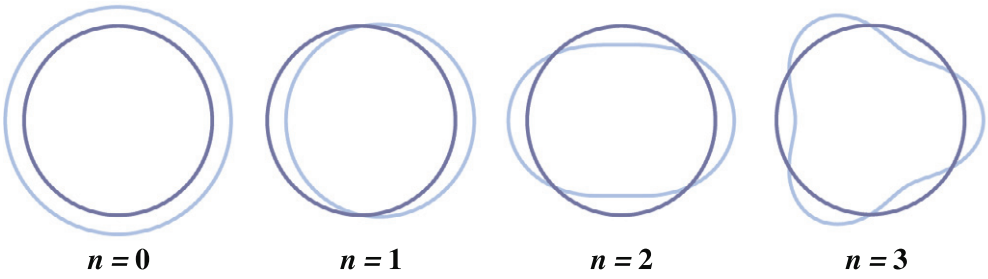

Figure 21. Low-order perturbations of a radially symmetric 2D bump exhibiting D_n symmetry.

of the dihedral group D_n. The perturbations also have a simple geometric interpretation. For example $n = 0$ corresponds to a uniform expansion or contraction of the bump, whereas $n = 1$ corresponds to a uniform shift of the bump.

Since the $n = 1$ mode represents pure shifts of the bump solution, we expect $\lambda_1 = 0$ from translation symmetry. In order to verify this, we evaluate the integral appearing in equation (4.29) using Bessel functions, along similar lines to the evaluation of $U(r)$, equation (4.21). That is,

$$\int_0^{2\pi} w(|\mathbf{a}-\mathbf{a}'|)\cos(n\phi')\,\mathrm{d}\phi' = \int_0^{2\pi}\left(\int_0^{\infty}\widehat{w}(\rho)J_0(\rho|\mathbf{a}-\mathbf{a}'|)\rho\mathrm{d}\rho\right)\cos\phi'\,\mathrm{d}\phi'$$
$$= 2\pi\int_0^{\infty}\widehat{w}(\rho)J_m(\rho\Delta)J_m(\rho\Delta)\rho\,\mathrm{d}\rho, \tag{4.30}$$

after reversing the order of integration and using the addition theorem (4.20). Moreover, differentiating equation (4.21) with respect to r gives

$$U'(\Delta) = -2\pi\Delta\int_0^{\infty}\widehat{w}(\rho)J_1(\Delta\rho)J_1(\Delta\rho)\rho\,\mathrm{d}\rho. \tag{4.31}$$

Hence, the eigenvalue (4.29) can be rewritten as

$$\lambda_n = -1 + \frac{\int_0^{\infty}\widehat{w}(\rho)J_n(\rho r)J_n(\rho\Delta)\rho\,\mathrm{d}\rho}{\int_0^{\infty}\widehat{w}(\rho)J_1(\rho r)J_1(\rho\Delta)\rho\,\mathrm{d}\rho}. \tag{4.32}$$

It immediately follows that $\lambda_1 = 0$. Hence, the 2D bump is linearly stable if $\lambda_n < 0$ for all $n \neq 1$. In the particular case of an excitatory network (corresponding to setting $A = 0$ in equation (4.22)), such that $w(r) \geqslant 0$ for all $r \geqslant 0$, we have

$$\int_0^{2\pi} w(2\Delta\sin(\phi/2))\cos(n\phi)\,\mathrm{d}\phi \leqslant \int_0^{2\pi} w(2\Delta\sin(\phi/2))|\cos(n\phi)|\,\mathrm{d}\phi$$
$$\leqslant \int_0^{2\pi} w(2\Delta\sin(\phi/2))\,\mathrm{d}\phi,$$

so that $\lambda_n \leqslant \lambda_0$ for all n. Since $\lambda_1 = 0$, it follows that $\lambda_0 \geqslant 0$ and, hence, an excitatory neural field cannot support stable radially symmetric bumps. In general, it is not possible to obtain analytical expressions for the eigenvalues. However, it is straightforward to evaluate the integral expressions numerically, and one typically finds that the low-order modes dominate. Using the Mexican hat function (4.22), Owen *et al* [144] have shown how the upper branch of rotationally symmetric bumps (see figure 20) can become unstable as the threshold is decreased toward zero, leading to the formation of a stationary multibump solution that breaks continuous rotational symmetry. The discrete rotational symmetry D_n of the resulting multibump solution reflects

the order n of the dominant eigenvalue λ_n at bifurcation. Interestingly, if linear adaptation is included in the neural field model, then these non-rotationally symmetric solutions can undergo a secondary instability leading to the formation of a rotating wave [88, 144]. Sufficiently strong adaptation can also destabilize a bump leading to a traveling spot.

4.3. Stimulus-driven bumps

In many applications of neural field models, the spatial location of the peak of an activity bump encodes information about a sensory stimulus or an item in working memory or positional information, as in the head direction or oculomotor systems [9, 145]. Hence, it is important to understand how the location of a bump is affected by external stimuli. In this section we consider various studies regarding the effects of external inputs on the location and stability of bumps.

Locking to a moving stimulus. Consider a scalar neural field with a time-dependent input of the form $I(x,t)$:

$$\frac{\partial u(x,t)}{\partial t} = -u(x,t) + \int_{-\infty}^{\infty} w(x-x')F(u(x',t))\,\mathrm{d}x' + I(x,t), \tag{4.33}$$

where $w(x)$ is a Mexican hat function. First, suppose that the input is small and slowly varying so we can write $I(x,t) = \delta\eta(x,\delta t)$ for a small parameter δ. Furthermore, assume that if $\delta = 0$ then the network supports a stable bump solution $U(x)$ centered at $x = 0$. A simple perturbative argument can be used to determine how the bump responds when $0 < \delta \ll 1$ [15]. That is, introduce the slow time variable $\tau = \delta t$ and set $u(x,t) = U(x+\phi(\tau)) + \delta u_1(x,\tau)$ where u_1 is orthogonal to $U'(x)$. Substituting into equation (4.33), Taylor expanding to first order in δ and using the fact that $U(x)$ satisfies $U(x) = \int_{-\infty}^{\infty} w(x-x')F(U(x')\,\mathrm{d}x'$, we obtain the inhomogeneous equation

$$\begin{aligned}\mathcal{L}u_1 &\equiv -u_1 + \int_{-\infty}^{\infty} w(x-x')F'(U(x'+\phi))u_1(x',\tau)\\ &= U'(x+\phi(\tau))\frac{\mathrm{d}\phi}{\mathrm{d}\tau} - \eta(x,\tau).\end{aligned} \tag{4.34}$$

Since the function $u_1(x)$ decays to zero as $x \to \pm\infty$, we will assume that $\mathcal{L}$ acts on the space $L^2(\mathbb{R})$ and introduce the generalized inner product

$$\langle u|v\rangle = \int_{-\infty}^{\infty} F'(U(x))u(x)v(x)\,\mathrm{d}x \tag{4.35}$$

for all $u, v \in L^2(\mathbb{R})$. With respect to this space, $\mathcal{L}$ is self-adjoint, since $w(x)$ is assumed to be an even function of x, and has a 1D null space spanned by $U'(x+\phi)$. Hence, taking the inner product of both sides of equation (4.34) with respect to $U'(x+\phi)$ and using the Fredholm alternative theorem shows that there only exists a bounded solution for u_1 if

$$\frac{\mathrm{d}\phi}{\mathrm{d}\tau} = \frac{\int F'(U(y+\phi))U'(y+\phi)I(y,\tau)\,\mathrm{d}y}{\int F'(U(y+\phi))U'(y+\phi)^2\,\mathrm{d}y} \equiv \mathcal{F}(\phi,\tau). \tag{4.36}$$

It follows that the phase ϕ, which determines the location of the peak of the bump will move so as to make $\mathcal{F}$ vanish. Since $F' > 0$ everywhere and $U'^2 > 0$ for all finite y, the denominator of $\mathcal{F}$ is positive definite. Therefore, vanishing of $\mathcal{F}$ is equivalent to the condition

$$\int \frac{\mathrm{d}F(U(y+\phi))}{\mathrm{d}y} I(y,\tau)\,\mathrm{d}y = 0.$$

For a symmetric weight distribution, the bump solution $U(x)$ is symmetric about its peak at $x = 0$. This implies that $F(U(y+\phi))$ is symmetric about $y = -\phi$, and $\mathrm{d}F/\mathrm{d}y$ is anti-symmetric

about $y = -\phi$. In the simple case of a stationary Gaussian input centered about $x = x_0$, we see that the above integral vanishes if the bump moves until its peak is located at $\phi = -x_0$. It also follows that the bump can track the Gaussian input if it moves sufficiently slowly. In the special case of a Gaussian stimulus moving with constant speed v, $I(x,t) = I(x - vt)$, stimulus locking can be analyzed by looking for traveling pulse solutions in the moving frame $\xi = x - vt$. This particular problem has been addressed both for scalar neural fields with Mexican hat weight distributions [146] and for purely excitatory neural fields with linear adaptation [112, 147], see below.

Neural field model for head-direction. Head direction cells in the brains of freely moving rats represent the instantaneous head direction of the animal in the horizontal plane irrespective of the animal's location [7]. The internal representation of head direction maintained by these cells is updated continually according to the head movement of the animal, even in total darkness. A simple model for head-direction was introduced by Zhang [29] in the form of a scalar neural field on a circular domain with time-dependent weights (see also [148]). The basic equation takes the form

$$\frac{\partial u}{\partial t} = -u(x,t) + \int_0^{2\pi} W(x-y;t)F(u(x,t))\,\mathrm{d}y, \tag{4.37}$$

with

$$W(x;t) = w(x) + \gamma(t)w'(x). \tag{4.38}$$

Here $w'(x)$ is the derivative of the weight function and $\gamma(t)$ represents the effective input to the system that causes head-direction shift. Suppose that there exists a stable bump solution $U(x)$ centered at $x = 0$ when $\gamma(t) = 0$. Since

$$U(x) = \int_0^{2\pi} w(x-y)F(U(y))\,\mathrm{d}y,$$

it immediately follows that equation (4.37) has the solution

$$u(x,t) = U\left(x + \int_0^t \gamma(s)\,\mathrm{d}s\right). \tag{4.39}$$

Thus, the location or phase $X(t)$ of the activity peak moves with the integrated signal

$$X(t) = -\int_0^t \gamma(s)\,\mathrm{d}s. \tag{4.40}$$

The instantaneous angular velocity is $-\gamma(t)$. We see that the bump only shifts whilst the signal is on (due to the head direction changing), and the activity bump maintains the current head direction once the signal is switched off. For example, a brief negative input will shift the bump counterclockwise, while a brief positive input will shift it clockwise. However, we expect the stimulus-locked bump to become unstable if the angular velocity $\gamma(t)$ becomes too large. One limitation of Zhang's model is that it makes use of instantaneous changes in synaptic strength, which is not biologically very plausible. This has led to a modified version of the model involving two coupled ring networks that receive differential velocity signals [149]. Interactions within a ring and between rings are taken to be rotationally invariant but asymmetric due to the introduction of constant phase offsets. When the inputs to the two rings are the same, a stable stationary bump can be supported in both rings. However, a head velocity signal breaks the symmetry between the inputs resulting in movement of the activity bumps that integrates the velocity signal.

Finally note that there are two basic components shared by any neural field model of the head-direction system. First, the network supports a continuous attractor, in the sense that the

peak of an activity bump can be located anywhere on the circle; indeed, the location of the peak encodes the head direction. An immediate consequence of this is that in the absence of an input, the resulting bump solution is marginally stable, since arbitrarily small fluctuations can shift its center or peak around the circle. The problem of noise is an issue in all applications of continuous attractor networks [145], see below. The second component of the head-direction models is a neural integrator, since the location of the bump is based on integrating the input signal $\gamma(t)$. A number of other neural systems involve a neural integrator, including the oculomotor control system in the goldfish [150].

Stimulus-induced breathers. So far we have focused on activity bumps that persist in the absence of external stimuli due to the combined action of local recurrent excitation and lateral inhibition. We now describe some interesting instabilities that arise in the case of non-persistent bumps. For the sake of illustration, consider a 2D excitatory neural field with linear adaptation and an external input I:

$$\frac{\partial u(\mathbf{r},t)}{\partial t} = -u(\mathbf{r},t) + \int_{\mathbb{R}^2} w(|\mathbf{r}-\mathbf{r}'|)H(u(\mathbf{r}',t)-\kappa)\,\mathrm{d}\mathbf{r}' - \beta q(\mathbf{r},t) + I(\mathbf{r})$$
$$\frac{1}{\epsilon}\frac{\partial q(\mathbf{r},t)}{\partial t} = -q(\mathbf{r},t) + u(\mathbf{r},t). \tag{4.41}$$

Suppose that the inhomogeneous input is a radially symmetric Gaussian centered about the origin, $I(\mathbf{r}) = I_0\,\mathrm{e}^{-r^2/\sigma_s^2}$. We know from section 3.2, that in the absence of an input, the resulting excitatory network supports traveling waves rather than stationary bumps. On the other hand, for sufficiently strong input amplitude I_0, the network supports a radially symmetric bump centered about the input. Such a bump is not persistent, since if the input is removed then the bump disappears as well. The basic problem we want to address is what happens to the stability of the bump as the input amplitude is slowly decreased.

The analysis of the existence and stability of radially symmetric 2D bumps proceeds as in section 4.2 with minor changes. First, the threshold condition for the existence of a bump becomes (see equation (4.21))

$$\kappa = U(\Delta) = 2\pi\Delta\int_0^\infty \widehat{w}(\rho)J_0(\rho\Delta)J_1(\rho\Delta)\,\mathrm{d}\rho + I(\Delta). \tag{4.42}$$

Second, the linear stability of the bump is determined by the pair of eigenvalues $\lambda = \lambda_n^{\pm}$ associated with the Fourier modes $[c_n\,\mathrm{e}^{\mathrm{i}n\phi} + c_n\,\mathrm{e}^{-\mathrm{i}n\phi}]\,\mathrm{e}^{\lambda t}$, where [133]

$$\lambda_n^{\pm} = \frac{1}{2}\big[-\Lambda_n \pm \sqrt{\Lambda_n^2 - 4\epsilon(1+\beta)(1-\Gamma_n)}\big], \tag{4.43}$$

$$\Lambda_n = 1 + \epsilon - \Gamma_n(1+\beta), \qquad \Gamma_n = \frac{\mu_n(\Delta)}{|U'(\Delta)|(1+\beta)}, \tag{4.44}$$

and

$$\mu_n(\Delta) = \Delta\int_0^{2\pi} w(2a\sin(\phi/2))\cos(n\phi)\,\mathrm{d}\phi. \tag{4.45}$$

It follows that stability of a radially symmetric bump require $\Lambda_n > 0$ and $\Gamma_n < 1$ for all $n \geqslant 0$. Given the form of Λ_n, this reduces to the following stability conditions:

$$\begin{aligned} &\epsilon > \beta : \Gamma_n < 1 && \text{for all } n \geqslant 0 \\ &\epsilon < \beta : \Gamma_n < \frac{1+\epsilon}{1+\beta} && \text{for all } n \geqslant 0. \end{aligned} \tag{4.46}$$

If the first condition is violated as some parameter is varied then there is a saddle-node bifurcation, whereas a breakdown of the second condition signals a Hopf bifurcation. In the

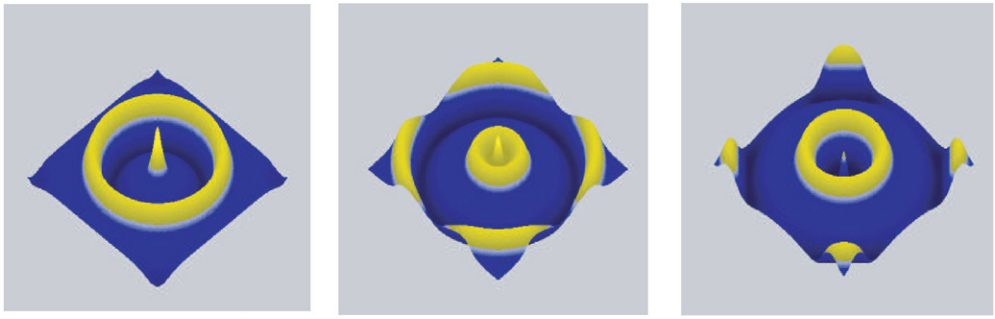

Figure 22. Sequence of snapshots of a 2D breather acting as a periodic pulse-emitter in the case of a 2D excitatory neural field with linear adaptation and exponential weight function. Parameters are $\beta = 4$, $\kappa = 0.2$, $\epsilon = 0.1$ and $I_0 = 0.2$. Lighter colors indicate higher activity [133].

latter case the bump instability leads to the formation of a breather. In section 4.2, we showed that for an excitatory network, $\mu_n \leqslant \mu_0$ for all $n \geqslant 0$, so that we expect any instability to involve the growth of radially symmetric perturbations and, hence, the resulting breather will be radially symmetric. On the other hand, if there is a Mexican hat weight distribution then non-radially symmetric breather and rotating waves can occur [136]. One way to induce a Hopf instability of a bump is to reduce the amplitude I_0 of the Gaussian input; this modifies both the pulse-width Δ and the slope of the bump at threshold, $|U'(\Delta)|$. Interestingly, as the input amplitude is further reduced, the breather can undergo a secondary instability such that it now acts as an oscillating core that emits circular target waves. An example of such a periodic wave emitter is shown in figure 22. Thus, a spatially localized stationary input provides a mechanism for the formation of a network pacemaker oscillator. The mechanism differs from that discussed in section 3.5, where the whole network acted as an oscillatory medium. Note that in the case of 1D breathers, Folias [151] has recently carried out a weakly nonlinear analysis of a stationary pulse undergoing a stimulus-induced Hopf bifurcation in a neural field model with Mexican hat weight function and a Heaviside nonlinearity. He shows that there are two spatial modes, that can undergo a Hopf bifurcation, producing a periodic orbit that either expands/contracts (breather) or moves side-to-side (slosher). Moreover, by calculating the critical third order coefficient of the associated normal form, he determines when the bifurcation switches from super- to subcritical. Given the normal form, it should be possible to extend this analysis to the case of weakly interacting breathers, extending previous work on weakly interacting bumps [152].

A stimulus-induced bump in an excitatory network with linear adaptation can also follow a moving stimulus. This problem has been studied in 1D using both the constructive method for Heaviside nonlinearities [112] and singular perturbation methods for smooth F [147]. We discuss the former approach here. Since the network supports natural traveling waves in the absence of inputs, we now expect stimulus-locking to occur for a band of stimulus velocities v around the natural velocity v_s of stable pulses. Moreover, in light of the above analysis of stationary inputs, we expect another band of stimulus-locked waves to exist for sufficiently small v, provided that the stimulus amplitude is sufficiently large to maintain a stationary bump when $v = 0$. This is indeed found to be the case, as illustrated in figure 23 for a Heaviside firing rate function. Moreover, one finds that waves in the low velocity tongue can undergo a Hopf instability resulting in either a traveling breather or a pulse emitter. These results can be established by looking for a traveling pulse solution in the moving frame of the input [112]. That is, set $u(x,t) = U(\xi)$ and $q(x,t) = Q(\xi)$, $\xi = x - vt$, such that $U(\xi) \to 0$ as $\xi \to \pm\infty$.

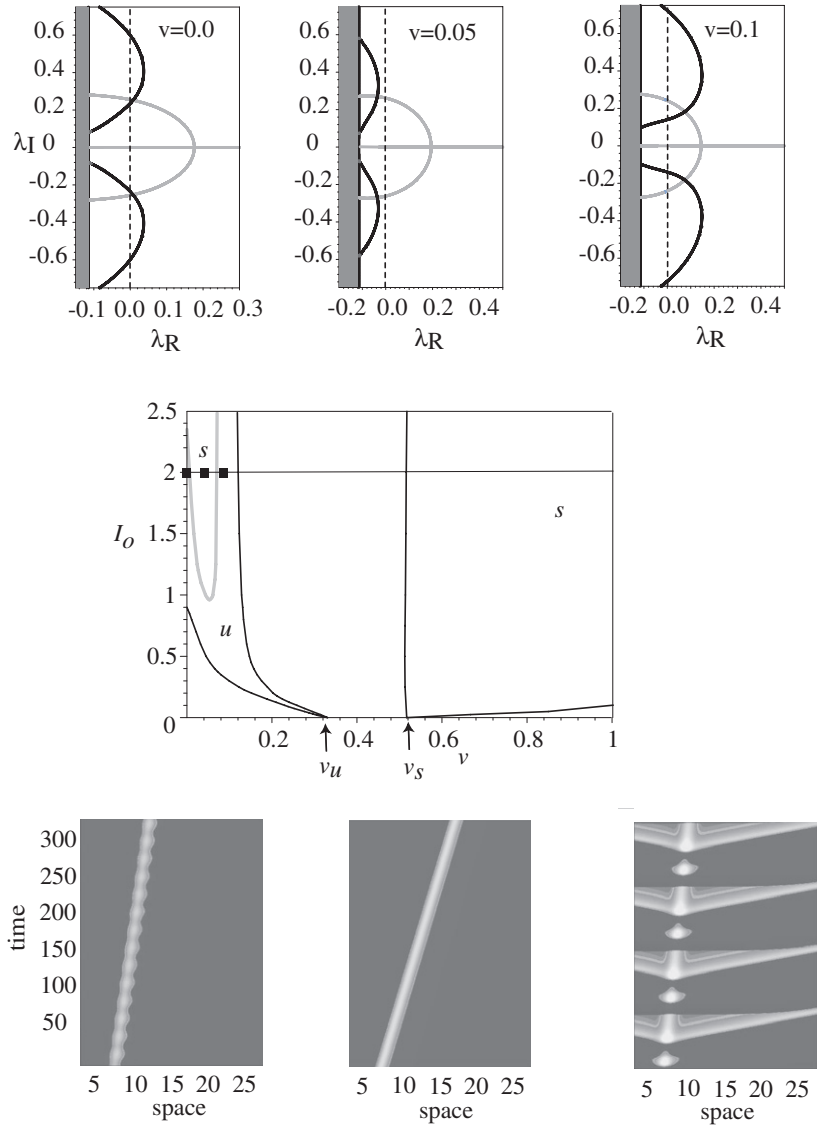

Figure 23. Stimulus-locked traveling pulses in an excitatory 1D neural field with linear adaptation and exponential weight function. Gaussian stimulus has velocity v, amplitude I_0 and width $\sigma_s = 1.0$. Other parameters are threshold $\kappa = 0.3$, rate constant $\epsilon = 0.03$, and amplitude of adaptation $\beta = 2.5$. *Center*: Regions of existence of stimulus-locked traveling pulses in the (v, I_0)-plane for a 1D excitatory neural field with linear adaptation. The left and right regions form tongues that issue from the unstable v_u and stable v_s natural traveling pulses of the homogeneous network, respectively. The Hopf curve within the left-hand tongue is shown in gray. Stationary pulses correspond to the intersection of the tongue and the line $v = 0$. Top row: graphs of the zero sets of the real (*dark curves*) and imaginary (*light curves*) parts of the Evans function determining the stability of a stimulus-locked bump for $I_0 = 2.0$ and a sequence of stimulus speeds v; intersection points indicate eigenvalues. The vertical shaded region indicates the essential spectrum. This sequence of plots indicates that two Hopf bifurcation points occur, thus defining the boundary of the stable region within the left tongue. Bottom row: corresponding sequence of spacetime plots, illustrating the transition from breather, to stimulus-locked pulse, to pulse-emitter as v increases through the left-hand and right-hand branches of the Hopf curve [112].

Furthermore, assume that $U(\xi)$ crosses threshold at the two points ξ_1, ξ_2 such that $U(\xi) > \kappa$ for $\xi \in (\xi_1, \xi_2)$ and $U(\xi) < \kappa$ for $\xi \notin [\xi_1, \xi_2]$. It follows that

$$-cU'(\xi) + U(\xi) + \beta Q(\xi) = \int_{\xi_1}^{\xi_2} w(\xi - \xi')\, \mathrm{d}\xi' + I(\xi)$$
$$-cQ'(\xi) + \epsilon[Q(\xi) - U(\xi)] = 0. \tag{4.47}$$

The existence of traveling pulse solutions can then be determined by solving this pair of equations using variation-of-parameters along similar lines to section 3.3.1. However, in contrast to the case of a traveling pulse in a homogeneous neural field, we cannot arbitrarily shift coordinates so that one of the threshold crossing points is at the origin. Thus two conditions are needed in order to determine the two threshold crossing points ξ_1, ξ_2 with $\Delta = \xi_2 - \xi_2$ the width of the pulse. On the other hand, the speed of the pulse is already specified to be the speed v of the input. Wave stability can also be determined by constructing the associated Evans function. Now stability requires that there exists a positive number K such that $\mathrm{Re}\,\lambda < -K$ for all zeros of the Evans function, that is, there no longer exists a zero eigenvalue arising from translation symmetry.

Robustness to noise and bistability. In our discussion of stimulus-driven bumps, we focused on how an external input can control the spatial location of a bump. In applications to working memory, it is necessary that the bump persists once the stimulus is removed. Moreover, there has to be some mechanism for initiating/removing a bump so that new memories can be stored. It is typically assumed that the network exhibits bistability, in which a stable homogeneous resting state coexists with a marginally stable bump. Marginal stability reflects the arbitrariness of bump location in the absence of inputs due to translation symmetry. Clearly, a transition from the resting state to a bump can be initiated by an excitatory stimulus of the form considered in section 4.3. In principle, a transition back to the resting state could be induced by a global inhibitory stimulus. An interesting alternative mechanism was proposed by Gutkin *et al* [153] (see also [139]). They carried out computer simulations of a lateral inhibition network consisting of conductance-based models of single neurons. They showed that a bump only persisted if the neurons fired asynchronously, so that one way to destroy the bump was to use an excitatory stimulus to induce transient synchrony.

Marginal stability of a persistent bump implies that arbitrarily small fluctuations can shift its location, so that over time noise can wash out the information encoded by the bump. One mechanism for enhancing the robustness of bumps to noise is to introduce bistability at the cellular level [27, 154, 155]. The basic model of Camperi and Wang [27] takes the form of an activity-based neural field equation on a ring:

$$\frac{\partial}{\partial t} v(x,t) = -K(v(x,t)) + F\left(\int_0^{2\pi} w(x-y) v(y,t)\, \mathrm{d}y + I_{\mathrm{ext}}(x,t) \right), \tag{4.48}$$

where the linear decay term is replaced by a cubic nonlinearity

$$K(v) = c + v - av^2 + bv^3. \tag{4.49}$$

The parameters are chosen so that the single neuron model $\dot{v} = -K(v) + F(I_{\mathrm{ext}})$ exhibits bistability when F is given by a linear threshold function, $F(I) = IH(I)$. That is, there are three fixed point solutions $v^* = K^{-1} \circ F(I_{\mathrm{ext}})$, two of which are stable. The spatially extended network with lateral inhibition then exhibits bistability between a resting state and a marginally stable bump solution. Although this model does generate bumps that are much more robust to external noise, the bistable regime is rather sensitive to the range of parameters [154]. Recently, a biologically plausible mechanism for generating cellular bistability has been

proposed, based on intracellular calcium Ca^{2+} [155]. The local function $K(v)$ is now taken to be monotonic whereas the firing rate F is multiplied by a factor $(1 + [Ca^{2+}]/C_0)$ where $[Ca^{2+}]$ denotes intracellular calcium concentration within the cytosol of the neuron. The latter evolves dynamically via IP3-modulated Ca^{2+}-induced Ca^{2+} release from intracellular stores combined with the action of ionic pumps and Ca^{2+} influx from synaptic activity as determined by F. The calcium subsystem provides the source of cellular bistability.

5. Neural pattern formation

So far we have considered the spatiotemporal dynamics of neural fields based upon constructing explicit solutions (or their approximations) in the fully nonlinear regime. An alternative approach is to investigate the emergence of spatially periodic stationary and oscillatory patterns through a combination of linear stability theory, weakly nonlinear analysis, and numerical simulations. In cases where the period of the pattern matches the size of the domain, this also provides a mechanism for the formation of persistent bumps. Turing originally considered the problem of how animal coat patterns develop, suggesting that chemical markers in the skin comprise a system of diffusion-coupled chemical reactions among substances called morphogens [156]. He showed that in a two-component reaction-diffusion system, a state of uniform chemical concentration can undergo a diffusion-driven instability leading to the formation of a spatially inhomogeneous state. Ever since the pioneering work of Turing on morphogenesis [156], there has been a great deal of interest in spontaneous pattern formation in physical and biological systems [157, 158]. In the neural context, Wilson and Cowan [11] proposed a non-local version of Turing's diffusion-driven mechanism, based on competition between short-range excitation and longer-range inhibition. Here interactions are mediated, not by molecular diffusion, but by long-range axonal connections. Since then, this neural version of the Turing instability has been applied to a number of problems concerning cortical dynamics. Examples in visual neuroscience include the ring model of orientation tuning [25, 26, 159], cortical models of geometric visual hallucinations [19, 74, 160] and developmental models of cortical maps [60]. (The latter involves pattern forming instabilities in the space of synaptic weights rather than neuronal activity states.) In most cases there exists some underlying symmetry in the model that plays a crucial role in the selection and stability of the resulting patterns.

In this section we review theoretical approaches to studying spontaneous pattern formation in neural field models. Throughout we emphasize the important role that symmetries play. In section 5.1 we consider the basic neural mechanism for Turing-like pattern formation developed by Wilson, Cowan and Ermentrout [11, 19]. We then focus our discussion on activity-based patterns generated in primary visual cortex (V1), which is the first cortical region to process visual information from the eyes. We begin by constructing a neural field model of V1 that takes into account the functional architecture of V1, in particular, its hypercolumnar structure (section 5.2). We then analyze pattern formation in a ring model of orientation tuning within a single hypercolumn (section 5.3), and then extend this to a coupled hypercolumn model of V1 (section 5.4) [74]. We end by relating cortical pattern formation to a theory of geometric visual hallucinations (section 5.5).

5.1. Turing mechanism for cortical pattern formation

Let us return to a 2D version of the scalar neural field equation (3.2):

$$\frac{\partial u(\mathbf{r},t)}{\partial t} = -u(\mathbf{r},t) + \int_{\mathbb{R}^2} w(\mathbf{r},\mathbf{r}')F(u(\mathbf{r}',t))\mathrm{d}\mathbf{r}', \tag{5.1}$$

with F given by a smooth sigmoid function (2.6). For the moment, we assume $w(\mathbf{r}, \mathbf{r}') = w(|\mathbf{r} - \mathbf{r}'|)$ so that it is invariant with respect to the Euclidean group $\mathbf{E}(2)$ of rigid body transformations in the plane. That is,

$$\gamma \cdot w(\mathbf{r}, \mathbf{r}') = w(\gamma^{-1} \cdot \mathbf{r}, \gamma^{-1} \cdot \mathbf{r}') = w(\mathbf{r}, \mathbf{r}')$$

for all $\gamma \in \mathbf{E}(2)$. The Euclidean group is composed of the (semi-direct) product of $\mathbf{O}(2)$, the group of planar rotations $\mathbf{r} \to R_\varphi \mathbf{r}$ and reflections $(x, y) \to (x, -y)$, with $\mathbb{R}^2$, the group of planar translations $\mathbf{r} \to \mathbf{r} + \mathbf{s}$. Here

$$R_\varphi = \begin{pmatrix} \cos\varphi & -\sin\varphi \\ \sin\varphi & \cos\varphi \end{pmatrix}, \qquad \varphi \in [0, 2\pi). \tag{5.2}$$

Most large-scale models of cortex assume Euclidean symmetric weights [15], but see section 5.2. Suppose that there exists a uniform fixed point solution u_0 so that

$$u_0 = \widehat{w}_0 F(u_0), \qquad \widehat{w}_0 = \int_{\mathbb{R}^2} w(\mathbf{r})\, d\mathbf{r}. \tag{5.3}$$

Linearizing equation (3.2) about the fixed point solution by writing $u(\mathbf{r}, t) = u_0 + p(\mathbf{r})e^{\lambda t}$ then leads to the eigenvalue equation

$$\lambda p(\mathbf{r}) = \mu \int_{\mathbb{R}^2} w(|\mathbf{r} - \mathbf{r}'|) p(\mathbf{r}')\, d\mathbf{r}', \tag{5.4}$$

where $\mu = F'(u_0)$ represents the gain of the firing rate function in the rest state u_0. Thus changes in μ, which is treated as a bifurcation parameter, reflect changes in the level of excitability of the network. The linear operator on the right-hand side has a continuous spectrum generated by the solutions $p(\mathbf{r}) = e^{i\mathbf{k}\cdot\mathbf{r}}$, which leads to the dispersion relation

$$\lambda = \lambda(k) \equiv -1 + \mu \widehat{w}(k), \tag{5.5}$$

with $\widehat{w}(k)$ the Fourier transform of $w(\mathbf{r})$ and $k = |\mathbf{k}|$. It is now straightforward to determine conditions under which the homogeneous state u_0 loses stability leading to the formation of spatially periodic patterns. The standard mechanism for such an instability, which is the neural analog of the Turing instability in reaction-diffusion equations, is a combination of short-range excitation and long-range inhibition, that is, a Mexican hat function. Consider for example the difference-of-Gaussians (see figure 24(*a*)):

$$w(|\mathbf{r}|) = e^{-r^2/2} - A\, e^{-r^2/2\sigma^2}, \tag{5.6}$$

the Fourier transform of which is

$$\widehat{w}(k) = \frac{1}{2} e^{-\frac{1}{4}k^2} - \frac{A\sigma^2}{2} e^{-\frac{1}{4}\sigma^2 k^2}. \tag{5.7}$$

Since $\widehat{w}(k)$ is a bounded function of k, it follows that for sufficiently small μ, $\mathrm{Re}\,\lambda < 0$ for all k, and the fixed point k is stable. However, as μ increases, the dispersion curve $\lambda(k)$ passes through zero at the critical value $\mu_c = \widehat{w}(k_c)^{-1}$ signaling the growth of spatially periodic patterns with wavenumber k_c, where $\widehat{w}(k_c) = \max_k\{\widehat{w}(k)\}$, see figure 24(*b*).

Close to the bifurcation point these patterns can be represented as linear combinations of plane waves

$$b(\mathbf{r}) = \sum_n (c_n e^{i\mathbf{k}_n\cdot\mathbf{r}} + c_n^* e^{-i\mathbf{k}_n\cdot\mathbf{r}}), \tag{5.8}$$

where the sum is over all wave vectors with $|\mathbf{k}_n| = k_c$. Rotation symmetry implies that the space of such modes is infinite-dimensional. That is, all plane-waves with wavevectors on the critical circle $|\mathbf{k}| = k_c$ are allowed. However, one of the simplifying features of many Turing-like patterns found in nature is that they tend to form a regular tiling of the

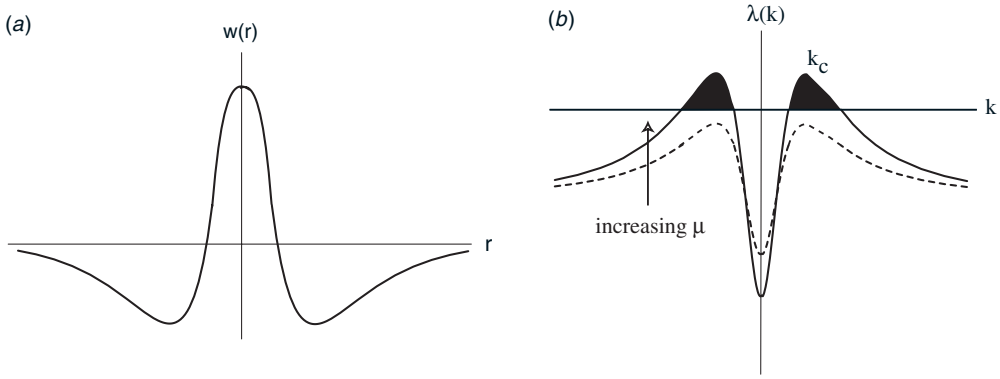

Figure 24. Neural basis of the Turing mechanism. (*a*) Mexican hat interaction function showing short-range excitation and long-range inhibition. (*b*) Dispersion curves $\lambda(k) = -1 + \mu\widehat{w}(k)$ for Mexican hat function. If the excitability μ of the cortex is increased, the dispersion curve is shifted upward leading to a Turing instability at a critical parameter $\mu_c = \widehat{w}(k_c)^{-1}$ where $\widehat{w}(k_c) = [\max_k\{\widehat{w}(k)\}]$. For $\mu_c < \mu < \infty$ the homogeneous fixed point is unstable.

cortical plane, that is, they are doubly-periodic with respect to some regular planar lattice (square, rhomboid or hexagonal). This is a common property of pattern forming instabilities in systems with Euclidean symmetry that are operating in the weakly nonlinear regime [157]. In the neural context, Euclidean symmetry reflects the invariance of synaptic interactions with respect to rotations, translations and reflections in the cortical plane. The emerging patterns spontaneously break Euclidean symmetry down to the discrete symmetry group of the lattice, and this allows techniques from bifurcation theory to be used to analyze the selection and stability of the patterns. The global position and orientation of the patterns are still arbitrary, however, reflecting the hidden Euclidean symmetry.

Hence, suppose that we restrict the space of solutions (5.8) to that of doubly-periodic functions corresponding to regular tilings of the plane. That is, $p(\mathbf{r} + \boldsymbol{\ell}) = p(\mathbf{r})$ for all $\boldsymbol{\ell} \in L$ where L is a regular square, rhomboid or hexagonal lattice. The sum over n is now finite with $N = 2$ (square, rhomboid) or $N = 3$ (hexagonal) and, depending on the boundary conditions, various patterns of stripes or spots can be obtained as solutions. Amplitude equations for the coefficients c_n can then be obtained using perturbation methods [84]. However, their basic structure can be determined from the underlying rotation and translation symmetries of the network model. In the case of a square or rhombic lattice, we can take $\mathbf{k}_1 = k_c(1, 0)$ and $\mathbf{k}_2 = k_c(\cos\varphi, \sin\varphi)$ such that (to cubic order)

$$\frac{\mathrm{d}c_n}{\mathrm{d}t} = c_n\left[\mu - \mu_c - \Gamma_0|c_n|^2 - 2\Gamma_\varphi \sum_{m\neq n} |c_m|^2\right], \qquad n = 1, 2, \tag{5.9}$$

where Γ_φ depends on the angle φ. In the case of a hexagonal lattice we can take $\mathbf{k}_n = k_c(\cos\varphi_n, \sin\varphi_n)$ with $\varphi_1 = 0, \varphi_2 = 2\pi/3, \varphi_3 = 4\pi/3$ such that

$$\frac{\mathrm{d}c_n}{\mathrm{d}t} = c_n[\mu - \mu_c - \Gamma_0|c_n|^2 - \eta c^*_{n-1}c^*_{n+1}] - 2\Gamma_{\varphi_2}c_n\big(|c_{n-1}|^2 + |c^2_{n+1}|\big), \tag{5.10}$$

where $n = 1, 2, 3 \pmod 3$. These ordinary differential equations can then be analyzed to determine which particular types of pattern are selected and to calculate their stability [19, 20, 84]. The results can be summarized in a bifurcation diagram as illustrated in figure 31(*a*) for the hexagonal lattice with $h > 0$ and $2\Gamma_{\varphi_2} > \Gamma_0$.

Oscillatory patterns. In the above analysis, we incorporated both excitation and inhibition into a one-population neural field model. However, as outlined in section 2.5, this is an approximation of a more realistic two-population model in which excitatory and inhibitory neurons are modeled separately. In the case of stationary patterns, the one-population model captures the basic pattern forming instability. However, the two-population model supports a wider range of dynamics and, in particular, can undergo a Turing–Hopf instability leading to the formation of oscillatory patterns [84, 160, 161]. Oscillatory patterns can also occur in a one-population model with adaptation or axonal/dendritic delays. For example, suppose that the temporal kernel $\Phi(t)$ in the integral version of the scalar neural field equation (3.10) is given by the Green's function of a semi-infinite dendritic cable, equation (2.22):

$$\Phi(t) = G(0, \xi_0, t) = \frac{1}{\sqrt{\pi D t}} \mathrm{e}^{-t/\tau_m} \mathrm{e}^{-\xi_0^2/4Dt} H(t), \tag{5.11}$$

where we have set $\lambda^2/\tau_m = D$. For the sake of illustration, all synaptic connections are assumed to be at a fixed location ξ_0 along the dendritic cable. Linearizing equation (3.10) about a homogeneous fixed point solution u_0 by writing $u(x,t) = u_0 + u_1 \mathrm{e}^{\lambda t + ikx}$ yields the eigenvalue equation

$$1 = \mu \widehat{w}(k) \mathcal{G}(\lambda), \tag{5.12}$$

where $\mathcal{G}(z)$ is the Laplace transform of $\Phi(t)$:

$$\mathcal{G}(z) = \int_0^\infty \mathrm{e}^{-zt} \Phi(t)\, \mathrm{d}t = \frac{1}{\sqrt{\epsilon + z}} \mathrm{e}^{-\xi_0 \sqrt{\epsilon + z}}, \tag{5.13}$$

with $\epsilon = \tau_m^{-1}$ and $D = 1$. In order to determine conditions for a Turing–Hopf bifurcation, set $\lambda = i\omega$ in the eigenvalue equation and equate real and imaginary parts using the fact that the Fourier transform $\widehat{w}(k)$ of the weight distribution is real. Writing $\mathcal{G}(\mathrm{i}\omega) = C(\omega) + \mathrm{i}S(\omega)$, we obtain the pair of equations

$$1 = \mu \widehat{w}(k) C(\omega), \qquad 0 = \mu \widehat{w}(k) S(\omega) \tag{5.14}$$

with

$$C(\omega) = \frac{1}{\sqrt{\epsilon^2 + \omega^2}} \mathrm{e}^{-A(\omega)\xi_0} \left[A(\omega) \cos\left(B(\omega)\xi_0\right) - B(\omega) \sin\left(B(\omega)\xi_0\right) \right] \tag{5.15}$$

$$S(\omega) = \frac{1}{\sqrt{\epsilon^2 + \omega^2}} \mathrm{e}^{-A(\omega)\xi_0} [A(\omega) \sin(B(\omega)\xi_0) + B(\omega) \cos(B(\omega)\xi_0)], \tag{5.16}$$

and $\sqrt{\epsilon + \mathrm{i}\omega} = A(\omega) + \mathrm{i}B(\omega)$ where

$$A(\omega) = \sqrt{[\sqrt{\epsilon^2 + \omega^2} + \epsilon]/2}, \qquad B(\omega) = \sqrt{[\sqrt{\epsilon^2 + \omega^2} - \epsilon]/2}. \tag{5.17}$$

The equation $S(\omega) = 0$ has an infinite set of roots. However, we are only interested in the root ω_c that generates the largest value of $|C(\omega)|$. The root corresponding to the largest positive value of $C(\omega)$ is $\omega = 0$ with $C(0) = \mathrm{e}^{-\epsilon\xi_0}/\sqrt{\epsilon}$. On the other hand, the root corresponding to the largest negative value of $C(\omega)$ (denoted by ω_0) has to be determined graphically. Finally, define

$$\widehat{w}(k_+) = \max_k \{\widehat{w}(k)\} > 0, \qquad \widehat{w}(k_-) = \min_k \{\widehat{w}(k)\} < 0.$$

It follows that if $\widehat{w}(k_+)C(0) > \widehat{w}(k_-)C(\omega_0)$ and $k_+ \neq 0$ then there is a standard Turing instability at $\mu_c = [\widehat{w}(k_+)C(0)]^{-1}$ with critical wavenumber $k_c = k_+$. On the other hand, if $\widehat{w}(k_+)C(0) < \widehat{w}(k_-)C(\omega_0)$ and $k_- \neq 0$, then there is a Turing–Hopf instability at $\mu_c = [\widehat{w}(k_-)C(\omega_0)]^{-1}$ with critical wavenumber $k_c = k_-$ and temporal frequency ω_0. It is clear that the Mexican hat function shown in figure 24 cannot support oscillatory patterns, since $k_- = 0$. However, an inverted Mexican hat function representing short-range inhibition and long-range excitation can. See [47] for a fuller discussion of the effects of dendritic processing on neural network dynamics.

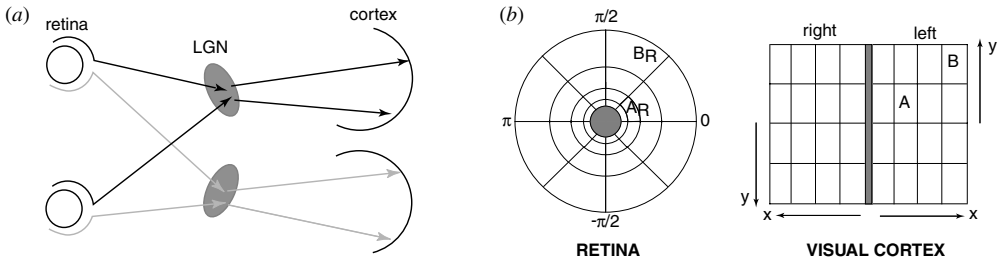

Figure 25. (*a*) Visual pathways from the retina through the lateral geniculate nucleus (LGN) of the thalamus to the primary visual cortex (V1). (*b*) Schematic illustration of the complex logarithmic mapping from retina to V1. Foveal region in retina is indicated by grey disc. Regions A_R and B_R in the visual field are mapped to regions A and B in cortex.

5.2. Neural field model of primary visual cortex (V1)

In standard treatments of cortical pattern formation, the synaptic weights are assumed to depend only on the Euclidean distance between points in cortex, that is, $w(\mathbf{r}, \mathbf{r}') = w(|\mathbf{r} - \mathbf{r}'|)$. However, a closer look at the detailed structure of cortical circuits shows that such an assumption is an oversimplification. We illustrate this by considering the functional architecture of the best known cortical area, primary visual cortex (V1), which is the first cortical region to process visual information from the eyes. This is then used to construct a more detailed neural field model of V1.

5.2.1. Functional architecture of V1. V1 is the first cortical area to receive visual information from the retina (see figure 25). The output from the retina is conveyed by ganglion cells whose axons form the optic nerve. The optic nerve conducts the output spike trains of the retinal ganglion cells to the lateral geniculate nucleus (LGN) of the thalamus, which acts as a relay station between retina and primary visual cortex (V1). Prior to arriving at the LGN, some ganglion cell axons cross the midline at the optic chiasm. This allows the left and right sides of the visual fields from both eyes to be represented on the right and left sides of the brain, respectively. Note that signals from the left and right eyes are segregated in the LGN and in input layers of V1. This means that the corresponding LGN and cortical neurons are monocular, in the sense that they only respond to stimuli presented to one of the eyes but not the other (ocular dominance).

Retinotopic map. One of the striking features of the visual system is that the visual world is mapped onto the cortical surface in a topographic manner. This means that neighboring points in a visual image evoke activity in neighboring regions of visual cortex. Moreover, one finds that the central region of the visual field has a larger representation in V1 than the periphery, partly due to a non-uniform distribution of retinal ganglion cells. The retinotopic map is defined as the coordinate transformation from points in the visual world to locations on the cortical surface. In order to describe this map, we first need to specify visual and cortical coordinate systems. Since objects located a fixed distance from one eye lie on a sphere, we can introduce spherical coordinates with the 'north pole' of the sphere located at the fixation point, the image point that focuses onto the fovea or center of the retina. In this system of coordinates, the latitude angle is called the eccentricity ϵ and the longitudinal angle measured from the horizontal meridian is called the azimuth φ. In most experiments the image is on a flat screen

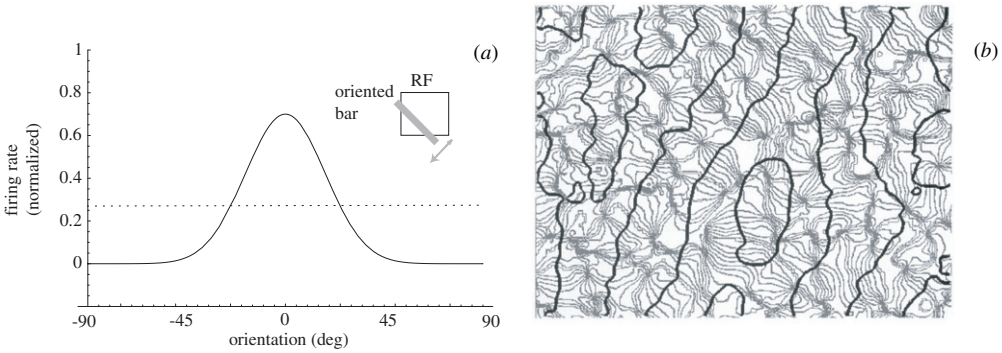

Figure 26. (a) Schematic illustration of an orientation tuning curve of a V1 neuron. Average firing rate is plotted as a function of the orientation of a bar stimulus that is moved back and forth within the receptive field (RF) of the neuron. The peak of the orientation tuning curve corresponds to the orientation preference of the cell. (b) Iso-orientation (light) and ocular dominance (dark) contours in a region of primate V1. A cortical hypercolumn consists of two orientation singularities or pinwheels per ocular dominance column. Reproduced with permission from figure 5A of [168].

such that, if we ignore the curvature of the sphere, the pair (ϵ, φ) approximately coincides with polar coordinates on the screen. One can also represent points on the screen using Cartesian coordinates (X, Y). In primary visual cortex the visual world is split in half with the region $-90^o \leqslant \varphi \leqslant 90^o$ represented on the left side of the brain, and the reflection of this region represented on the right side brain. Note that the eccentricity ϵ and Cartesian coordinates (X, Y) are all based on measuring distance on the screen. However, it is customary to divide these distances by the distance from the eye to the screen so that they are specified in terms of angles. The structure of the retinotopic map is illustrated in figure 25(b). One finds that away from the fovea concentric circles are approximately mapped to vertical lines and radial lines to horizontal lines. More precisely, for eccentricities greater than 1^o, the retinotopic map can be approximated by a complex logarithm [162]. That is, introducing the complex representations $Z = (\epsilon/\epsilon_0)\mathrm{e}^{-\mathrm{i}\pi\varphi/180^o}$ and $z = x + \mathrm{i}y$, where (x, y) are Cartesian cortical coordinates, then $z = \lambda \log Z$.

Feature maps. Superimposed upon the retinotopic map are additional maps reflecting the fact that neurons respond preferentially to stimuli with particular features [60]. Neurons in the retina, LGN and primary visual cortex respond to light stimuli in restricted regions of the visual field called their classical receptive fields (RFs). Patterns of illumination outside the RF of a given neuron cannot generate a response directly, although they can significantly modulate responses to stimuli within the RF via long-range cortical interactions (see below). The RF is divided into distinct ON and OFF regions. In an ON (OFF) region illumination that is higher (lower) than the background light intensity enhances firing. The spatial arrangement of these regions determines the selectivity of the neuron to different stimuli. For example, one finds that the RFs of most V1 cells are elongated so that the cells respond preferentially to stimuli with certain preferred orientations (see figure 26). Similarly, the width of the ON and OFF regions within the RF determines the optimal spacing of alternating light and dark bars to elicit a response, that is, the cell's spatial frequency preference. In recent years much information has accumulated about the spatial distribution of orientation selective cells in V1 [164]. One finds that orientation preferences rotate smoothly over the surface of V1, so that approximately every 300 μm the same preference reappears, i.e. the distribution is π–periodic

in the orientation preference angle. One also finds that cells with similar feature preferences tend to arrange themselves in vertical columns so that to a first approximation the layered structure of cortex can be ignored. A more complete picture of the two-dimensional distribution of both orientation preference and ocular dominance in layers 2/3 has been obtained using optical imaging techniques [163, 165, 166]. The basic experimental procedure involves shining light directly on to the surface of the cortex. The degree of light absorption within each patch of cortex depends on the local level of activity. Thus, when an oriented image is presented across a large part of the visual field, the regions of cortex that are particularly sensitive to that stimulus will be differentiated. The topography revealed by these methods has a number of characteristic features [167], see figure 26(*b*): (i) orientation preference changes continuously as a function of cortical location, except at singularities or *pinwheels*. (ii) There exist *linear zones*, approximately 750 × 750 μm^2 in area (in primates), bounded by pinwheels, within which iso-orientation regions form parallel slabs. (iii) Linear zones tend to cross the borders of ocular dominance stripes at right angles; pinwheels tend to align with the centers of ocular dominance stripes. These experimental findings suggest that there is an underlying periodicity in the microstructure of V1 with a period of approximately 1 mm (in cats and primates). The fundamental domain of this approximate periodic (or quasiperiodic) tiling of the cortical plane is the hypercolumn [168–170], which contains two sets of orientation preferences $\theta \in [0, \pi)$ per eye, organized around a pair of singularities, see figure 26(*b*).

Long-range horizontal connections. Given the existence of a regularly repeating set of feature preference maps, how does such a periodic structure manifest itself anatomically? Two cortical circuits have been fairly well characterized: there is a local circuit operating at sub-millimeter dimensions in which cells make connections with most of their neighbors in a roughly isotropic fashion. It has been suggested that such circuitry provides a substrate for the recurrent amplification and sharpening of the tuned response of cells to local visual stimuli [25, 26], see section 5.3. The other circuit operates between hypercolumns, connecting cells separated by several millimetres of cortical tissue. The axons of these connections make terminal arbors only every 0.7 mm or so along their tracks [171, 172], such that local populations of cells are reciprocally connected in a patchy fashion to other cell populations. Optical imaging combined with labeling techniques has generated considerable information concerning the pattern of these connections in superficial layers of V1 [173–175]. In particular, one finds that the patchy horizontal connections tend to link cells with similar feature preferences. Moreover, in certain animals such as tree shrew and cat there is a pronounced anisotropy in the distribution of patchy connections, with differing iso-orientation patches preferentially connecting to neighboring patches in such a way as to form continuous contours following the topography of the retinotopic map [175]. This is illustrated schematically figure 27. That is, the major axis of the horizontal connections tends to run parallel to the visuotopic axis of the connected cells' common orientation preference. There is also a clear anisotropy in the patchy connections of primates [176, 177]. However, in these cases most of the anisotropy can be accounted for by the fact that V1 is expanded in the direction orthogonal to ocular dominance columns [177]. Nevertheless, it is possible that when this expansion is factored out, there remains a weak anisotropy correlated with orientation selectivity. Moreover, patchy feedback connections from higher-order visual areas in primates are strongly anisotropic [177]. Stimulation of a hypercolumn via lateral connections modulates rather than initiates spiking activity [178], suggesting that the long-range interactions provide local cortical processes with contextual information about the global nature of stimuli. As a consequence horizontal and feedback connections have been invoked to explain a wide variety of context-dependent visual processing phenomena [177, 179].

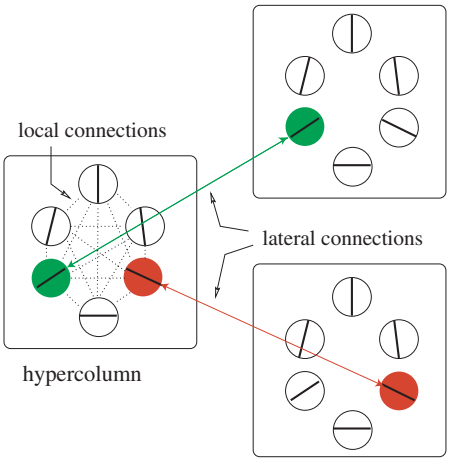

Figure 27. Schematic illustration of anisotropic horizontal connections. Orientation selective cells within a hypercolumn tend to connect to all neighbors in a roughly isotropic fashion. On the other hand, longer range horizontal connections link cells between hypercolumns with similar orientation preferences along a particular visuotopic axis.

5.2.2. Planar model of V1. One of the immediate implications of the existence of regularly repeating feature maps and patchy horizontal (or feedback) connections is that we can no longer treat the weight distribution w in the neural field equation (5.1) as Euclidean invariant. That is, we have to consider a more general weight distribution of the form

$$w(\mathbf{r}, \mathbf{r}') = w(|\mathbf{r} - \mathbf{r}'|) + \rho w^{\Delta}(\mathcal{F}(\mathbf{r}), \mathcal{F}(\mathbf{r}')), \tag{5.18}$$

where $\mathcal{F}(\mathbf{r})$ denotes a cortical feature map, w^{Δ} represents the dependence of excitatory horizontal connections on the feature preferences of the presynaptic and postsynaptic neuron populations, and ρ is a positive coupling parameter. Since horizontal connections modulate rather than drive a neuron's response to a visual stimulus, we can treat ρ as a small parameter. The local connections span a single hypercolumn, whereas the patchy horizontal connections link cells with similar feature preferences in distinct hypercolumns.

In the absence of long-range connections ($\rho = 0$), the resulting weight distribution is invariant under the action of the Euclidean group. However, the long-range connections break Euclidean symmetry due to correlations with the feature map $\mathcal{F}(\mathbf{r})$. A certain degree of symmetry still remains under the approximation that the feature map is periodic. For example, figure 26(*b*) suggests partitioning V1 into a set of hypercolumns organized around a lattice of orientation pinwheels. Therefore, suppose we treat the distribution of pinwheels as a regular planar lattice L. The resulting weight distribution for $\rho \neq 0$ is then doubly periodic with respect to L:

$$w(\mathbf{r} + \boldsymbol{\ell}, \mathbf{r}' + \boldsymbol{\ell}) = w(\mathbf{r}, \mathbf{r}') \tag{5.19}$$

for all $\boldsymbol{\ell} \in L$. Additional symmetries may also exist depending on the particular form of w^{Δ}. There are number of distinct ways in which w^{Δ} may depend on the underlying feature map $\mathcal{F}$. The first reflects the 'patchiness' of the horizontal connections that link cells with similar feature preferences. In the case of a periodic feature map, this may be implemented by taking [75–77]

$$w^{\Delta}(\mathcal{F}(\mathbf{r}), \mathcal{F}(\mathbf{r}')) = \sum_{\boldsymbol{\ell} \in \mathcal{L}} J_{\boldsymbol{\ell}} \Delta(\mathbf{r} - \mathbf{r}' - \boldsymbol{\ell}), \tag{5.20}$$

where $\Delta(\mathbf{r})$ is some localized unimodal function that is maximal when $\mathbf{r} = 0$, thus ensuring that presynaptic and postsynaptic cells with similar feature preferences are connected. The width of Δ determines the size of the patches and $J_{\boldsymbol{\ell}}, \boldsymbol{\ell} \neq 0$ is a monotonically decreasing function of $\boldsymbol{\ell}$. In this particular example, the patchy horizontal connections break continuous rotation symmetry down to the discrete rotation symmetry of the lattice. On the other hand, continuous translation symmetry (homogeneity) still holds, since w^{Δ} only depends on the relative separation $\mathbf{r} - \mathbf{r}'$ in cortex. However, if the anisotropy of horizontal connections is taken into account (figure 27), then continuous translation symmetry is broken as well. That is, the direction of anisotropy is correlated with the orientation preference map and thus rotates periodically across cortex [175]. Anisotropy can be incorporated into the model by modifying the weight distribution w^{Δ} along the following lines [20, 180]:

$$w^{\Delta}(\mathcal{F}(\mathbf{r}), \mathcal{F}(\mathbf{r}')) = \sum_{\boldsymbol{\ell} \in \mathcal{L}} J_{\boldsymbol{\ell}} \mathcal{A}_{\mathcal{F}(\mathbf{r}')}(\boldsymbol{\ell}) \Delta(\mathbf{r} - \mathbf{r}' - \boldsymbol{\ell}), \tag{5.21}$$

with

$$\mathcal{A}_{\mathcal{F}(\mathbf{r})}(\boldsymbol{\ell}) = \frac{1}{4\eta(\mathbf{r})} (H[\eta(\mathbf{r}) - |\arg \boldsymbol{\ell} - \theta(\mathbf{r})|] + H[\eta(\mathbf{r}) - |\arg \boldsymbol{\ell} - \theta(\mathbf{r}) - \pi|]), \tag{5.22}$$

where $\theta(\mathbf{r})$ denotes the orientation preference map. The second term takes account of the fact that $\theta \in [0, \pi)$ whereas $\arg \boldsymbol{\ell} \in [0, 2\pi)$. The parameter $\eta(\mathbf{r})$ determines the degree of anisotropy, that is the angular spread of the horizontal connections around the axis joining cells with similar orientation preferences. The degree of anisotropy is also likely to depend on position $\mathbf{r}$ relative to pinwheels, since populations of cells around pinwheels have zero average orientation preference so that we expect the corresponding distribution of weights to be isotropic, in contrast to cells in the linear zones of the orientation preference map, see figure 26.

We conclude that at the submillimeter length scale, there is an approximately periodic modulation of the synaptic connections. We have already explored one implication of this in a simple model of traveling waves, see section 3.3, namely that it can cause wave propagation failure [20, 101, 102]. Another consequence of such an inhomogeneity is that it can lead to the pinning of a spatially periodic pattern to the underlying lattice of pinwheels [75, 76].

5.2.3. Coupled hypercolumn model of V1. Treating the distribution of pinwheels as a regular lattice does not take into account the considerable degree of disorder in the distribution of feature preferences across cortex. One way to avoid such complexity is to collapse each hypercolumn into a single point (through some form of spatial coarse-graining) and to treat V1 as a continuum of hypercolumns [20, 181]. Thus cortical position $\mathbf{r}$ is replaced by the pair $\{\mathbf{r}, \mathcal{F}\}$ with $\mathbf{r} \in \mathbb{R}^2$ now labeling the hypercolumn at (coarse-grained) position $\mathbf{r}$ and $\mathcal{F}$ labeling the feature preferences of neurons within the hypercolumn. Let $u(\mathbf{r}, \mathcal{F}, t)$ denote the activity of a neuronal population at $(\mathbf{r}, \mathcal{F})$, and suppose that u evolves according to the neural field equation

$$\frac{\partial u(\mathbf{r}, \mathcal{F}, t)}{\partial t} = -u(\mathbf{r}, \mathcal{F}, t) + \int_{\mathbb{R}^2} \int w(\mathbf{r}, \mathcal{F} | \mathbf{r}', \mathcal{F}') F(u(\mathbf{r}', \mathcal{F}', t)) D\mathcal{F}' \mathrm{d}\mathbf{r}' \tag{5.23}$$

with $D\mathcal{F}'$ an appropriately defined measure on feature space. We decompose w into local and long-range parts by assuming that the local connections mediate interactions within a hypercolumn whereas the patchy horizontal connections mediate interactions between hypercolumns:

$$w(\mathbf{r}, \mathcal{F} | \mathbf{r}', \mathcal{F}') = \delta(\mathbf{r} - \mathbf{r}') w(\mathcal{F}, \mathcal{F}') + \rho J(|\mathbf{r} - \mathbf{r}'|) \mathcal{A}_{\mathcal{F}'}(\mathbf{r} - \mathbf{r}') w^{\Delta}(\mathcal{F}, \mathcal{F}'), \tag{5.24}$$

where $w(\mathcal{F},\mathcal{F}')$ and $w^{\Delta}(\mathcal{F},\mathcal{F}')$ represent the dependence of the local and long-range interactions on the feature preferences of the pre- and post-synaptic cell populations, and $J(\mathbf{r})$ with $J(0)=0$ is a positive function that determines the variation in the strength of the long-range interactions with cortical distance. We have also included the anisotropy factor $\mathcal{A}_{\mathcal{F}}$ of equation (5.22). The advantage of collapsing each hypercolumn to a single point in the cortical plane is that a simpler representation of the internal structure of a hypercolumn can be developed that captures the essential tuning properties of the cells as well as incorporating the modulatory effects of long-range connections.

For the sake of illustration, suppose that we identify $\mathcal{F}$ in equations (5.23) and (5.24) with the orientation preference $\theta\in[0,\pi)$ of cells within a hypercolumn. The weight distribution (5.24) is taken to have the form [20]

$$w(\mathbf{r},\theta|\mathbf{r}',\theta')=\delta(\mathbf{r}-\mathbf{r}')w(\theta-\theta')+\rho J(|\mathbf{r}-\mathbf{r}'|)\mathcal{P}(\arg(\mathbf{r}-\mathbf{r}')-\theta)w^{\Delta}(\theta-\theta') \tag{5.25}$$

with

$$\mathcal{P}(\psi)=\frac{1}{4\eta}[H(\eta-|\psi|)+H(\eta-|\psi-\pi)|]. \tag{5.26}$$

(Note that the direction $\arg(\mathbf{r}-\mathbf{r}')$ can be taken to be correlated with either θ or θ', since w^{Δ} is a sharply peaked function.) The functions $w(\theta)$ and $w^{\Delta}(\theta)$ are assumed to be even, π-periodic functions of θ, with corresponding Fourier expansions

$$\begin{aligned} w(\theta) &= w_0+2\sum_{n\geqslant 1}w_n\cos 2n\theta\\ w^{\Delta}(\theta) &= w_0^{\Delta}+2\sum_{n\geqslant 1}w_n^{\Delta}\cos 2n\theta. \end{aligned} \tag{5.27}$$

The distribution $w^{\Delta}(\theta)$ is taken to be a positive, narrowly tuned distribution with $w^{\Delta}(\theta)=0$ for all $|\theta|>\theta_c$ and $\theta_c\ll\pi/2$; the long-range connections thus link cells with similar orientation preferences. Equation (5.23) then describes a continuum of coupled ring networks, each of which corresponds to a version of the so-called ring model of orientation tuning [25, 26, 159].

If there is no orientation-dependent anisotropy then the weight distribution (5.25) is invariant with respect to the symmetry group $\mathbf{E}(2)\times\mathbf{O}(2)$ where $\mathbf{O}(2)$ is the group of rotations and reflections on the ring S^1 and $\mathbf{E}(2)$ is the Euclidean group acting on $\mathbb{R}^2$. The associated group action is

$$\begin{aligned} &\zeta\cdot(\mathbf{r},\theta)=(\zeta\mathbf{r},\theta), \qquad \zeta\in\mathbf{E}(2)\\ &\xi\cdot(\mathbf{r},\theta)=(\mathbf{r},\theta+\xi)\\ &\kappa\cdot(\mathbf{r},\theta)=(\mathbf{r},-\theta). \end{aligned} \tag{5.28}$$

Invariance of the weight distribution can be expressed as

$$\gamma\cdot w(\mathbf{r},\theta|\mathbf{r}',\theta)=w(\gamma^{-1}\cdot(\mathbf{r},\theta)|\gamma^{-1}\cdot(\mathbf{r}',\theta'))=w(\mathbf{r},\theta|\mathbf{r}',\theta')$$

for all $\gamma\in\Gamma$ where $\Gamma=\mathbf{E}(2)\times\mathbf{O}(2)$. Anisotropy reduces the symmetry group Γ to $\mathbf{E}(2)$ with the following *shift-twist* action on $\mathbb{R}^2\times S^1$ [74, 181]:

$$\begin{aligned} &\mathbf{s}\cdot(\mathbf{r},\theta)=(\mathbf{r}+\mathbf{s},\theta)\\ &\xi\cdot(\mathbf{r},\theta)=(R_{\xi}\mathbf{r},\theta+\xi)\\ &\kappa\cdot(\mathbf{r},\theta)=(R_{\kappa}\mathbf{r},-\theta), \end{aligned} \tag{5.29}$$

where R_{ξ} denotes the planar rotation through an angle ξ and R_{κ} denotes the reflection $(x_1,x_2)\mapsto(x_1,-x_2)$. It can be seen that the discrete rotation operation comprises a translation

or *shift* of the orientation preference label θ to $\theta + \xi$, together with a rotation or *twist* of the position vector $\mathbf{r}$ by the angle ξ.

It is instructive to establish explicitly the invariance of anisotropic long-range connections under shift-twist symmetry. Let us define

$$w_{\rm hoz}(\mathbf{r}, \theta|\mathbf{r}', \theta') = J(|\mathbf{r} - \mathbf{r}'|)\mathcal{P}(\arg(\mathbf{r} - \mathbf{r}') - \theta)w^{\Delta}(\theta - \theta'). \tag{5.30}$$

Translation invariance of $w_{\rm hoz}$ follows immediately from the spatial homogeneity of the interactions, which implies that

$$w_{\rm hoz}(\mathbf{r} - \mathbf{s}, \theta|\mathbf{r}' - \mathbf{s}, \theta') = w_{\rm hoz}(\mathbf{r}, \theta|\mathbf{r}', \theta').$$

Invariance with respect to a rotation by ξ follows from

$$\begin{aligned} w_{\rm hoz}(R_{-\xi}\mathbf{r}, \theta - \xi|R_{-\xi}\mathbf{r}', \theta' - \xi) &= J(|R_{-\xi}(\mathbf{r} - \mathbf{r}')|)\mathcal{P}(\arg[R_{-\xi}(\mathbf{r} - \mathbf{r}')] - \theta + \xi)w^{\Delta}(\theta - \xi - \theta' + \xi) \\ &= J(|\mathbf{r} - \mathbf{r}'|)\mathcal{P}(\arg(\mathbf{r} - \mathbf{r}') - \theta)w^{\Delta}(\theta - \theta') \\ &= w_{\rm hoz}(\mathbf{r}, \theta|\mathbf{r}', \theta'). \end{aligned}$$

We have used the conditions $|R_{\xi}\mathbf{r}| = |\mathbf{r}|$ and $\arg(R_{-\xi}\mathbf{r}) = \arg(\mathbf{r}) - \xi$. Finally, invariance under a reflection κ about the x-axis holds since

$$\begin{aligned} w_{\rm hoz}(\kappa\mathbf{r}, -\theta|\kappa\mathbf{r}', -\theta') &= J(|\kappa(\mathbf{r} - \mathbf{r}')|)\mathcal{P}(\arg[\kappa(\mathbf{r} - \mathbf{r}')] + \theta)w^{\Delta}(-\theta + \theta') \\ &= J(|\mathbf{r} - \mathbf{r}'|)\mathcal{P}(-\arg(\mathbf{r} - \mathbf{r}') + \theta)w^{\Delta}(\theta - \theta') \\ &= w_{\rm hoz}(\mathbf{r}, \theta|\mathbf{r}', \theta'). \end{aligned}$$

We have used the conditions $\arg(\kappa\mathbf{r}) = -\arg(\mathbf{r})$, $w^{\Delta}(-\theta) = w^{\Delta}(\theta)$, and $\mathcal{P}(-\psi) = \mathcal{P}(\psi)$. The fact that the weight distribution is invariant with respect to this shift-twist action has important consequences for the global dynamics of V1 in the presence of anisotropic horizontal connections.

5.3. Pattern formation in the ring model of a single hypercolumn

The analysis of pattern formation in the coupled hypercolumn model (5.23) differs considerably from the standard planar model of section 5.1. The first step is to consider a Turing instability of a single hypercolumn in the absence of long-range horizontal connections by setting $\rho = 0$. This is of interest in its own right, since the resulting pattern consists of a stationary activity bump on a compact domain. In the case of the ring model of a hypercolumn, the compact domain is the circle S^1 and the bump represents a spontaneously formed orientation tuning curve. If a weak orientation-dependent stimulus is also presented to the network, then this fixes the location of the peak of the bump. The Turing instability thus provides a mechanism for amplifying a weak oriented stimulus [25, 26, 159]. For the sake of illustration, we will focus on orientation tuning and the ring model of a hypercolumn. However, it is also possible to incorporate additional feature preferences into a hypercolumnar model with appropriate symmetries. Two examples are a spherical network model of orientation and spatial frequency tuning with $\mathbf{O}(3)$ symmetry [118], and a model of texture processing where the associated network has a non-Euclidean hyperbolic geometry [182]. Finally, note that one could also analyze orientation tuning curves (bumps) on a circular domain by restricting the weights to low-order harmonics and constructing an exact solution [141].

Ring model of orientation tuning. Suppose that we represent a hypercolumn by the following one-population ring model:

$$\frac{\partial u(\theta, t)}{\partial t} = -u(\theta, t) + \int_0^{\pi} \frac{\mathrm{d}\theta'}{\pi} w(\theta - \theta')F(u(\theta', t)) + h(\theta, t), \tag{5.31}$$

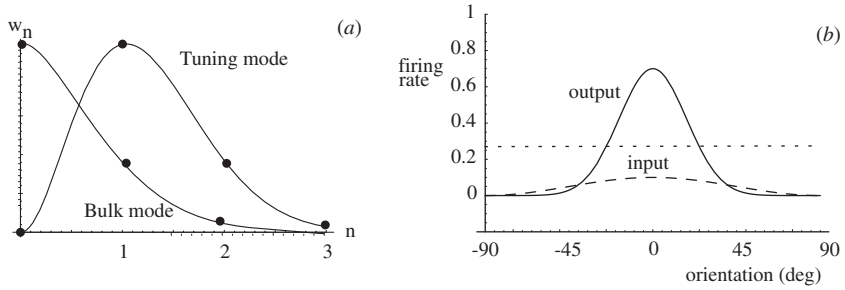

Figure 28. (*a*) Spectrum w_n of local weight distribution with a maximum at $n = 1$ (tuning mode) and a maximum at $n = 0$ (bulk mode). (*b*) Sharp orientation tuning curve in a single hypercolumn. Local recurrent excitation and inhibition amplifies a weakly modulated input from the LGN. Dotted line is the base-line output without orientation tuning.

where $u(\theta, t)$ denotes the activity at time t of a local population of cells with orientation preference $\theta \in [0, \pi)$, $w(\theta - \theta')$ is the strength of synaptic weights between cells with orientation preference θ' and θ, and $h(\theta, t)$ is an external input expressed as a function of θ. The weight distribution has the Fourier expansion (5.27). In the case of a constant input $h(\theta, t) = h_0$ there exists at least one equilibrium solution of equation (5.31), which satisfies $u_0 = w_0 F(u_0) + h_0$ with $w_0 = \int_0^\pi w(\theta) \mathrm{d}\theta/\pi$. If h_0 is sufficiently small relative to the threshold κ of the neurons then the equilibrium is unique and stable. The stability of the fixed point can be determined by setting $u(\theta, t) = u_0 + u(\theta)\mathrm{e}^{\lambda t}$ and linearizing about u_0. This leads to the eigenvalue equation

$$\lambda u(\theta) = -u(\theta) + \mu \int_0^\pi w(\theta - \theta')u(\theta')\frac{\mathrm{d}\theta'}{\pi}, \tag{5.32}$$

where $\mu = F'(u_0)$. The linear operator on the right-hand side of equation (5.32) has a discrete spectrum (since it is a compact operator) with eigenvalues

$$\lambda_n = -1 + \mu w_n, \ n \in \mathbf{Z} \tag{5.33}$$

and corresponding eigenfunctions $a(\theta) = z_n \mathrm{e}^{2\mathrm{i}n\theta} + z_n^* \mathrm{e}^{-2\mathrm{i}n\theta}$, where z_n is a complex amplitude with complex conjugate z_n^*. It follows that for sufficiently small μ, corresponding to a low activity state, $\lambda_n < 0$ for all n and the fixed point is stable. However, as μ is increased beyond a critical value μ_c the fixed point becomes unstable due to excitation of the eigenfunctions associated with the largest Fourier component of $w(\theta)$, see equation (5.27). We refer to such eigenfunctions as *excited modes*.

Two examples of discrete Fourier spectra are shown in figure 28(*a*). In the first case $w_1 = \max_m\{w_m\}$ so that $\mu_c = 1/w_1$ and the excited modes are of the form

$$u(\theta) = Z \mathrm{e}^{2\mathrm{i}\theta} + Z^* \mathrm{e}^{-2\mathrm{i}\theta} = |Z| \cos(2[\theta - \theta_0]) \tag{5.34}$$

with complex amplitude $Z = |Z|\mathrm{e}^{-2\mathrm{i}\theta_0}$. Since these modes have a single maximum around the ring, the network supports an activity profile consisting of a tuning curve centered about the point θ_0. The location of this peak is arbitrary and depends only on random initial conditions, reflecting the $\mathbf{O}(2)$ symmetry of the weight distribution w. Such a symmetry is said to be spontaneously broken by the action of the pattern forming instability. Since the dominant component is w_1, the distribution $w(\theta)$ is excitatory (inhibitory) for neurons with sufficiently similar (dissimilar) orientation preferences. (This is analogous to the Mexican hat function.) The inclusion of an additional small amplitude input $\Delta h(\theta) \sim \cos[2(\theta - \Theta)]$ explicitly breaks $\mathbf{O}(2)$ symmetry, and locks the peak of the tuning curve to the stimulus orientation, that is,

$\theta_0 = \Theta$. As one moves further away from the point of instability, the amplitude of the tuning curve increases and sharpening occurs due to the nonlinear effects of the firing rate function (2.6). This is illustrated in figure 28(*b*), where the input and output (normalized) firing rate of the excitatory population of a single hypercolumn are shown. Thus the local intracortical connections within a hypercolumn serve both to amplify and sharpen a weakly oriented input signal from the LGN [25, 26]. On the other hand, if the local level of inhibition is reduced such that w_n is a monotonically decreasing function of $|n|$ (see figure 28(*a*)), then the homogeneous fixed point undergoes a bulk instability at $\mu_c = 1/w_0$, resulting in a broadening of the tuning curve. This is consistent with experimental data demonstrating a loss of stable orientation tuning in cats with blocking of intracortical inhibition [183].

Amplitude equation and $\mathbf{O}(2)$ *symmetry.* So far we used linear theory to show how a hypercolumn can undergo a pattern forming instability through the spontaneous breaking of $\mathbf{O}(2)$ symmetry, leading to the growth of an orientation tuning curve. However, as the activity profile increases in amplitude the linear approximation breaks down and nonlinear theory is necessary in order to investigate whether or not a stable pattern ultimately forms. Sufficiently close to the bifurcation point $\mu = \mu_c$ where the homogeneous state becomes unstable, we can treat $\mu - \mu_c = \varepsilon \Delta\mu$ as a small parameter and carry out a perturbation expansion in powers of ε. The dominant temporal behavior just beyond bifurcation is the slow growth of the excited mode at a rate $\mathrm{e}^{\varepsilon \Delta\mu t}$. This motivates the introduction of a slow time-scale $\tau = \epsilon t$. Finally, assuming that the input is only weakly orientation-dependent (and possibly slowly varying), we write $h(\theta, t) = h_0 + \varepsilon^{3/2} \Delta h(\theta, \tau)$. Weakly nonlinear analysis then generates a dynamical equation for the amplitude of the pattern that can be used to investigate stability as well as the effects of a weakly biased external input [15, 84]. That is, writing the amplitude of the excited mode (5.34) as $Z = \varepsilon^{1/2} z(\tau)$ we find that (after rescaling)

$$\frac{\mathrm{d}z}{\mathrm{d}\tau} = z(\Delta\mu - \Lambda|z|^2) + h_1(\tau), \tag{5.35}$$

where $h_1 = \int_0^\pi \mathrm{e}^{-2\mathrm{i}\theta} \Delta h(\theta, \tau)\, \mathrm{d}\theta/\pi$ and

$$\Lambda = -3F'''(u_0) - 2F''(u_0)^2 \left[\frac{w_2}{1 - \mu_c w_2} + \frac{2w_0}{1 - \mu_c w_0} \right]. \tag{5.36}$$

In the case of a uniform external input ($\Delta h = 0$), the phase of z is arbitrary (reflecting a marginal state) whereas the amplitude is given by $|z| = \sqrt{|\mu - \mu_c|/\Lambda}$. It is clear that a stable marginal state will bifurcate from the homogeneous state if and only if $\Lambda < 0$. One finds that the bifurcation is indeed supercritical when the firing rate function F is a sigmoid. Now suppose that there is a weakly biased, slowly rotating input of the form $\Delta h(\theta, \tau) = C \cos(2[\theta - \omega\tau])$ with frequency ω. Then, $\overline{\Delta h} = C\mathrm{e}^{-2\mathrm{i}\omega\tau}$. Writing $z = v\, \mathrm{e}^{-2\mathrm{i}(\phi + \omega\tau)}$ (with the phase ϕ defined in a rotating frame) we obtain the pair of equations

$$\dot{v} = v(\Delta\mu - \Lambda v^2) + C\cos 2\phi, \qquad \dot{\phi} = -\omega - \frac{C}{2v} \sin(2\phi). \tag{5.37}$$

Thus, provided that ω is sufficiently small, equation (5.37) will have a stable fixed point solution in which the peak θ of the pattern is entrained to the signal. Note that when $\omega = 0$ there also exists an unstable solution for which $\phi = \pi/2$. This corresponds to the so-called illusory tuning curve analyzed in some depth by Veltz and Faugeras [86].

Considerable information about the basic structure of the amplitude equation can be deduced from the underlying symmetries of the weight distribution w. Since symmetric bifurcation theory proves an invaluable tool in analysing the coupled hypercolumn model,

we introduce some of the basic ideas here. The weight distribution $w(\theta,\theta') = w(\theta-\theta')$ is invariant with respect to the action of the group $\mathbf{O}(2)$ on S^1:

$$\gamma \cdot w(\theta,\theta') = w(\gamma^{-1}\cdot\theta, \gamma^{-1}\cdot\theta') = w(\theta,\theta'),$$

with $\gamma \in \{\xi,\kappa\}$ such that $\xi\cdot\theta = \theta+\xi$ (rotations) and $\kappa\cdot\theta = -\theta$ (reflections). Consider the corresponding action of γ on equation (5.31) for zero input $h=0$:

$$\begin{aligned}\frac{\partial u(\gamma^{-1}\theta,t)}{\partial t} &= -u(\gamma^{-1}\theta,t) + \int_0^\pi w(\gamma^{-1}\theta,\theta')F[u(\theta',t)]\frac{\mathrm{d}\theta'}{\pi}\\ &= -u(\gamma^{-1}\theta,t) + \int_0^\pi w(\theta,\gamma\theta')F[u(\theta',t)]\frac{\mathrm{d}\theta'}{\pi}\\ &= -u(\gamma^{-1}\theta,t) + \int_0^\pi w(\theta,\theta'')F[u(\gamma^{-1}\theta'',t)]\frac{\mathrm{d}\theta''}{\pi}\end{aligned}$$

since $\mathrm{d}[\gamma^{-1}\theta] = \pm\mathrm{d}\theta$ and w is $\mathbf{O}(2)$ invariant. If we rewrite equation (5.31) as an operator equation, namely,

$$\mathsf{F}[u] \equiv \frac{\mathrm{d}u}{\mathrm{d}t} - \mathsf{G}[u] = 0, \tag{5.38}$$

then it follows that $\gamma\mathsf{F}[u] = \mathsf{F}[\gamma u]$. Thus F commutes with $\gamma\in\mathbf{O}(2)$ and F is said to be equivariant with respect to the symmetry group $\mathbf{O}(2)$ [184]. The equivariance of the operator F with respect to the action of $\mathbf{O}(2)$ has major implications for the nature of solutions bifurcating from a uniform resting state u_0. Sufficiently close to the bifurcation point these states are characterized by (finite) linear combinations of eigenfunctions of the linear operator $\hat{L} = D_0\mathsf{G}$ obtained by linearizing equation (5.31) about u_0. (Since the linear operator commutes with the $\mathbf{O}(2)$ group action, the eigenfunctions consist of irreducible representations of the group, that is, the Fourier modes $u_n(\theta) = z_n\,\mathrm{e}^{2\mathrm{i}n\theta} + z_n^*\,\mathrm{e}^{-2\mathrm{i}n\theta}$.) The original infinite-dimensional equation (5.31) can then be projected on to this finite-dimensional space leading to a system of ODEs that constitute the amplitude equation (the so-called center manifold reduction). The major point to note is that the resulting amplitude equation for these modes is also equivariant with respect to $\mathbf{O}(2)$ but with a different group action. For example, suppose that there is a single bifurcating mode given by $n=1$, see equation (5.34). Under the action of $\mathbf{O}(2)$,

$$u_1(\theta+\xi) = z\,\mathrm{e}^{2\mathrm{i}\xi}\,\mathrm{e}^{2\mathrm{i}\theta} + z^*\,\mathrm{e}^{-2\mathrm{i}\xi}\,\mathrm{e}^{-2\mathrm{i}\theta}, \qquad u_1(-\theta) = z\,\mathrm{e}^{-2\mathrm{i}\theta} + z^*\,\mathrm{e}^{2\mathrm{i}\theta}. \tag{5.39}$$

It follows that the action of $\mathbf{O}(2)$ on (z,z^*) is

$$\xi\cdot(z,z^*) = (z\,\mathrm{e}^{2\mathrm{i}\xi}, z^*\,\mathrm{e}^{-2\mathrm{i}\xi}), \qquad \kappa\cdot(z,z^*) = (z^*,z). \tag{5.40}$$

Equivariance of the amplitude equation with respect to these transformations implies that quadratic and quartic terms are excluded from equation (5.35) and the quintic term is of the form $z|z|^4$. Once the basic form of the amplitude equation has been obtained, it still remains to determine the different types of patterns that are selected and their stability. In the case of the cubic amplitude equation (5.35) for a single eigenmode this is relatively straightforward. On the other hand, if more than one eigenmode is excited above the bifurcation point (due to additional degeneracies), then finding solutions is more involved. Again group theoretic methods can be used to identify the types of solution that are expected to occur.

5.4. Pattern formation in a coupled hypercolumn model

Now suppose that we switch on the horizontal connections by taking $\rho > 0$ in equation (5.25). Since ρ is small, we expect any resulting pattern to involve a spatially periodic modulation in

the tuning curves of the individual hypercolumns. In order to show this, consider the coupled hypercolumn model

$$\frac{\partial u(\mathbf{r},\theta,t)}{\partial t} = -u(\mathbf{r},\theta,t) + \int_0^\pi w(\theta-\theta')F(u(\mathbf{r},\theta',t))\frac{\mathrm{d}\theta'}{\pi} + \rho\int_{\mathbb{R}^2}\int_0^\pi w_{\mathrm{hoz}}(\mathbf{r},\theta|\mathbf{r}',\theta')F(u(\mathbf{r}',\theta',t))\frac{\mathrm{d}\theta'}{\pi}\,\mathrm{d}^2\mathbf{r}', \tag{5.41}$$

with w_{hoz} given by equation (5.30). Since we are interested in spontaneous pattern formation, we ignore any external inputs. Following along similar lines to section 5.3, it is simple to establish that in the case of isotropic weights ($\eta = \pi/2$) the coupled hypercolumn model (5.41) is equivariant with respect to the $\mathbf{E}(2)\times\mathbf{O}(2)$ group action (5.28) and for anisotropic weights it is equivariant with respect to the Euclidean shift-twist group action (5.29). We shall focus on the anisotropic case.

5.4.1. Linear stability analysis. Linearizing equation (5.41) about a uniform equilibrium u_0 leads to the eigenvalue equation

$$\lambda u = \widehat{L}u \equiv -u + \mu(w * u + \rho w_{\mathrm{hoz}} \circ u). \tag{5.42}$$

The convolution operation $*$ and $\circ$ are defined according to

$$w * u(\mathbf{r},\theta) = \int_0^\pi w(\theta-\theta')u(\mathbf{r},\theta')\frac{\mathrm{d}\theta'}{\pi} \tag{5.43}$$

and

$$w_{\mathrm{hoz}} \circ u(\mathbf{r},\theta) = \int_{\mathbb{R}^2} J(\mathbf{r}-\mathbf{r}',\theta)w^\Delta * u(\mathbf{r}',\theta)\,\mathrm{d}^2\mathbf{r}', \tag{5.44}$$

with $J(\mathbf{r},\theta) = J(|\mathbf{r}|)\mathcal{P}(\arg(\mathbf{r})-\theta)$ and $\mathcal{P}$ given by equation (5.26). Translation symmetry implies that in the case of an infinite domain, the eigenfunctions of equation (5.42) can be expressed in the form

$$u(\mathbf{r},\theta) = u(\theta-\varphi)\,\mathrm{e}^{\mathrm{i}\mathbf{k}\cdot\mathbf{r}} + \mathrm{c.c.}, \tag{5.45}$$

with $\mathbf{k} = q(\cos\varphi, \sin\varphi)$ and

$$\lambda u(\theta) = -u(\theta) + \mu[w * u(\theta) + \rho\widehat{J}(\mathbf{k},\theta+\varphi)w^\Delta * u(\theta)]. \tag{5.46}$$

Here $\widehat{J}(\mathbf{k},\theta)$ is the Fourier transform of $J(\mathbf{r},\theta)$,

$$\widehat{J}(\mathbf{k},\theta) = \int_{\mathbb{R}^2} \mathrm{e}^{-\mathrm{i}\mathbf{k}\cdot\mathbf{r}}J(\mathbf{r},\theta)\,\mathrm{d}^2\mathbf{r}. \tag{5.47}$$

Invariance of the full weight distribution under the Euclidean group action (5.29) restricts the structure of the solutions of the eigenvalue equation (5.46).

(i) The Fourier transform $\widehat{J}(\mathbf{k},\theta+\varphi)$ is independent of the direction $\varphi = \arg(\mathbf{k})$. This is easy to establish as follows:

$$\begin{aligned}\widehat{J}(\mathbf{k},\theta+\varphi) &= \int_{\mathbb{R}^2} \mathrm{e}^{-\mathrm{i}\mathbf{k}\cdot\mathbf{r}}J(\mathbf{r},\theta+\varphi)\,\mathrm{d}^2\mathbf{r}\\ &= \int_0^\infty\int_{-\pi}^{\pi} \mathrm{e}^{-\mathrm{i}qr\cos(\psi-\varphi)}J(r)\mathcal{P}(\psi-\theta-\varphi)\,\mathrm{d}\psi\, r\,\mathrm{d}r\\ &= \int_0^\infty\int_{-\pi}^{\pi} \mathrm{e}^{-\mathrm{i}qr\cos(\psi)}J(r)\mathcal{P}(\psi-\theta)\,\mathrm{d}\psi\, r\,\mathrm{d}r\\ &= \widehat{J}(q,\theta).\end{aligned} \tag{5.48}$$

Therefore, λ and $u(\theta)$ only depend on the magnitude $k = |\mathbf{k}|$ of the wave vector $\mathbf{k}$ and there is an infinite degeneracy due to rotational invariance. Note, however, that the eigenfunction (5.45) depends on $u(\theta - \varphi)$, which reflects the shift-twist action of the rotation group.

(ii) For each $\mathbf{k}$ the associated subspace of eigenfunctions

$$V_{\mathbf{k}} = \{u(\theta - \varphi)\, \mathrm{e}^{\mathrm{i}\mathbf{k}\cdot\mathbf{r}} + \text{c.c.}\} \tag{5.49}$$

decomposes into two invariant subspaces

$$V_{\mathbf{k}} = V_{\mathbf{k}}^{+} \oplus V_{\mathbf{k}}^{-}, \tag{5.50}$$

corresponding to even and odd functions, respectively:

$$V_{\mathbf{k}}^{+} = \{v \in V_{\mathbf{k}} : u(-\theta) = u(\theta)\}, \qquad V_{\mathbf{k}}^{-} = \{v \in V_{\mathbf{k}} : u(-\theta) = -u(\theta)\}. \tag{5.51}$$

This is a consequence of reflection invariance, as we now indicate. That is, let $\kappa_{\mathbf{k}}$ denote reflections about the wavevector $\mathbf{k}$ so that $\kappa_{\mathbf{k}}\mathbf{k} = \mathbf{k}$. Then $\kappa_{\mathbf{k}} u(\mathbf{r}, \theta) = u(\kappa_{\mathbf{k}}\mathbf{r}, 2\varphi - \theta) = u(\varphi - \theta)\mathrm{e}^{\mathrm{i}\mathbf{k}\cdot\mathbf{r}} + \text{c.c.}$ Since $\kappa_{\mathbf{k}}$ is a reflection, any space that it acts on decomposes into two subspaces—one on which it acts as the identity I and one on which it acts as $-I$. The even and odd functions correspond to scalar and pseudoscalar representations of the Euclidean group studied in a more general context by Bosch *et al* [185].

A further reduction of equation (5.46) can be achieved by expanding the π-periodic function $u(\theta)$ as a Fourier series with respect to θ, $u(\theta) = \sum_{n\in\mathbf{Z}} u_n \mathrm{e}^{2\mathrm{i}n\theta}$. This then leads to the matrix eigenvalue equation

$$\lambda u_n = (-1 + \mu w_n)u_n + \rho \sum_{m\in\mathbf{Z}} \widehat{J}_{n-m}(k)\mathcal{P}_{n-m} w_m^{\Delta} u_m, \tag{5.52}$$

where a factor of μ has been absorbed into ρ and

$$\widehat{J}_n(k) = \int_0^{\infty}\int_{-\pi}^{\pi} \mathrm{e}^{-\mathrm{i}kr\cos(\psi)}\, \mathrm{e}^{-2\mathrm{i}n\psi} J(r)\, \mathrm{d}\psi\, r\mathrm{d}r. \tag{5.53}$$

We have used equation (5.48) together with the Fourier series expansions (5.27) and $\mathcal{P}(\psi) = \sum_{n\in\mathbf{Z}} \mathrm{e}^{2\mathrm{i}n\psi}\mathcal{P}_n$. In the following we will take $w^{\Delta}(\theta) = \delta(\theta)$ so that $w_n^{\Delta} = 1$ for all n. Equation (5.26) implies that

$$\mathcal{P}_n = \frac{\sin 4n\eta}{4n\eta}. \tag{5.54}$$

We now exploit the experimental observation that the long-range horizontal connections appear to be weak relative to the local connections. Equation (5.52) can then be solved by expanding as a power series in ρ and using Rayleigh–Schrödinger perturbation theory. In the limiting case of zero horizontal interactions we recover the eigenvalues of the ring model, see section 5.3. In particular, suppose that $w_1 = \max\{w_n, n \in \mathbf{Z}\} > 0$. The homogeneous fixed point is then stable for sufficiently small μ, but becomes marginally stable at the critical point $\mu_c = 1/w_1$ due to the vanishing of the eigenvalue λ_1. In this case both even and odd modes $\cos(2\phi)$ and $\sin(2\phi)$ are marginally stable. Each hypercolumn spontaneously forms an orientation tuning curve of the form $u(\mathbf{r}, \theta) = A_0 \cos(2[\theta - \theta_0(\mathbf{r})])$ such that the preferred orientation $\theta_0(\mathbf{r})$ is arbitrary at each point $\mathbf{r}$. If we now switch on the lateral connections, then there is a k–dependent *splitting* of the degenerate eigenvalue λ_1 that also separates out odd and even solutions. Denoting the characteristic size of such a splitting by $\delta\lambda = \mathcal{O}(\rho)$, we impose the condition that $\delta\lambda \ll \mu\Delta w$, where $\Delta w = \min\{w_1 - w_m, m \neq 1\}$. This ensures that the perturbation does not excite states associated with other eigenvalues of the unperturbed problem. We can then restrict ourselves to calculating perturbative corrections to

the degenerate eigenvalue λ_1 and its associated eigenfunctions. Therefore, introduce the power series expansions

$$\lambda = -1 + \mu w_1 + \rho\lambda^{(1)} + \rho^2\lambda^{(2)} + \cdots \tag{5.55}$$

and

$$U_n = z_{\pm 1}\delta_{n,\pm 1} + \rho U_n^{(1)} + \rho^2 U_n^{(2)} + \cdots, \tag{5.56}$$

where $\delta_{n,m}$ is the Kronecker delta function. Substitute these expansions into the matrix eigenvalue equation (5.52) and systematically solve the resulting hierarchy of equations to successive orders in ρ using (degenerate) perturbation theory. This analysis leads to the following result valid to $\mathcal{O}(\rho)$ [74]: $\lambda = \lambda_\pm(k)$ for even (+) and odd (−) solutions where

$$\lambda_\pm(k) = -1 + \mu w_1 + \rho[\widehat{J}_0(k) \pm \mathcal{P}_2\widehat{J}_2(k)] \tag{5.57}$$

with corresponding eigenfunctions

$$u_+(\phi) = \cos(2\phi) + \rho \sum_{m\geqslant 0, m\neq 1} u_m^+(k)\cos(2m\phi) \tag{5.58}$$

$$u_-(\phi) = \sin(2\phi) + \rho \sum_{m>1} u_m^-(k)\sin(2m\phi) \tag{5.59}$$

with

$$u_0^+(k) = \frac{\mathcal{P}_1\widehat{J}_1(k)}{w_1 - w_0}, \qquad u_m^\pm(k) = \frac{\mathcal{P}_{m-1}\widehat{J}_{m-1}(k) \pm \mathcal{P}_{m+1}\widehat{J}_{m+1}(k)}{w_1 - w_m}, \qquad m > 1. \tag{5.60}$$

5.4.2. Marginal stability and doubly periodic planforms. Before using equation (5.57) to determine how the horizontal interactions modify the condition for marginal stability, we need to specify the form of the weight distribution $J(r)$. From experimental data based on tracer injections it appears that the patchy lateral connections extend several mm on either side of a hypercolumn and the field of axon terminals within a patch tends to diminish in size the further away it is from the injection site [171–174]. The total extent of the connections depends on the particular species under study. In the continuum hypercolumn model we assume that

$$J(r) = \mathrm{e}^{-(r-r_0)^2/2\xi^2}\Theta(r - r_0), \tag{5.61}$$

where ξ determines the range and r_0 the minimum distance of the (non-local) horizontal connections. There is growing experimental evidence to suggest that horizontal connections tend to have an inhibitory effect in the presence of high contrast visual stimuli but an excitatory effect at low contrasts [179]. In light of this, we take $\rho < 0$. An important point to note in the following is that it is possible to generate a pattern forming instability using a purely inhibitory weight distribution with a gap at the center. Thus it is not necessary to take $J(r)$ to be the standard Mexican hat function consisting of short-range excitation and longer range inhibition.

In figure 29 we plot $J_\pm(k) = \widehat{J}_0(k) \pm \mathcal{P}_2\widehat{J}_2(k)$ as a function of wavenumber k for the given weight distribution (5.61) and two values of $\mathcal{P}_2$. (*a*) *Strong anisotropy*: If $\eta < \pi/4$ then $J_\pm(k)$ has a unique minimum at $k = k_\pm \neq 0$ and $J_-(k_-) < J_+(k_+)$. This is shown in the limit $\eta \to 0$ for which $\mathcal{P}_2 = 1$. If $\rho < 0$ then the homogeneous state becomes marginally stable at the modified critical point $\mu_c' = \mu_c[1 - \rho J_-(k_-)]$. The corresponding marginally stable modes are of the form

$$a(\mathbf{r}, \theta) = \sum_{j=1}^{N} z_j\, \mathrm{e}^{\mathrm{i}\mathbf{k}_j\cdot\mathbf{r}} \sin(2[\theta - \varphi_j]) + \text{c.c.}, \tag{5.62}$$

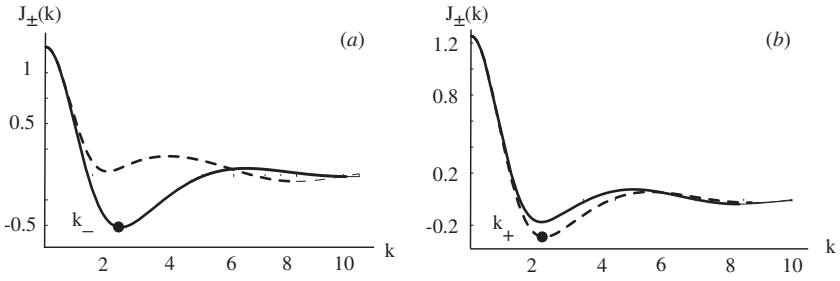

Figure 29. (*a*) Plot of functions $J_-(k)$ (solid line) and $J_+(k)$ (dashed line) in the case $\mathcal{P}_2 = 1$ (strong anisotropy) and $J(r)$ defined by (5.61) for $\xi = 1$ and $r_0 = 1$. The critical wavenumber for spontaneous pattern formation is k_-. The marginally stable eigenmodes are odd functions of θ. (*b*) Same as (*a*) except that $\mathcal{P}_2 = \sin 4\eta/4\eta$ with lateral spread of width $\eta = \pi/3$. The marginally stable eigenmodes are now even functions of θ.

where $\mathbf{k}_j = k_-(\cos\varphi_j, \sin\varphi_j)$ and z_j is a complex amplitude. These modes will be recognized as linear combinations of plane waves modulated by *odd* (phase-shifted) π-periodic functions $\sin[2(\theta - \varphi_j)]$. The infinite degeneracy arising from rotation invariance means that all modes lying on the circle$|\mathbf{k}| = k_-$ become marginally stable at the critical point. However, this can be reduced to a finite set of modes by restricting solutions to be doubly periodic functions, see section 5.4.2. (*b*) *Weak anisotropy*. If $\eta > \pi/4$ then $J_+(k_+) < J_-(k_-)$ as illustrated in figure 29(*b*) for $\eta = \pi/3$. It follows that the homogeneous state now becomes marginally stable at the critical point $\mu_c' = \mu_c[1 - \rho J_+(k_+)]$ due to excitation of *even* modes given by

$$a(\mathbf{r}, \theta) = \sum_{j=1}^{N} z_j \, \mathrm{e}^{\mathrm{i}\mathbf{k}_j \cdot \mathbf{r}} \cos(2[\theta - \varphi_j]) + \text{c.c.}, \tag{5.63}$$

where $\mathbf{k}_j = k_+(\cos(\varphi_j), \sin(\varphi_j))$.

In the above analysis we assumed that each isolated hypercolumn spontaneously forms an orientation tuning curve; the long-range horizontal connections than induce correlations between the tuning curves across the cortex. Now suppose that each hypercolumn undergoes a bulk instability for which $w_0 = \max_n\{w_n\}$. Repeating the above linear stability analysis, we find that there are only even eigenmodes, which are θ-independent (to leading order), and take the form

$$a(\mathbf{r}) = \sum_{j=1}^{N} [z_j \mathrm{e}^{\mathrm{i}\mathbf{k}_j \cdot \mathbf{r}} + \text{c.c.}]. \tag{5.64}$$

The corresponding eigenvalue equation is

$$\lambda = -1 + \mu w_0 + \rho \widehat{J_0}(k) + \mathcal{O}(\rho^2). \tag{5.65}$$

Thus $|\mathbf{k}_j| = k_0$ where k_0 is the minimum of $\widehat{J_0}(k)$. It follows that there are three classes of eigenmode that can bifurcate from the homogeneous fixed point. These are represented, respectively, by linear combinations of one of the three classes of roll pattern shown in figure 30. The $n = 0$ roll corresponds to modes of the form (5.64), and consists of alternating regions of high and low cortical activity in which individual hypercolumns do not amplify any particular orientation: the resulting patterns are said to be *non-contoured*. The $n = 1$ rolls correspond to the odd and even oriented modes of equations (5.62) and (5.63). These are constructed using a winner-take-all rule in which only the orientation with maximal response is shown at each point in the cortex (after some coarse-graining). The resulting patterns are said

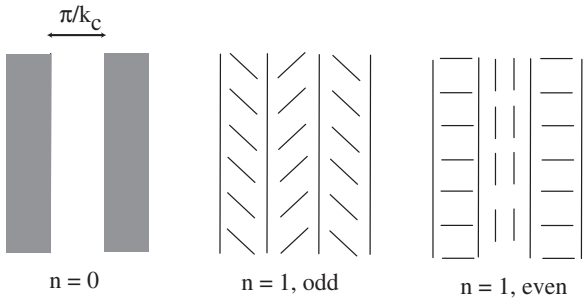

Figure 30. Three classes of rolls found in cortical pattern formation.

to be *contoured*. To lowest order in ρ one finds that the preferred orientation alternates between parallel and orthogonal directions relative to the stripe boundary in the case of even modes, whereas the preferred orientation alternates between $\pi/4$ and $-\pi/4$ relative to the stripe boundary in the case of odd modes. (One would still obtain stripes of alternating orientations θ_0 and $\theta_0 + \pi/2$ in the case of isotropic horizontal connections. However, the direction of preferred orientation θ_0 relative to the stripe boundaries would now be arbitrary so that the distinction between even and odd modes would disappear.) The particular class of mode that is selected depends on the detailed structure of the local and horizontal weights. The $n = 0$ type will be selected when the local inhibition within a hypercolumn is sufficiently weak, whereas the $n = 1$ type will occur when there is strong local inhibition, with the degree of anisotropy in the horizontal connections determining whether the patterns are even or odd.

Doubly periodic planforms. Rotation symmetry implies that in the case of non-zero critical wavenumber k_c, the space of marginally stable eigenfunctions is infinite-dimensional, consisting of all solutions of the form $u(\theta - \varphi)\, e^{i\mathbf{k}_\varphi \cdot \mathbf{r}}$ where $u(\theta)$ is either an even or odd function of θ, $\mathbf{k}_\varphi = k_c(\cos\varphi, \sin\varphi)$ and $0 \leqslant \varphi < 2\pi$. However, following the analysis of the planar model, we restrict the space of solutions of the original equation (5.41) to that of doubly-periodic functions. That is, we impose the condition $u(\mathbf{r} + \boldsymbol{\ell}, \theta) = u(\mathbf{r}, \theta)$ for every $\boldsymbol{\ell} \in L$ where L is a regular planar lattice (square, rhombic or hexagonal). Restriction to double periodicity means that the original Euclidean symmetry group is now restricted to the symmetry group of the lattice, $\Gamma = \mathbf{D}_n \dot{+} \mathbf{T}^2$, where $\mathbf{D}_n$ is the *holohedry* of the lattice, the subgroup of $\mathbf{O}(2)$ that preserves the lattice, and $\mathbf{T}^2$ is the two torus of planar translations modulo the lattice. Thus, the holohedry of the rhombic lattice is $\mathbf{D}_2$, the holohedry of the square lattice is $\mathbf{D}_4$ and the holohedry of the hexagonal lattice is $\mathbf{D}_6$. There are only a finite number of shift-twists and reflections to consider for each lattice (modulo an arbitrary rotation of the whole plane). Consequently, a finite set of specific eigenfunctions can be identified as candidate planforms, in the sense that they approximate time-independent solutions of equation (5.41) sufficiently close to the critical point where the homogeneous state loses stability.

Imposing double periodicity on the marginally stable eigenfunctions restricts the critical wavevector $\mathbf{k}$ to lie on the dual lattice. Linear combinations of eigenfunctions that generate doubly-periodic solutions corresponding to dual wave vectors of shortest length are then given by

$$u(\mathbf{r}, \theta) = \sum_{j=1}^{N} z_j u(\theta - \varphi_j)\, e^{i\mathbf{k}_j \cdot \mathbf{r}} + \text{c.c.}, \tag{5.66}$$

Table 1. Left: $\mathbf{D}_2\dot{+}\mathbf{T}^2$ action on rhombic lattice; center: $\mathbf{D}_4\dot{+}\mathbf{T}^2$ action on square lattice; right: $\mathbf{D}_6\dot{+}\mathbf{T}^2$ action on hexagonal lattice. For $u(\phi)$ even, $\epsilon = +1$; for $u(\phi)$ odd, $\epsilon = -1$. In each case the generators of $\mathbf{D}_n$ are a reflection and a rotation. For the square and hexagonal lattices, the reflection is κ, the reflection across the x axis where $\mathbf{r} = (x, y)$. For the rhombic lattice, the reflection is κ_η. The counterclockwise rotation ξ, through angles $\frac{\pi}{2}$, $\frac{\pi}{3}$, and π, is the rotation generator for the three lattices.

$\mathbf{D}_2$	Action	$\mathbf{D}_4$	Action	$\mathbf{D}_6$	Action
$\mathbf{1}$	(z_1, z_2)	$\mathbf{1}$	(z_1, z_2)	$\mathbf{1}$	(z_1, z_2, z_3)
ξ	(z_1^*, z_2^*)	ξ	(z_2^*, z_1)	ξ	(z_2^*, z_3^*, z_1^*)
κ_η	$\epsilon(z_2, z_1)$	ξ^2	(z_1^*, z_2^*)	ξ^2	(z_3, z_1, z_2)
$\kappa_\eta\xi$	$\epsilon(z_2^*, z_1^*)$	ξ^3	(z_2, z_1^*)	ξ^3	(z_1^*, z_2^*, z_3^*)
		κ	$\epsilon(z_1, z_2^*)$	ξ^4	(z_2, z_3, z_1)
		$\kappa\xi$	$\epsilon(z_2^*, z_1^*)$	ξ^5	(z_3^*, z_1^*, z_2^*)
		$\kappa\xi^2$	$\epsilon(z_1^*, z_2)$	κ	$\epsilon(z_1, z_3, z_2)$
		$\kappa\xi^3$	$\epsilon(z_2, z_1)$	$\kappa\xi$	$\epsilon(z_2^*, z_1^*, z_3^*)$
				$\kappa\xi^2$	$\epsilon(z_3, z_2, z_1)$
				$\kappa\xi^3$	$\epsilon(z_1^*, z_3^*, z_2^*)$
				$\kappa\xi^4$	$\epsilon(z_2, z_1, z_3)$
				$\kappa\xi^5$	$\epsilon(z_3^*, z_2^*, z_1^*)$
$[\theta_1, \theta_2]$	$(\mathrm{e}^{-2\pi\mathrm{i}\theta_1}z_1, \mathrm{e}^{-2\pi\mathrm{i}\theta_2}z_2)$				$(\mathrm{e}^{-2\pi\mathrm{i}\theta_1}z_1, \mathrm{e}^{-2\pi\mathrm{i}\theta_2}z_2, \mathrm{e}^{2\pi\mathrm{i}(\theta_1+\theta_2)}z_3)$

where the z_j are complex amplitudes. Here $N = 2$ for the square lattice with $\mathbf{k}_1 = \mathbf{k}_c$ and $\mathbf{k}_2 = R_{\pi/2}\mathbf{k}_c$, where R_ξ denotes rotation through an angle ξ. Similarly, $N = 3$ for the hexagonal lattice with $\mathbf{k}_1 = \mathbf{k}_c$, $\mathbf{k}_2 = R_{2\pi/3}\mathbf{k}_c$ and $\mathbf{k}_3 = R_{4\pi/3}\mathbf{k}_c = -\mathbf{k}_1 - \mathbf{k}_2$. It follows that the space of marginally stable eigenfunctions can be identified with the N–dimensional complex vector space spanned by the vectors $(z_1, \ldots, z_N) \in \mathbf{C}^N$ with $N = 2$ for square or rhombic lattices and $N = 3$ for hexagonal lattices. It can be shown that these form irreducible representations of the group $\Gamma = \mathbf{D}_n\dot{+}\mathbf{T}^2$ whose action on $\mathbf{C}^N$ is induced by the corresponding shift-twist action (5.29) of Γ on $a(\mathbf{r}, \theta)$. For example, on a hexagonal lattice, a translation $a(\mathbf{r}, \theta) \to a(\mathbf{r}-\mathbf{s}, \theta)$ induces the action

$$\gamma \cdot (z_1, z_2, z_3) = (z_1\,\mathrm{e}^{-\mathrm{i}\xi_1}, z_2\,\mathrm{e}^{-\mathrm{i}\xi_2}, z_3\,\mathrm{e}^{\mathrm{i}(\xi_1+\xi_2)}) \tag{5.67}$$

with $\xi_j = \mathbf{k}_j \cdot \mathbf{s}$, a rotation $a(\mathbf{r}, \theta) \to a(R_{-2\pi/3}\mathbf{r}, \theta - 2\pi/3)$ induces the action

$$\gamma \cdot (z_1, z_2, z_3) = (z_3, z_1, z_2), \tag{5.68}$$

and a reflection across the x-axis (assuming $\mathbf{k}_c = q_c(1, 0)$) induces the action

$$\gamma \cdot (z_1, z_2, z_3) = (z_1, z_3, z_2). \tag{5.69}$$

The full shift-twist action of $\mathbf{D}_n\dot{+}\mathbf{T}^2$ on $\mathbf{C}^N$ for the various lattices has been calculated elsewhere [74, 181] and is given in table 1.

5.4.3. Amplitude equation and Euclidean shift-twist symmetry. The next important observation is that using weakly nonlinear analysis and perturbation methods, it is possible to reduce the infinite-dimensional system (5.41) to a finite set of coupled ODEs constituting an amplitude equation for $\mathbf{z}$,

$$\frac{\mathrm{d}z_j}{\mathrm{d}t} = F_j(\mathbf{z}), \qquad j = 1, \ldots, N. \tag{5.70}$$

This has been carried out explicitly to cubic order in [20], and leads to the cubic amplitude equation (after appropriate rescalings)

$$\frac{\mathrm{d}z_l}{\mathrm{d}\tau} = \Delta\mu z_l + \gamma_2 \sum_{i,j=1}^{N} z_i^* z_j^* \delta_{\mathbf{k}_i+\mathbf{k}_j+\mathbf{k}_l,0} + 3z_l \left[\gamma_3(0)|z_l|^2 + 2\sum_{j\neq l}\gamma_3(\varphi_j - \varphi_l)|z_j|^2\right], \tag{5.71}$$

with γ_2 and γ_3 given by

$$\gamma_2 = \int_0^\pi u(\theta)u(\theta - 2\pi/3)u(\theta + 2\pi/3)\frac{\mathrm{d}\theta}{\pi} \tag{5.72}$$

and

$$\gamma_3(\varphi) = \int_0^\pi u(\theta - \varphi)^2 u(\theta)^2 \frac{\mathrm{d}\theta}{\pi}. \tag{5.73}$$

Note that for odd eigenmodes $\gamma_2 \equiv 0$ whereas for even eigenmodes $\gamma_2 \neq 0$ so that there is a quadratic term in the even mode amplitude equation in the case of a hexagonal lattice.

As in the simpler case of the ring model (section 5.3), the basic structure of the amplitude equation (5.71) including higher order terms can be determined from its equivariance under the shift-twist action of the symmetry group $\Gamma = \mathbf{D}_n \dot{+} \mathbf{T}^2$. This also allows us to systematically explore the different classes of equilibrium solutions $\mathbf{z} = (z_1, \ldots, z_N)$ of the amplitude equation (5.71) and their associated bifurcations. In order to understand how this is carried out, it is first necessary to review some basic ideas from symmetric bifurcation theory [184]. In the following we consider a general system of ODEs

$$\dot{\mathbf{z}} = F(\mathbf{z}), \tag{5.74}$$

where $\mathbf{z} \in V$ with $V = \mathbb{R}^n$ or $\mathbf{C}^n$ and F is assumed to be equivariant with respect to some symmetry group Γ acting on the vector space V. We also assume that $F(0) = 0$ so that the origin is an equilibrium that is invariant under the action of the full symmetry group Γ.

Isotropy subgroups. The symmetries of any particular equilibrium solution $\mathbf{z}$ form a subgroup called the *isotropy* subgroup of $\mathbf{z}$ defined by

$$\Sigma_{\mathbf{z}} = \{\sigma \in \Gamma : \sigma\mathbf{z} = \mathbf{z}\}. \tag{5.75}$$

More generally, we say that Σ is an isotropy subgroup of Γ if $\Sigma = \Sigma_{\mathbf{z}}$ for some $\mathbf{z} \in V$. Isotropy subgroups are defined up to some conjugacy. A group Σ is conjugate to a group $\widehat{\Sigma}$ if there exists $\sigma \in \Gamma$ such that $\widehat{\Sigma} = \sigma^{-1}\Sigma\sigma$. The *fixed-point subspace* of an isotropy subgroup Σ, denoted by $\mathrm{Fix}(\Sigma)$, is the set of points $\mathbf{z} \in V$ that are invariant under the action of Σ,

$$\mathrm{Fix}(\Sigma) = \{\mathbf{z} \in V : \sigma\mathbf{z} = \mathbf{z}\ \forall\, \sigma \in \Sigma\}. \tag{5.76}$$

Finally, the *group orbit* through a point $\mathbf{z}$ is

$$\Gamma\mathbf{z} = \{\sigma\mathbf{z} : \sigma \in \Gamma\}. \tag{5.77}$$

If $\mathbf{z}$ is an equilibrium solution of equation (5.74) then so are all other points of the group orbit (by equivariance). One can now adopt a strategy that restricts the search for solutions of equation (5.74) to those that are fixed points of a particular isotropy subgroup. In general, if a dynamical system is equivariant under some symmetry group Γ and has a solution that is a fixed point of the full symmetry group then we expect a loss of stability to occur upon variation of one or more system parameters. Typically such a loss of stability will be associated with the occurrence of new solution branches with isotropy subgroups Σ smaller than Γ. One says that the solution has spontaneously broken symmetry from Γ to Σ. Instead of a unique solution with the full set of symmetries Γ a set of symmetrically related solutions (orbits under Γ modulo Σ) each with symmetry group (conjugate to) Σ is observed.

Equivariant branching lemma. Suppose that the system of equations (5.74) has a fixed point of the full symmetry group Γ. The *equivariant branching lemma* [184] basically states that generically there exists a (unique) equilibrium solution bifurcating from the fixed point for each of the axial subgroups of Γ under the given group action—a subgroup $\Sigma \subset \Gamma$ is *axial* if $\dim \mathrm{Fix}(\Sigma) = 1$. The heuristic idea underlying this lemma is as follows. Let Σ be an axial subgroup and $\mathbf{z} \in \mathrm{Fix}(\Sigma)$. Equivariance of F then implies that

$$\sigma F(\mathbf{z}) = F(\sigma \mathbf{z}) = F(\mathbf{z}) \tag{5.78}$$

for all $\sigma \in \Sigma$. Thus $F(\mathbf{z}) \in \mathrm{Fix}(\Sigma)$ and the system of coupled ODEs (5.74) can be reduced to a single equation in the fixed point space of Σ. Such an equation is expected to support a codimension 1 bifurcation. Thus one can systematically identify the various expected primary bifurcation branches by constructing the associated axial subgroups and finding their fixed points.

Example. For the sake of illustration, consider the full symmetry group $\mathbf{D}_3$ of an equilateral triangle acting on the plane. The action is generated by the matrices (in an appropriately chosen orthonormal basis)

$$R = \begin{pmatrix} 1/2 & -\sqrt{3}/2 \\ \sqrt{3}/2 & 1/2 \end{pmatrix}, \qquad S = \begin{pmatrix} 1 & 0 \\ 0 & -1 \end{pmatrix}. \tag{5.79}$$

Here R is a rotation by $\pi/3$ and S is a reflection about the x-axis. Clearly, R fixes only the origin, while S fixes any point $(x, 0)$. We deduce that the isotropy subgroups are as follows: (i) the full symmetry group $\mathbf{D}_3$ with single fixed point $(0, 0)$; (ii) the two-element group $\mathbf{Z}_2(S)$ generated by S, which fixes the x-axis, and the groups that are conjugate to $\mathbf{Z}_2(S)$ by the rotations R and R^2; (iii) the identity matrix forms a trivial group in which every point is a fixed point. The isotropy subgroups form the hierarchy

$$\{I\} \subset \mathbf{Z}_2(S) \subset \mathbf{D}_3.$$

It follows that up to conjugacy the only axial subgroup is $\mathbf{Z}_2(S)$. Thus we expect the fixed point $(0, 0)$ to undergo a symmetry breaking bifurcation to an equilibrium that has reflection symmetry. Such an equilibrium will be given by one of the three points $\{(x, 0), R(x, 0), R^2(x, 0)\}$ on the group orbit generated by discrete rotations. Which of these states is selected will depend on initial conditions, that is, the broken rotation symmetry is hidden. Note that a similar analysis can be carried out for the symmetry group $\mathbf{D}_4$ of the square. Now, however, there are two distinct types of reflection axes: those joining the middle of opposite edges and those joining opposite vertices. Since these two types of reflections are not conjugate to each other, there are now two distinct axial subgroups.

Let us return to the amplitude equation (5.71). Since it is equivariant with respect to the shift-twist action of the group $\mathbf{D}_n \dot{+} \mathbf{T}^2$, it follows from the equivariant branching lemma that the primary patterns (planforms) bifurcating from the homogeneous state are expected to be fixed points of the corresponding axial subgroups. The calculation of these subgroups is considerably more involved than the above example [20]. Here we simply list the resulting even and odd planforms in tables 2 and 3.

5.4.4. Selection and stability of patterns. We now discuss solutions of the cubic amplitude equation (5.71) for each of the basic lattices, supplementing our analysis with additional information that can be gained using group theoretic arguments.

Table 2. Even planforms with $u(-\theta) = u(\theta)$. The hexagon solutions (0) and (π) have the same isotropy subgroup, but they are not conjugate solutions.

Lattice	Name	Planform eigenfunction
Square	Even square	$u(\theta)\cos x + u\left(\theta - \frac{\pi}{2}\right)\cos y$
	Even roll	$u(\theta)\cos x$
Rhombic	Even rhombic	$u(\theta)\cos(\mathbf{k}_1\cdot\boldsymbol{\ell}) + u(\theta-\eta)\cos(\mathbf{k}_2\cdot\boldsymbol{\ell})$
	Even roll	$u(\theta)\cos(\mathbf{k}_1\cdot\boldsymbol{\ell})$
Hexagonal	Even hexagon (0)	$u(\theta)\cos(\mathbf{k}_1\cdot\boldsymbol{\ell}) + u\left(\theta+\frac{\pi}{3}\right)\cos(\mathbf{k}_2\cdot\boldsymbol{\ell}) + u\left(\theta-\frac{\pi}{3}\right)\cos(\mathbf{k}_3\cdot\boldsymbol{\ell})$
	Even hexagon (π)	$u(\theta)\cos(\mathbf{k}_1\cdot\boldsymbol{\ell}) + u\left(\theta+\frac{\pi}{3}\right)\cos(\mathbf{k}_2\cdot\boldsymbol{\ell}) - u\left(\theta-\frac{\pi}{3}\right)\cos(\mathbf{k}_3\cdot\boldsymbol{\ell})$
	Even roll	$u(\theta)\cos(\mathbf{k}_1\cdot\boldsymbol{\ell})$

Table 3. Odd planforms with $u(-\theta) = -u(\theta)$.

Lattice	Name	Planform eigenfunction
Square	Odd square	$u(\theta)\cos x - u\left(\theta - \frac{\pi}{2}\right)\cos y$
	Odd roll	$u(\theta)\cos x$
Rhombic	Odd rhombic	$u(\theta)\cos(\mathbf{k}_1\cdot\boldsymbol{\ell}) + u(\theta-\eta)\cos(\mathbf{k}_2\cdot\boldsymbol{\ell})$
	Odd roll	$u(\theta)\cos(\mathbf{k}_1\cdot\boldsymbol{\ell})$
Hexagonal	Odd hexagon	$u(\theta)\cos(\mathbf{k}_1\cdot\boldsymbol{\ell}) + u\left(\theta+\frac{\pi}{3}\right)\cos(\mathbf{k}_2\cdot\boldsymbol{\ell})u\left(\theta-\frac{\pi}{3}\right)\cos(\mathbf{k}_3\cdot\boldsymbol{\ell})$
	Triangle	$u(\theta)\sin(\mathbf{k}_1\cdot\boldsymbol{\ell}) + u\left(\theta+\frac{\pi}{3}\right)\sin(\mathbf{k}_2\cdot\boldsymbol{\ell}) + u\left(\theta-\frac{\pi}{3}\right)\sin(\mathbf{k}_3\cdot\boldsymbol{\ell})$
	Patchwork quilt	$u\left(\theta+\frac{\pi}{3}\right)\cos(\mathbf{k}_2\cdot\boldsymbol{\ell}) - u\left(\theta-\frac{\pi}{3}\right)\cos(\mathbf{k}_3\cdot\boldsymbol{\ell})$
	Odd roll	$u(\theta)\cos(\mathbf{k}_1\cdot\boldsymbol{\ell})$

Square or rhombic lattice. First, consider planforms corresponding to a bimodal structure of the square or rhombic type ($N = 2$). Take $\mathbf{k}_1 = k_c(1,0)$ and $\mathbf{k}_2 = k_c(\cos(\varphi), \sin(\varphi))$, with $\varphi = \pi/2$ for the square lattice and $0 < \varphi < \pi/2$, $\varphi \neq \pi/3$ for a rhombic lattice. The amplitudes evolve according to a pair of equations of the form

$$\frac{\mathrm{d}z_1}{\mathrm{d}\tau} = z_1[1 - \gamma_3(0)|z_1|^2 - 2\gamma_3(\varphi)|z_2|^2], \tag{5.80}$$

$$\frac{\mathrm{d}c_2}{\mathrm{d}\hat{\tau}} = z_2[1 - \gamma_3(0)|z_2|^2 - 2\gamma_3(\varphi)|z_1|^2]. \tag{5.81}$$

Since $\gamma_3(\varphi) > 0$, three types of steady state are possible.

(1) The homogeneous state: $z_1 = z_2 = 0$.
(2) Rolls: $z_1 = \sqrt{1/\gamma_3(0)}\,\mathrm{e}^{\mathrm{i}\psi_1}$, $z_2 = 0$ or $z_1 = 0$, $z_2 = \sqrt{1/\gamma_3(0)}\,\mathrm{e}^{\mathrm{i}\psi_2}$.
(3) Squares or rhombics: $z_j = \sqrt{1/[\gamma_3(0) + 2\gamma_3(\varphi)]}\,\mathrm{e}^{\mathrm{i}\psi_j}$, $j = 1, 2$,

for arbitrary phases ψ_1, ψ_2. A standard linear stability analysis shows that if $2\gamma_3(\varphi) > \gamma_3(0)$then rolls are stable whereas the square or rhombic patterns are unstable. The opposite holds if $2\gamma_3(\theta) < \gamma_3(0)$. Note that here stability is defined with respect to perturbations with the same lattice structure.

Hexagonal lattice. Next consider planforms on a hexagonal lattice with $N = 3$, $\varphi_1 = 0$, $\varphi_2 = 2\pi/3$, $\varphi_3 = -2\pi/3$. The cubic amplitude equations take the form

$$\frac{\mathrm{d}z_j}{\mathrm{d}\tau} = z_j\left[1 - \gamma_3(0)|z_j|^2 - 2\gamma_3(2\pi/3)(|z_{j+1}|^2 + |z_{j-1}|^2)\right] + \gamma_2 z_{j+1}^* z_{j-1}^*, \tag{5.82}$$

where $j = 1, 2, 3 \bmod 3$. Unfortunately, equation (5.82) is not sufficient to determine the selection and stability of the steady-state solutions bifurcating from the homogeneous state.

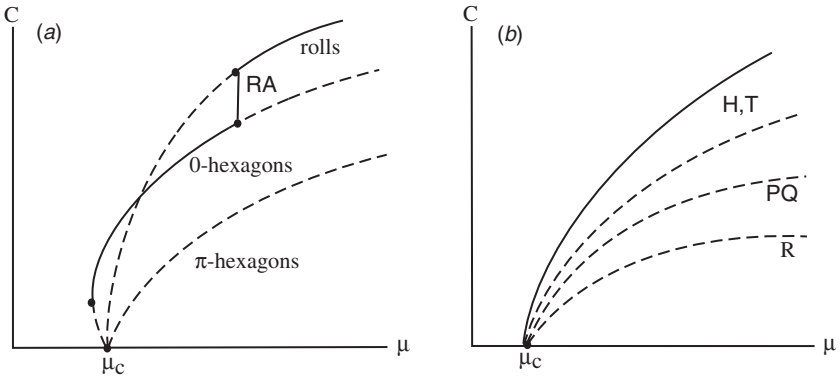

Figure 31. Bifurcation diagram showing the variation of the amplitude C with the parameter μ for patterns on a hexagonal lattice. Solid and dashed curves indicate stable and unstable solutions respectively. (*a*) Even patterns: Stable hexagonal patterns are the first to appear (subcritically) beyond the bifurcation point. Subsequently the stable hexagonal branch exchanges stability with an unstable branch of roll patterns due to a secondary bifurcation that generates rectangular patterns *RA*. Higher-order terms in the amplitude equation are needed to determine its stability. (*b*) Odd patterns: either hexagons (H) or triangles (T) are stable (depending on higher-order terms in the amplitude equation) whereas patchwork quilts (PQ) and rolls (*R*) are unstable. Secondary bifurcations (not shown) may arise from higher-order terms.

One has to carry out an *unfolding* of the amplitude equation that includes higher-order terms (quartic and quintic) in $z, \bar{z}$. One can classify the bifurcating solutions by finding the axial subgroups of the symmetry group of the lattice (up to conjugacy) as explained in the previous section. Symmetry arguments can also be used to determine the general form of higher-order contributions to the amplitude equation (5.82), and this leads to the bifurcation diagrams shown in figure 31 [74, 181]. It turns out that stability depends crucially on the sign of the coefficient $2\gamma(2\pi/3) - \gamma(0)$, which is assumed to be positive in figure 31. The subcritical bifurcation to hexagonal patterns in the case of even patterns is a consequence of an additional quadratic term appearing on the right-hand side of equation (5.82).

5.5. Geometric visual hallucinations

One of the interesting applications of the mechanism of neural pattern formation outlined above is that it provides an explanation for the occurrence of certain basic types of geometric visual hallucinations. The idea was originally developed by Ermentrout and Cowan [19] using neural field equations of the form (5.1) to represent spontaneous population activity in V1. Under the action of hallucinogenic drugs on the brain stem, they hypothesized that the level of excitability of V1 (or gain of F) is increased leading to the spontaneous formation of spatially periodic patterns of activity across V1. In figure 32 we show some examples of regular planar patterns that are interpreted as alternating regions of low and high cortical activity that cover the cortical plane in regular stripes, squares, rhomboids or hexagons. The corresponding images that would be generated by mapping such activity patterns back into visual field coordinates using the inverse of the retinotopic map shown in figure 25 are sketched in figure 32. These images bear a striking resemblance to the non-contoured form constants or basic hallucinations classified by the Chicago neurologist Kluver [186]. However, some of the form constants are better characterized as lattices of oriented edges rather than alternating regions of light and dark shading. These contoured images (as well as the non-contoured

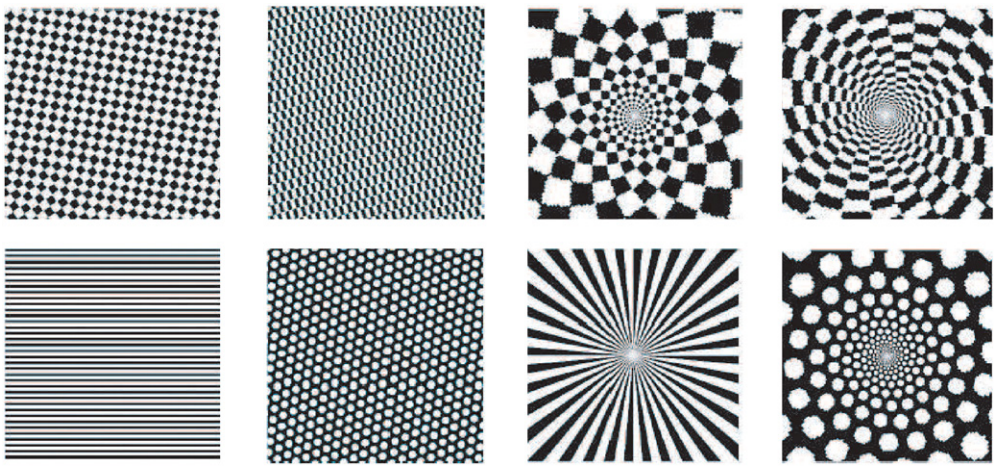

Figure 32. Left: periodic planar patterns representing alternating regions of high and low activity in V1. Right: corresponding hallucinatory images generated using the inverse retinotopic map.

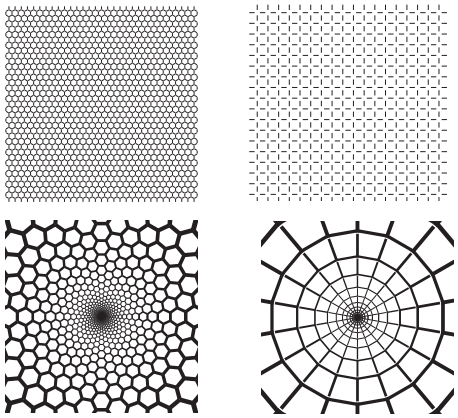

Figure 33. First row: (I) hexagonal and (II) square even-contoured V1 planforms. Second row: corresponding visual field images.

ones) can be reproduced by mapping back into visual field coordinates the contoured (non-contoured) planforms generated by the coupled hypercolumn model of section 5.4, as detailed in [74]. Two examples of contoured V1 planforms and their associated visual images are shown in figure 33.

The success of the coupled hypercolumn model in reproducing the various hallucination form constants is quite striking. However, certain caution must be exercised since there is a degree of ambiguity in how the cortical patterns should be interpreted. A working assumption is that the basic visual hallucinations can be understood without the need to invoke higher-order processing from extrastriate (higher-order) visual areas. Given this assumption, the interpretation of non-contoured planforms is relatively straightforward, since to lowest order in ρ the solutions are θ–independent and can thus be directly treated as activity patterns $a(\mathbf{r})$

with $\mathbf{r} \in \mathbb{R}^2$. At the simplest level, such patterns can be represented as contrasting regions of high and low activity depending on whether $a(\mathbf{r})$ is above or below threshold. These regions form square, triangular, or rhombic cells that tile the cortical plane as illustrated in figure 32. When such patterns are mapped back to the visual field they generate alternating light and dark contrast images. The case of contoured planforms is more subtle. At a given location $\mathbf{r}$ in V1 we have a sum of two or three sinusoids with different phases and amplitudes (see tables 2 and 3), which can be written as $a(\mathbf{r}, \phi) = A(\mathbf{r}) \cos[2\theta - 2\theta_0(\mathbf{r})]$ (to lowest order in ρ). The phase $\theta_0(\mathbf{r})$ determines the peak of the orientation tuning curve at $\mathbf{r}$ (see figure 28(*b*)). Hence the contoured solutions generally consist of iso-orientation regions or patches over which $\theta_0(\mathbf{r})$ is constant but the amplitude $A(\mathbf{r})$ varies. As in the non-contoured case these patches are either square, triangular, or rhombic in shape. The contoured patterns in figure 33 are constructed by representing each patch by a locally oriented contour centered at the point of maximal amplitude $A(\mathbf{r}_{\max})$ within the patch. Thus, a particular choice has been made in how to sample and interpret the activity patterns. For example, each patch contains a distribution of hypercolumns within the continuum model framework so that picking out a single orientation preference corresponds to a discrete sampling of the pattern. Additional difficulties arise when higher order terms in ρ are included, since it is possible to have more than one preferred orientation within a patch [181].

A very interesting recent addition to the theory of visual hallucinations has been developed by Rule *et al* [187], who present a model for flicker phosphenes, the spontaneous appearance of geometric patterns in the visual field when a subject is exposed to diffuse flickering light. The authors' model suggests that the phenomenon results from the interaction of cortical lateral inhibition with resonant periodic stimuli. They find that the best temporal frequency for eliciting phosphenes is a multiple of intrinsic (damped) oscillatory rhythms in the cortex. Moreover, using a combination of Floquet theory and the theory of pattern formation highlighted in this review, they determine how the form of the phosphenes changes with the frequency of stimulation. In particular, they show why low frequency flicker should produce hexagonal patterns while high frequency produces pinwheels, targets, and spirals.

6. Stochastic neural field theory

Experimentally it has been found that the spike trains of individual cortical neurons *in vivo* tend to be very noisy, having interspike interval (ISI) distributions that are close to Poisson [188]. The main source of intrinsic fluctuations is channel noise arising from the variability in the opening and closing of a finite number of ion channels. The resulting conductance-based model of a neuron can be formulated as a stochastic hybrid system, in which a continuous deterministic dynamics describing the time evolution of the membrane potential is coupled to a jump Markov process describing channel dynamics [189]. Extrinsic fluctuations in membrane voltage at the single cell level are predominantly due to synaptic noise. That is, cortical neurons are bombarded by thousands of synaptic inputs, many of which are not correlated with a meaningful input and can thus be treated as background synaptic noise [190]. It is not straightforward to determine how noise at the single cell level translates into noise at the population or network level. One approach is to formulate the dynamics of a population of spiking neurons in terms of the evolution of the probability density of membrane potentials—the so-called population density method [51, 52, 70, 191–197]. Typically, a very simple model of a spiking neuron is used such as the integrate-and-fire (IF) model [48] and the network topology is assumed to be either fully connected or sparsely connected. It can then be shown that under certain conditions, even though individual neurons exhibit Poisson-like statistics, the neurons fire asynchronously so that the total population activity evolves according to a

mean-field rate equation with a characteristic activation or gain function. This gain firing rate function can then be used to construct rate-based models along the lines of sections 2.4 and 2.5. Formally speaking, the asynchronous state only exists in the thermodynamic limit $N \to \infty$, where N determines the size of the population. This then suggests a possible source of intrinsic noise at the network level arises from fluctuations about the asynchronous state due to finite size effects [198–202].

Recall from section 2 that neural field equations can be derived under two basic assumptions: (i) the spike trains of individual neurons are decorrelated (asynchronous) so that the total synaptic input to a neuron is slowly varying and deterministic, and (ii) there exists a well-defined continuum limit of the resulting network rate equations. So far there has been no rigorous proof that either of these assumptions hold in large-scale spiking network models of cortex. In particular, there has been no systematic scaling up of population density methods to derive continuum neural field models that take proper account of noise-induced fluctuations and statistical correlations between neurons at multiple spatial and temporal scales. Consequently, current formulations of stochastic neural field theory tend to be phenomenologically based. One approach is to consider a Langevin version of the deterministic neural field equations involving some form of extrinsic spatiotemporal white noise [72, 203], whereas another is to treat the neural field equations as the thermodynamic limit of an underlying master equation [204–207]. In the latter case, a diffusion approximation leads to an effective Langevin equation with multiplicative noise.

In this section we review the population density method for analyzing the stochastic dynamics of a local population of IF neurons (section 6.1), following along similar lines to Gerstner and Kistler [48]. We then show in section 6.2 how finite-size effects at the level of local populations can be incorporated into stochastic versions of the rate-based models derived in section 2.4. Some applications of stochastic PDE methods to studying noise in spatially extended neural fields are discussed in section 6.3, and path integral methods are reviewed in section 6.4. For a recent survey of stochastic methods in neuroscience see [208].

6.1. Population density method and mean field theory

IF neuron models neglect details regarding the spike generation process by reducing the latter to an all-or-nothing threshold event. That is, whenever the membrane potential crosses a firing threshold, the neuron fires a spike, typically modeled as a Dirac delta function, and the membrane potential is reset to some subthreshold value. Although they are less realistic than conductance-based models, they have provided a very useful platform for exploring probabilistic models of spiking neurons [48]. In the case of the leaky integrate-and-fire (LIF) model, the conductance-based model (2.1) simplifies to the form

$$C\frac{\mathrm{d}V}{\mathrm{d}t} = -\frac{V(t)}{R} + I(t) \tag{6.1}$$

where C, R are the capacitance and resistance of the cell membrane and $I(t)$ represents the sum of synaptic and external currents. The form of the action potential is not described explicitly. Spikes are formal events characterized by the ordered sequence of firing times $\{T^m, m \in \mathbf{Z}\}$ determined by the threshold crossing conditions

$$T^m = \inf\{t, t > T^{m-1} | V(t) = \kappa, \dot{V} > 0\}, \tag{6.2}$$

where κ is the firing threshold. Immediately after firing, the potential is reset to a value $V_r < \kappa$,

$$\lim_{t \to T^m_+} V(t) = V_r. \tag{6.3}$$

For simplicity we set $V_r = 0$, $CR = \tau$ and absorb C into $I(t)$. In the following we review the population density method for analyzing stochastically driven IF neurons

[51, 52, 70, 191–197]. We begin by considering a single IF neuron and then show how the analysis can be extended to the population level as detailed in chapter 6 of Gerstner and Kistler [48]. When dealing with stochastic models we will use the standard convention of distinguishing between a random variable and the particular value it takes by writing the former as uppercase and the latter as lowercase.

Stochastically driven IF neuron. Suppose that an IF neuron receives a set of N input spike trains generated by N background neurons. Denote the arrival times of the spikes from the kth presynaptic neuron by $\{t_k^n, n \in \mathbf{Z}\}$ for $k = 1, \ldots, N$. The membrane potential evolves according to the equation

$$\frac{\mathrm{d}V}{\mathrm{d}t} = -\frac{V}{\tau} + \sum_{n\in\mathbf{Z}} \sum_{k=1}^{N} w_k \Phi\big(t - t_k^n\big), \tag{6.4}$$

together with the reset condition that $V(t^+) = 0$ whenever $V(t) = \kappa$. Here $\Phi(t)$ represents a normalized synaptic kernel and w_k is the strength or efficacy of the kth synapse. As a further simplification, we will set $\Phi(t) = \delta(t)$, where $\delta(t)$ is a Dirac delta function. Each input spike from the kth neuron then generates a change in the postsynaptic potential of the form

$$\Delta V(t) = w_k h\big(t - t_k^n\big), \qquad h(t) = \mathrm{e}^{-t/\tau} H(t),$$

where $H(t)$ is the Heaviside function. Thus each spike induces a jump of size w_k, which represents the strength of the connection or synapse from the kth presynaptic neuron, and then decays exponentially. Suppose that the spikes at synapse k are generated by an inhomogeneous Poisson process with arrival rate $\nu_k(t)$. This means that in each small time interval $[t, t + \Delta t]$ the probability that a spike arrives on the kth synapse is $\nu_k(t)\Delta t$, and each spike is uncorrelated with any other. We will derive a Fokker–Planck equation for the probability density $p(v, t)$ for V evolving according to the stochastic ODE (6.4), assuming that the neuron last fired at $t = 0$.

The probability that no spike arrives in a short time interval Δt is

$$\text{Prob}\{\text{no spike in } [t, t + \Delta t]\} = 1 - \sum_k \nu_k(t)\Delta t. \tag{6.5}$$

If no spike arrives then the membrane potential changes from $V(t) = v'$ to $V(t + \Delta t) = v'\,\mathrm{e}^{-\Delta t//\tau}$. On the other hand, if a spike arrives at synapse k, the membrane changes from v' to $v'\,\mathrm{e}^{-\Delta t//\tau} + w_k$. Therefore, given a value v' at time t, the probability density of finding a membrane potential v at time $t + \Delta t$ is

$$\begin{aligned} P(v, t + \Delta t|v', t) = &\left[1 - \Delta t \sum_k \nu_k(t)\right] \delta\left(v - v'\,\mathrm{e}^{-\Delta t/\tau}\right) \\ &+ \Delta t \sum_k \nu_k(t) \delta\left(v - v'\,\mathrm{e}^{-\Delta t/\tau} - w_k\right). \end{aligned} \tag{6.6}$$

Since the input spikes are generated by a Poisson process, it follows that the random variable $V(t)$ evolves according to a Markov process:

$$p(v, t + \Delta t) = \int P(v, t + \Delta t|v', t) p(v', t)\,\mathrm{d}v'. \tag{6.7}$$

Substituting for P using equation (6.6) shows that

$$\begin{aligned} p(v, t + \Delta) = &\left[1 - \Delta t \sum_k \nu_k(t)\right] \mathrm{e}^{\Delta t/\tau} p(\mathrm{e}^{\Delta t/\tau} v, t) \\ &+ \Delta t \sum_k \nu_k(t)\,\mathrm{e}^{\Delta t/\tau} p(\mathrm{e}^{\Delta t/\tau} v - w_k, t). \end{aligned} \tag{6.8}$$

Rearranging and taking the limit $\Delta t \to 0$ leads to the Chapman–Kolmogorov equation

$$\frac{\partial p}{\partial t} = \frac{1}{\tau}\frac{\partial}{\partial v}[vp(v,t)] + \sum_k \nu_k(t)[p(v-w_k,t) - p(v,t)]. \tag{6.9}$$

If the jump amplitudes w_k in equation (6.9) are sufficiently small, then we can formally Taylor expand the right-hand side of the master equation as a series in w_k corresponding to the so-called Kramers–Moyall expansion [209, 210]. Neglecting terms of order w_k^3 then yields the Fokker–Planck equation

$$\frac{\partial p}{\partial t} = -\frac{\partial}{\partial v}\left[-v/\tau + \sum_k \nu_k(t)w_k\right]p(v,t) + \frac{1}{2}\left[\sum_k \nu_k(t)w_k^2\right]\frac{\partial^2}{\partial v^2}p(v,t). \tag{6.10}$$

The Fokker–Planck equation determines the time evolution of the probability density of a membrane potential evolving according to the equivalent stochastic differential equation (Langevin equation)

$$\mathrm{d}V = -\frac{V(t)}{\tau}\,\mathrm{d}t + \mu(t)\,\mathrm{d}t + \sigma(t)\,\mathrm{d}W(t). \tag{6.11}$$

Here $\mu(t)$ is the mean background synaptic input

$$\mu(t) = \sum_k \nu_k(t)w_k, \tag{6.12}$$

where $W(t)$ is a Wiener process

$$\langle \mathrm{d}W(t)\rangle = 0, \qquad \langle \mathrm{d}W(t)\,\mathrm{d}W(t)\rangle = \mathrm{d}t \tag{6.13}$$

and $\sigma(t)$ determines the size of the membrane fluctuations,

$$\sigma^2(t) = \sum_k \nu_k(t)w_k^2. \tag{6.14}$$

In the case of constant rates, the resulting Langevin equation describes the well-known Ornstein–Uhlenbeck process. Note that in the derivation of the Fokker–Planck equation we have suppressed higher-order terms of the form

$$\sum_{n=3}^{\infty}\frac{(-1)^n}{n!}A_n(t)\frac{\partial^n}{\partial u^n}p(u,t),$$

with $A_n = \sum_k \nu_k(t)w_k^n$. This becomes exact in the so-called diffusion limit $w_k \to 0$ such that $\mu(t), \sigma^2(t)$ are unchanged and $A_n \to 0$ for $n \geqslant 3$.

In our derivation of the Fokker–Planck equation we neglected the threshold κ. This can be incorporated as an absorbing boundary condition

$$p(\kappa, t) \equiv 0 \text{ for all } t. \tag{6.15}$$

We can then look for the solution $p = p(v,t|v_0,0)$ of the Fokker–Planck equation assuming the initial condition $p(v,0|v_0,0) = \delta(v - v_0)$. At any time $t > 0$, the probability that the neuron has not reached threshold is

$$S(v_0,t) = \int_{-\infty}^{\kappa} p(v,t|v_0,0)\,\mathrm{d}v. \tag{6.16}$$

Let $\psi(v_0,t)\Delta t$ be the probability that the neuron fires its next spike between t and $t+\Delta t$. It follows that $\psi(v_0,t)\Delta t = S(v_0,t) - S(v_0,t+\Delta t)$ so that in the limit $\Delta t \to 0$,

$$\psi(v_0,t) = -\frac{\mathrm{d}}{\mathrm{d}t}\int_{-\infty}^{\kappa} p(v,t|v_0,0)\,\mathrm{d}v. \tag{6.17}$$

The density $\psi(v_0, t)$ determines the distribution of first passage times. When this is combined with the reset condition $v_0 = 0$, we see that it also determines the distribution of interspike intervals $\Delta^n = T^{n+1} - T^n$. Unfortunately, no general solution is known for the first passage time problem of the Ornstein–Uhlenbeck process. However, in the case of constant inputs such that $\mu(t) = \mu_0$ and $\sigma(t) = \sigma_0$, one can carry out a moment expansion of the first passage time distribution. In particular, a closed form expression for the mean first passage time (MFPT) T can be obtained [48, 210]:

$$T = \int_0^\infty t\psi(0,t)\,\mathrm{d}t = \tau\sqrt{\pi}\int_{-\sqrt{\tau}\mu_0/\sigma_0}^{(\kappa-\tau\mu_0)/\sqrt{\tau}\sigma_0} \mathrm{e}^{v^2}(1+\mathrm{erf}(v))\,\mathrm{d}v. \tag{6.18}$$

Note that various generalizations of equation (6.9) have been used to develop numerical schemes for tracking the probability density of a population of synaptically coupled spiking neurons [194, 195], which in the case of simple neuron models, can be considerably more efficient than classical Monte Carlo simulations that follow the states of each neuron in the network. On the other hand, as the complexity of the individual neuron model increases, the gain in efficiency of the population density method decreases, and this has motivated the development of a moment closure scheme that leads to a Boltzmann-like kinetic theory of IF networks [70, 197]. However, as recently shown by [196], considerable care must be taken when carrying out the dimension reduction, since it can lead to an ill-posed problem over a wide range of physiological parameters. That is, the truncated moment equations may not support a steady-state solution even though a steady-state probability density exists for the full system. Another approach is to extend the analysis of a single IF neuron using mean field theory (see below).

Homogeneous population of IF neurons. Let us first consider a large population of identical uncoupled IF neurons each being driven by a set of Poisson distributed spike trains. We assume that the kth synapse of every neuron receives a Poisson spike train with the same instantaneous rate $\nu_k(t)$, but that the spike trains across the population are statistically independent. The derivation of the Fokker–Planck equation proceeds along very similar lines to the single neuron case, and takes the form [48]

$$\frac{\partial p}{\partial t} = -\frac{\partial}{\partial v}\left[\frac{-v}{\tau} + \mu(t) + I_{\mathrm{ext}}(t)\right]p(v,t) + \frac{\sigma^2(t)}{2}\frac{\partial^2}{\partial v^2}p(v,t), \tag{6.19}$$

with $\mu(t), \sigma(t)$ given by equations (6.12) and (6.14) and $I_{\mathrm{ext}}(t)$ an external input. However, there are a number of important differences between the single neuron and population cases. First, $p(v,t)$ is now interpreted as the probability density of membrane potentials across the population of neurons. Consequently, the normalization is different. In the case of a single neuron, the integrated density $\int_{-\infty}^{\kappa} p(v,t)\mathrm{d}v \leqslant 1$ was interpreted as the probability that the neuron under consideration has not yet fired, which changes over time. On the other hand, if a neuron in the population fires, it remains part of the population so that we have the constant normalization $\int_{-\infty}^{\kappa} p(v,t)\mathrm{d}v = 1$.

The second major difference is that we now have to incorporate the reset condition explicitly in the evolution of the probability density. First, note that the Fokker–Planck equation can be rewritten as a continuity equation reflecting conservation of probability:

$$\frac{\partial}{\partial t}p(v,t) = -\frac{\partial}{\partial v}J(v,t) \quad \text{for } v \neq \kappa, 0, \tag{6.20}$$

where

$$J(v,t) = \frac{1}{\tau}\left[-v + \mu(t) + I_{\mathrm{ext}}(t)\right]p(v,t) - \frac{\sigma^2(t)}{2}\frac{\partial}{\partial v}p(v,t). \tag{6.21}$$

In a population of N neurons, the fraction of active neurons is calculated by counting the number of output spikes $n(t; t + \Delta t)$ in a small time interval Δt and dividing by N. Further division by Δt yields the population activity

$$a(t) = \lim_{\Delta t \to 0} \frac{1}{\Delta t} \frac{n(t, t + \Delta t)}{N} = \frac{1}{N} \sum_{j=1}^{N} \sum_{m} \delta(t - T_j^m). \tag{6.22}$$

The double sum runs over all firing times T_j^m of all neurons in the population. The fraction of neurons that flow across the threshold per unit time should then be equal to the population averaged activity $a(t)$, that is, $a(t) = J(\kappa, t)$. Equation (6.21) together with the absorbing boundary condition

$$p(\kappa, t) = 0 \tag{6.23}$$

implies that

$$\frac{\partial}{\partial v} p(\kappa, t) = -\frac{2a(t)}{\sigma^2(t)}. \tag{6.24}$$

Due to the reset condition, the neurons that 'disappear' across threshold are reinjected at the reset potential $v = 0$, which implies that there is a discontinuity in the flux at zero, $J(0^+, t) - J(0^-, t) = a(t)$. Continuity of p,

$$p(0^+, t) = p(0^-, t), \tag{6.25}$$

together with equation (6.21) then shows that there is a discontinuity in the first derivative of $p(v, t)$ at $v = 0$:

$$\frac{\partial}{\partial v} p(0^+, t) - \frac{\partial}{\partial v} p(0^-, t) = -\frac{2a(t)}{\sigma^2(t)}. \tag{6.26}$$

In summary, one has to solve the Fokker–Planck equation (6.19) together with the boundary conditions (6.23), (6.24), (6.25) and (6.26).

Now suppose that the background rates ν_k and external input I_{ext} are time-independent so that the total mean input

$$I_0 = I_{\text{ext}} + \sum_k \nu_k w_k \tag{6.27}$$

is a constant. The steady-state Fokker–Planck equation implies that the flux

$$J(v) = (-v/\tau + I_0) p(v) - \frac{\sigma_0^2}{2} \frac{\partial}{\partial v} p(v) \tag{6.28}$$

is constant except at $v = 0$ where it jumps by an amount a_0, which is the steady-state population activity. Taking $J(v) = 0$ for $v < 0$ we can solve equation (6.28) to obtain the Gaussian distribution

$$p_0(v) = \frac{c_1}{\sigma_0} \exp\left[-\frac{(v/\tau - I_0)^2}{\sigma_0^2} \right] \quad \text{for } v \leqslant 0 \tag{6.29}$$

for some constant c_1. However, such a solution cannot be valid for $v > 0$, since it does not satisfy the absorbing boundary condition $p_0(\kappa) = 0$. It turns out that in this domain the solution is of the form [51, 48]

$$p_0(v) = \frac{c_2}{\sigma_0^2} \exp\left[-\frac{(v/\tau - I_0)^2}{\sigma_0^2} \right] \int_v^\kappa \exp\left[\frac{(x/\tau - I_0)^2}{\sigma_0^2} \right] \mathrm{d}x, \quad \text{for } 0 < v \leqslant \kappa \tag{6.30}$$

for some constant c_2. Equation (6.28) shows that $c_2 = 2J(v)$ for $0 < v \leqslant \kappa$ with $J(v) = a_0$. Continuity of the solution at $u = 0$ implies that

$$c_1 = \frac{c_2}{\sigma_0} \int_v^\kappa \exp\left[\frac{(x/\tau - I_0)^2}{\sigma_0^2} \right] \mathrm{d}x. \tag{6.31}$$

Finally, the constant c_2 is determined by the normalization condition for p. On setting $a_0 = c_2/2\kappa$, one finds a firing rate that is consistent with the MFPT of equation (6.18):

$$a_0 = \left[\tau\sqrt{\pi} \int_{-\sqrt{\tau}I_0/\sigma_0}^{(\kappa-\tau I_0)/\sqrt{\tau}\sigma_0} \mathrm{e}^{v^2}(1+\mathrm{erf}(v))\,\mathrm{d}v \right]^{-1} \equiv F(I_0), \tag{6.32}$$

where F is the so-called gain function for the population [48, 51, 194].

Asynchronous states in recurrent networks. The above analysis assumed that the neurons were independent of each other so that the only synaptic inputs were from some stochastic background. Now suppose that we have a fully connected network such that there is an additional contribution to the synaptic input into each neuron of the form

$$I_{\mathrm{rec}}(t) = \frac{\Gamma_0}{N} \sum_{j=1}^{N} \sum_m \delta(t - T_j^m) = \Gamma_0 a(t), \tag{6.33}$$

where Γ_0/N is the strength of connection between any pair of neurons within the population, and we have used the definition (6.22) of the population activity $a(t)$. Suppose that the neuronal population is in a macroscopic state with constant activity $a(t) = a_0$, which is referred to as a state of asynchronous firing. (Formally speaking, such an asynchronous state only makes sense in the thermodynamic limit $N \to \infty$.) The steady-state activity can then be determined self-consistently from equation (6.32) by setting

$$I_0 = I_{\mathrm{text}} + \left[\sum_k \nu_k w_k + \Gamma_0 a_0 \right], \tag{6.34}$$

which leads to an effective gain function. One can also determine the stability of the asynchronous state by considering small perturbations of the steady-state probability distribution. One finds that in the limit of low noise, the asynchronous state is unstable and the neurons tend to split up into several synchronized groups that fire alternately. The overall activity then oscillates several times faster than the individual neurons [51, 192, 211]. One of the interesting properties of the asynchronous state from a computational perspective is that the population activity can respond rapidly to a step input [48]. The basic intuition behind this is that in the asynchronous state there will always be a significant fraction of neurons that are sitting close to the firing threshold so that as soon as a step increase in input current occurs they can respond immediately. However, the size of the step has to be at least as large as the noise amplitude σ, since the threshold acts as an absorbing boundary, that is, the density of neurons vanishes as $v \to \kappa$.

In the above example noise is added explicitly in the form of stochastic background activity. It is also possible for a network of deterministic neurons with fixed random connections to generate its own noise [51, 193, 212, 213]. In particular, suppose that each neuron in the population of N neurons receives input from C randomly selected neurons in the population with $C \ll N$. The assumption of sparse connectivity means that two neurons share only a small number of common inputs. Hence, if the presynaptic neurons fire stochastically then the input spike trains that arrive at distinct postsynaptic neurons can be treated as statistically independent. Since the presynaptic neurons belong to the same population, it follows that each neuron's output should itself be stochastic in the sense that it should have a sufficiently broad distribution of interspike intervals. This will tend to occur if the neurons operate in a subthreshold regime, that is, the mean total input is below threshold so that threshold crossings are fluctuation driven.

6.2. Stochastic rate-based models

Now suppose that a network of synaptically coupled spiking neurons is partitioned into a set of P homogeneous populations with $N_\alpha = \delta_\alpha N$ neurons in each population, $\alpha = 1, \ldots, P$. Let p denote the population function that maps the single neuron index $i = 1, \ldots, N$ to the population index α to which neuron i belongs: $p(i) = \alpha$. Furthermore, suppose the synaptic interactions between populations are the same for all neuron pairs, so that $\Phi_{ij} = \Phi_{\alpha\beta}/N_\beta$ for all i, j such that $p(i) = \alpha$, $p(j) = \beta$. (Relaxing this assumption can lead to additional sources of stochasticity as explored in [72]; see also the discussion below.) The synaptic current of equation (2.25) can then be decomposed as

$$u_i(t) = \int_{-\infty}^{t} \sum_\beta \Phi_{\alpha\beta}(t-t') \frac{1}{N_\beta} \sum_{j;p(j)=\beta} a_j(t')\,\mathrm{d}t' \text{ for all } \quad p(i) = \alpha. \tag{6.35}$$

It follows that after transients have decayed away, $u_i(t) = U_\alpha(t)$ with

$$U_\alpha(t) = \sum_{\beta=1}^{P} \int_{-\infty}^{t} \Phi_{\alpha\beta}(t-t') A_\beta(t')\,\mathrm{d}t', \tag{6.36}$$

and $A_\alpha(t)$ is the output activity of the αth population:

$$A_\alpha(t) = \frac{1}{N_\alpha} \sum_{j;p(j)=\beta} a_j(t). \tag{6.37}$$

If each local network is in an asynchronous state as outlined above, then we can set the population activity $A_\alpha = F_\alpha(U_\alpha)$ with F_α identified with the population gain function calculated in section 6.1. The observation that finite-size effects provide an intrinsic source of noise within a local population then suggests one way to incorporate noise into rate-based models, namely, to take the relationship between population output activity $A_\alpha(t)$ and effective synaptic current $U_\alpha(t)$ to be governed by a stochastic process.

The simplest approach is to assume that population activity is a stochastic variable $A_\alpha(t)$ evolving according to a Langevin equation of the form

$$\tau_\alpha\,\mathrm{d}A_\alpha(t) = [-A_\alpha(t) + F(U_\alpha(t))]\,\mathrm{d}t + \sigma_\alpha\,\mathrm{d}W_\alpha(t) \tag{6.38}$$

with the stochastic current $U_\alpha(t)$ satisfying the integral equation (6.36). Here $W_\alpha(t)$, $\alpha = 1, \ldots, P$ denotes a set of P independent Wiener processes with

$$\langle \mathrm{d}W_\alpha(t) \rangle = 0, \qquad \langle \mathrm{d}W_\alpha(t)\,\mathrm{d}W_\beta(t) \rangle = \delta_{\alpha,\beta}\,\mathrm{d}t, \tag{6.39}$$

and σ_α is the strength of noise in the αth population. In general, the resulting stochastic model is non-Markovian. However, if we take $\Phi_{\alpha\beta}(t) = w_{\alpha\beta}\Phi(t)$ with $\Phi(t) = \tau^{-1}\,\mathrm{e}^{-t/\tau}H(t)$, then we can convert the latter equation to the form

$$\tau\,\mathrm{d}U_\alpha(t) = \left[-U_\alpha(t) + \sum_{\beta=1}^{P} w_{\alpha\beta}A_\beta(t) \right] \mathrm{d}t. \tag{6.40}$$

It is important to note that the time constant τ_α cannot be identified directly with membrane or synaptic time constants. Instead, it determines the relaxation rate of a local population to the mean-field firing rate. In the limit $\tau_\alpha \to 0$, equations (6.38) and (6.40) reduce to a voltage-based rate model perturbed by additive noise:

$$\tau\,\mathrm{d}U_\alpha(t) = \left[-U_\alpha(t) + \sum_{\beta=1}^{P} w_{\alpha\beta}F(U_\beta(t)) \right] \mathrm{d}t + \mathrm{d}\widetilde{W}_\alpha(t). \tag{6.41}$$

Here $\widetilde{W}_\alpha(t) = \sum_{\beta=1}^{P} w_{\alpha\beta}\sigma_\beta W_\beta(t)$ so that

$$\langle \mathrm{d}\widetilde{W}_\alpha(t)\rangle = 0, \qquad \langle \mathrm{d}\widetilde{W}_\alpha(t)\,\mathrm{d}\widetilde{W}_\beta(t)\rangle = \left[\sum_\gamma w_{\alpha\gamma}w_{\beta\gamma}\sigma_\gamma^2\right]\mathrm{d}t. \tag{6.42}$$

Thus eliminating the dynamics of the firing rate leads to spatially correlated noise for the dynamics of U_α. On the other hand, in the limit $\tau \to 0$, we obtain a stochastic activity-based model

$$\tau_\alpha\,\mathrm{d}A_\alpha(t) = \left[-A_\alpha(t) + F\left(\sum_\beta w_{\alpha\beta}A_\alpha(t)\right)\right]\mathrm{d}t + \sigma_\alpha\,\mathrm{d}W_\alpha(t). \tag{6.43}$$

Here the dynamical variable A_α represents the firing rate of a local population rather than the synaptic drive as in equation (2.33). Finally, note that the reduction to a stochastic population-based rate model is less straightforward if some form of local adaptation such as synaptic depression is included (see section 2.4). In the latter case, equation (6.35) becomes

$$u_i(t) = \int_{-\infty}^{t}\sum_\beta \Phi_{\alpha\beta}(t-t')\frac{1}{N_\beta}\sum_{j;p(j)=\beta} q_j a_j \quad \text{for all } p(i)=\alpha. \tag{6.44}$$

In order to write down a population model, it would be necessary to make an additional mean-field approximation of the form

$$\frac{1}{N_\beta}\sum_{j;p(j)=\beta} q_j a_j = \frac{1}{N_\beta}\sum_{j;p(j)=\beta} q_j \frac{1}{N_\beta}\sum_{j;p(j)=\beta} a_j \equiv Q_\beta A_\beta. \tag{6.45}$$

An alternative approach to incorporating noise into the population firing rate has been developed in terms of a jump Markov process [204–207, 214]. Such a description is motivated by the idea that each local population consists of a discrete number of spiking neurons, and that finite-size effects are a source of intrinsic rather than extrinsic noise [201, 202]. The stochastic output activity of a local population of N neurons is now expressed as $A_\alpha(t) = N_\alpha(t)/(N\Delta t)$ where $N_\alpha(t)$ is the number of neurons in the αth population that fired in the time interval $[t-\Delta t, t]$, and Δt is the width of a sliding window that counts spikes. Suppose that the discrete stochastic variables $N_\alpha(t)$ evolve according to a one-step jump Markov process:

$$N_\alpha(t) \to N_\alpha(t) \pm 1: \quad \text{transition rate } \Omega_\alpha^\pm(t), \tag{6.46}$$

in which $\Omega_\alpha^\pm(t)$ are functions of $N_\alpha(t)$ and $U_\alpha(t)$ with $U_\alpha(t)$ evolving according to the integral equation (6.36) or its differential version (6.40). Thus, synaptic coupling between populations occurs via the transition rates. The transition rates are chosen in order to yield a deterministic rate-based model in the thermodynamic limit $N \to \infty$. One such choice is

$$\Omega_\alpha^+(t) = \frac{N\Delta t}{\tau_\alpha}F(U_\alpha(t)), \qquad \Omega_\alpha^-(t) = \frac{N_\alpha(t)}{\tau_\alpha}. \tag{6.47}$$

The resulting stochastic process defined by equations (6.46), (6.47) and (6.40) is an example of a stochastic hybrid system based on a piecewise deterministic process. That is, the transition rates $\Omega_\alpha^\pm(t)$ depend on $U_\alpha(t)$, with the latter itself coupled to the associated jump Markov according to equation (6.40), which is only defined between jumps, during which $U_\alpha(t)$ evolves deterministically. (Stochastic hybrid systems also arise in applications to genetic networks [215] and to excitable neuronal membranes [189, 216].) A further simplification is obtained in the limit $\tau \to 0$, since the continuous variables $U_\alpha(t)$ can be eliminated to give a pure birth–death process for the discrete variables $N_\alpha(t)$. Let $P(\mathbf{n}, t) = \mathrm{Prob}[\mathbf{N}(t) = \mathbf{n}]$ denote the probability that the network of interacting populations has configuration $\mathbf{n} = (n_1, n_2, \ldots, n_P)$

at time $t, t > 0$, given some initial distribution $P(\mathbf{n}, 0)$. The probability distribution then evolves according to the birth–death master equation

$$\frac{\mathrm{d}P(\mathrm{n},t)}{\mathrm{d}t} = \sum_{\alpha}\left[(\mathbb{E}_\alpha - 1)\big(\Omega_\alpha^-(\mathrm{n})P(\mathrm{n},t)\big) + \big(\mathbb{E}_\alpha^{-1} - 1\big)\big(\Omega_\alpha^+(\mathrm{n})P(\mathrm{n},t)\big)\right], \tag{6.48}$$

where $\Omega_\alpha^\pm(\mathrm{n}) = \Omega_\alpha^\pm(t)$ with $N_\alpha(t) = n_\alpha$ and $U_\alpha(t) = \sum_\beta w_{\alpha\beta}n_\beta/(N\Delta t)$, and $\mathbb{E}_\alpha$ is a translation operator: $\mathbb{E}_\alpha^{\pm 1}F(\mathrm{n}) = F(\mathrm{n}_{\alpha\pm})$ for any function F with $\mathrm{n}_{\alpha\pm}$ denoting the configuration with n_α replaced by $n_\alpha \pm 1$. Equation (6.48) is supplemented by the boundary conditions $P(\mathrm{n}, t) \equiv 0$ if $n_\alpha = N_\alpha + 1$ or $n_\alpha = -1$ for some α. The birth–death master equation (6.48) has been the starting point for a number of recent studies of the effects of intrinsic noise on neural fields, which adapt various methods from the analysis of chemical master equations including system size expansions and path integral representations [204–206]. However, there are a number of potential problems with the master equation formulation. First, there is no unique prescription for choosing transition rates that yield a given rate-based model in the mean-field limit. Moreover, depending on the choice of how the transition rates scale with the system size N, the statistical nature of the dynamics can be Gaussian-like [206] or Poisson-like [204, 205]. Second, the interpretation of $N_\alpha(t)$ as the number of spikes in a sliding window of width Δt implies that $\tau \gg \Delta t$ so the physical justification for taking the limit $\tau \to 0$ is not clear. Finally, for large N the master equation can be approximated by a Langevin equation with multiplicative noise (in the sense of Ito), and thus reduces to the previous class of stochastic neural field model [207].

In the above formulations, it was assumed that the main source of noise arises from fluctuations about the asynchronous state in a local population of spiking neurons. An alternative approach is to introduce noise at the single cell level. For example, consider a stochastic version of a voltage-based model

$$\tau \mathrm{d}U_i(t) = \left[-U_i(t) + \sum_{j=1}^{N_\beta} w_{ij}F_j(U_j(t))\right]\mathrm{d}t + \sigma_i\,\mathrm{d}W_i(t) \tag{6.49}$$

for $p(i) = \alpha$. Suppose that the neurons are again partitioned into local populations with $w_{ij} = w_{\alpha\beta}/N_\beta$, $F_j = F_\beta$ and $\sigma_i = \sigma_\beta$ for all i, j such that $p(i) = \alpha$, $p(j) = \beta$. It can then be proven that in the thermodynamic limit, $N \to \infty$ for fixed $\delta_\alpha = N_\alpha/N$, and provided the initial condition is drawn independently from the same distribution for all neurons of each population, the solutions of the full stochastic equation converge toward solutions U_α of the implicit population equations [217]

$$\tau \mathrm{d}U_\alpha(t) = \left[-U_\alpha(t) + \sum_{\beta=1}^{P} w_{\alpha\beta}\mathbb{E}[F_\beta(U_\beta(t))]\right]\mathrm{d}t + \sigma_\alpha\,\mathrm{d}W_\alpha(t). \tag{6.50}$$

Although the implicit equation (6.50) is difficult to solve in general, it turns out that solutions are Gaussian so that their moments satisfy a closed system of nonlinear ODEs. One advantage of the given approach is that it utilizes powerful probabilistic methods that provide a rigorous procedure to go from single neuron to population level dynamics. The analysis can also be generalized to the case of quenched disorder in the weights between individual neurons [72, 218]. One possible limitation of the approach, however, is that it rests on the assumption that the dynamics of individual neurons can be expressed in terms of a rate model, whereas conversion to a rate model might only be valid at the population level.

6.3. Patterns and waves in stochastic neural fields

In the previous section, we indicated how to incorporate noise into the rate equations introduced in section 2.4. The next step is to take an appropriate continuum limit in order

to obtain a corresponding stochastic neural field equation. For simplicity, we will focus on the simplest rate model given by equations (6.38) and (6.40). The continuum limit of equation (6.40) proceeds heuristically along similar lines to section 2.5. That is, we set $U_\alpha(t) = U(\alpha\Delta d, t), A_\alpha(t) = A(\alpha\Delta d, t)$ and $w_{\alpha\beta} = \rho\Delta\, dw(\alpha\Delta d, \beta\Delta d)$ where ρ is a density and Δd is an infinitesimal length scale. Taking the limit $\Delta d \to 0$ and absorbing ρ into w gives

$$\tau dU(x,t) = \left[-U(x,t) + \int w(x-y)A(y)\,dy\right]dt. \tag{6.51}$$

We also assume that the noise strength $\sigma_\alpha = \sigma/\sqrt{\Delta d}$ and define $W_\alpha(t)/\sqrt{\Delta d} = W(\alpha\Delta d, t)$. Taking the limit $\Delta d \to 0$ with $\tau_\alpha = \hat{\tau}$ for all α gives

$$\hat{\tau}\, dA(x,t) = [-A(x,t) + F(U(x,t))]\,dt + \sigma\, dW(x,t) \tag{6.52}$$

with

$$\langle dW(x,t)\rangle = 0, \qquad \langle dW(x,t)\, dW(y,t)\rangle = \delta(x-y)\,dt. \tag{6.53}$$

In the limit $\hat{\tau} \to 0$, we obtain a stochastic version of the scalar neural field equation (3.2), namely

$$\tau dU(x,t) = \left[-U(x,t) + \int w(x-y)F(U(y,t))\,dy\right]dt + \sigma\, d\widetilde{W}(x,t) \tag{6.54}$$

with

$$\langle d\widetilde{W}(x,t)\rangle = 0, \quad \langle d\widetilde{W}(x,t)\, d\widetilde{W}(y,t)\rangle = dt\int w(x-z)w(y-z)\,dz. \tag{6.55}$$

Similarly, in the limit $\tau \to 0$ we have a stochastic version of an activity-based neural field equation

$$\hat{\tau} dA(x,t) = \left[-A(x,t) + F\left(\int w(x-y)A(y,t)\right)dy\right]dt + dW(x,t). \tag{6.56}$$

So far there has been very little work on the dynamics of stochastic neural fields. From a numerical perspective, any computer simulation would involve rediscretizing space and then solving a time-discretized version of the resulting stochastic ODE. On the other hand, in order to investigate analytically the effects of noise on pattern forming instabilities and traveling waves, it is more useful to work directly with continuum neural fields. One can then adapt various PDE methods for studying noise in spatially extended systems [219]. We briefly describe two applications of these methods to a scalar neural field equation, one involving pattern-forming instabilities and the other front propagation [220].

6.3.1. Pattern forming instabilities. Consider the stochastic neural field equation (6.54), which is conveniently rewritten in the form

$$\tau dV(x,t) = \left[-V(x,t) + F\left(\int w(x-y)V(y,t)\,dy\right)\right]dt + dW(x,t), \tag{6.57}$$

with $U(x,t) = \int w(x-y)V(y,t)$. Following studies of pattern-forming instabilities in PDE models such as Swift–Hohenberg [221], the effects of noise close to a bifurcation can be determined by a linear stability analysis of a homogeneous solution v_0 of the deterministic neural field equation, where $v_0 = F(w_0 v_0)$, $w_0 = \int w(y)\,dy$. Linearizing equation (6.57) about v_0 gives

$$\tau dV(x,t) = [-V(x,t) + \mu\int w(x-y)V(y,t)\,dy]dt + \sigma dW(x,t), \tag{6.58}$$

where $\mu = F'(w_0 v_0)$. It is convenient to restrict x to a bounded domain, $0 \leqslant x \leqslant L$ and to introduce the discrete Fourier series

$$V(x,t) = \frac{1}{L}\sum_n \mathrm{e}^{\mathrm{i}k_n x} V_n(t), \qquad W(x,t) = \frac{1}{L}\sum_n \mathrm{e}^{\mathrm{i}k_n x} W_n(t) \tag{6.59}$$

with $k_n = 2\pi n/L$ and $W_n(t)$ an independent Wiener process such that

$$\langle \mathrm{d}W_n(t)\rangle = 0, \qquad \langle \mathrm{d}W_n(t)\,\mathrm{d}W_m(t)\rangle = L\delta_{m+n,0}\,\mathrm{d}t. \tag{6.60}$$

Fourier transforming equation (6.58) then gives

$$\tau \mathrm{d}V_n(t) = [-1 + \mu w_n]V_n(t)\,\mathrm{d}t + \sigma\,\mathrm{d}W_n(t). \tag{6.61}$$

The corresponding Fokker–Planck equation for the probability density $P[\mathbf{v},t]$, $\mathbf{v} = \{v_n, n \in \mathbf{Z}\}$, takes the form

$$\frac{\partial P}{\partial t} = -\sum_n \frac{\partial}{\partial v_n}[(-1+\mu w_n)v_n P] + \frac{L\sigma^2}{2}\sum_n \frac{\partial^2 P}{\partial v_n \partial v_{-n}}. \tag{6.62}$$

The mean Fourier coefficient $\langle V_n\rangle$ evolves as

$$\tau \frac{\mathrm{d}\langle V_n\rangle}{\mathrm{d}t} = [-1+\mu w_n]\langle V_n\rangle, \tag{6.63}$$

so for sufficiently small μ such that $\mu w_n < 1$ for all n, the average value of any perturbation decays to zero, and the finite-time dynamics can be described in terms of zero mean Gaussian fluctuations about the homogeneous state. (In the large-t limit there can be noise-induced transitions to other stable attractors of the deterministic system.) However, a noisy precursor of a pattern-forming instability can be detected by looking at the structure function S_n, which is the Fourier transform of the spatial correlation function [221]

$$C(x,t) = \frac{1}{L}\int \langle V(y,t)V(x+y,t)\rangle\,\mathrm{d}y, \tag{6.64}$$

that is

$$S_n = \frac{1}{L}\langle V_n V_{-n}\rangle. \tag{6.65}$$

The time evolution of S_n is

$$\frac{\mathrm{d}S_n}{\mathrm{d}t} = \frac{1}{L}\int v_n v_{-n}\frac{\partial P}{\partial t}\prod_m \mathrm{d}v_m. \tag{6.66}$$

Substituting for $\partial P/\partial t$ using the Fokker–Planck equation (6.62) and integrating by parts shows that

$$\frac{\mathrm{d}S_n}{\mathrm{d}t} = 2[-1+\mu w_n]S_n + \sigma^2. \tag{6.67}$$

Below the bifurcation point, we have a steady state solution for the structure function given by (in the limit $L \to \infty$ with $S_n \to S(k)$)

$$S(k) = \frac{\sigma^2}{\mu\hat{w}(k) - 1} \tag{6.68}$$

with $\hat{w}(k)$ the Fourier transform of the weight distribution $w(x)$, which is assumed to be an even function of x. Hence, $S(k)$ has a peak at the critical wavenumber k_c where $\hat{w}(k)$ has its maximum, and is the critical wavenumber of Turing patterns that form beyond the bifurcation point $\mu_c = 1/\hat{w}(k_c)$ of the deterministic system.

When the homogeneous state becomes linearly unstable the combination of additive noise and nonlinearities of the firing rate function can lead to additional effects. This has recently been found using a stochastic center manifold reduction that generates a stochastic

amplitude equation in Fourier space [203]. It turns out that in the case of spatially constant fluctuations, whereby $dW(x,t) = dW(t)$ for all x, the Turing bifurcation point μ_c is increased by an amount proportional to the variance σ^2; no such shift occurs for spatially uncorrelated noise. Another well known mechanism for shifting a bifurcation point is multiplicative noise of the Stratonovich form [219, 221]. In order to illustrate this, suppose that the additive noise term on the right-hand side of equation (6.58) is replaced by the multiplicative noise term $\sigma g(V(x,t))\, dW(x,t)$. Fourier transforming the resulting Stratonovich Langevin equation gives

$$\tau dV_n(t) = [-1 + \mu w_n]V_n(t)\, dt + \sigma \sum_m g_{n-m}(t)\, dW_m(t). \tag{6.69}$$

The associated Stratonovich Fokker–Planck equation takes the form [221]

$$\tau \frac{\partial P}{\partial t} = -\sum_l \frac{\partial}{\partial v_l}[(-1 + \mu w_l)v_n P] + \frac{\sigma^2}{2L}\sum_{l,m,q} \frac{\partial}{\partial v_l} g_{l-q} \frac{\partial}{\partial v_m} g_{m+q} P. \tag{6.70}$$

Multiplying both sides of this equation by v_n and integrating with respect to $\mathbf{v}$ leads to the following evolution equation for the mean:

$$\tau \frac{d\langle V_n\rangle}{dt} = [-1 + \mu w_n]\langle V_n\rangle + \frac{\sigma^2}{2L}\sum_{m,q}\left\langle \frac{\partial g_{n-q}}{\partial v_m} g_{m+q}\right\rangle. \tag{6.71}$$

In the simple case that $g(V) = V$, this reduces to

$$\tau \frac{d\langle V_n\rangle}{dt} = [-1 + \mu w_n + \sigma^2/(2\Delta x)]\langle V_n\rangle. \tag{6.72}$$

Note that one has to introduce a cut-off in the frequencies, which is equivalent to introducing a fundamental lattice spacing of Δx. (Alternatively, the multiplicative noise can be taken to have a finite correlation length in space.) In the continuum limit, we obtain the modified bifurcation condition

$$\mu_c = \frac{1 - \sigma^2/(2\Delta x)}{\hat{w}(k_c)}. \tag{6.73}$$

The multiplicative noise thus shifts the bifurcation point to a parameter regime where patterns do not exist in the deterministic neural field equation. Finally, note that such a shift would not occur in the case of the Ito form of multiplicative noise; the latter would occur when carrying out a diffusion approximation of the master equation formulation of stochastic neural fields [207].

6.3.2. Traveling waves. Another well known result from the study of stochastic PDEs is the non-trivial effects of multiplicative noise on front propagation in reaction–diffusion systems [219, 222]. This result carries over to the case of front propagation in a stochastic neural field, which can be established by combining the front construction carried out in section 3.1 with the multitime scale analysis of [222]. For the sake of illustration, consider a stochastic neural field equation with multiplicative noise under the Stratonovich interpretation:

$$dU = \left[-U(x,t) + \int_{-\infty}^{\infty} w(x-y)F(U(y,t))\, dy\right] dt + \varepsilon^{1/2} g(U(x,t))\, dW(x,t). \tag{6.74}$$

We assume that $dW(x,t)$ represents an independent Wiener process such that

$$\langle dW(x,t)\rangle = 0, \qquad \langle dW(x,t)\, dW(x',t')\rangle = 2C([x-x']/\lambda)\delta(t-t')\, dt\, dt'. \tag{6.75}$$

Here λ is the spatial correlation length of the noise such that $C(x/\lambda) \to \delta(x)$ in the limit $\lambda \to 0$, and ϵ determines the strength of the noise, which is assumed to be weak. The

multiplicative factor $g(U)$ could arise from some form of Langevin approximation of a neural master equation, or reflect some form of parametric noise such as threshold noise [223].

The Stratonovich version of multiplicative noise contributes to an effective shift in the mean speed of a front (assuming that it exists when $\varepsilon = 0$) due to the fact that $\langle g(U)\eta\rangle \neq 0$ even though $\langle\eta\rangle = 0$. The former average can be calculated using Novikov's theorem [224]:

$$\varepsilon^{1/2}\langle g(U(x,t))\eta(x,t)\rangle = \varepsilon C(0)\langle g'(U)g(U)\rangle. \tag{6.76}$$

The above result can be derived by Fourier transforming (6.74) and evaluating averages using the Fokker–Planck equation in Fourier space. This leads to an equation similar to (6.71), which on applying the inverse transform gives the desired result. Note that in the limit $\lambda \to 0$, $C(0) \to 1/\Delta x$ where Δx is a lattice cut-off. The method developed in [222] is to construct an approximation scheme that separates out the diffusive effects of noise from the mean drift. The first step is to rewrite the neural field equation (6.74) as

$$\mathrm{d}U(x,t) = \left[h(U(x,t)) + \int_{-\infty}^{\infty} w(x-y)F(U(y,t))\,\mathrm{d}y\right]\mathrm{d}t + \varepsilon^{1/2}R(U,x,t), \tag{6.77}$$

where

$$h(U) = -U + \varepsilon C(0)g'(U)g(U) \tag{6.78}$$

and

$$R(U,x,t) = g(U)\eta(x,t) - \varepsilon^{1/2}C(0)g'(U)g(U). \tag{6.79}$$

The stochastic process R has zero mean (so does not contribute to the effective drift) and correlation

$$\langle R(U,x,t)R(U,x',t')\rangle = \langle g(U(x,t))\eta(x,t)g(U(x',t')\eta(x',t')\rangle + \mathcal{O}(\varepsilon^{1/2}). \tag{6.80}$$

The next step in the analysis is to assume that the fluctuating term in equation (6.77) generates two distinct phenomena that occur on different time-scales: a diffusive-like displacement of the front from its uniformly translating position at long time scales, and fluctuations in the front profile around its instantaneous position at short time scales [219, 222]. In particular, following [222], we express the solution U of equation (6.77) as a combination of a fixed wave profile U_0 that is displaced by an amount $\Delta(t)$ from its uniformly translating mean position $\xi = x - c_\varepsilon t$, and a time-dependent fluctuation Φ in the front shape about the instantaneous position of the front:

$$U(x,t) = U_0(\xi - \Delta(t)) + \varepsilon^{1/2}\Phi(\xi - \Delta(t), t). \tag{6.81}$$

Here c_ε denotes the mean speed of the front. To a first approximation, the stochastic variable $\Delta(t)$ undergoes Brownian motion with a diffusion coefficient $D(\varepsilon) = \mathcal{O}(\varepsilon)$ (see below), which represents the effects of slow fluctuations, whereas Φ represents the effects of fast fluctuations. Note that expansion (6.81) is not equivalent to a standard small-noise expansion, since the wave profile U_0 implicitly depends on ε. Substituting into equation (6.77) and taking averages generates to lowest order the following deterministic equation for U_0:

$$-v_{\mathrm{eff}}(\varepsilon)\frac{\mathrm{d}U_0}{\mathrm{d}\xi} - h(U_0(\xi)) = \int_{-\infty}^{\infty} w(\xi-\xi')F(U_0(\xi'))\,\mathrm{d}\xi'. \tag{6.82}$$

We will assume that there exists a traveling wave solution for U_0. In the particular case that $g(U) = U$, such a solution can be constructed explicitly using the methods reviewed in section 3.1. For example, taking the high-gain limit so that $F(U) = H(U-\kappa)$, the effective velocity is (see also equation (3.6))

$$v_{\mathrm{eff}} = \frac{\sigma}{2\kappa}[1 - 2\kappa(1 - \epsilon C(0))], \tag{6.83}$$

which implies that multiplicative noise increases the mean speed of front propagation. Proceeding to the next order and imposing equation (6.82), we find that $\Delta(t) = \mathcal{O}(\varepsilon^{1/2})$ and

$$\mathrm{d}\Phi(\xi,t) = \widehat{L}\circ\Phi(\xi,t)\,\mathrm{d}t + \varepsilon^{-1/2}U_0'(\xi)\,\mathrm{d}\Delta(t) + \mathrm{d}R(U_0,\xi,t), \tag{6.84}$$

where $\widehat{L}$ is the non-self-adjoint linear operator

$$\widehat{L}\circ A(\xi) = v_{\mathrm{eff}}(\varepsilon)\frac{\mathrm{d}A(\xi)}{\mathrm{d}\xi} + h'(U_0(\xi))A(\xi) + \int_{-\infty}^{\infty} w(\xi-\xi')F'(U_0(\xi'))A(\xi')\,\mathrm{d}\xi' \tag{6.85}$$

for any function $A(\xi)\in L_2(\mathbb{R})$.

We can now proceed along similar lines to section 3.4.1. The non-self-adjoint linear operator $\widehat{L}$ has a 1D null space spanned by $U_0'(\xi)$, which follows from differentiating equation (6.82) with respect to ξ. We then have the solvability condition for the existence of a nontrivial solution of equation (6.85), namely, that the inhomogeneous part is orthogonal to the null space of the adjoint operator. Taking the latter to be spanned by the function $\mathcal{V}(\xi)$, we have

$$\int_{-\infty}^{\infty}\mathcal{V}(\xi)[U_0'(\xi)\,\mathrm{d}\Delta(t) + \varepsilon^{1/2}\,\mathrm{d}R(U_0,\xi,t)]\,\mathrm{d}\xi = 0. \tag{6.86}$$

Thus, $\Delta(t)$ satisfies the stochastic ODE

$$\mathrm{d}\Delta(t) = -\varepsilon^{1/2}\frac{\int_{-\infty}^{\infty}\mathcal{V}(\xi)\,\mathrm{d}R(U_0,\xi,t)\,\mathrm{d}\xi}{\int_{-\infty}^{\infty}\mathcal{V}(\xi)U_0'(\xi)\,\mathrm{d}\xi}. \tag{6.87}$$

Using the lowest order approximation $\mathrm{d}R(U_0,\xi,t) = g(U_0(\xi))\,\mathrm{d}W(\xi,t)$, we deduce that (for $\Delta(0)=0$)

$$\langle\Delta(t)\rangle = 0, \qquad \langle\Delta(t)^2\rangle = 2D(\varepsilon)t, \tag{6.88}$$

where $D(\varepsilon)$ is the effective diffusivity

$$\begin{aligned} D(\varepsilon) &= \varepsilon\langle\mathrm{d}\Delta(t)\,\mathrm{d}\Delta(t')\rangle \\ &= \varepsilon\frac{\int_{-\infty}^{\infty}\int_{-\infty}^{\infty}\mathcal{V}(\xi)\mathcal{V}(\xi')g(U_0(\mathbf{x}))g(U_0(\xi'))\langle\mathrm{d}W(\xi,t)\,\mathrm{d}W(\xi',t')\rangle\mathrm{d}\xi\mathrm{d}\xi'}{\left[\int_{-\infty}^{\infty}\mathcal{V}(\xi)U_0'(\xi)\,\mathrm{d}\xi\right]^2} \\ &= \varepsilon\frac{\int_{-\infty}^{\infty}\mathcal{V}(\xi)^2g^2(U_0(\xi))\,\mathrm{d}\xi}{\left[\int_{-\infty}^{\infty}\mathcal{V}(\xi)U_0'(\xi)\,\mathrm{d}\xi\right]^2}. \end{aligned} \tag{6.89}$$

Again, in the case $g(U)=U$ and $F(U)=H(U-\kappa)$, we can explicitly determine the function $\mathcal{V}(\xi)$ and evaluate the integral expressions for $D(\varepsilon)$, see section 3.4.1. In figure 34 we show results of a numerical simulation, which establishes that both the mean and variance of $z(t)$ are linear functions of t with slopes corresponding to $v_{\mathrm{eff}}(\epsilon)$ and $D(\epsilon)$, respectively.

6.4. Path integral representation of stochastic neural fields

Recently, Buice and Cowan [204] have used path integral methods and renormalization group theory to establish that a stochastic neural field model based on a continuum version of a birth–death master equation belongs to the universality class of directed percolation, and consequently exhibits power law behavior suggestive of many measurements of spontaneous cortical activity *in vitro* and *in vivo* [225, 226]. Although the existence of power law behavior is still controversial [227], the application of path integral methods provides yet another example of how analytical techniques familiar in the study of PDEs are being adapted to studies of continuum neural fields. (For reviews on path integral methods for stochastic differential equations see [228–230].) In this section, we indicate how a stochastic neural field can be reformulated as a path integral.

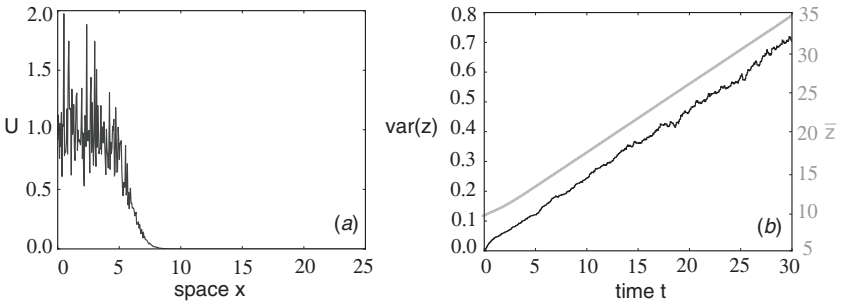

Figure 34. Numerical simulation of wavefront propagation in the stochastic scalar field equation (6.74) for Heaviside weight function $F(U) = H(U-\kappa)$ with $\kappa = 0.35$, exponential weight function $w(x) = \mathrm{e}^{-2|x|}$ and multiplicative noise $g(U) = U$. Noise strength $\epsilon = 0.005$ and $C(0) = 10$. (*a*) Snapshot of noisy traveling front. (*b*) Plot of var(z) (black curve) and mean $\bar{z}$ (gray curve) as a function of time t.

Derivation of path integral representation. For simplicity, we consider a scalar neural field with multiplicative white noise of the Ito form:

$$\mathrm{d}U = \left[-U + \int_{-\infty}^{\infty} w(x-y)F(U(y,t))\,\mathrm{d}y\right]\mathrm{d}t + g(U)\,\mathrm{d}W(x,t), \tag{6.90}$$

for $0 \leqslant t \leqslant T$ and initial condition $U(x,0) = \Phi(x)$. Discretizing both space and time with $U_{i,m} = u(m\Delta d, i\Delta t)$, $W_{i,m} = \Delta d^{-1/2} W(m\Delta d, i\Delta t)$, $\Delta d w_{mn} = w(m\Delta d, n\Delta d)$ gives

$$U_{i+1,m} - U_{i,m} = \left[-U_{i,m} + \Delta d \sum_n w_{mn} F(U_{i,n})\right]\Delta t + \frac{\sqrt{\Delta t}}{\sqrt{\Delta d}} g(U_{i,m})\,\mathrm{d}W_{i,m} + \Phi_m \delta_{i,0}, \tag{6.91}$$

with $i = 0, 1, \ldots, N$, $T = N\Delta t$ and

$$\langle \mathrm{d}W_{i,m}\rangle = 0, \qquad \langle \mathrm{d}W_{i,m}\,\mathrm{d}W_{i',m'}\rangle = \delta_{i,i'}\delta_{m,m'}. \tag{6.92}$$

Let $\mathbf{U}$ and $\mathbf{W}$ denote the vectors with components $U_{i,m}$ and $W_{i,m}$ respectively. Formally, the conditional probability density function for $\mathbf{U}$ given a particular realization of the stochastic process $\mathbf{W}$ (and initial condition Φ) is

$$P[\mathbf{U}|\mathbf{W}] = \prod_n \prod_{i=0}^{N} \delta\left(U_{i+1,m} - U_{i,m} + \left[U_{i,m} - \Delta d \sum_n w_{mn} F(U_{i,n})\right]\Delta t - \frac{\sqrt{\Delta t}}{\sqrt{\Delta d}} g(U_{i,m})\,\mathrm{d}W_{i,m} - \Phi_m \delta_{i,0}\right). \tag{6.93}$$

Inserting the Fourier representation of the Dirac delta function,

$$\delta(U_{i,m}) = \frac{1}{2\pi}\int \mathrm{e}^{-\mathrm{i}\widetilde{U}_{i,m}U_{i,m}}\,\mathrm{d}\widetilde{U}_{i,m}, \tag{6.94}$$

gives

$$P[\mathbf{U}|\mathbf{W}] = \int \prod_n \prod_{j=0}^{N} \frac{\mathrm{d}\widetilde{U}_{j,n}}{2\pi}\, \mathrm{e}^{-\mathrm{i}\sum_{i,m}\widetilde{U}_{i,m}\left(U_{i+1,m} - U_{i,m} + \left[U_{i,m} - \Delta d \sum_n w_{mn}F(U_{i,n})\right]\Delta t\right)} \times \mathrm{e}^{\mathrm{i}\sum_{i,m}\widetilde{U}_{i,m}\left(\frac{\sqrt{\Delta t}}{\sqrt{\Delta d}} g(U_{i,m})\,\mathrm{d}W_{i,m} + \Phi_m \delta_{i,0}\right)}. \tag{6.95}$$

For a Gaussian white noise process, $W_{i,n}$ has the probability density function $P(W_{i,m}) = (2\pi)^{-1/2}\,\mathrm{e}^{-W_{i,m}^2/2}$. Hence, setting

$$P[\mathbf{U}] = \int P[\mathbf{U}|\mathbf{W}] \prod_{j,n} P(W_{j,n})\,\mathrm{d}W_{j,n}$$

and performing the integration with respect to $W_{j,n}$ by completing the square, we obtain the result

$$P[\mathbf{U}] = \int \prod_{n} \prod_{j=0}^{N} \frac{\mathrm{d}\widetilde{U}_{j,n}}{2\pi}\, \mathrm{e}^{-\mathrm{i}\sum_{i,m}\widetilde{U}_{i,m}\left(U_{i+1,m}-U_{i,m}+\left[U_{i,m}-\Delta d\sum_n w_{mn}F(U_{i,n})\right]\Delta t\right)}$$
$$\times\, \mathrm{e}^{\sum_{i,m}\left([\mathrm{i}\widetilde{U}_{i,m}]^2 g^2(U_{i,m})\frac{\Delta t}{2\Delta d}+\mathrm{i}\widetilde{U}_{i,m}\Phi_m\delta_{i,0}\right)}. \tag{6.96}$$

Finally, taking the continuum limits $\Delta d \to 0$, and $\Delta t \to 0$, $N \to \infty$ for fixed T with $U_{i,m} \to U(x,t)$ and $\mathrm{i}\widetilde{U}_{i,m}/\Delta d \to \widetilde{U}(x,t)$ gives the following path integral representation of a stochastic neural field:

$$P[U] = \int \mathcal{D}\widetilde{U}\, \mathrm{e}^{-S[U,\widetilde{U}]} \tag{6.97}$$

with

$$S[U,\widetilde{U}] = \int \mathrm{d}x \int_0^T \mathrm{d}t\, \widetilde{U}(x,t)\left[U_t(x,t) + U(x,t) - \int w(x-y)F(U(y,t))\,\mathrm{d}y\right.$$
$$\left. -\Phi(x)\delta(t) - \frac{1}{2}\widetilde{U}(x,t)g^2(U(x,t))\right]. \tag{6.98}$$

Generating functional. Given the probability functional $P[U]$, we can write down path integral
representations of various moments of the stochastic field U. For example, the mean field is

$$\langle\langle U(x,t)\rangle\rangle = \int \mathcal{D}U\mathcal{D}\widetilde{U}\, U(x,t)\,\mathrm{e}^{-S[U,\widetilde{U}]}, \tag{6.99}$$

whereas the two-point correlation is

$$\langle\langle U(x,t)U(x',t')\rangle\rangle = \int \mathcal{D}U\mathcal{D}\widetilde{U}\, U(x,t)U(x',t')\,\mathrm{e}^{-S[U,\widetilde{U}]}. \tag{6.100}$$

Another important characterization of the stochastic neural field is how the mean activity (and other moments) respond to small external inputs (linear response theory). First, suppose that we add a small external source term $h(x,t)$ on to the right-hand side of the deterministic version ($g \equiv 0$) of the field equation (6.90). Linearizing about the time-dependent solution $U(x,t)$ of the unperturbed equation ($h \equiv 0$) leads to an inhomogeneous linear equation for the perturbed solution $\varphi(x,t) = U^h(x,t) - U(x,t)$:

$$\frac{\partial\varphi}{\partial t} = -\varphi(x,t) + \int_{-\infty}^{\infty} w(x-y)F'(U(y,t))\varphi(y,t)\,\mathrm{d}y + h(x,t). \tag{6.101}$$

Introducing the deterministic Green's function or propagator $\mathcal{G}_0(x,t;x',t')$ according to the adjoint equation

$$-\frac{\partial\mathcal{G}_0}{\partial t'} = -\mathcal{G}_0(x,t;x',t') + F'(U(x',t))\int_{-\infty}^{\infty} w(x'-y)\mathcal{G}_0(x,t;y,t')\,\mathrm{d}y + \delta(x-x')\delta(t-t'), \tag{6.102}$$

with $\mathcal{G}_0(x,t;x',t') = 0$ for $t \leqslant t'$ (causality), we can express the linear response as

$$\varphi(x,t) = \int_{-\infty}^{\infty} \mathrm{d}x' \int^{t} \mathrm{d}t' \mathcal{G}_0(x,t;x',t') h(x',t'). \tag{6.103}$$

In other words, in terms of functional derivatives

$$\frac{\delta U(x,t)}{\delta h(x',t')} = \mathcal{G}_0(x,t;x',t'). \tag{6.104}$$

Now suppose that we add a small source term within the path integral representation (6.97). This corresponds to adding a term $\int \mathrm{d}x \int \mathrm{d}t\, h(x,t)\widetilde{U}(x,t)$ to the action (6.98). The associated Green's function for the full stochastic model is defined according to

$$\mathcal{G}(x,t;x',t') \equiv \frac{\delta \langle\langle U(x,t)\rangle\rangle}{\delta h(x',t')} = \langle\langle U(x,t)\widetilde{U}(x',t')\rangle\rangle \tag{6.105}$$

with

$$\lim_{t \to t'_+} \mathcal{G}(x,t;x',t') = \delta(x-x')$$

and $\mathcal{G}(x,t;x',t') = 0$ for $t \leqslant t'$. The above analysis motivates the introduction of the generating functional

$$Z[J,\widetilde{J}] = \int \mathcal{D}U\mathcal{D}\widetilde{U}\, \mathrm{e}^{-S[U,\widetilde{U}]}\, \mathrm{e}^{\int \mathrm{d}x \int_0^T \mathrm{d}t [\widetilde{U}(x,t)J(x,t) + \widetilde{J}(x,t)U(x,t)]}. \tag{6.106}$$

Various moments of physical interest can then be obtained by taking functional derivatives with respect to the 'current sources' $\boldsymbol{J}, \widetilde{\boldsymbol{J}}$. For example,

$$\langle\langle U(x,t)\rangle\rangle = \frac{\delta}{\delta \widetilde{J}(x,t)} Z[J,\widetilde{J}]\bigg|_{J=\widetilde{J}=0} \tag{6.107}$$

$$\langle\langle U(x,t)U(x',t')\rangle\rangle = \frac{\delta}{\delta \widetilde{J}(x,t)} \frac{\delta}{\delta \widetilde{J}(x',t')} Z[J,\widetilde{J}]\bigg|_{J=\widetilde{J}=0} \tag{6.108}$$

$$\langle\langle U(x,t)\widetilde{U}(x',t')\rangle\rangle = \frac{\delta}{\delta \widetilde{J}(x,t)} \frac{\delta}{\delta J(x',t')} Z[J,\widetilde{J}]\bigg|_{J=\widetilde{J}=0}. \tag{6.109}$$

Perturbation theory. Suppose for the moment that the firing-rate function is linear, $F(U) = \mu U$, and consider the so-called free generating functional $Z_0[J,\widetilde{J}]$ obtained from equation (6.106) by taking the action $S \to S_0$ with

$$\begin{aligned} S_0[U,\widetilde{U}] &= \int \mathrm{d}x \int_0^T \mathrm{d}t\, \widetilde{U}(x,t) \left[\dot{U}(x,t) + U(x,t) - \mu \int w(x-y)U(y,t)\,\mathrm{d}y \right] \\ &= \int \mathrm{d}x \int \mathrm{d}x' \int_0^T \mathrm{d}t \int_0^T \mathrm{d}t'\, \widetilde{U}(x,t)\mathcal{G}_0^{-1}(x,t;x',t')U(x',t'). \end{aligned} \tag{6.110}$$

Here $\mathcal{G}_0^{-1}$ is the inverse of the propagator $\mathcal{G}_0(x,t;x',t') = G(x-x',t-t')$ with $G(x,t)$ satisfying the linear homogeneous equation (for $F'(U) = \mu$)

$$\frac{\partial G}{\partial t} = -G(x,t) + \beta \int_{-\infty}^{\infty} w(x-y)G(y,t)\,\mathrm{d}y + \delta(x)\delta(t). \tag{6.111}$$

The latter can be solved using Fourier transform to give

$$G(x,t) = H(t) \int_{-\infty}^{\infty} \mathrm{e}^{\mathrm{i}kx} \mathrm{e}^{-(1-\mu\widehat{w}(k))t} \frac{\mathrm{d}k}{2\pi}, \tag{6.112}$$

where $\widehat{w}(k)$ is the Fourier transform of the weight distribution $w(x)$ and $H(0) = 0$ for Ito calculus. Having expressed the free action S_0 in terms of the inverse propagator, the free functional can be calculated explicitly by completing the square:

$$Z_0[J,\widetilde{J}] = \mathrm{e}^{\int \mathrm{d}x \int \mathrm{d}x' \int_0^T \mathrm{d}t \int_0^T \mathrm{d}t' \left[\widetilde{J}(x,t)G(x-x',t-t')J(x',t')\right]}. \tag{6.113}$$

Finally, the full generating functional can be expressed in terms of Z_0 by decomposing the full action as $S = S_0 + S_I$, where S_I is the interacting part of the action that includes the terms arising from initial conditions, multiplicative noise and nonlinear contributions to the firing rate function. Then

$$\begin{aligned} Z[J,\widetilde{J}] &= \int \mathcal{D}U\mathcal{D}\widetilde{U} \sum_{n=0}^{\infty} \frac{(-S_I[U,\widetilde{U}])^n}{n!} \mathrm{e}^{-S_0[U,\widetilde{U}]} \mathrm{e}^{\int \mathrm{d}x \int_0^T \mathrm{d}t [\widetilde{U}(x,t)J(x,t)+\widetilde{J}(x,t)U(x,t)]} \\ &= \sum_{n=0}^{\infty} \frac{(-S_I[\delta/\delta\widetilde{J},\delta/\delta J])^n}{n!} Z_0[J,\widetilde{J}]. \end{aligned} \tag{6.114}$$

Assuming that S_I is scaled by a small parameter, equation (6.114) is the starting point for a diagrammatic perturbation expansion of the moments and propagators based on Wicks theorem and Feynman graphs [228]. This has been developed in some detail by Buice *et al* [204, 205] within the context of a path integral representation of the neural master equation (6.48), which generalizes previous work on reaction diffusion systems [229, 231, 232]. One of the specific features assumed by Buice *et al* is that the zero activity state is an absorbing state. Consequently, renormalization group methods can be used to show that the associated stochastic neural field model belongs to the universality class of directed percolation. However, the existence of an absorbing state is not a general feature of stochastic neural field models such as equation (6.90), for which $g(U) > 0$ for all U.

Weak-noise limit. Another form of perturbation expansion occurs in the weak-noise limit. Suppose that the multiplicative noise term $g(U) \to \sigma g(U)$ with $\sigma \ll 1$. (In the case of a Langevin approximation of the neural master equation (6.48), $\sigma = 1/\sqrt{N}$, where N is the size of each local population [206, 207].) Performing the rescalings $\widetilde{U} \to \widetilde{U}/\sigma^2$ and $\widetilde{J} \to \widetilde{J}/\sigma^2$, the generating functional (6.106) becomes

$$Z[J,\widetilde{J}] = \int \mathcal{D}U\mathcal{D}\widetilde{U}\, \mathrm{e}^{-\frac{1}{\sigma^2}S[U,\widetilde{U}]} \mathrm{e}^{\frac{1}{\sigma^2}\int \mathrm{d}x \int_0^T \mathrm{d}t \left[\widetilde{U}(x,t)J(x,t)+\widetilde{J}(x,t)U(x,t)\right]}. \tag{6.115}$$

In the limit $\sigma \to 0$, the path integral is dominated by the 'classical' solutions $u(x,t), \widetilde{u}(x,t)$, which extremize the exponent of the generating functional:

$$\left.\frac{\delta S[U,\widetilde{U}]}{\delta U(x,t)}\right|_{\widetilde{U}=\widetilde{u},U=u} = -\widetilde{J}(x,t), \qquad \left.\frac{\delta S[U,\widetilde{U}]}{\delta \widetilde{U}(x,t)}\right|_{\widetilde{U}=\widetilde{u},U=u} = -J(x,t). \tag{6.116}$$

In the case of zero currents $J = \widetilde{J} = 0$, these equations reduce to

$$\frac{\partial u(x,t)}{\partial t} = \frac{\delta \mathcal{H}[u,\widetilde{u})}{\delta \widetilde{u}(x,t)}, \qquad \frac{\partial \widetilde{u}(x,t)}{\partial t} = -\frac{\delta \mathcal{H}[u,\widetilde{u})}{\delta u(x,t)}, \tag{6.117}$$

where we have set

$$S[U,\widetilde{U}] = \int \mathrm{d}x \int_0^T \mathrm{d}t\, \widetilde{U}(x,t)\dot{U}(x,t) - \int_0^T \mathrm{d}t\, \mathcal{H}[U,\widetilde{U}] - \int \mathrm{d}x\, \widetilde{U}(x,0)\Phi(x),$$

such that

$$\mathcal{H}[U,\widetilde{U}] = \int \mathrm{d}x\, \widetilde{U}(x,t) \left[-U(x,t) + \int w(x-y)F(U(y,t))\,\mathrm{d}y + \frac{1}{2}\widetilde{U}(x,t)g^2(U(x,t)) \right]. \tag{6.118}$$

Equations (6.117) take the form of a Hamiltonian dynamical system in which u is a 'coordinate' variable, $\widetilde{u}$ is its 'conjugate momentum' and $\mathcal{H}$ is the Hamiltonian. It immediately follows from the form of $\mathcal{H}$ that one type of classical solution is the mean-field solution $\widetilde{u}(x,t) \equiv 0$, which implies that $u(x,t)$ satisfies the scalar neural field equation (3.2). Interestingly, there are also non-mean-field classical solutions, $\widetilde{u}(x,t) \neq 0$, which play an important role in determining large deviations or rare event statistics in terms of optimal paths [207, 233]. Finally, note that the path integral (6.115) can be used to calculate 'semi-classical' corrections to the deterministic neural field equation in the weak noise limit by carrying out a perturbation expansion in σ and constructing the corresponding effective action [205, 228]. For example, the leading order correction to equation (3.2) takes the form

$$\frac{\partial v}{\partial t} = -v(x,t) + \int w(x-y)F(v(y,t))\,\mathrm{d}y + \frac{\sigma^2}{2}\int w(x-y)C(y,y,t)F''(v(y,t))\,\mathrm{d}y + \mathcal{O}(\sigma^4), \tag{6.119}$$

where C is the $\mathcal{O}(1)$ two-point correlation function

$$C(x,x',t) = \frac{1}{\sigma^2}\langle\langle U(x,t)U(x',t)\rangle\rangle - \langle\langle U(x,t)\rangle\rangle\langle\langle U(x',t)\rangle\rangle. \tag{6.120}$$

It is also possible to derive a corresponding evolution equation for the correlation function C [228, 205].

7. Discussion

As we have highlighted in this review, neural field theory provides a mathematical framework for developing large-scale population models of cortical dynamics. In particular, a continuum description of spatially structured biological neural networks allows many techniques from PDE theory to be adapted to the neural context. Although neural field models neglect information at the level of individual spikes, as well as the associated conductance-based mechanisms for generating such spikes, they have been remarkably successful in describing a wide range of phenomena at the population level. One of the outstanding challenges is determining to what extent the various spatially coherent dynamical states supported by neural fields persist when the discrete-like nature of spiking neurons is taken into account. In certain cases coherent states have been shown to persist. For example, a 1D network of spiking neurons can support a stable activity bump, although the bump can destabilize in the case of sufficiently fast synapses, which is not seen in the corresponding rate model [139, 140]. Spiking networks also support traveling pulses analogous to those found in rate-based neural field models with adaptation [234, 235]. Another important issue concerns how to go beyond mean-field theories so that higher-order statistical correlations between populations of neurons can also be determined. This in turn raises a number of questions regarding the nature of stochasticity at the population level (which we touched upon in section 6), the role of statistical correlations in information processing, and the spatial/temporal scale of such correlations.

Broadly speaking, current applications of neural fields can be divided into three distinct problem domains. The first, as exemplified by the phenomena of population tuning curves [26], geometric visual hallucinations [20] and binocular rivalry waves [117], requires understanding the feature-based anatomy of cortical connections. That is, in order to relate patterns of cortical activity predicted by neural field models with visual psychophysics and neurophysiology, it is necessary to consider how the spatial distribution of synaptic connections correlates with corresponding stimulus-based feature maps; in general such connections will be heterogeneous. Extensions to other sensory modalities such as audition also need to be

developed. Another important application domain concerns the use of neural fields in the forward modeling of brain imaging data based on EEG and functional magnetic imaging (fMRI), for example. One particularly interesting recent development is the use of brain-wave equations [21, 65, 22–24] to relate co-registered imaging modalities that combine the spatial resolution of EEG with the temporal resolution of fMRI [236]. Such forward modeling has to take into account the large-scale structural connectivity of the brain, the geometry of the folded three-dimensional cortical sheet, and the coupling between neural activity and blood flow (in order to determine the so-called fMRI BOLD signal) [237–240]. Moreover, in order to take proper account of the effects of dendritic filtering on the generation of extracellular electric fields and the EEG signal [241], it will be necessary to incorporate dendritic structure into neural field models along the lines outlined in [47]. The third problem domain involves more abstract neural field representations of dynamic cognitive processes [242, 243]. Here one of the major challenges is solving the associated inverse problem, that is, finding an appropriate synaptic weight kernel that generates a given trajectory in cognitive space. Such an inverse problem tends to be high-dimensional and ill-posed.

The last example suggests yet another interesting future direction of neural field theory, namely, to build upon the early work of Amari and collaborators on self-organizing neural fields [244, 245]. The basic idea is to combine the theory of bump formation in a lateral inhibition network (cortical layer) with competitive Hebbian learning dynamics on the feedforward weights from an input layer. It is found numerically that starting from a crude topographic map between the input layer and the cortical layer, the system evolves to a more refined continuous map that is dynamically stable. In the simpler one-dimensional case, conditions for the existence and stability of such a map can be derived analytically. Moreover, it can be shown that under certain circumstances the continuous topographic map undergoes a pattern forming instability that spontaneously breaks continuous translation symmetry, and the map becomes partitioned into discretized blocks; it has been suggested that these blocks could be a precursor for the columnar microstructure of cortex [244, 245]. Given that cortical columns tend to be associated with stimulus features such as ocular dominance and orientation (see section 5.2), this raises the interesting question whether or not such features could also emerge through the spontaneous symmetry breaking of self-organizing neural fields. This issue has recently been addressed in terms of spontaneous symmetry breaking [246]. For example, it can be shown that a binocular one-dimensional topographic map can undergo a pattern forming instability that breaks the underlying $\mathbb{Z}_2$ symmetry between left and right eyes. This leads to the spatial segregation of eye specific activity bumps consistent with the emergence of ocular dominance columns. Moreover a two-dimensional isotropic topographic map can undergo a pattern forming instability that breaks the underlying rotation symmetry. This leads to the formation of elongated activity bumps consistent with the emergence of orientation preference columns. A particularly interesting property of the latter symmetry breaking mechanism is that the linear equations describing the growth of the orientation columns exhibits a rotational shift-twist symmetry (see section 5.4), in which there is a coupling between orientation and topography. Such coupling has been found in experimentally generated orientation preference maps.

Acknowledgments

PCB would like to thank the National Science Foundation for its continuing support. PCB is also grateful to Professor Steve Coombes (University of Nottingham) for his careful reading of the manuscript.

References

[1] Milton J and Jung P 2003 *Epilepsy as a Dynamic Disease* (Berlin: Springer)
[2] Chervin R D, Pierce P A and Connors B W 1988 Periodicity and directionality in the propagation of epileptiform discharges across neocortex *J. Neurophysiol.* **60** 1695–713
[3] Pinto D, Patrick S L, Huang W C and Connors B W 2005 Initiation, propagation, and termination of epileptiform activity in rodent neocortex in vitro involve distinct mechanisms *J. Neurosci.* **25** 8131–40
[4] Richardson K A, Schiff S J and Gluckman B J 2005 Control of traveling waves in the mammalian cortex *Phys. Rev. Lett.* **94** 028103
[5] Wu J 2008 Propagating waves of activity in the neocortex: what they are, what they do *Neuroscientist* **14** 487–502
[6] Sompolinsky H and Shapley R 1997 New perspectives on the mechanisms for orientation selectivity *Curr. Opin. Neurobiol.* **5** 514–22
[7] Taube J S and Bassett J P 2003 Persistent neural activity in head direction cells *Cereb. Cortex* **13** 1162–72
[8] Fuster J M and Alexander G 1971 Neuron activity related to short-term memory *Science* **173** 652
[9] Wang X-J 2001 Synaptic reverberation underlying mnemonic persistent activity *Trends Neurosci.* **24** 455–63
[10] Wilson H R and Cowan J D 1972 Excitatory and inhibitory interactions in localized populations of model neurons *Biophys. J.* **12** 1–23
[11] Wilson H R and Cowan J D 1973 A mathematical theory of the functional dynamics of cortical and thalamic nervous tissue *Kybernetik* **13** 55–80
[12] Amari S 1977 Dynamics of pattern formation in lateral inhibition type neural fields *Biol. Cybern.* **27** 77–87
[13] Keener J P 1981 Waves in excitable media *SIAM J. Appl. Math.* **39** 528–48
[14] Kuramoto Y 1984 *Chemical Oscillations, Waves and Turbulence* (New York: Springer)
[15] Ermentrout G B 1998 Neural networks as spatio-temporal pattern-forming systems *Rep. Prog. Phys.* **61** 353–430
[16] Coombes S 2005 Waves, bumps and patterns in neural field theories *Biol. Cybern.* **93** 91–108
[17] Pinto D and Ermentrout G B 2001 Spatially structured activity in synaptically coupled neuronal networks: I. Traveling fronts and pulses *SIAM J. Appl. Math.* **62** 206–25
[18] Huang X, Troy W C, Yang Q, Ma H, Laing C R, Schiff S J and Wu J 2004 Spiral waves in disinhibited mammalian neocortex *J. Neurosci.* **24** 9897–902
[19] Ermentrout G B and Cowan J 1979 A mathematical theory of visual hallucination patterns *Biol. Cybern.* **34** 137–50
[20] Bressloff P C, Cowan J D, Golubitsky M, Thomas P J and Wiener M 2001 Geometric visual hallucinations, Euclidean symmetry and the functional architecture of striate cortex *Phil. Trans. R. Soc.* B **356** 299–330
[21] Nunez P I 1995 *Neocortical Dynamics and Human EEG Rhythms* (New York: Oxford University Press)
[22] Robinson P A, Rennie C J, Wright J J, Bahramali H, Gordon E and Rowe D I 2001 Prediction of electroencephalographic spectra from neurophysiology *Phys. Rev.* E **63** 021903
[23] Liley D J T, Cadusch P J and Dafilis M P 2002 A spatially continuous mean field theory of electrocortical activity *Network* **13** 67–113
[24] Steyn-Ross M L, Steyn-Rossand D A, Sleigh J W and Whiting D R 2003 Theoretical predictions for spatial covariance of the electroencephalographic signal during the anesthetic-induced phase transition: increased correlation length and emergence of spatial self-organization *Phys. Rev.* E **68** 021902
[25] Somers D C, Nelson S and Sur M 1995 An emergent model of orientation selectivity in cat visual cortical simple cells *J. Neurosci.* **15** 5448–65
[26] Ben-Yishai R, Lev Bar-Or R and Sompolinsky H 1995 Theory of orientation tuning in visual cortex *Proc. Natl Acad. Sci.* **92** 3844–8
[27] Camperi M and Wang X-J 1998 A model of visuospatial short-term memory in prefrontal cortex: recurrent network and cellular bistability *J. Comput. Neurosci.* **5** 383–405
[28] Laing C R, Troy W C, Gutkin B and Ermentrout G B 2002 Multiple bumps in a neuronal model of working memory *SIAM J. Appl. Math.* **63** 62–97
[29] Zhang K 1996 Representation of spatial orientation by the intrinsic dynamics of the head-direction cell ensemble: a theory *J. Neurosci.* **16** 2112–26
[30] Geise M A 1999 *Neural Field Theory for Motion Perception* (Dordrecht: Kluwer)
[31] Ermentrout G B and Terman D 2010 *Mathematical Foundations of Neuroscience* (Berlin: Springer)
[32] Hopfield J J 1984 Neurons with graded response have collective computational properties like those of two-state neurons *Proc. Natl Acad. Sci. USA* **81** 3088–92
[33] Connors B W and Long M A 2004 Electrical synapses in the mammalian brain *Annu. Rev. Neurosci.* **27** 393–418

[34] Hodgkin A L and Huxley A F 1952 A quantitative description of membrane and its application to conduction and excitation in nerve *J. Physiol.* **117** 500–44
[35] Coombes S and Bressloff P C 2005 *Bursting: The Genesis of Rhythm in the Nervous System* (Singapore: World Scientific Press)
[36] Izhikevich E 2006 *Dynamical Systems in Neuroscience: The Geometry of Excitability and Bursting* (Cambridge, MA: MIT Press)
[37] Byrne J H and Roberts J L 2004 *From Molecules to Networks: An Introduction to Cellular and Molecular Neuroscience* (Amsterdam: Elsevier)
[38] Fogelson A and Zucker R S 1985 Presynaptic calcium diffusion from various arrays of single channels. Implications for transmitter release and synaptic facilitation *Biophys. J.* **48** 1003–17
[39] Bertram R, Smith G D and Sherman A 1999 Modeling study of the effects of overlapping calcium microdomains on neurotransmitter release *Biophys. J.* **76** 735–50
[40] Markram H and Tsodyks M 1996 Redistribution of synaptic efficacy between neocortical pyramidal neurons *Nature* **382** 807–10
[41] Abbott L F, Varela J A, Sen K and Nelson S B 1997 Synaptic depression and cortical gain control *Science* **275** 220–4
[42] Abbott L F and Marder E 1998 Modelling small networks *Methods in Neuronal Modelling* 2nd edn ed C Koch and I Segev (Cambridge, MA: MIT Press) pp 361–410
[43] Zucker R S 1989 Short term synaptic plasticity *Annu. Rev. Neurosci.* **12** 13–31
[44] Rall W and Snir H A 1998 Cable theory for dendritic neurons *Methods in Neuronal Modelling* 2nd edn ed C Koch and I Segev (Cambridge, MA: MIT Press)
[45] Koch C 1999 *Biophysics of Computation* (Oxford: Oxford University Press)
[46] Tuckwell H C 1988 *Introduction to Theoretical Neurobiology* vol 1*: Linear Cable Theory and Dendritic Structure (Cambridge Studies in Mathematical Biology)* (Cambridge: Cambridge University Press)
[47] Bressloff P C and Coombes S 1997 Physics of the extended neuron *Int. J. Mod. Phys.* B **11** 2343–92
[48] Gerstner W and Kistler W 2002 *Spiking Neuron Models* (Cambridge: Cambridge University Press)
[49] Ermentrout G B 1994 Reduction of conductance-based models with slow synapses to neural nets *Neural Comput.* **6** 679–95
[50] Bressloff P C and Coombes S 2000 Dynamics of strongly coupled spiking neurons *Neural Comput.* **12** 91–129
[51] Brunel N and Hakim V 1999 Fast global oscillations in networks of integrate-and-fire neurons with low firing rates *Neural Comput.* **11** 1621–71
[52] Renart A, Brunel N and Wang X-J 2004 Mean-field theory of irregularly spiking neuronal populations and working memory in recurrent cortical networks *Computational Neuroscience: A Comprehensive Approach* ed J Feng (Boca Raton, FL: CRC Press) pp 431–90
[53] Tsodyks M, Pawelzik K and Markram H 1998 Neural networks with dynamic synapses *Neural Comput.* **10** 821–35
[54] Tabak J, Senn W, O'Donovan M J and Rinzel J 2000 Modeling of spontaneous activity in developing spinal cord using activity-dependent depression in an excitatory network *J. Neurosci.* **20** 3041–56
[55] Bart E, Bao S and Holcman D 2005 Modeling the spontaneous activity of the auditory cortex *J. Comput. Neurosci.* **19** 357–78
[56] Vladimirski B B, Tabak J, ODonovan M J and Rinzel J 2008 Episodic activity in a heterogeneous excitatory network, from spiking neurons to mean field *J. Comput. Neurosci.* **25** 39–63
[57] Benda J and Herz A V M 2003 A universal model for spike-frequency adaptation *Neural Comput.* **15** 2523–64
[58] Madison D V and Nicoll R A 1984 Control of the repetitive discharge of rat CA1 pyramidal neurones *in vitro* *J. Physiol.* **354** 319–31
[59] Stocker M, Krause M and Pedarzani P 1999 An apamin-sensitive Ca^{2+}-activated K^+ current in hippocampal pyramidal neurons *Proc. Natl Acad. Sci. USA* **96** 4662–7
[60] Swindale N V 1996 The development of topography in the visual cortex: a review of models *Network* **7** 161–274
[61] Kilpatrick Z P and Bressloff P C 2010 Effects of synaptic depression and adaptation on spatiotemporal dynamics of an excitatory neuronal network *Physica* D **239** 547–60
[62] Kilpatrick Z P and Bressloff P C 2010 Spatially structured oscillations in a two-dimensional neuronal network with synaptic depression *J. Comput. Neurosci.* **28** 193–209
[63] Kilpatrick Z P and Bressloff P C 2010 Stability of bumps in piecewise smooth neural fields with nonlinear adaptation *Physica* D **239** 1048–60
[64] Coombes S and Owen M R 2005 Bumps, breathers, and waves in a neural network with spike frequency adaptation *Phys. Rev. Lett.* **94** 148102
[65] Jirsa V K and Haken H 1997 A derivation of a macroscopic field theory of the brain from the quasi-microscopic neural dynamics *Physica* D **99** 503–26

[66] Coombes S, Lord G J and Owen M R 2006 Waves and bumps in neuronal networks with axo-dendritic synaptic interactions *SIAM J. Appl. Dyn. Syst.* **5** 552–74
[67] Hutt A, Bestehorn M and Wennekers T 2003 Pattern formation in intracortical neuronal fields *Network* **14** 351–68
[68] Atay F M and Hutt A 2005 Stability and bifurcations in neural fields with finite propagation speed and general connectivity *SIAM J. Appl. Math.* **65** 644–6
[69] Pinto D and Ermentrout G B 2001 Spatially structured activity in synaptically coupled neuronal networks: II. Lateral inhibition and standing pulses *SIAM J. Appl. Math.* **62** 226–43
[70] Cai D, Tao L, Shelley M and McLaughlin D W 2004 An effective kinetic representation of fluctuation-driven neuronal networks with application to simple and complex cells in visual cortex *Proc. Natl Acad. Sci. USA* **101** 7757–62
[71] Deco G, Jirsa V, Robinson P A, Breakspear M and Friston K 2008 The dynamic brain: from spiking neurons to neural masses and cortical fields *PLoS Comput. Biol.* **4** e1000092
[72] Faugeras O, Touboul J and Cessac B 2009 A constructive mean-field analysis of multi-population neural networks with random synaptic weights and stochastic inputs *Frontiers Comput. Neurosci.* **3** 1–28
[73] Jirsa V K and Kelso J A S 2000 Spatiotemporal pattern formation in neural systems with heterogeneous topologies *Phys. Rev.* E **62** 8462–5
[74] Bressloff P C 2001 Traveling fronts and wave propagation failure in an inhomogeneous neural network *Physica* D **155** 83–100
[75] Bressloff P C 2002 Bloch waves, periodic feature maps and cortical pattern formation *Phys. Rev. Lett.* **89** 088101
[76] Bressloff P C 2003 Spatially periodic modulation of cortical patterns by long-range horizontal connections *Physica* D **185** 131–57
[77] Robinson P A 2006 Patchy propagator, brain dynamics, and the generation of spatially structured gamma oscillations *Phys. Rev.* E **73** 041904
[78] Zhang L 2003 On the stability of traveling wave solutions in synaptically coupled neuronal networks *Differ. Integral Eqns.* **16** 513–36
[79] Coombes S and Owen M R 2004 Evans functions for integral neural field equations with Heaviside firing rate function *SIAM J. Appl. Dyn. Syst.* **4** 574–600
[80] Sandstede B 2007 Evans functions and nonlinear stability of traveling waves in neuronal network models *Int. J. Bifurcation Chaos Appl. Sci. Eng.* **17** 2693–704
[81] Kishimoto K and Amari S 1979 Existence and stability of local excitations in homogeneous neural fields *J. Math. Biol.* **7** 303–18
[82] Ermentrout G B and McLeod J B 1993 Existence and uniqueness of travelling waves for a neural network *Proc. R. Soc.* A **123** 461–78
[83] Coombes S and Schmidt H 2010 Neural fields with sigmoidal firing rates: approximate solutions *Discrete Continuous Dyn. Syst.* A **28** 1369–79
[84] Bressloff P C 2005 Pattern formation in visual cortex *Les Houches 2003: Methods and Models in Neurophysics* ed C C Chow, B Gutkin, D Hansel, C Meunier and J Dalibard (Amsterdam: Elsevier) pp 477–574
[85] Faugeras O, Veltz R and Grimbert F 2009 Persistent neural states: Stationary localized activity patterns in nonlinear continuous n-population, q-dimensional neural networks *Neural Comput.* **21** 147–87
[86] Veltz R and Faugeras O 2010 Local/global analysis of the stationary solutions of some neural field equations *SIAM J. Appl. Dyn. Syst.* **9** 954–98
[87] Coombes S, Venkov N A, Bojak I, Liley D T J and Laing C R 2007 Modeling electrocortical activity through improved local approximations of integral neural field equations *Phys. Rev.* E **76** 051901
[88] Laing C R and Troy W C 2003 PDE methods for nonlocal models *SIAM J. Appl. Dyn. Syst.* **2** 487–516
[89] Golomb D and Amitai Y 1997 Propagating neuronal discharges in neocortical slices: computational and experimental study *J. Neurophysiol.* **78** 1199–211
[90] Wu J-Y, Guan L and Tsau Y 1999 Propagating activation during oscillations and evoked responses in neocortical slices *J. Neurosci.* **19** 5005–15
[91] Lam Y W, Cohen L B, Wachowiak M and Zochowski M R 2000 Odors elicit three different oscillations in the turtle olfactory bulb *J. Neurosci.* **20** 749–62
[92] Delaney K R, Galperin A, Fee M S, Flores J A, Gervais R, Tank D W and Kleinfeld D 1994 Waves and stimulus-modulated dynamics in an oscillating olfactory network *Proc. Natl Acad. Sci. USA* **91** 669–73
[93] Prechtl J C, Cohen L B, Pesaran B, Mitra P P and Kleinfeld D 1997 Visual stimuli induce waves of electrical activity in turtle cortex *Proc. Natl Acad. Sci. USA* **94** 7621–6
[94] Xu W, Huang X, Takagaki K and Wu J 2007 Compression and reflection of visually evoked cortical waves *Neuron* **55** 119–29

[95] Benucci A, Frazor R A and Carandini M 2007 Standing waves and traveling waves distinguish two circuits in visual cortex *Neuron* **55** 103–17
[96] Han F, Caporale N and Dan Y 2008 Reverberation of recent visual experience in spontaneous cortical waves *Neuron* **60** 321–7
[97] Petersen C C H, Grinvald A and Sakmann B 2003 Spatiotemporal dynamics of sensory responses in layer 2/3 of rat barrel cortex measured *in vivo* by voltage-sensitive dye imaging combined with whole-cell voltage recordings and neuron reconstructions *J. Neurosci.* **23** 1298–309
[98] Rubino D, Robbins K A and Hatsopoulos N G 2006 Propagating waves mediate information transfer in the motor cortex *Nature Neurosci.* **9** 1549–57
[99] Lee U, Kim S and Jung K 2006 Classification of epilepsy types through global network analysis of scalp electroencephalograms *Phys. Rev.* E **73** 041920
[100] Ermentrout G B and Kleinfeld D 2001 Traveling electrical waves in cortex: insights from phase dynamics and speculation on a computational role *Neuron* **29** 33–44
[101] Kilpatrick Z P, Folias S E and Bressloff P C 2008 Traveling pulses and wave propagation failure in inhomogeneous neural media *SIAM J. Appl. Dyn. Syst.* **7** 161–85
[102] Coombes S and Laing C R 2011 Pulsating fronts in periodically modulated neural field models *Phys. Rev.* E **83** 011912
[103] Troy W C and Shusterman V 2007 Patterns and features of families of traveling waves in large-scale neuronal networks *SIAM J. Appl. Dyn. Syst.* **6** 263–92
[104] Shusterman V and Troy W C 2008 From baseline to epileptiform activity: a path to synchronized rhythmicity in large-scale neural networks *Phys. Rev.* E **77** 061911
[105] Bressloff P C and Folias S E 2005 Front bifurcations in an excitatory neural network *SIAM J. Appl. Math.* **65** 131–51
[106] Chen X 1997 Existence, uniqueness, and asymptotic stability of traveling waves in nonlocal evolution equations *Adv. Differ. Eqns.* **2** 125–60
[107] Kreyszig E 1978 *Introductory Functional Analysis with Applications* (New York: Wiley)
[108] Sandstede B 2002 Stability of travelling waves *Handbook of Dynamical Systems* vol 2 (Amsterdam: North-Holland) pp 983–1055
[109] Evans J 1975 Nerve axon equations iv: the stable and unstable impulse *Indiana Univ. Math. J.* **24** 1169–90
[110] Rubin J E 2004 A nonlocal eigenvalue problem for the stability of a traveling wave in a neuronal medium *Discrete Continuous Dyn. Syst.* **10** 925–40
[111] Pinto D, Jackson R K and Wayne C E 2005 Existence and stability of traveling pulses in a continuous neuronal network *SIAM J. Appl. Dyn. Syst.* **4** 954–84
[112] Folias S E and Bressloff P C 2005 Stimulus-locked traveling pulses and breathers in an excitatory neural network *SIAM J. Appl. Math.* **65** 2067–92
[113] Kapitula T, Kutz N and Sandstede B 2004 The Evans function for nonlocal equations *Indiana Univ. Math. J.* **53** 1095–126
[114] Wilson H R, Blake R and Lee S H 2001 Dynamics of traveling waves in visual perception *Nature* **412** 907–10
[115] Lee S H, Blake R and Heeger D J 2005 Traveling waves of activity in primary visual cortex during binocular rivalry *Nature Neurosci.* **8** 22–3
[116] Kang M, Heeger D J and Blake R 2009 Periodic perturbations producing phase-locked fluctuations in visual perception *J. Vision* **9** 8
[117] Bressloff P C and Webber M 2011 Neural field model of binocular rivalry waves *J. Comput. Neurosci.* at press (doi:10.1007/s10827-011-0351-y)
[118] Bressloff P C, Folias S E, Prat A and Li Y-X 2003 Oscillatory waves in inhomogeneous neural media *Phys. Rev. Lett.* **91** 178101
[119] Rinzel J and Terman D 1982 Propagation phenomena in a bistable reaction-diffusion system *SIAM J. Appl. Math.* **42** 1111–37
[120] Hagberg A and Meron E 1994 Pattern formation in non-gradient reaction-diffusion systems: the effects of front bifurcations *Nonlinearity* **7** 805–35
[121] Schutz P, Bode M and Purwins H-G 1995 Bifurcations of front dynamics in a reaction-diffusion system with spatial inhomogeneities *Physica* D **82** 382–97
[122] Hagberg A, Meron E, Rubinstein I and Zaltzman B 1996 Controlling domain patterns far from equilibrium *Phys. Rev. Lett.* **76** 427–30
[123] Blake R 2001 A primer on binocular rivalry, including current controversies *Brain Mind* **2** 5–38
[124] Blake R and Logothetis N 2002 Visual competition *Nature Rev. Neurosci.* **3** 1–11
[125] Laing C R and Chow C C 2002 A spiking neuron model for binocular rivalry *J. Comput. Neurosci.* **12** 39–53

[126] Shpiro A, Moreno-Bote R, Rubin N and Rinzel J 2007 Dynamical characteristics common to neuronal competition models *J. Neurophysiol.* **97** 37–54
[127] Shpiro A, Curtu R, Rinzel J and Rubin N 2009 Balance between noise and adaptation in competition models of perceptual bistability *J. Comput. Neurosci.* **27** 462–73
[128] Kilpatrick Z P and Bressloff P C 2010 Binocular rivalry in a competitive neural network with synaptic depression *SIAM J. Appl. Dyn. Syst.* **9** 1303–47
[129] Kang M, Lee S H, Kim J, Heeger D J and Blake R 2010 Modulation of spatiotemporal dynamics of binocular rivalry by collinear facilitation and pattern-dependent adaptation *J. Vision* **10** 1–15
[130] Keener J P 2000 Propagation of waves in an excitable medium with discrete release sites *SIAM J. Appl. Math.* **61** 317–4
[131] Coombes S, Schmidt H, Laing C R, Svansredt N and Wyller J A 2012 Waves in random neural media *Discrete Continuous Dyn. Syst.* A at press
[132] Schiff S J, Huang X and Wu J Y 2007 Dynamical evolution of spatiotemporal patterns in mammalian middle cortex *Phys. Rev. Lett.* **98** 178102
[133] Folias S E and Bressloff P C 2004 Breathing pulses in an excitatory neural network *SIAM J. Appl. Dyn. Syst.* **3** 378–407
[134] Laing C R 2005 Spiral waves in nonlocal equations *SIAM J Appl. Dyn.* **4** 588–606
[135] O'Keefe J and Recce M L 1993 Phase relationship between hippocampal place units and the EEG theta rhythm *Hippocampus* **3** 317–30
[136] Folias S E and Bressloff P C 2005 Breathers in two-dimensional neural media *Phys. Rev. Lett.* **95** 208107
[137] Lund J S, Angelucci A and Bressloff P C 2003 Anatomical substrates for functional columns in macaque monkey primary visual cortex *Cerebral Cortex* **12** 15–24
[138] Guo Y and Chow C C 2005 Existence and stability of standing pulses in neural networks: II. Stability *SIAM J. Appl. Dyn. Syst.* **4** 249–81
[139] Laing C R and Chow C C 2001 Stationary bumps in networks of spiking neurons *Neural Comput.* **13** 1473–94
[140] Chow C C and Coombes S 2006 Existence and wandering of bumps in a spiking neural network model *SIAM J. Appl. Dyn. Syst.* **5** 552–74
[141] Hansel D and Sompolinsky H 2004 Modeling feature selectivity in local cortical circuits *Methods of Neuronal Modeling* 2nd edn ed C Koch and I Segev (Cambridge, MA: MIT Press) pp 499–567
[142] Taylor J G 1999 Neural bubble dynamics in two dimensions: foundations *Biol. Cybern.* **80** 393–409
[143] Werner H and Richter T 2001 Circular stationary solutions in two-dimensional neural fields *Biol. Cybern.* **85** 211–7
[144] Owen M R, Laing C R and Coombes S 2007 Bumps and rings in a two-dimensional neural field: splitting and rotational instabilities *New J. Phys.* **378** 1–24
[145] Brody C D, Romo R and Kepecs A 2003 Basic mechanisms for graded persistent activity: discrete attractors, continuous attractors, and dynamic representations *Curr. Opin. Neurol.* **13** 204–11
[146] Xie X and Giese M 2002 Nonlinear dynamics of direction-selective recurrent neural media *Phys. Rev.* E **65** 051904
[147] Ermentrout G B, Jalics J Z and Rubin J E 2010 Stimulus-driven traveling solutions in continuum neuronal models with a general smooth firing rate function *SIAM J. Appl. Math.* **70** 3039–64
[148] Redish A, Elga A N and Touretzky D 1996 A coupled attractor model of the rodent head direction system *Network: Comput. Neural Syst.* **7** 671–85
[149] Xie X, Hahnsloer R H R and Seung H S 2002 Double-ring network model of the head-direction system *Phys. Rev.* E **66** 041902
[150] Seung H S, D D Lee D D, Reis B Y and Tank D W 2000 Stability of the memory of eye position in a recurrent network of conductance-based model neurons *Neuron* **26** 259–71
[151] Folias S E 2011 Nonlinear analysis of breathing pulses in synaptically coupled neural networks *SIAM J. Appl. Dyn. Syst.* **10** 744–87
[152] Bressloff P C 2005 Weakly interacting pulses in synaptically coupled excitable neural media *SIAM J. Appl. Math.* **66** 57–81
[153] Gutkin B, Laing C R, Colby C L, Chow C C and Ermentrout G B 2001 Turning on and off with excitation: the role of spike-timing asynchrony and synchrony in sustained neural activity *J. Comput. Neurosci.* **11** 121–34
[154] Fall C P, Lewis T J and Rinzel J 2005 Background-activity-dependent properties of a network model for working memory that incorporates cellular bistability *Biol. Cybern.* **93** 109–18
[155] Fall C P and Rinzel J 2006 An intracellular Ca^{2+} subsystem as a biologically plausible source of intrinsic conditional bistability in a network model of working memory *J. Comput. Neurosci.* **20** 97–107
[156] Turing A M 1952 The chemical basis of morphogenesis *Phil. Trans. Roy Soc.* B **237** 32–72

[157] Cross M C and Hohenberg P C 2003 Pattern formation outside of equilibrium *Rev. Mod. Phys.* **65** 851–1111
[158] Murray J D 2002 *Mathematical Biology* vols 1 and 2 (Berlin: Springer)
[159] Bressloff P C and Cowan J D 2002 Amplitude equation approach to contextual effects in visual cortex *Neural Comput.* **14** 493–525
[160] Tass P 2007 Oscillatory cortical activity during visual hallucinations *J. Biol. Phys.* **23** 21–66
[161] Ermentrout G B and Cowan J 1979 Temporal oscillations in neuronal nets *J. Math. Biol.* **7** 265–80
[162] Schwartz E 1977 Spatial mapping in the primate sensory projection: analytic structure and relevance to projection *Biol. Cybern.* **25** 181–94
[163] Blasdel G G 1992 Orientation selectivity, preference, and continuity in monkey striate cortex *J. Neurosci.* **12** 3139–61
[164] Gilbert C D 1992 Horizontal integration and cortical dynamics *Neuron* **9** 1–13
[165] Blasdel G G and Salama G 1986 Voltage-sensitive dyes reveal a modular organization in monkey striate cortex *Nature* **321** 579–85
[166] Bonhoeffer T and Grinvald A 1991 Iso-orientation domains in cat's visual cortex are arranged in pinwheel like patterns *Nature* **353** 429–31
[167] Obermayer K and Blasdel G G 1993 Geometry of orientation and ocular dominance columns in monkey striate cortex *J. Neurosci.* **13** 4114–29
[168] Hubel D H and Wiesel T N 1974 Sequence regularity and geometry of orientation columns in the monkey striate cortex *J. Comput. Neurol.* **158** 267–94
[169] Hubel D H and Wiesel T N 1974 Uniformity of monkey striate cortex: A parallel relationship between field size, scatter, and magnification factor *J. Comput. Neurol.* **158** 295–306
[170] LeVay S and Nelson S B 1991 Columnar organization of the visual cortex *The Neural Basis of Visual Function* ed A G Leventhal (Boca Raton, FL: CRC Press) pp 266–315
[171] Rockland K S and Lund J 1983 Intrinsic laminar lattice connections in primate visual cortex *J. Comput. Neurol.* **216** 303–18
[172] Gilbert C D and Wiesel T N 1983 Clustered intrinsic connections in cat visual cortex *J. Neurosci.* **3** 1116–33
[173] Malach R, Amirand Y, Harel M and Grinvald A 1993 Relationship between intrinsic connections and functional architecture revealed by optical imaging and *in vivo* targeted biocytin injections in primate striate cortex *Proc. Natl Acad. Sci. USA* **90** 0469–10473
[174] Yoshioka T, Blasdel G G, Levitt J B and Lund J S 1996 Relation between patterns of intrinsic lateral connectivity, ocular dominance, and cytochrome oxidase-reactive regions in macaque monkey striate cortex *Cerebral Cortex* **6** 297–310
[175] Bosking W H, Zhang Y, Schofield B and Fitzpatrick D 1997 Orientation selectivity and the arrangement of horizontal connections in tree shrew striate cortex *J. Neurosci.* **17** 2112–27
[176] Sincich L C and Blasdel G G 2001 Oriented axon projections in primary visual cortex of the monkey *J. Neurosci.* **21** 4416–26
[177] Angelucci A, Levitt J B, Walton E J S, Hupe J-M, Bullier J and Lund J S 2002 Circuits for local and global signal integration in primary visual cortex *J. Neurosci.* **22** 8633–46
[178] Hirsch J D and Gilbert C D 1991 Synaptic physiology of horizontal connections in the cat's visual cortex *J. Neurosci.* **11** 1800–9
[179] Gilbert C D, Das A, Ito M, Kapadia M and Westheimer G 1996 Spatial integration and cortical dynamics *Proc. Natl Acad. Sci. USA* **93** 615–22
[180] Bressloff P C and Cowan J D 2002 The visual cortex as a crystal *Physica* D **173**
[181] Bressloff P C, Cowan J D, Golubitsky M and Thomas P J 2001 Scalar and pseudoscalar bifurcations: pattern formation on the visual cortex *Nonlinearity* **14** 739–75
[182] Chossat P and Faugeras O 2009 Hyperbolic planforms in relation to visual edges and textures perception *PLoS Comput. Biol.* **5** e1000625
[183] Phleger B and Bonds A B 1995 Dynamic differentiation of $Gaba_A$-sensitive influences on orientation selectivity of complex cells in the cat striate cortex *Exp. Brain Res.* **104**
[184] Golubitsky M, Stewart I and Schaeffer D G 1988 *Singularities and Groups in Bifurcation Theory II* (Berlin: Springer)
[185] Bosch Vivancos I, Chossat P and Melbourne I 1995 New planforms in systems of partial differential equations with Euclidean symmetry *Arch. Ration. Mech.* **131** 199–224
[186] Kluver H 1966 *Mescal and Mechanisms of Hallucinations* (Chicago, IL: University of Chicago Press)
[187] Connors M, Stoffregen M and Ermentrout G B 2011 A model for the origin and properties of flicker-induced geometric phosphenes *PLoS Comput. Biol.* **7** e1002158
[188] Softky W R and Koch C 1993 The highly irregular firing of cortical cells is inconsistent with temporal integration of random EPSPS *J. Neurosci.* **13** 334–50

[189] Pakdaman K, Thieullen M and Wainrib G 2010 Fluid limit theorems for stochastic hybrid systems with application to neuron models *Adv. Appl. Probab.* **42** 761–94
[190] Faisal A A, Selen L P J and Wolpert D M 2008 Noise in the nervous system *Nature Rev. Neurosci.* **9** 292
[191] Abbott L F and van Vresswijk C 1993 Asynchronous states in networks of pulse-coupled oscillators *Phys. Rev.* E **48** 1483–90
[192] Gerstner W and Van Hemmen J L 1993 Coherence and incoherence in a globally coupled ensemble of pulse-emitting units *Phys. Rev. Lett.* **71** 312–5
[193] Brunel N 2000 Dynamics of sparsely connected networks of excitatory and inhibitory spiking neurons *J. Comput. Neurosci.* **8** 183–208
[194] Nykamp D and Tranchina D 2000 A population density method that facilitates large-scale modeling of neural networks: analysis and application to orientation tuning *J. Comput. Neurosci.* **8** 19–50
[195] Omurtag A, Knight B W and Sirovich L 2000 On the simulation of large populations of neurons *J. Comput. Neurosci.* **8** 51–63
[196] Ly C and Tranchina D 2007 Critical analysis of a dimension reduction by a moment closure method in a population density approach to neural network modeling *Neural Comput.* **19** 2032–92
[197] Rangan A V, Kovacic G and Cai D 2008 Kinetic theory for neuronal networks with fast and slow excitatory conductances driven by the same spike train *Phys. Rev.* E **77** 041915
[198] Ginzburg I and Sompolinsky H 1994 Theory of correlations in stochastic neural networks *Phys. Rev.* E **50** 3171–91
[199] Meyer C and van Vreeswijk C 2002 Temporal correlations in stochastic networks of spiking neurons *Neural Comput.* **14** 369–404
[200] Mattia M and Del Guidice P 2002 Population dynamics of interacting spiking neurons *Phys. Rev.* E **66** 051917
[201] Soula H and Chow C C 2007 Stochastic dynamics of a finite-size spiking neural network *Neural Comput.* **19** 3262–92
[202] El Boustani S and Destexhe A 2009 A master equation formalism for macroscopic modeling of asynchronous irregular activity states *Neural Comput.* **21** 46–100
[203] Hutt A, Longtin A and Schimansky-Geier L 2008 Additive noise-induces turing transitions in spatial systems with application to neural fields and the swift-Hohenberg equation *Physica* D **237** 755–73
[204] Buice M and Cowan J D 2007 Field-theoretic approach to fluctuation effects in neural networks *Phys. Rev.* E **75** 051919
[205] Buice M, Cowan J D and Chow C C 2010 Systematic fluctuation expansion for neural network activity equations *Neural Comput.* **22** 377–426
[206] Bressloff P C 2009 Stochastic neural field theory and the system-size expansion *SIAM J. Appl. Math.* **70** 1488–521
[207] Bressloff P C 2010 Metastable states and quasicycles in a stochastic Wilson–Cowan model of neuronal population dynamics *Phys. Rev.* E **85** 051903
[208] Laing C and Lord G J (eds) 2010 *Stochastic Methods in Neuroscience* (Oxford: Oxford University Press)
[209] van Kampen N G 1992 *Stochastic Processes in Physics and Chemistry* (Amsterdam: North-Holland)
[210] Gardiner C W 2009 *Handbook of Stochastic Methods* 4th edn (Berlin: Springer)
[211] van Vreeswijk C and Abbott L F 1993 Self-sustained firing in populations of integrate-and-fire neurons *SIAM J. Appl. Math.* **53** 253–64
[212] van Vreeswijk C and Sompolinsky H 1998 Chaotic balanced state in a model of cortical circuits *Neural Comput.* **10** 1321–71
[213] Amit D J and Brunel N 1997 Model of global spontaneous activity and local structured activity during delay periods in the cerebral cortex *Cereb Cortex* **7** 237–52
[214] Ohira T and Cowan J D 1997 Stochastic neurodynamics and the system size expansion *Proc. First Int. Conf. on Mathematics of Neural Networks* ed S Ellacott and I J Anderson (New York: Academic) pp 290–4
[215] Zeisler S, Franz U, Wittich O and Liebscher V 2008 Simulation of genetic networks modelled by piecewise deterministic Markov processes *IET Syst. Biol.* **2** 113–35
[216] Buckwar E and Riedler M G 2011 An exact stochastic hybrid model of excitable membranes including spatio-temporal evolution *J. Math. Biol.* **63** 1051–93
[217] Touboul J, Ermerntrout B, Faugeras O and Cessac B 2011 Stochastic firing rate models arXiv:1001.3872v1
[218] Touboul J, Hermann G and Faugeras O 2011 Noise-induced behaviors in neural mean field dynamics arXiv:1104.5425v1
[219] Sagues F, Sancho J M and Garcia-Ojalvo J 2007 Spatiotemporal order out of noise *Rev. Mod. Phys.* **79** 829–82
[220] Webber M and Bressloff P C 2011 Front propagation in stochastic neural fields *SIAM J. Appl. Dyn. Syst.* submitted

[221] Garcia-Ojalvo J and Sancho J M 1996 External fluctuations in a pattern-forming instability *Phys. Rev.* E **53** 5680–9
[222] Armero J, Casademunt J, Ramirez-Piscina L and Sancho J M 1998 Ballistic and diffusive corrections to front propagation in the presence of multiplicative noise *Phys. Rev.* E **58** 5494–500
[223] Brackley C A and Turner M S 2007 Random fluctuations of the firing rate function in a continuum neural field model *Phys. Rev.* E **75** 041913
[224] Novikov E A 1965 Functionals and the random-force method in turbulence theory *Sov. Phys.—JETP* **20** 1290
[225] Beggs J M and Plenz D 2004 Neuronal avalanches are diverse and precise activity patterns that are stable for many hours in cortical slice cultures *J. Neurosci.* **24** 5216–29
[226] Plenz D and Thiagarajan T C 2007 The organizing principles of neuronal avalanches: cell assemblies in the cortex? *Trends Neurosci.* **30** 101–10
[227] Bedard C and Destexhe A 2009 Macroscopic models of local field potentials the apparent $1/f$ noise in brain activity *Biophys. J.* **96** 2589–603
[228] Zinn-Justin J 2002 *Quantum Field Theory and Critical Phenomena* 4th edn (Oxford: Oxford University Press)
[229] Tauber U C 2007 Field-theory approaches to nonequilibrium dynamics *Lecture Notes Phys.* **716** 295–348
[230] Chow C C and Buice M 2011 Path integral methods for stochastic differential equations arXiv:nlin/105966v1
[231] Doi M 1976 Second quantization representation for classical many-particle systems *J. Phys. A: Math. Gen.* **9** 1465–77
[232] Peliti L 1985 Path integral approach to birth–death processes on a lattice *J. Physique* **46** 1469–83
[233] Elgart V and Kamenev A 2004 Rare event statistics in reaction-diffusion systems *Phys. Rev.* E **70** 041106
[234] Ermentrout G B 1998 The analysis of synaptically generated travelling waves *J. Comput. Neurosci.* **5** 191–208
[235] Bressloff P C 1999 Synaptically generated wave propagation in excitable neural media *Phys. Rev. Lett.* **82** 2979–82
[236] Bojak I, Ostendorp T F, Reid A T and Kotter R 2010 Connecting mean field models of neural activity to EEG and fMRI data *Brain Topogr.* **23** 139–49
[237] Jirsa V K, Jantzen K J, Fuchs A and Scott Kelso J A 2001 Neural field dynamics on the folded three-dimensional cortical sheet and its forward EEG and MEG *Information Processing in Medical Imaging* ed V K Jirsa (Berlin: Springer) pp 286–99
[238] Breakspear M and Jirsa V K 2007 Neuronal dynamics and brain connectivity *Handbook of Brain Connectivity* ed V K Jirsa and A R McIntosh (Berlin: Springer) pp 3–64
[239] Honey C J, Kotter R, Breakspear M and Sporns O 2007 Network structure of cerebral cortex shapes functional connectivity on multiple time scales *Proc. Natl Acad. Sci. USA* **104** 10240–5
[240] Valdes-Sosa P A, Sanchez-Bornot J M, Sotero R C, Iturria-Medina Y, Aleman-Gomez Y, Bosch-Bayard Y J, Carbonell F and Ozaki T 2009 Model driven EEG/fMRI fusion of brain oscillations *Human Brain Mapping* **30** 2701–21
[241] Linden H, Pettersen K H and Einevoll G T 2010 Intrinsic dendritic filtering gives low-pass power spectra of local field potentials *J. Comput. Neurosci.* **29** 423–44
[242] Erlhagen W and Schroner G 2002 Dynamic field theory of movement preparation *Psych. Rev.* **109** 545–72
[243] Graben P B and Potthast R 2009 Inverse problems in dynamic cognitive modeling *Chaos* **19** 015103
[244] Takeuchi A and Amari S 1979 Formation of topographic maps and columnar microstructures in nerve fields *Biol. Cybern.* **35** 63–72
[245] Amari S 1980 Topographic organization of nerve fields *Bull. Math. Biol.* **42** 339–64
[246] Bressloff P C 2005 Spontaneous symmetry breaking in self-organizing neural fields *Biol. Cybern.* **93** 256–74
[247] Amari S 2011 private communication